Measurement of the J/ψ–Cross Section and Double–Spin Asymmetries in Vector Meson Production in Polarised Lepton–Nucleon Scattering at HERMES

D i s s e r t a t i o n

zur Erlangung des akademischen Grades

d o c t o r r e r u m n a t u r a l i u m

(Dr. rer. nat.)

im Fach Physik

eingereicht an der

Mathematisch–Naturwissenschaftlichen Fakultät I

der Humboldt–Universität zu Berlin

von

Diplom Physiker

Falk Meißner

geboren am 28. Januar 1967 in Quedlinburg

Präsident der Humboldt–Universität zu Berlin
Prof. Dr. Dr. h.c. Hans Meyer

Dekan der Mathematisch–Naturwissenschaftlichen Fakultät I
Prof. Dr. Jürgen Rabe

Gutachter:
Prof. Dr. Thomas Lohse
Prof. Dr. Paul Söding
Prof. Dr. Klaus Rith

Tag der mündlichen Prüfung:
14. Februar 2000

Contents

1. Introduction **1**

2. Phenomenology of Vector Meson Production **5**
2.1. Diffractive Vector Meson Production 5
2.1.1. Kinematics 5
2.1.2. Simple Optical Model of Diffraction 7
2.1.3. Vector Meson Dominance Model 9
2.1.4. Regge Theory 11
2.1.5. Two–Gluon Exchange Model 14
2.1.6. Off–Forward Parton Distributions 17
2.1.7. Perturbative QCD at HERMES Energy 22
2.2. Photon–Gluon Fusion and J/ψ Production 24
2.2.1. Colour Singlet Model 25
2.2.2. Colour Octet Mechanism 27
2.2.3. Spin Asymmetries in Inelastic Charm Production 28

3. The HERMES Experiment **31**
3.1. Polarised Beam 32
3.2. Internal Gas Target 33
3.3. The HERMES-Spectrometer 36

4. Measurement of the J/ψ Cross Section **41**
4.1. Data Samples 42
4.2. Burst Selection and Data Quality 43
4.3. Event Selection 46
4.4. Comparison of Data to Monte Carlo Simulation 51
4.5. Luminosity Determination 54
4.6. Trigger 56
4.7. Yields 61
4.8. Acceptance and Efficiencies 63
4.9. Electroproduction Cross Section 70
4.10. Photon Flux for J/ψ Production at HERMES 73
4.11. J/ψ Photoproduction Cross Section 77

5. Spin Dependence in Exclusive Vector Meson Production **79**
5.1. Helicity Analysis 79
5.1.1. Spin Density Matrix Elements and Determination of R 80
5.1.2. Spin Density Matrix Elements for a Polarised Target 84
5.2. Double–Spin Asymmetries in QCD Models 85

5.2.1. Double–Spin Asymmetries in Exclusive J/ψ Production 85
5.2.2. Double–Spin Asymmetry in Exclusive ρ Production 87

6. Analysis of Double–Spin Asymmetries **89**
6.1. Experimental Aspects 89
6.1.1. Experimental Extraction of Spin Asymmetries 89
6.1.2. Data Quality for Beam and Target Polarisation 91
6.2. Spin Asymmetries in J/ψ Production 93
6.3. Event Selection for Exclusive ρ Mesons 95
6.4. Comparison of ρ Data to Monte Carlo Simulation 98
6.5. Treatment of Background in ρ Data Sample 99
6.6. Experimental Asymmetry $A_{||}^{\rho}$ in Exclusive ρ Production 103
6.6.1. Systematic Studies on $A_{||}^{\rho}$ 103
6.6.2. Dependence of $A_{||}^{\rho}$ on Kinematic Variables 106
6.7. Photon Absorption Asymmetry A_1^{ρ} in Exclusive ρ Production 108
6.7.1. Determination of A_1^{ρ} 108
6.7.2. Dependence of A_1^{ρ} on Kinematic Variables 110
6.8. Possible Interpretations of A_1^{ρ} 113

7. Summary and Outlook **115**

A. Appendices **117**
A.1. Deep–Inelastic Lepton–Nucleon Scattering and Structure Functions 117
A.2. Definition of Photon Polarisations 120
A.3. Photon–Nucleon Scattering and Determination of Photon Fluxes 121
A.4. Polarised Deep–Inelastic Scattering 125

Bibliography **129**

1. Introduction

This thesis describes the measurement of double–spin asymmetries in ρ and J/ψ vector meson production in lepton–nucleon scattering. A measurement of the J/ψ cross section was performed complementing the asymmetry analysis. The analysis is based on the 1995 through 1997 data taken at the HERMES experiment. No previous data exist on double–spin asymmetries in exclusive processes; possible interpretations of such asymmetries are presently under intense theoretical discussion.

Deep–inelastic lepton–nucleon scattering experiments have been a powerful tool to investigate the internal structure of the nucleon. Deep–inelastic scattering (DIS) is defined by the kinematic region of large energy and momentum transfer by the virtual photon, where its wavelength is small enough to resolve the internal structure of the nucleon. In the quark–parton model, the structure of the nucleon can be described by the unpolarised structure functions F_1 and F_2 and the polarised spin structure functions g_1 and g_2. About half of the nucleon momentum is carried by valence and sea quarks, the other half by gluons, the mediators of the strong interaction between quarks. Information on the composition of the nucleon spin can be acquired by experiments using a polarised lepton beam and a polarised target, like the HERMES experiment. A summary of the nucleon structure functions in deep–inelastic scattering is presented in Appendix A.1.

The spin of the nucleon can be expressed as the sum of the contributions from quarks ($\Delta\Sigma$), gluons (ΔG) and angular momenta (ΔL)

$$\frac{1}{2}\hbar = S_z = \frac{1}{2}\Delta\Sigma + \Delta G + \Delta L. \tag{1.1}$$

The spin fraction carried by the quarks $\Delta\Sigma = \Delta u + \Delta d + \Delta s$ includes both valence and sea contributions $\Delta q = \Delta q_v + \Delta q_s$ of the three light quark flavours. It is accessible by the measurements of spin asymmetries in inclusive deep–inelastic scattering, where only the scattered lepton is analysed (cf. Appendix A.4). As a surprise, it was found in 1988 that the fraction of the nucleon spin carried by quarks is consistent with zero: $\Delta\Sigma = 0.14 \pm 0.23$ [EMC:88]. Present data yield a value of $\Delta\Sigma = 0.29 \pm 0.09$ [E143:98], still much less than $\Delta\Sigma = 0.57$ as expected from the quark–parton model. The contribution of the different quark flavours can be separated by semi–inclusive asymmetry measurements, when a hadron is analysed in addition to the scattered lepton. This hadron is the result of the fragmentation process the quark undergoes after it is struck by the photon, hence it can serve as a tag for the flavour of the struck quark [SMC:98b, HERMES:99b].

In the quark–parton model the nucleon consists of non–interacting point–like objects, therefore it cannot describe the contribution of gluons to the total momentum and spin of the nucleon. In perturbative QCD the interaction between quarks is mediated by gluons yielding

to a Q^2 dependence of the structure functions. The analysis of this Q^2 dependence of the spin structure function g_1 in terms of QCD–evolution equations [GL:72, Dok:77, AP:77] allows an indirect determination of the polarised gluon distributions with presently large theoretical uncertainties [E154:97, SMC:98a, LSS:98, dFSS:98, ABFR:98].

A more direct measurement of the gluon contribution ΔG to the nucleon spin can be achieved in polarised lepton–nucleon scattering through the analysis of double–spin asymmetries in the photon–gluon fusion process. This process can be identified by detection of final hadronic states containing charm quarks. An asymmetry in inelastic charm production can be related to $\Delta G/G$, since the mass of the charm quark provides the hard scale of the process and allows for reliable QCD calculations [Wat:81, GR:88]. In open charm production, the $c\bar{c}$ pair emitted by the photon does not form a bound state and both charm quarks independently undergo a fragmentation process into D mesons. Open charm production is theoretically well understood, but the detection of D mesons is difficult. In the case of the J/ψ meson, the two di–leptonic decay channels are a clean experimental signature, but several production processes have to be distinguished: Inelastic J/ψ production in photon–gluon fusion can be successfully described by the Colour Singlet Model [BJ:81] and its extension, the Colour Octet Mechanism [BBL:95]. In addition, a significant contribution from diffractive processes to J/ψ production has to be considered.

If a pair of light quarks is produced instead of a pair of charm quarks, the photon–gluon fusion process cannot be clearly identified via the hadronic final state. Nevertheless, it is accessible by analysing events with two jets (or at lower energy by analysing pairs of hadrons) with high transverse momenta that are characteristic of this process [BvHK:98].

Spin dependence in diffractive vector meson production has been a field of interest for a long time. The spin degrees of freedom in the cross section can be described by spin density matrix elements, measured via angular distributions of vector meson production and decay [SW:73]. By now, only the helicity transfer from the virtual photon to the vector meson and the nature of the exchanged particle in a diffractive interaction have been considered. The spin of the target nucleon was not taken into account, yet.

The theoretical understanding of double–spin asymmetries in diffractive processes, i.e. its dependence from the polarisation of beam and target, is rather limited. This is in contrast to the case of deep–inelastic scattering, were spin asymmetries are analysed to measure the spin structure functions of the nucleon. The naive expectation from models of vector meson production based on Regge theory is a zero asymmetry. In perturbative QCD the diffractive process can be described as exchange of two gluons. In this model only small asymmetries are predicted for exclusive J/ψ production [VM:98b, VM:98a].

Recently the description of certain exclusive leptoproduction processes like deep–virtual Compton scattering (DVCS) [Ji:97a, Ji:97b, Rad:96] and meson production [Rad:97, CFS:97] in terms of off–forward parton distributions (OFPD's) became a field of increasing theoretical interest. Off-forward parton distributions combine the properties of the usual parton distributions and of elastic form factors. It was shown [Ji:97a, Ji:97b] that their second moments are related to the sum of quark spins and angular momenta. Their study may open the way for an experimental access to the completely unknown contribution ΔL of angular momenta to the nucleon spin. For the analysis of vector meson production, OFPD's are of special interest since they might become a tool to relate the diffractive process to the internal (spin) structure of the nucleon.

This thesis is ordered as follows: The phenomenology of vector meson production is summarised in Chapter 2. Here, a general discussion of diffractive processes is followed by the discussion of Regge theory, QCD models of two–gluon exchange, and a summary of the concept of off–forward parton distributions and their relation to exclusive processes. Inelastic charm production in photon–gluon fusion and the relation of spin asymmetries in this process to the contribution of gluons to the nucleon spin are discussed in Section 2.2.

The HERMES experiment is capable of studying vector meson production because of the large angular and momentum acceptance of its forward spectrometer and its good particle identification system. In Chapter 3 the experimental setup is briefly described. An extensive search for charm signals has been carried out in the HERMES data of the years 1995 to 1997 to evaluate the possibility to provide information on $\Delta G/G$ via charm production at HERMES. By now, only a very small signal could be verified for D–mesons; this subject is still under study and not part of this thesis. Small but clean signals were extracted in both di–leptonic J/ψ decay channels. In order to understand these signals a J/ψ cross section measurement described in in Chapter 4 was performed: Sections 4.1 to 4.4 cover the extraction of the signals from the data and the comparison with Monte Carlo simulations. Sections 4.5 to 4.9 describe systematic studies, and the determination of acceptance and efficiency corrections. The photon flux for J/ψ production at HERMES and the comparison of the present cross section result to world data are discussed in Sections 4.10 and 4.11.

Spin dependence in diffractive vector meson production is discussed in Chapter 5. The formalism of the helicity analysis is reviewed in Section 5.1. As a necessary prerequisite for the asymmetry analysis, the results of the HERMES experiment [HERMES:99c] on a measurement of spin density matrix elements and the ratio R of the photon absorption cross sections for longitudinal and transverse photons are summarised in Section 5.1.1. Predictions of two QCD models for double–spin asymmetries in exclusive J/ψ and ρ production are discussed in Section 5.2.

Chapter 6 describes in detail the analyses of double–spin asymmetries in exclusive vector meson production: The ρ meson decay $\rho^0 \to \pi^+\pi^-$ and the two di–leptonic J/ψ decays $J/\psi \to e^+e^-$, $J/\psi \to \mu^+\mu^-$ have been analysed. About 2800 ρ and 20 J/ψ events were found using the 1996 and 1997 data taken with the longitudinally polarised hydrogen target.

For the analysis of double–spin asymmetries in exclusive vector meson production, the formalism of asymmetry measurements in polarised deep–inelastic scattering is employed which is summarised in Appendix A.4. The asymmetry analysis for the small J/ψ signal is described in Section 6.2. In the case of the ρ meson the available statistics allow for detailed systematic studies covered by Sections 6.3 to 6.6; they include the comparison of the data to Monte Carlo simulations, different methods of background subtraction, and stability studies for the spin asymmetry. The conversion of the measured lepton–nucleon asymmetry to the photon–nucleon asymmetry is discussed in Section 6.7.

A significant positive longitudinal double–spin asymmetry in exclusive ρ vector meson production is observed at the HERMES experiment. Possible interpretations of this surprising result are discussed in Section 6.8.

2. Phenomenology of Vector Meson Production

2.1. Diffractive Vector Meson Production

Diffraction combines the aspects of the particle and the wave–like nature of the strong interaction in high–energy scattering. The differential cross sections found in elastic hadron–hadron scattering show the characteristic pattern known from diffractive processes in classical optics. A dominant peak in the forward direction is accompanied by minima and maxima and the cross section varies slowly with energy for short wavelengths, i.e. large energies. No quantum numbers, except angular momentum are exchanged.

Diffractive vector meson production in lepton–nucleon scattering can be described by the vector meson dominance model (VMD). The virtual photon fluctuates into an intermediate hadronic $q\bar{q}$ state. This intermediate state scatters off the target nucleon by a strong hadronic interaction similar to the hadron–hadron scattering discussed above, subsequently the final vector meson is formed. The strong interaction itself can be either described by the exchange of trajectories in the phenomenological Regge theory or by exchange of gluons and quarks in perturbative QCD models.

2.1.1. Kinematics

Exclusive diffractive vector meson production in lepton–nucleon scattering is depicted in Figure 2.1. At HERMES energies $(E_e = 27.5)$ GeV, the lepton–nucleon interaction is dominated by the exchange of a virtual photon, its invariant mass is defined by the square of its four–momentum q

$$q^2 = (k-k')^2 < 0; \qquad Q^2 = -q^2 \stackrel{lab}{=} 4EE'sin^2\left(\frac{\theta}{2}\right). \tag{2.1}$$

Here k and k' denote the four–momenta of the incoming and outgoing leptons and the variable Q^2 was introduced for convenience. In the laboratory frame, Q^2 is related to the polar scattering angle θ and the energy E' of the outgoing lepton. Here, the electron mass is neglected. At HERMES, the target nucleons are at rest $p = (M, \vec{0})$ and the centre–of–mass energy s of the lepton–nucleon system is defined by the beam energy E

$$s = (k+p)^2 \stackrel{lab}{=} M^2 + 2ME. \tag{2.2}$$

The centre–of–mass energy of the photon-nucleon system is given by

$$W^2 = (q+p)^2 \stackrel{lab}{=} M^2 + 2M\nu - Q^2, \tag{2.3}$$

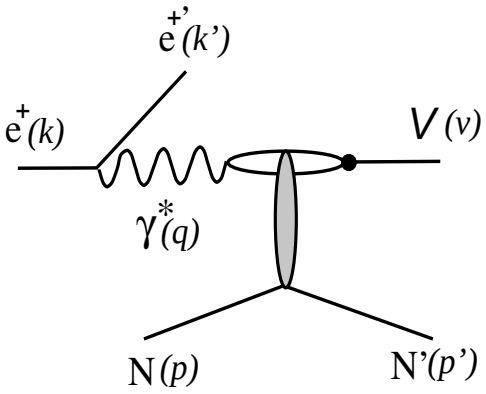

Figure 2.1.: Exclusive diffractive vector meson production in lepton nucleon scattering.

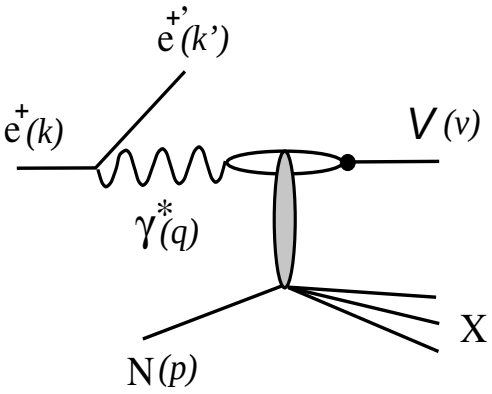

Figure 2.2.: Diffractive vector meson production with dissociation of the target.

where ν denotes the photon energy

$$\nu = \frac{p \cdot q}{M} \overset{lab}{=} E - E'. \tag{2.4}$$

In diffractive vector meson production the photon–nucleon cross section primarily depends on the four–momentum transfer t to the target

$$t = (q - v)^2, \tag{2.5}$$

where v is the four–momentum of the vector meson. At the minimum $t = t_{min}$ that is kinematically necessary for the interaction to take place, the momentum of the final state vector meson V is parallel to the direction of the incoming photon γ in the photon–nucleon centre–of–mass system [1]

$$t_{min} = t(\mathrm{V}||\gamma^*). \tag{2.6}$$

The difference t' between t and t_{min} is the four–momentum–transfer above the threshold

$$t' = t - t_{min} \tag{2.7}$$

Note that all three variables t, t_{min} and t' have negative values by definition. In order to select the exclusive diffractive process the energy transfer ΔE between the photon and the target can be used as a measure of exclusivity

$$\Delta E = \frac{(M_X^2 - M^2)}{2M} \overset{lab}{=} \nu - E_v + \frac{t}{2M}. \tag{2.8}$$

In the case of the exclusive process shown in Figure 2.1, no energy is transfered to the target and the target nucleon stays intact ($p'^2 = p^2$). Both ΔE and t_{min} are close to zero hence t' corresponds to the total four–momentum transfer t

$$\Delta E \cong 0; \quad t_{min} \cong 0; \quad t' \sim t.$$

[1] In the photon–nucleon centre–of–mass system t_{min} can be calculated using the relations [C+:98]

$$t_{min} = (\hat{E}_\gamma - \hat{E}_V)^2 - (|\hat{p}_\gamma| - |\hat{p}_\rho|)^2,$$

$$\hat{E}_\gamma = \frac{W^2 - Q^2 - M^2}{2W}, \quad |\hat{p}_\gamma| = \sqrt{\hat{E}_\gamma^2 + Q^2}, \quad \hat{E}_V = \frac{W^2 + M_V^2 - M_x^2}{2W}, \quad |\hat{p}_V| = \sqrt{\hat{E}_V^2 - M_V^2},$$

with M_V the reconstructed mass of the vector meson.

The exclusive diffractive process is also refered to as 'elastic' since it can be viewed as the elastic scattering of the virtual hadronic $q\bar{q}$ state with the target nucleon.

In the case of a non–zero energy transfer ΔE to the target the target nucleon dissociates. Figure 2.2 depicts diffractive vector meson production with target dissociation. The background of these non–exclusive diffractive events as well as the background from deep–inelastic scattering can be suppressed by the requirement of $\Delta E \sim 0$.

2.1.2. Simple Optical Model of Diffraction

Elastic hadron-hadron scattering, depicted in Figure 2.3 can be explained using concepts of classical optical diffraction. A detailed discussion of this ansatz and its comparison with data can be found in [Per:74] or [FH:95].

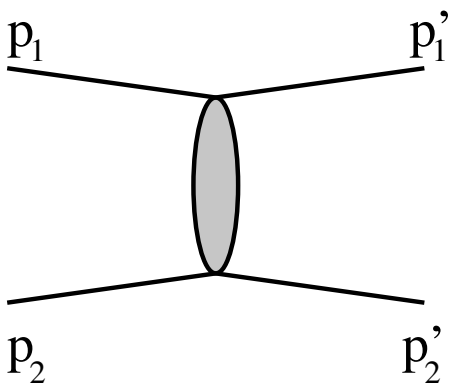

Figure 2.3.: Two body interaction of elastic hadron–hadron scattering.

In the simplest optical model of diffraction, an incident plane wave is scattered on a totally absorbing black disk, or sphere, of well defined radius R. The resulting angular distribution of the scattering process reflects the Fourier transform of the spatial distribution of the obstacle; it shows a strong peak in the forward direction ($\theta = 0$) and first minima at $\theta_{min} = \pm\lambda/2R$. Here the wavelength is given by $\lambda = 2\pi/k$ with the wave vector $k = p/\hbar$ and $\hbar = c = 1$.

The differential hadron–hadron cross section primarily depends on the four–momentum transfer squared between the two hadrons $t = (p_1 - p_1')^2 = (p_2' - p_2)^2$. With the momentum p of the colliding particles and the scattering angle θ in the centre–of–mass system, the four–momentum transfer t is defined by $-t \equiv q^2 = (2p \sin\frac{\theta}{2})^2$. At small scattering angles t can be approximated by $t \sim (p\theta)^2$. In the optical model an expression for the differential cross section in terms of the first order Bessel function J_1 is given that is independent of the energy of the incident particle [Per:74]

$$\frac{d\sigma_{el}}{d|t|} = \pi R^4 \left| \frac{J_1(R\sqrt{|t|})}{R\sqrt{|t|}} \right|^2 , \tag{2.9}$$

where J_1 has minima at $R\sqrt{|t|} = 3.83, 7.02, ...$ and R is the nucleon radius.

Figure 2.4 combines data on elastic proton–proton scattering from various experiments, where the energy of the incident protons is given beside the curves. Clearly visible is the diffractive forward peak at low $|t| \leq 1\ \mathrm{GeV}^2$. At $|t| \to 0$ the differential cross section depends only weakly on the energy and is about the same for all curves. For higher energies, a first minimum appears at $|t| = 1.15\ \mathrm{GeV}^2$. Using Equation 2.9 yields an approximate nucleon radius of about of $R = 0.7$ fm. In Figure 2.5 a simulation of Equation 2.9 is shown. Even the simple model of scattering a plane wave is able to reproduce the basic properties of the elastic pp interaction. However, it fails to predict quantitatively the ratio of the elastic to the total cross section and their energy dependence.

Nucleons do not have a sharply defined surface and the optical model can be improved by using a 'grey' scattering centre with a Gaussian density distribution. This density or profile

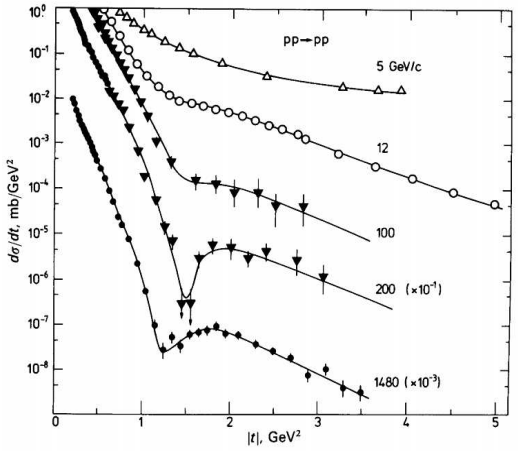

Figure 2.4.: Differential cross section $d\sigma/d|t|$ for elastic pp scattering. The figure is taken from [Per:87].

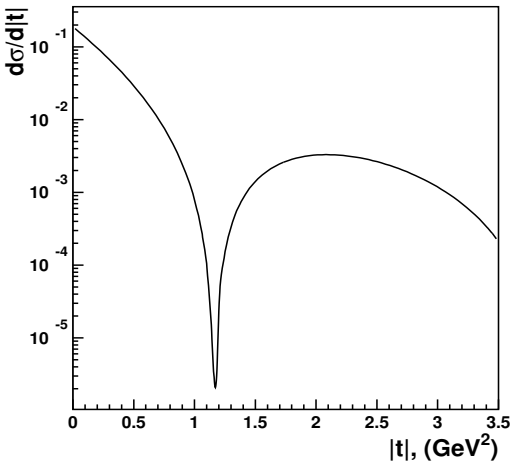

Figure 2.5.: Simulation of the differential cross section $d\sigma/d||t|$ for elastic pp scattering using Equation 2.9; the radius R is taken to be 0.7 fm.

describes the probability that the scattering takes place at a certain radius from the centre. The Gaussian shape yields a cross section that falls exponentially with t

$$\frac{d\sigma}{d|t|} = \left.\frac{d\sigma}{d|t|}\right|_{|t|=0} e^{-b|t|}. \tag{2.10}$$

The exponential slope b for the 'grey' disk can be related to the radius R of the 'black' disk by $b = R^2/4$ [Per:74]. In the region of small $|t| \lesssim 0.5$ GeV^2 the slope b can be obtained by the fit of a straight line to the semilogarithmic plots of Figure 2.4; typical values of b are between 5 to 13 GeV^{-2}.

At high energies, b cannot be interpreted as the radius of a single proton. But instead, it describes the strong interaction of two extended hadronic objects and can be interpreted as the quadratic sum of the Gaussian width of both objects [FH:95]

$$b \propto R_1^2 + R_2^2. \tag{2.11}$$

A diffractive peak at small values of $|t|$ has been observed in many hadron–hadron interactions: in baryon–baryon scattering like pp and $p\bar{p}$, as well as in meson–baryon interactions like πp, $\bar{\pi} p$, $\bar{K} p$, and Kp. Predicted by the Pomerancuk theorem, the cross sections for diffractive scattering of particle and antiparticle off the same target become equal at higher energies [Per:74], which is a consequence of the isospin invariance of the strong interaction. Therefore, the basic properties of diffraction are independent of the quark composition of the hadrons.

The optical wave description neglects the spin of the particles and diffractive scattering takes place between two spin-1/2 particles as well as between pseudo–scalar and spin–1/2 particles. Therefore, no dependence of the interaction on a possible spin polarisation of the two interacting hadrons is expected. On the other hand, large single–spin [2] and double–spin asymmetries have been observed in elastic pp scattering on transversely polarised targets with polarised and unpolarised beams. [C$^+$:78, F$^+$:78, C$^+$:90]. The nature of these observed

[2] If only the target is polarised and the beam is unpolarised (or vice versa) a single–spin cross–section asymmetry is measured between two opposite spin states of the target (or the beam).

asymmetries is still unexplained. They are most prominent at large momentum transfer outside of the region of the diffractive forward peak, which might point to an underlying hard scattering process. A review can be found in [Kri:90].

2.1.3. Vector Meson Dominance Model

In the previous section diffraction has been discussed in the context of elastic hadron–hadron scattering. Diffractive vector meson production in lepton–nucleon scattering can be related to the hadron–hadron interaction via the hadronic structure of the photon described by the vector meson dominance model (VMD) [Sak:60].

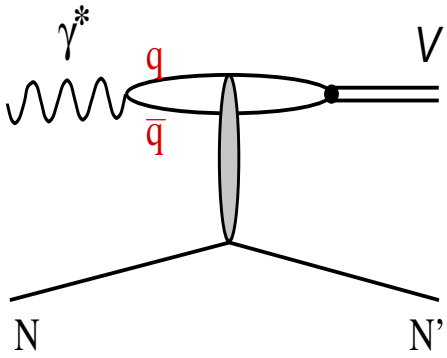

Figure 2.6.: Schematic graph of elastic vector meson photoproduction in the vector meson dominance model.

Figure 2.6 depicts the principle of the photon–nucleon interaction. The lepton–photon vertex is omitted here, since it is exactly calculable in QED and replaced by a flux of virtual photons (cf. Appendix A.3 and Section 4.10). The virtual photon fluctuates into a virtual $q\bar{q}$ pair with photon quantum numbers. Subsequently, by a purely hadronic strong interaction the intermediate $q\bar{q}$ state is shifted onto the mass shell and forms the vector meson. An extended discussion of the model can be found in [BSYP:78].

The physical virtual photon is described by the superposition of a direct coupling bare 'QED' photon $|\gamma\rangle_B$ with various vector meson states $|V\rangle$ [BSYP:78]

$$|\gamma\rangle = |\gamma\rangle_B + \sum_V \frac{e}{f_V} |V\rangle \,. \tag{2.12}$$

The bare photon $|\gamma\rangle_B$ accounts for the cross section contribution of the purely electromagnetic interaction between the photon and the spin 1/2 nucleon. It is several orders of magnitude smaller than the cross section of the hadronic interaction and can be neglected [Per:74].

All hadronic states $|V\rangle$ in the superposition have to conserve the quantum numbers of the photon: $J^{PC} = 1^{--}, Q = B = S = 0$. Therefore, they are restricted to vector mesons with spin equal to unity. Originally, the sum in Equation 2.12 included the light vector mesons ρ, ω, and ϕ. Heavier vector meson states (like the later discovered J/ψ) are included in the generalisation of the vector dominance model (GVMD) [SS:72, FRS:75, SSS:99]. This generalisation also allows for 'off-diagonal' transitions like $\rho^0 p \to \rho^{'0} p$ between vector meson states of different masses through the diffractive scattering process.

The factor e/f_V describes the strength of the coupling between the virtual photon and the various vector meson states $V = \rho, \omega, \phi, J/\psi, \cdots$, where $e = \sqrt{4\pi\alpha}$. The VMD coupling constants f_V are a matter of convention, but assumed to be independent of the photon energy ν. They can be related to the mass of the vector mesons and their leptonic decay width [BSYP:78]:

$$\frac{4\pi}{f_V^2} = \frac{3\Gamma_{ee}^V}{\alpha^3 m_V}. \tag{2.13}$$

The probability for the transition of the photon into a certain vector meson is given by e^2/f_V^2. For example, the probability for the photon to fluctuate into a J/ψ meson can be estimated

to be about 9.5% with $\Gamma_{ee}^{J/\psi} = 5.26 \pm 0.37$ keV [C$^+$:98]. With e^2/f_V^2, the photon–nucleon cross section for vector meson production can be related to the cross section of diffractive (elastic) vector meson–nucleon scattering, which is similar to the hadron–hadron interaction discussed in the previous section:

$$\left.\frac{d\sigma^{\gamma N\to VN}}{d|t|}\right|_{t=0} = \frac{e^2}{f_V^2}\left.\frac{d\sigma^{VN\to VN}}{d|t|}\right|_{t=0}. \tag{2.14}$$

In the first place, the model is valid for real photons at $Q^2 = 0$. It can be extended to virtual photons by the assumption that the Q^2 dependence of the photon–nucleon cross section is fully determined by the propagation of a single vector meson state, described by a propagator term $(1 + \frac{Q^2}{m_V^2})$. In the case of virtual photons, the photon–nucleon cross sections for transverse photons σ_T and longitudinal photons σ_L (cf. Appendix A.3) have to be distinguished [BSYP:78]:

$$\sigma_T^{VMD}(\nu, Q^2) = \sum_V \frac{e^2}{f_V^2}\left(1 + \frac{Q^2}{m_V^2}\right)^{-2} \sigma_T^{VN\to VN}(\nu, Q^2 = 0), \tag{2.15}$$

$$\sigma_L^{VMD}(\nu, Q^2) = \sum_V \frac{e^2}{f_V^2}\left(1 + \frac{Q^2}{m_V^2}\right)^{-2} \xi_V^2\frac{Q^2}{m_V^2}\,\sigma_T^{VN\to VN}(\nu, Q^2 = 0). \tag{2.16}$$

Here the dependence on the photon energy ν rather than the centre–of–mass energy in the photon nucleon system W has been chosen for the later discussion in the context of the HERMES fixed target experiment. The term $\xi_V^2 Q^2/m_V^2$ was introduced [Sak:69] to account for the fact that longitudinal and transverse contributions do not necessarily have to have the same cross section. In analogy to DIS (cf. Appendix A.3), the ratio R of the cross sections for longitudinal and transverse photons is defined

$$R = \frac{\sigma_L}{\sigma_T} = \xi_V^2\frac{Q^2}{m_V^2}. \tag{2.17}$$

In the VMD model, the value of ξ_V^2 is predicted to be of order unity, but still remains unclear. Recent measurements of E665 [E665:97] on ρ production and a preliminary result of the HERMES experiment [Bor:99] yield values for ξ_ρ^2 close to zero, which are in disagreement with the VMD model prediction.

From Equations 2.15 and 2.16 the cross section for the production of a certain vector meson by virtual photons $\gamma^\star$ can be expressed as

$$\sigma^{\gamma^\star N\to VN}(\nu, Q^2) = \left(1 + \frac{Q^2}{m_V^2}\right)^{-2}\left(1 + \epsilon\,\xi_V^2\frac{Q^2}{m_V^2}\right)\sigma^{\gamma N\to VN}(\nu, Q^2 = 0), \tag{2.18}$$

where the coupling e^2/f_V^2 is absorbed by the cross section definition 2.14 and $\epsilon = \Gamma_L/\Gamma_T$ is the ratio of fluxes of longitudinal and transverse photons. Relation 2.18 allows comparison of the cross section for virtual photons in lepton–nucleon scattering at HERMES with those obtained in experiments with real photon beams.

The cross sections for ρ and ϕ production are well reproduced by the VMD model. Only small normalisation corrections of 0.84 and 0.5, respectively, are necessary to match the model with the data. Its prediction for J/ψ production lies about two orders of magnitude above the data, which might indicate that the VMD model is not applicable for high meson masses. [DL:95].

2.1.4. Regge Theory

Regge theory is based on the idea of singularities in the S–matrix, the Regge poles, that appear in a partial–wave analysis of two body reactions. Depending on the form of the potential assumed for the interaction, these poles move in a complex angular momentum space with energy, where the trace of the Regge pole is called the Regge trajectory. The interaction takes place by the t–channel exchange of these Regge trajectories.

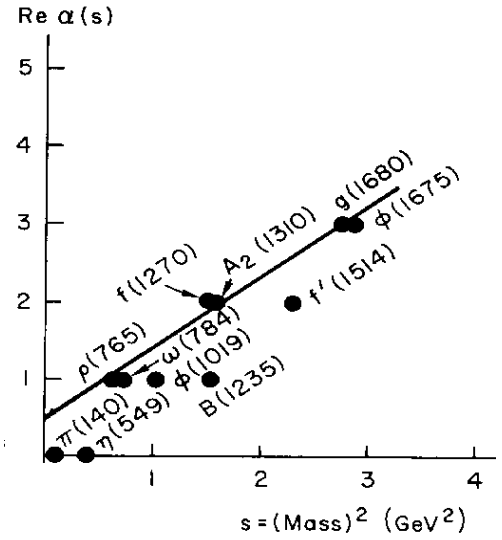

Figure 2.7.: Chew–Frautschi plot for mesons. The plot is taken from [Per:74].

Hadronic states with the same isospin, baryon number, and strangeness appear to lie on a straight line, a Regge trajectory, if their spin is plotted versus the mass squared [CF:61, CF:62]. With the slope α' and the intercept $\alpha(0)$ these trajectories are parameterised as

$$\alpha(t) = \alpha(0) + \alpha' \cdot t, \tag{2.19}$$

relating the four–momentum transfer to the target (the squared invariant mass of the exchange particle) to the intrinsic spin. A Chew–Frautschi plot for light mesons is shown in Figure 2.7. The line indicates the isospin-1 $(\rho{-}g)$ and the isospin-0 $(\omega{-}\phi)$ Regge trajectories, which lay on top of each other. Their intercepts are about 0.5 and the slopes on the order of 1 GeV^2.

An additional trajectory represents the exchange of vacuum quantum numbers: isospin, baryon number, and strangeness are equal to zero. This Pomeron trajectory has no hadronic states lying on it. Its intercept is slightly greater than unity and will be discussed below.

Hadron–hadron interaction can be considered to proceed by the exchange of these Regge trajectories with variable angular momentum and masses instead of the exchange of a certain particle with fixed quantum numbers. However, the straight trajectories are a phenomenological observation and they cannot be calculated from first principles. Thus, Regge theory cannot explain the nature of the strong interaction. Nevertheless, Regge theory delivers the correct energy dependence of the strong interaction cross section in powers of $\alpha(t)$

$$\frac{d\sigma^{\gamma^* N \to VN}(W^2)}{d|t|} \propto e^{-b_0|t|} \left(\frac{W^2}{W_0^2}\right)^{2(\alpha(t)-1)}, \tag{2.20}$$

where W^2 is the centre–of–mass energy of the photon-nucleon system and W_0^2 is a scale factor of order 1 GeV^2. The t dependence is not given by the theory, and based on data an exponential fall–off for diffractive interactions is assumed. Using the parameterisation 2.19 yields

$$\frac{\sigma^{\gamma^* N \to VN}(W^2)}{d|t|} \propto e^{-b|t|} \left(\frac{W^2}{W_0^2}\right)^{2(\alpha(0)-1)} \quad \text{with} \quad b = b_0 + 2\alpha' \ln \frac{W^2}{W_0^2}. \tag{2.21}$$

For a nonzero α' the exponential slope b depends on the energy; with increasing energy the slope b increases, which corresponds in the interpretation of Equation 2.11 to the scattering of two larger objects. The steeper exponential fall–off with t is called the 'shrinkage' of the

diffractive forward peak. There are no predictions for the values of b_0, W_0 and α' from Regge theory and these parameters have to be obtained experimentally.

By using the exponential t dependence of Equation 2.10, integration over t yields

$$\sigma^{\gamma^\star N\to VN} = \frac{1}{b}\left.\frac{d\sigma^{\gamma^\star N\to VN}}{d|t|}\right|_{t=0} \propto \frac{1}{b}\left(\frac{W^2}{W_0^2}\right)^{2(\alpha(0)-1)}, \tag{2.22}$$

resulting in a W dependence of $W^{4(\alpha_0-1)}$. Taking the energy dependence of b into account yields an effective power of the W dependence of

$$\sigma^{\gamma^\star N\to VN} \propto W^{4\left(\alpha_0-\frac{\alpha'}{b}-1\right)}. \tag{2.23}$$

A part of the incident particles is absorbed by inelastic interaction with the target and another part is scattered elastically, both vanish from the incoming particle flux in the forward direction. The interference between incoming and scattered waves is described by the optical theorem, which relates the imaginary part of the elastic scattering amplitude $f(t)$ at zero degrees $(t = 0)$ to the total hadron–hadron cross section: $\mathrm{Im}f(0) = \frac{k}{4\pi}\sigma_{VN}$. The real part of the scattering amplitude is small and can be neglected. The forward cross section at $t = 0$ is then directly related to the square of the total hadron–hadron cross section

$$\left.\frac{d\sigma^{\gamma^\star N\to VN}}{d|t|}\right|_{t=0} = \frac{\sigma_{VN}^2}{16\pi}. \tag{2.24}$$

Using Equation 2.21 for the W^2 dependence of the elastic forward meson–nucleon cross section yields the total meson–nucleon cross section

$$\sigma_{VN} \propto \left(\frac{W^2}{W_0^2}\right)^{\alpha(0)-1}. \tag{2.25}$$

Assuming that the vector meson–nucleon cross section has the typical behaviour of hadron–hadron cross sections, the intercepts of the Regge and Pomeron trajectories have been determined by a fit of the form

$$\sigma_{tot} = Xs^{\epsilon} + Ys^{-\eta} \tag{2.26}$$

to data of total cross sections in hadron–hadron interactions [DL:92]. Here X and Y are arbitrary normalisations and $s = W^2$ is the hadron–hadron centre–of–mass energy. The first term in Equation 2.26 stands for the exchange of one or multiple Pomeron trajectories, while the second term denotes the exchange of $\rho, \omega, ..$ Regge trajectories. The parameters have been determined to $\epsilon = \alpha_P(0) - 1 = 0.08$ and $\eta = 1 - \alpha_R(0) = 0.45$ with $\alpha_P(0)$ and $\alpha_R(0)$ the intercepts of the Pomeron and Regge trajectories, respectively. The slope of the Pomeron trajectory has been obtained from elastic pp and $p\bar{p}$ scattering data to be $\alpha'_P \sim 0.25$ GeV^2 [DL:84].

Figure 2.8 shows a compilation of data on vector meson production from fixed target experiments in comparison to data of the HERA collider experiments. The fixed target data at low energies show a decrease of the cross section with energy. This decrease is determined by the intercept $\alpha(0) \sim 0.5$ for the exchange of Regge trajectories. At higher energies the cross section is dominated by the exchange of Pomeron trajectories and a slow increase of the vector meson cross section with energy has been observed. Using Equation 2.23, an average exponential slope of $b \sim 10$ GeV^{-2}, and the intercept and slope of the Pomeron

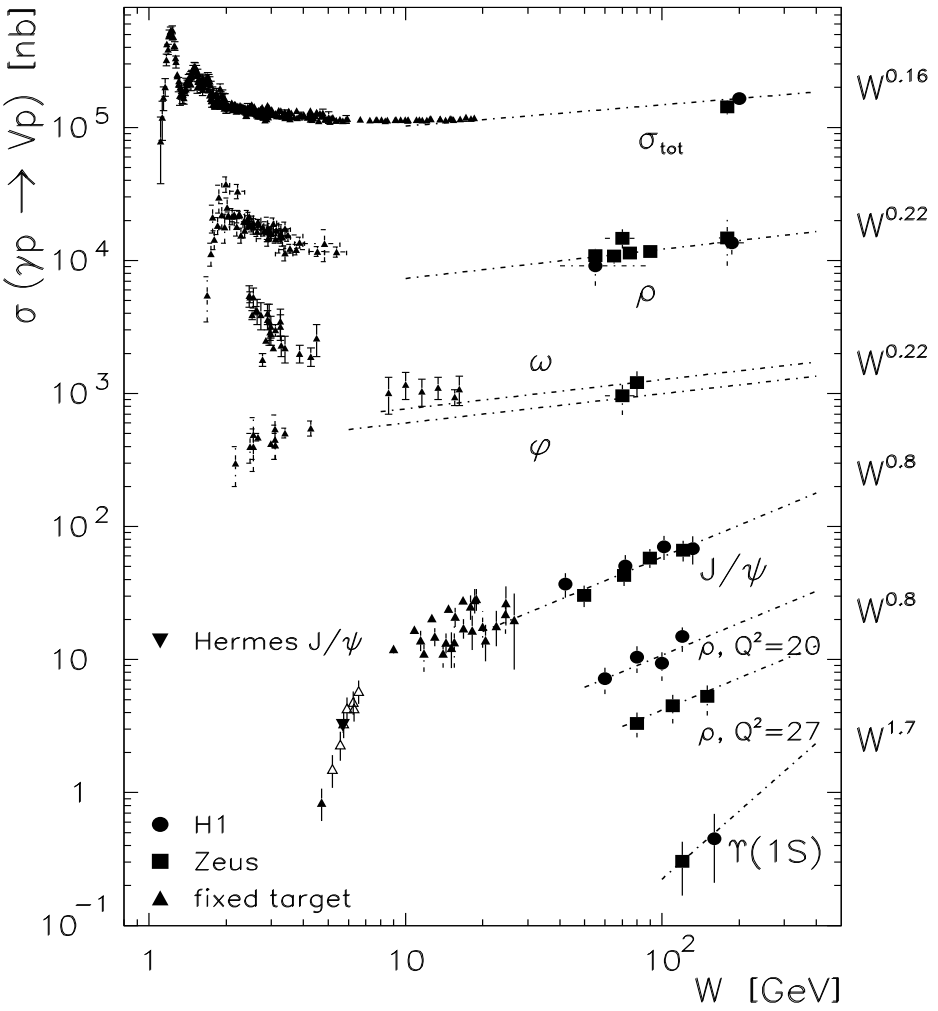

Figure 2.8.: Energy dependence of the cross section of exclusive vector meson photoproduction and of the total photoproduction cross section. The lines indicate the $\alpha(t)$ power–law energy dependence. The Figure is taken from Ref. [Cri:97, Mer:99]. Added are the data of ρ production at high Q^2 from [H1:99, ZEUS:99] and low energy data on J/ψ production of this analysis and from [C$^+$:75, G$^+$:75, BFP:79].

trajectory yields an energy dependence of $\sigma \propto W^{4(1.08-0.25/10-1)} = W^{0.22}$, which agrees well with the data. Only Pomeron exchange contributes to ϕ production [Fre:67], therefore the ϕ cross section does not show a decrease with energy in the low energy region. The more rapid increase of $W^{0.8}$ for the J/ψ meson and for the ρ meson at high Q^2 points to the breakdown of the Regge model at high meson masses or four–momenta.

2.1.5. Two–Gluon Exchange Model

Regge theory fails to describe the steep W dependence of the diffractive J/ψ cross section shown in Figure 2.8. Before the data of the HERA collider experiments have been available, it was suggested to describe so called 'hard' diffractive J/ψ production in perturbative QCD by the exchange of gluons [Rys:93, RRML:97]. Later on this has been generalised to the light vector mesons [BFG$^+$:94, FKS:96, FKS:98]. The discussion of perturbative QCD models for diffractive vector meson production is focused on the kinematic range of the HERA collider experiments. A review of theoretical approaches can be found in [Cri:97], detailed descriptions of recent experimental results on vector meson production by the HERA collider experiments and their comparison to world data and theoretical models can be found in [ZEUS:99, H1:99].

Figure 2.9 depicts the three steps of the interaction; the photon fluctuates into a $q\bar{q}$ pair which scatters off the target within a 'short' time, and finally the J/ψ is formed a 'long' time after this interaction. In lowest order QCD, the interaction takes place by the exchange of two gluons in a colour singlet state, therefore no colour quantum numbers are transfered in the diffractive interaction. Since all three steps are well separated in time they can be factorised. The scattering amplitude is then given by the convolution

$$\mathcal{A} = \Psi_{\gamma \to q\bar{q}} \otimes \mathcal{A}_{q\bar{q},N} \otimes \Psi_{q\bar{q} \to V}\,. \qquad (2.27)$$

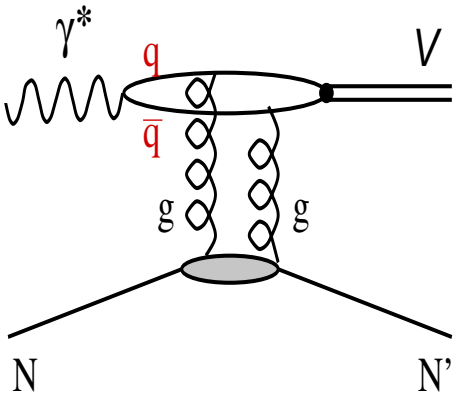

Figure 2.9.: Schematic graph of elastic vector meson production in lowest order QCD.

Here the Ψ_i's are the amplitudes for the splitting of the initial photon into a $q\bar{q}$ pair and the formation of final vector meson, respectively. The amplitude $\mathcal{A}_{q\bar{q},N}$ for the hard scattering of a small-size $q\bar{q}$ configuration off any target is proportional to the gluon distribution in the target

$$\mathcal{A}_{q\bar{q},N} \propto \alpha_s(\bar{Q}^2)\, x\, g(x). \qquad (2.28)$$

As an important consequence of this relation the diffractive cross section is sensitive to the square of the gluon density.

Ryskin Model for J/ψ Production

In the Ryskin model [Rys:93] the scale or effective photon virtuality $\bar{Q}^2$ and the fractional gluon momentum $\bar{x}$ are defined by

$$\bar{Q}^2 = \frac{Q^2 + m_{J/\psi}^2}{4} \quad \text{and} \quad \bar{x} = 4\frac{\bar{Q}^2}{W^2}. \qquad (2.29)$$

The QCD–scale of a process is given by the ensemble of its characteristic momenta like Q^2, m^2, and t. It determines the strength of the strong coupling constant α_s, i.e. the energy at which α_s is calculated. Diffraction is characterised by the forward peak with four–momentum transfer t close to zero, thus t does not contribute to the scale of the process.

For diffractive J/ψ photoproduction at low Q^2 (and low t) already the high mass of the J/ψ ensures that the scale $\bar{Q}^2$ is 'hard' (large) enough compared to Λ_{QCD} for α_s to be small so that perturbative QCD can be applied. The forward ($t = 0$) differential photon–nucleon cross section is calculated in the leading-logarithm approximation, where only terms of the order $\alpha_s \ln(\bar{Q}^2/\Lambda^2_{QCD})$ are counted in the integration of the gluon loop, neglecting terms of order α_s and higher

$$\frac{d\sigma^{\gamma^\star N \to J/\psi N}}{dt}\Big|_{t=0} = \frac{\Gamma_{ee} m^3_{J/\psi} \pi^3}{48\alpha} \frac{\alpha_s^2(\bar{Q}^2)}{\bar{Q}^8} \left[\, \bar{x}\, g(\bar{x}, \bar{Q}^2) \,\right]^2 \left(1 + \frac{Q^2}{m^2_{J/\psi}}\right). \tag{2.30}$$

Here the leptonic decay width $\Gamma^{J/\psi}_{ee}$ provides the normalisation of the model. The last term in 2.30 takes the contribution of longitudinal photons into account, where the ratio R is approximated as

$$R = \frac{\sigma_L}{\sigma_T} \approx \frac{Q^2}{m^2_{J/\psi}}. \tag{2.31}$$

Equation 2.30 relates the forward differential cross section to the square of the gluon density $\bar{x}g(\bar{x})$. A measurement of the total cross section in diffractive J/ψ production can be therefore used to determine the gluon distribution in the nucleon via Equations 2.22 and 2.30.

In [Rys:93] the J/ψ is described by a non–relativistic wave function with the charm quarks having no Fermi motion and carrying half of the J/ψ's momentum; the gluon transverse momenta are assumed to be small: $k_T^2 \ll \bar{Q}^2$. The model has been extended beyond the leading order $\ln(\bar{Q}^2)$ approximation including transverse gluon momenta k_T^2 [RRML:97]. Relativistic effects in the J/ψ wave function due to Fermi motion, rescattering and absorption of the $c\bar{c}$ pair, and next–to–leading–order QCD radiative corrections were discussed. Although some of these corrections have significant effects, their contributions compensate each other and the full calculation yields the same W dependence and a similar normalisation as the first order approximation of Equation 2.30. In comparison to data, the model has a normalisation uncertainty of 30%. In the kinematic range of HERMES these corrections are negligible, since they decrease with decreasing energy and become insignificant for $W < 20$ GeV [RRML:97].

Generalisation to Light Vector Mesons

The two–gluon exchange model has been extended to the light vector meson states in [BFG$^+$:94], where the production of ρ, ω, ϕ, J/ψ and Υ from *longitudinal* photons has been calculated. For the diffractive production of light vector mesons at small four–momentum transfer t the hard scale of the processes can not be given any longer by the meson mass. Rather, it has to be provided by a higher photon virtuality Q^2. The assumption that pQCD becomes valid at the scale given by the J/ψ mass leads to corresponding values of Q^2 in the order of 10 GeV^2. The kinematic constraints

$$t \ll Q^2, \quad \frac{W^2}{m_V^2} \gg 1, \quad \frac{W^2}{Q^2} \gg 1, \quad \text{and} \quad \frac{Q^2}{m_V^2} \gg 1 \tag{2.32}$$

are quoted in [BFG$^+$:94] for the validity of the calculation. Reference [FKS:96] discusses the validity of the factorisation described in Equation 2.27: the steps of the interaction are

well separated only if the coherence length $l_c = \frac{1}{2m_N x}$, i.e. the time in which the $q\bar{q}$ pair exists, exceeds the diameter R of the target. A limit for the applicability of pQCD to vector meson leptoproduction is derived

$$x \ll \frac{1}{4m_N R} \approx 0.06, \tag{2.33}$$

where x is the scaling variable defined in Appendix A.1. The forward differential cross section for the production of vector mesons from longitudinal photons is obtained in the leading logarithm $\alpha_s \ln(Q^2/\Lambda^2_{QCD})$ approximation as [FKS:96]

$$\left.\frac{d\sigma_L^{\gamma^\star N\to VN}}{dt}\right|_{t=0} = \frac{4\pi^3\Gamma_V m_V \eta_V^2}{3\alpha}\,\frac{\alpha_s^2(Q^2_{eff})}{Q^6_{eff}}\left|\left(1+\frac{i\pi}{2}\frac{d}{d\ln x}\right) x g(x,Q^2_{eff})\right|^2 \cdot T(Q^2). \tag{2.34}$$

Similar to Equation 2.30, the forward cross section depends on the square of the gluon distribution and an absolute normalisation is provided by the leptonic decay width Γ_V. The parameter η_V is defined as an effective inverse momentum, also called a leading twist [3] correction for the suppression of states with higher particle numbers; values for η_V are given in the range of 2 to 5. The effective photon virtuality Q^2_{eff} is related to the transverse size of the $q\bar{q}$ pair. It is smaller than the photon virtuality for ρ production: $Q^2_{eff} < Q^2$, in the case of J/ψ production it is about twice as large as $\bar{Q}^2$ of Equation 2.29.

The logarithmic derivative of the gluon momentum in Equation 2.34 accounts for the small contribution of the real part of the scattering amplitude. A suppression factor $T(Q^2)$ takes the effect of Fermi motion and of the relativistic vector meson wave function into account. In contrast to the Ryskin model of [RRML:97] that was basically left unaltered by the use of a relativistic J/ψ wave function, the correction $T(Q^2)$ depends on the meson type and strongly suppresses the cross section at $Q^2 \approx 0$ [FKS:96, FKS:98].

General Properties of Two–Gluon Exchange Models

Although the particular assumptions and the details of the perturbative QCD calculations are still controversial, they have common properties and reproduce the high energy data on vector meson production [ZEUS:99, H1:99].

- Hard diffractive vector meson production provides a sensitive probe of the the gluon content in the target, since the forward differential cross section can be related to the square of the gluon distribution.

- The observed energy dependence of the J/ψ photoproduction cross section of about $W^{0.8}$ is reproduced. For the light vector mesons a similar steep dependence is observed at high values of Q^2 (cf. Figure 2.8), that significantly exceeds the prediction $W^{0.22}$ of the Pomeron exchange in Regge theory.

[3] In the operator–product–expansion (OPE), the twist t of an operator is the power of the mass scale M^t that appears in the operator. It is defined as $t = d - s$, where d is the dimension of the operator and s its spin. At leading order only twist–2 operators contribute, while twist–3 operators are suppressed by 1/Q. As an example, in the Bjorken limit the spin structure function g_1 is a twist-2 object, while g_2 is related to twist-3 [Jaf:95].

- At high momentum transfer the size of the $q\bar{q}$ system should be independent of energy. The slope b is then given by the t dependence of the gluon–nucleon scattering amplitude and no shrinkage effects occur. At high Q^2 the slope b for light vector mesons is similar to the slope of J/ψ production, i.e. the t dependence of the diffractive process is independent of the quark flavour.

- At higher values of Q^2 the contribution from longitudinal photons dominates the cross section i.e. the ratio $R = \sigma_L/\sigma_T$ increases.

- The Q^2 dependence for longitudinal photons is predicted as $\sigma_L \propto 1/Q^6$. An effective $\sim 1/Q^5$ dependence is obtained if the Q^2 dependence of α_s and the increase in the gluon density due to its Q^2 evolution are taken into account that compensate some of the fall off at low x. For transverse photons the prediction of the order $\sigma_T \propto 1/Q^8$ is too steep compared to the data [BFG$^+$:94, RRML:97].

- Assuming a flavour independent interaction mechanism at large scales, a production ratio $\rho : \omega : \phi : J/\psi$ of $9 : 1 : 2 : 8$ is predicted by quark counting rules, taking the quark charges into account. At low Q^2 this relation is broken, since the heavier vector mesons ϕ and J/ψ are strongly suppressed. At high Q^2 values the contribution from heavier mesons is enhanced, supporting an underlying flavour independent process.

2.1.6. Off–Forward Parton Distributions

In inclusive and semi–inclusive deep–inelastic scattering the structure of the nucleon is described in the framework of QCD by unpolarised and polarised parton distribution functions (PDF's). Their generalisation to off–forward (also called off-diagonal, non–forward, or skewed) parton distributions (OFPD's) is suited to describe certain exclusive processes like deep–virtual Compton scattering (DVCS) [Ji:97a, Ji:97b, Rad:96] and meson production [Rad:97, CFS:97] in terms of the nucleon structure. Although OFPD's have been discussed already earlier [BL:82, GLR:83, GRBH:85], they recently became a field of increasing theoretical interest, since it was shown that their second moments are related to the sum of quark spins and quark angular momenta [Ji:97a, Ji:97b]. Therefore, OFPD's might provide access to the still unknown contribution of angular momenta to the nucleon spin.

In the analysis of exclusive processes in polarised lepton–nucleon scattering, OFPD's are of special interest, since they might allow to interpret these processes in terms of the spin structure of the nucleon. In the following the concept of OFPD's will be summarised; basic introductions to this rather new field of theoretical discussion can be found in [DGP:98, GV:99, Kro:99].

Concept

Off–forward parton distributions can be best explained by starting from the optical theorem in DIS, illustrated by the graphs of Figure 2.10. Similar to Equation 2.24, the cross section of the inclusive deep–inelastic scattering process $\gamma^\star N \to X$ is proportional to the imaginary part of the forward $(t = 0)$ amplitude of elastic $\gamma^\star N \to \gamma^\star N$ scattering. No momentum is transfered across the cut in the right graph of Figure 2.10, and the parton lines connected to the nucleon on the left and right side carry equal momenta k or, in the infinite momentum

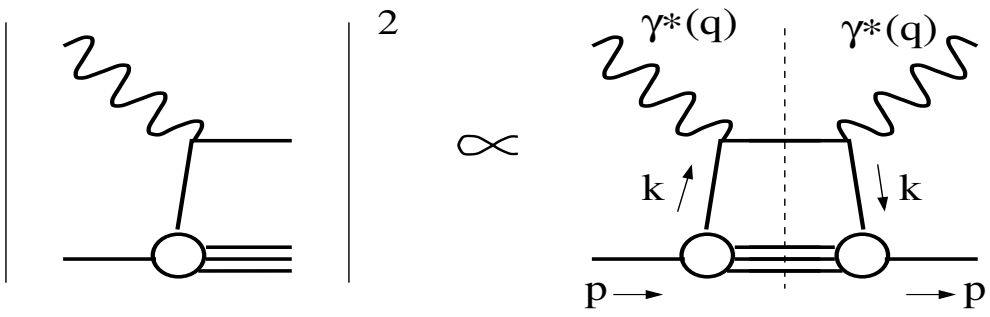

Figure 2.10.: Illustration of the optical theorem for DIS.

frame, equal fractional momenta x. The nucleon is described by the usual forward $(t = 0)$ unpolarised and polarised parton distribution functions $q_f(x)$, $g(x)$, $\Delta q_f(x)$, and $\Delta g(x)$.

In Figure 2.11 the virtual photon on the right side is replaced by a real one, yielding the 'handbag' diagram for the exclusive process of deep–virtual Compton scattering (DVCS) $\gamma^* N \to \gamma N'$. Due to the momentum transfer $\Delta = p' - p = q - q'$ with $\Delta^2 = t < 0$, the parton lines attached on the left and the right side to the 'blob', representing the nucleon, carry different momenta k, k', introducing an imbalance or 'skewedness' to the graph. In the Bjorken-limit of high Q^2 at fixed x and additionally small and fixed t, the DVCS amplitude can be factorised into a hard scattering part, exactly calculable in pQCD, and a 'soft' non–perturbative part describing the nucleon structure by off–forward $(t \neq 0)$ parton distributions.

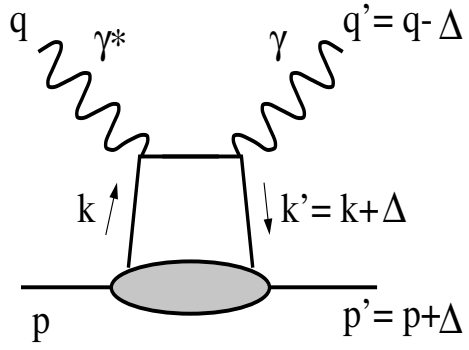

Figure 2.11.: Born level diagram for DVCS.

Meson production can be discussed in a similar way, shown in Figure 2.12. The difference between the meson mass and the photon virtuality Q^2 determines the momentum transfer Δ^2. As mentioned previously, Reference [CFS:97] gives the general proof of factorisation for diffractive vector meson $(\rho^0, \omega, \cdots)$ and pseudo–scalar meson $(\pi^0, \eta \cdots)$ production from longitudinal photons. At high Q^2 $(Q^2 \gg \Lambda^2_{QCD})$ and small t, meson production

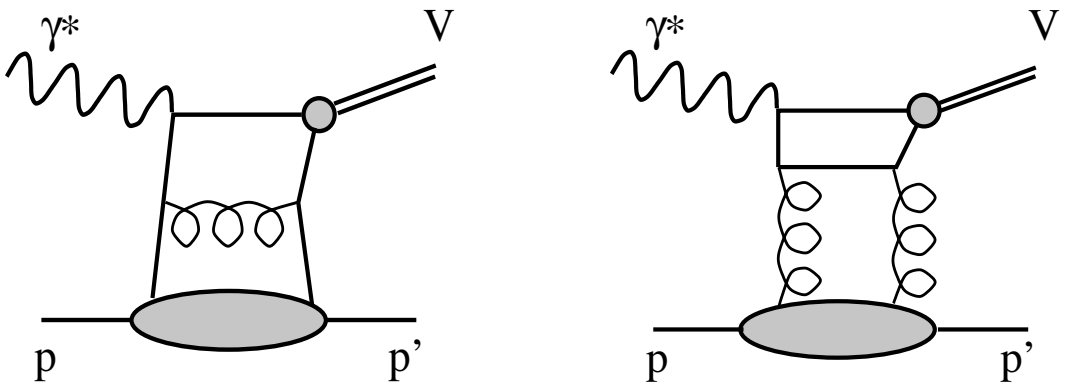

Figure 2.12.: Born level diagrams contributing to vector meson production from longitudinal photons, involving off–forward quark (left) and gluon distributions (right).

factorises into a distribution amplitude for the meson, a hard scattering amplitude, and off-forward distributions of partons (left graph) and gluons (right graph) in the nucleon.

Kinematics

In the literature, the kinematic frame is simplified by the assumption that all momenta become collinear, thus transverse momenta are zero. All momenta are expressed as linear combinations of two light–cone vectors $p^\mu = P^+(1,0,0,1)$ and $n^\mu = (1,0,0,-1)/(2P^+)$ with the negative z–axis defined along the photon momentum. The momentum transfer is denoted by $\Delta = p' - p = q - q'$ with $\Delta^2 = t < 0$. The longitudinal momentum fractions x and x' are defined by the longitudinal momenta of the exchange partons k, k' with respect to the incident nucleon momentum; the 'skewness' of the interaction is expressed by the variable ξ

$$x = \frac{k}{P+}, \quad x' = \frac{k'}{P+}, \quad \xi = \frac{-\Delta}{P+}. \tag{2.35}$$

In the given frame x has values between -1 and 1, the difference of the fractional momenta is approximately equal to Bjorken-x: $x - x' \approx x_{Bj}$, and ξ is bound between 0 and $\sqrt{-\Delta^2}/\sqrt{m_N^2 - \Delta^2/4}$ [Ji:97a, VM:98b, DGP:98]. The detailed definitions of kinematic variables and their notations vary throughout the literature, the notation used here is based on Ref. [Ji:97a]

Nucleon Structure and OFPD's

The usual parton distributions in deep–inelastic scattering are defined as matrix–elements of operators between identical nucleon states. In connection to the graphs 2.10 to 2.12 they can be interpreted as the probability for the nucleon to emit a parton of a given flavour f and momentum fraction x. Off–forward parton distributions are defined as matrix–elements of the same QCD operators, but arranged between nucleon states of different momenta and spin. Thus, OFPD's characterise a process where a parton is emitted from the nucleon and another is returned at a different momentum fraction, or a quark anti–quark pair of unequal momenta is emitted. These new parton distributions represent a generalisation of the usual parton distribution functions on one hand, and of nucleon form factors on the other hand. They reduce to the PDF's in the forward limit $t = 0$, where both parton momenta are the same; their integrals reproduce the nucleon form factors.

In leading order pQCD, the nucleon structure is parameterised by four off–forward parton distributions per flavour: the spin independent H_f and E_f and the spin dependent $\tilde{H}_f$ and $\tilde{E}_f$. Here the quark flavours are $f = u, d, s$ and the OFPD's are functions of three independent kinematic variables, e.g. x, ξ, t. Since OFPD's are closely related to the usual PDF's, H and $\tilde{H}$ reduce at $t = 0$ to the unpolarised and polarised quark distribution functions q_f and Δq_f

$$H_f(x, \xi = 0, t = 0) = q_f(x), \quad \tilde{H}_f(x, \xi = 0, t = 0) = \Delta q_f(x) \tag{2.36}$$

The off–forward parton distributions E and $\tilde{E}$ do not have such an immediate interpretation and they are usually neglected in the near–forward region of small t. At finite momentum transfer, model independent sum rules relate the 1st moments of H, E, $\tilde{H}$, and $\tilde{E}$ to the

Dirac, Pauli, axial-vector, and the unknown pseudo-scalar elastic form factors, respectively [Ji:97a]

$$\int_{-1}^{1} dx\, H(x,\xi,t) = F_1(|t|), \qquad \int_{-1}^{1} dx\, E(x,\xi,t) = F_2(|t|),$$
$$\int_{-1}^{1} dx\, \tilde{H}(x,\xi,t) = G_A(|t|), \qquad \int_{-1}^{1} dx\, \tilde{E}(x,\xi,t) = G_P(|t|). \tag{2.37}$$

Here the quark flavours are already summed up according to the nucleon type (for detailed discussion see [VGG:98]). In the forward limit the second moments of E and H are related to the total angular momentum carried by the quarks which is given by the sum of the contributions from intrinsic quark spins and quark orbital angular momenta [Ji:97a, Ji:97b]

$$\frac{1}{2}\int_{-1}^{1} dx\, x\, \left[H(x,\xi,t) + E(x,\xi,t)\right] \stackrel{t\to 0}{=} \Delta\Sigma + \Delta L_q. \tag{2.38}$$

Since there is currently no data on OFPD's, these distributions are completely unknown. Constraints are given only by the forward limit and their integrals. Various (simple) models for OFPD's derived from usual parton distributions are employed by the various authors, yielding predictions with only limited accuracy at the moment.

Relation of OFPD's to Exclusive Processes

Off-forward parton distributions reflect the nucleon structure independent of the reaction which probes the nucleon. Nevertheless, the different exclusive processes are related in different ways to combinations of OFPD's.

Deep–Virtual Compton Scattering The discussion of deep–virtual Compton scattering in terms of OFPD's and their relation to the nucleon spin initiated the recent interest [Ji:97b, Ji:97a]. All four OFPD's, unpolarised and polarised, contribute to the Compton process, even in the case that the initial polarisations are not measured. Calculations using off–forward parton distributions predict non–zero longitudinal and zero or small transverse spin asymmetries in real and virtual Compton scattering. A detailed discussion and comparison to other models can be found in Ref. [DFJK:99]. Although the Compton scattering process is most interesting, its experimental observation is difficult. It interferes with the Bethe–Heitler process where the final state photon is emitted by the incoming lepton, and with background from π^0 decay.

Neutral Meson Production Exclusive meson production is a promising channel for the study of off–forward parton distributions, because of its clean experimental signature. In contrast to the Compton process, neutral mesons are not sensitive to all four OFPD's at the same time. At leading order pQCD (α_s) and twist-2, vector meson production (ρ, ω, ϕ) is sensitive only to the unpolarised OFPD's H_f and E_f, while pseudo-scalar meson production (π^0, η) depends only on the polarised ones $\tilde{H}_f$ and $\tilde{E}_f$ [CFS:97]. Hence, although the cross section for π^0 production is lower by an order of magnitude than that for ρ production, the pseudo–scalar meson seems more suitable for the investigation of the nucleon spin structure. The analysis of different vector mesons will probe different quark flavour combinations of unpolarised OFPD's [VGG:98].

The two–gluon exchange model of vector meson production can be generalised to unpolarised and polarised off-forward gluon distributions G and $\tilde{G}$. Again, at leading order, vector meson production is sensitive only to the unpolarised off–forward gluon distribution G [VM:98b, VM:98a]. This will be discussed in more detail in Section 5.2.1. Due to C–parity conservation pseudo-scalar meson production does not have a leading order contribution from two-gluon exchange. At least three gluons have to be exchanged beyond leading order [MPW:98].

Exclusive production of neutral pseudo-scalar and light vector mesons is investigated in terms of OFPD's for the kinematic domain of the HERA collider experiments in Ref. [MPW:98]. The predicted cross sections are higher than the observed ones by an order of magnitude. Agreement is achieved by using the correction factor T of order 0.1 for the relativistic vector meson wave function introduced in Equation 2.34 [FKS:96]. Calculations performed for ρ production at HERMES [VGG:98] and their comparison to HERMES data will be discussed in Section 2.1.7.

Charged Meson Pair Production Closely related to the exclusive production of light vector mesons is the process of diffractive charged meson pair production $(\pi^+\pi^-, K^+K^-)$. Here the quarks in the $q\bar{q}$ pair do not form a bound vector meson state but fragment directly into charged mesons. Contributions from the off–forward gluon distribution G dominate the cross section. Similar to the vector mesons, all contributions from the polarised gluon distribution $\tilde{G}$ cancel at leading order. Only interference terms between polarised and unpolarised OFPD's contribute to spin asymmetries. Calculations for the HERMES kinematics predict large longitudinal spin asymmetries of about 0.25 for diffractive $\pi^+\pi^-$ and K^+K^- pairs [LDMS$^+$:99]. Here the ρ and ϕ resonance are explicitly removed from the numerical simulations, the extrapolation of the results to vector meson production is currently under discussion [Sch:99].

Charged Meson Production In contrast to the production of neutral mesons, exclusive charged meson production requires an exchange of quantum numbers between the photon–meson vertex and the target. Therefore the term 'diffractive' does not seem to be justified for these reactions. The production of charged pseudo–scalar and vector mesons $(\pi^\pm, \rho^\pm)$ involves generalised parton distributions $H_{ud}, \tilde{H}_{ud}, \cdots$ which are non–diagonal in quark flavour. For example, an up-quark is emitted from a proton and a down-quark is absorbed to form a neutron. In contrast to the production of neutral vector mesons, no gluons are involved here at leading order because of the necessary charge transfer [MPW:99, MPR:99]. Large single–spin asymmetries between 0.5 and 0.7 that are most sensitive to the spin–flip parton distribution $\tilde{E}$ are predicted for pseudo–scalar meson production [FPPS:99].

2.1.7. Perturbative QCD at HERMES Energy

For the later discussion of double–spin asymmetries in ρ meson production it is important to evaluate the applicability of perturbative QCD models at the HERMES centre–of–mass energy of $\sqrt{s} \sim 7.5$ GeV which is more than an order of magnitude lower than $\sqrt{s} \sim 300$ GeV of the HERA collider experiments.

Scale of the Diffractive Process

For the application of perturbative QCD models of vector meson production at HERMES kinematics the question arises, if the scale of the diffractive processes is large enough, i.e. α_s small enough to allow for perturbative calculations ? In the case of J/ψ production the hard scale is given by its high mass even at low Q^2 near the production threshold. For the diffractive production of light vector mesons the hard scale of the processes must be provided by the photon virtuality Q^2. Using the definition of $\bar{Q}^2$ from Equation 2.29, replacing $m_{J/\psi}$ with m_ρ and assuming that pQCD becomes valid at the scale given by the J/ψ mass, yields a minimum Q^2 value of the order 10 GeV^2, well outside of the HERMES kinematic range. On the other hand, the kinematic constraints of the Relations 2.32 and the upper limit of $x \leq 0.06$ in Relation 2.33 are given by the References [BFG$^+$:94] and [FKS:96], respectively to validate their pQCD calculations. Exclusive ρ production at HERMES has average values of $W^2 = 25$ GeV^2, $x = 0.07$ and $Q^2 = 1.7$ GeV^2 with highest Q^2 values of about 6 GeV^2 (cf. Section 6.4). The highest Q^2 bin defined in the analysis of double–spin asymmetries has an average Q^2 of 3.2 GeV^2 (cf. Table 6.4). Therefore, with respect to the kinematic constraints given by the Relations 2.32 and 2.33, it might be possible to apply pQCD at least to highest Q^2 bin of the HERMES ρ data.

Transverse Photons and Factorisation

In the kinematic range of ρ production at HERMES the contributions of longitudinal and transverse photons are about equally important (cf. Section 5.1.1). A general proof of factorisation in diffractive meson production (not only restricted to vector mesons) for *longitudinal* photons has been given in [CFS:97]. The production of longitudinal vector mesons is characterised by the small size of the $q\bar{q}$ system with respect to the distances between the steps of the interaction: photon fluctuation, hard scattering, and formation of the final meson. In the case of large Q^2 or heavy flavour masses, the factorisation theorem can be applied and the diffractive process is described by three distinct components: a non–perturbative description of the target nucleon by off–forward parton distributions, explained below, a distribution amplitude for the meson, and a hard scattering amplitude.

For *transverse* photons factorisation holds true only in the case of heavy quarks, since the transverse size of the $q\bar{q}$ state shrinks with increasing mass. The production of the heavy vector mesons J/ψ and Υ from transverse photons has been calculated in [FKS:98] and an expression similar to Equation 2.30 was obtained.

The distribution amplitude for transverse light vector mesons involves large size and very asymmetric $q\bar{q}$ configurations. Singularities occur in the integration of the vector meson wave function at the endpoints of the integration range. Divergences might also arise from the integration over the (off-forward) parton distributions describing the nucleon. These divergences cannot be regularised in current QCD frameworks. It follows that the factorisation theorem, an important prerequisite for pQCD calculations, does not hold for the production

of light vector mesons from *transverse* photons. A suppression of the production amplitudes by $1/Q$ for meson production from transverse photons is predicted [CFS:97, FKS:98, MP:99].

As a consequence of the not proven validity of factorisation, predictions for light meson production from transverse photons become dependent on the detailed assumptions of the model used [Man:99c]. An ansatz using parton–hadron duality will be discussed in Section 5.2.2.

Cross Section of Exclusive ρ Production at HERMES

At HERMES, a measurement of the cross section for exclusive ρ electroproduction was performed [Kol:98a, Bor:99] which will be briefly summarised in the following. The cross section was extracted in two bins of W and several bins of Q^2. A preliminary result indicates that it decreases with increasing energy W.

In models of vector meson production based on Regge theory, both Reggeon and Pomeron exchange are expected to contribute to the ρ cross section at the intermediate W range of 3 to 6 GeV accessible at HERMES [HKK:96]. From the decrease of the cross section with W, typical for Reggeon exchange, can be concluded that in the description of ρ production at HERMES energy based on Regge theory, Reggeon exchange dominates the cross section [Bor:99].

First cross section estimates in the HERMES kinematic range for Compton scattering and meson production based on pQCD calculations using off–forward parton distributions (cf. Figures 2.11 and 2.12) are given in Reference [VGG:98]. In Figure 2.13 the predictions for the cross section σ_L^ρ for ρ production from longitudinal photons at HERMES energy are shown in two bins of Q^2. The dashed lines denote quark exchange, the dotted ones the exchange of gluons, the solid line is the sum of both contributions. Open circles are previous data, and the filled circles denote the preliminary HERMES measurement. In this model predictions, quark exchange clearly dominates the cross section of exclusive ρ production in the HERMES energy range. The contribution from gluon exchange becomes more important at higher Q^2 as can be seen when comparing the dashed lines of both plots in the figure. The model calculations are in reasonable agreement with the data showing that pQCD calculations are able to reproduce the experimental data already at intermediate energies and rather low Q^2.

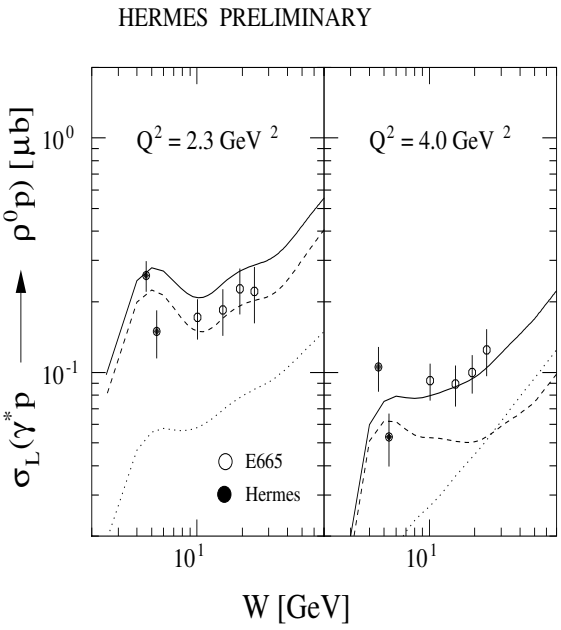

Figure 2.13.: Cross section of exclusive ρ production from longitudinal photons in comparison with previous data and calculations based on off–forward parton distributions [VGG:98]. The dashed lines denote quark exchange, the dotted lines the exchange of gluons, the solid line their sum. The Figure is taken from [Bor:99].

2.2. Photon–Gluon Fusion and J/ψ Production

Photon–gluon fusion (PGF) is shown in lowest order QCD in Figure 2.14: a $q\bar{q}$ quark pair is produced by a photon and undergoes a hard scattering with a gluon of the nucleon. Charm production in *inelastic* lepton-nucleon scattering can be used as a clean tag of the PGF process, since charmed final state hadrons are dominantly produced by PGF. The intrinsic charm content of the nucleon, the charmed sea, is suppressed with respect to the light quarks by the high charm quark mass of 1.1-1.4 GeV [C$^+$:98]. Therefore, the contribution to charm production of the QCD–Compton process shown in Figure 2.15 is small and can be neglected [FPS:81]. A measurement of the spin dependence in charm production via photon–gluon fusion is believed to be a clean probe of the gluon contribution ΔG to the nucleon spin.

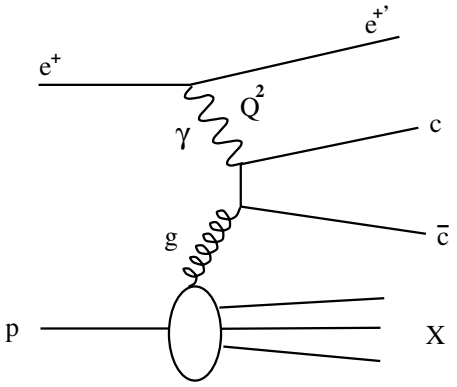

Figure 2.14.: Charm production in leading order QCD via photon–gluon fusion.

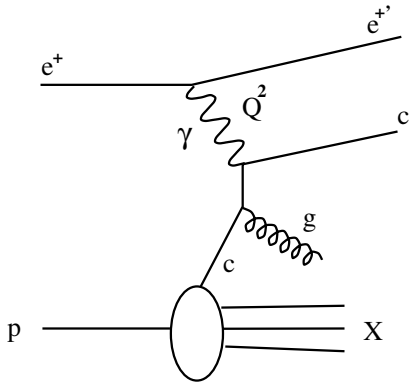

Figure 2.15.: Gluon radiation via the QCD–Compton process.

For D mesons $(c\bar{q}, \bar{c}q)$ that contain a light quark flavour besides charm (open charm), the photon–gluon process and the subsequent independent fragmentation of the two c–quarks shown in Figure 2.14 to the final meson states are well understood. It appears to be favourable to measure the longitudinal spin asymmetry for the photon–gluon fusion process by open charm production in polarised lepton–nucleon scattering since this asymmetry can be directly related to the gluon polarisation $\Delta g(x_g)/g(x_g)$ as discussed in Section 2.2.3.

Open charm production is theoretically 'cleanest'; nevertheless, open charm detection is experimentally a non–trivial task. D–mesons have a large number of decay modes, none with an especially large branching ratio, but usually with high multiplicities. An extensive search for open charm signals has been carried out for the HERMES data of the years 1995 to 1997. The reconstruction of the two–body decay $D^0 \to K\pi$ suffers from large combinatorial hadronic background. Semi-leptonic decays, like $D^0 \to K\mu X$ have a unique muon–kaon signature, but the missing energy carried by the undetected neutrino does not allow reconstruction of a sharp peak. For the detection of these decay modes a clean pion–kaon–proton separation and muon identification are required. Both have not been available for the 1995 to 1997 data and no confirmed signal could be extracted so far. A small, but significant signal has been found for the decay of the D^* meson into a D^0 and a pion with low momentum: $D^* \to \bar{D}^0(\to K\pi)\,\pi$. The few open charm events detected at HERMES do not allow an asymmetry analysis yet [Bro:97, Mei:98, Bro:98b].

Experimentally easier accessible than D mesons is the $J/\psi(c\bar{c})$ vector meson (hidden charm), since the two di–leptonic J/ψ decay channels are an unique experimental signature. Inelastic J/ψ production is described by the Colour–Singlet Model and its extension the Colour–Octet

Mechanism, where the bound $c\bar{c}$ vector meson state is formed under the emission of one or more additional gluons. These two models will be discussed in the following.

In contrast to open charm production, the interpretation of spin asymmetries in J/ψ production in polarised lepton–nucleon scattering is more difficult since the different production mechanisms have to be distinguished. The relation of spin asymmetries in inelastic J/ψ production via photon–gluon fusion is discussed in Section 2.2.3, while spin asymmetries in the diffractive process are discussed in Section 5.2.

If light quarks are produced, photon–gluon fusion cannot be identified by the particle type of its hadronic final states. On the other hand, it is characterised by high transverse momenta passed to the quarks and other competing processes can be suppressed by a corresponding kinematic requirement. However, the different processes cannot be distinguished on an event by event basis, and their relative contributions have to be obtained from Monte Carlo simulations. At high enough energies the two quarks fragment into jets. The analysis of events with two–jets of high transverse momenta has been used to extract the unpolarised gluon distribution in hadron–hadron [E665:96] and lepton–nucleon collisions [H1:95]. At fixed target experiments with lower centre–of–mass energies quark fragmentation into single hadrons has to be considered instead. A measurement of the polarised gluon distribution in polarised lepton–nucleon scattering through the analysis of high-p_T hadron pairs was originally proposed for the COMPASS experiment [BvHK:98]. Recently, such an analysis has been published by the HERMES experiment [HERMES:99e, Mar:99]. A non–zero asymmetry was found within limited statistics, indicating a positive value of $\Delta G/G$. Potentially large theoretical uncertainties remain due to the present uncertainties in the Monte Carlo model and possible non–zero background asymmetry contributions.

2.2.1. Colour Singlet Model

Inelastic production of J/ψ mesons via photon–gluon fusion has been successfully described by the Colour Singlet Model (CSM) [BJ:81]. As shown in Figure 2.16, the virtual photon fluctuates into a $c\bar{c}$-pair which interacts with a gluon of the nucleon and forms the colour singlet spin-1 $c\bar{c}$-state with the quantum numbers of the final J/ψ. To form the colour neutral state, the colour charge has to be carried away by the emission of an additional hard gluon. This photon–gluon subprocess is calculable in pQCD. To ensure that the emitted second gluon is hard, i.e. a minimum transverse momentum is carried away, the model is restricted to the inelastic region

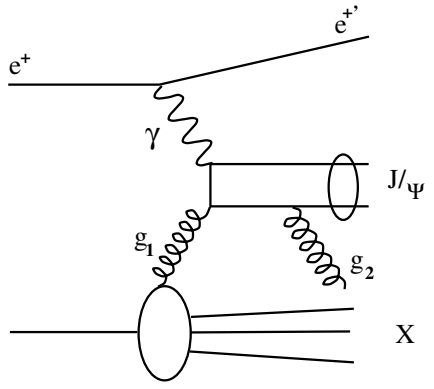

Figure 2.16.: J/ψ production via the colour singlet model in leading order QCD.

$$z = \frac{p \cdot p_{J/\psi}}{p \cdot Q} \overset{lab}{=} \frac{E_{J/\psi}}{\nu} < 0.9 \quad \text{and} \quad p_T^2 \geq 0.1 \cdot m_{J/\psi}^2, \tag{2.39}$$

where z is the fractional energy of the J/ψ and p_T its transverse momentum with respect to the photon. In the calculation of the CSM matrix element the J/ψ is represented by an s-wave function, where each charm quark carries half of the J/ψ's mass and 4-momentum.

The formation of the final bound $c\bar{c}$ state proceeds well separated in time and is proportional to the J/ψ wave function at its origin $\Psi(0)$

$$M(\gamma + g \to J/\psi + g) \propto \Psi(0)\, M(\gamma + g \to c\bar{c} + g). \tag{2.40}$$

A normalisation is provided by the leptonic width of the J/ψ decay $\Gamma^{J/\psi}_{e^+e^-}$ that is related to $\Psi(0)$ by

$$\Gamma^{J/\psi}_{e^+e^-} = \frac{16\pi\alpha_e^2 e_c^2}{m^2_{J/\psi}} |\Psi(0)|^2. \tag{2.41}$$

The double differential photon–nucleon cross section $\sigma^{\gamma N \to J/\psi X}$ is obtained by a convolution of the photon–gluon subprocess $\gamma g \to c\bar{c}$ with the gluon density g [BJ:81, MNS:87]

$$\frac{d^2\sigma}{dz dp_T^2} = g(x_g)\, \frac{128\pi^2 m_{J/\psi}\alpha_s^2\alpha_e e_c^2}{3s[m^2_{J/\psi}(1-z) + p_T^2]}\, |\Psi(0)|^2 \otimes \left(\frac{1}{M_T^4} + \frac{(1-z)^4}{K_T^4} + \frac{z^4 p_T^4}{M_T^4 K_T^4} \right). \tag{2.42}$$

Here x_g is the fractional momentum of the gluon with respect to the nucleon momentum

$$x_g = \frac{s_{\gamma^\star g}}{s_{\gamma^\star N}} = \frac{1}{s}\left[\frac{m^2_{J/\psi}}{z} + \frac{p_T^2}{z(1-z)} \right] \simeq \frac{M^2_{J/\psi}}{W^2_{\gamma N}}, \tag{2.43}$$

and the notations $M_T^2 = m^2_{J/\psi} + p_T^2$, $K_T^2 = m^2_{J/\psi}(1-z)^2 + p_T^2$ are used. Available data [EMC:92b, NMC:91, H1:96] suggest that the Q^2 dependence of the photon–nucleon cross section for inelastic J/ψ production can be described by a propagator term similar to the Q^2 dependence of the the elastic process in the vector meson dominance model [BR:82]:

$$\sigma^{\gamma^\star N \to J/\psi X}(Q^2) = \left(1 + \frac{Q^2}{m^2_{J/\psi}} \right)^{-2} \sigma^{\gamma N \to J/\psi X}(Q^2 = 0). \tag{2.44}$$

Differential cross sections for inelastic J/ψ production measured at different centre–of–mass energies in fixed target experiments [dJ:91, EMC:92b] and at HERA [H1:96, ZEUS:97] are well described by the colour singlet model. However, arbitrary normalisation factors between two [dJ:91] and six [MMMG:94] had to be introduced for the normalisation of the model to the data. Taking the finite relative momentum of the c-quarks [JKGW:93, MM:97] and higher order QCD corrections [KZSZ:95, Krä:96] into account reduces this discrepancy.

In order to extract the gluon density $g(x_g)$ in the nucleon, the cross section in Equation 2.42 can be rewritten as a function of x_g [MNS:87]

$$\frac{d\sigma}{dx_g} = x_g\, g(x_g)\, \frac{\Gamma_{e^+e^-}}{m^3_{J/\psi}} f(x_g, s/m^2_{J/\psi}). \tag{2.45}$$

The function f is sharply peaked at $x_g = 2.28\ m^2_{J/\psi}/s$ and approximately independent of s for $s > m^2_{J/\psi}$. Thus the inelastic J/ψ cross section is up to a known numerical constant equal to the gluon distribution. Based on this relation $g(x_g)$ has been directly measured at CERN [EMC:92b, NMC:91].

2.2.2. Colour Octet Mechanism

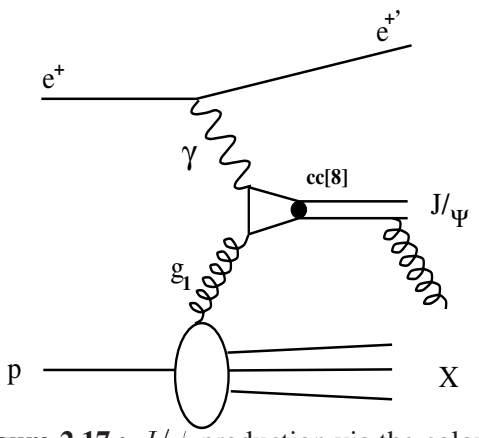

Figure 2.17.: J/ψ production via the colour octet mechanism in leading order QCD.

The colour octet mechanism (COM) [BBL:95] was developed because data on J/ψ production at high transverse momenta in pp collisions [CDF:92, CDF:93] could not be described with the CSM. It represents a generalisation of the colour singlet model. An intermediate colour octet state is formed in the hard interaction, shown in Figure 2.17. This intermediate state transforms into the final colour neutral state by the emission of one or more 'soft' gluons with low momenta, a process that cannot be calculated in perturbative QCD.

Based on non-relativistic QCD (NRQCD), the cross section is represented by a sum of sub–cross sections, each factorised into i) a short distance cross section $\hat{\sigma}$ for the production of an on-shell $c\bar{c}$ pair of a given spin and angular momentum state n and ii) a long distance matrix element $\left\langle 0|\mathcal{O}^{J/\psi}[n]|0\right\rangle$ which describes the probability of the colour octet state to form a J/ψ [BBL:95, CK:96]

$$d\sigma(\gamma + g \to J/\psi + X) = \sum_n d\hat{\sigma}(\gamma + g \to c\bar{c}[n] + X)\left\langle 0|\mathcal{O}^{J/\psi}[n]|0\right\rangle. \tag{2.46}$$

The NRQCD matrix elements in Equation 2.46 can be expanded in powers of v^2 where v is the relative velocity of the c quarks. At leading order in v^2, the colour singlet process (denoted by 1) is reproduced

$$\gamma + g \to c\bar{c}[1,^3S_1] + g. \tag{2.47}$$

Here the usual notation of spectroscopy $^{2S+1}L_J$ for states with spin S and total angular momentum J is used. Colour octet states (denoted by 8) are produced at leading order α_s by the $2 \to 1$ parton processes

$$\gamma + g \to c\bar{c}[8,^1S_0] \quad \text{and} \quad \gamma + g \to c\bar{c}[8,^3P_{0,2}]. \tag{2.48}$$

These colour octet matrix elements cannot be calculated from first principles and have to be obtained from the data. At leading order the colour octet terms contribute only to the kinematic domain of elastic scattering at $z = 1$ and $p_T \approx 0$. In this case a 'soft' gluon with low momentum is emitted to form the colour neutral state. At next–to–leading order and non–zero p_T the COM predicts a strong rise of the cross section already at intermediate z values when approaching $z \simeq 1$, while the cross section stays flat in z within the colour singlet model [CK:96]. Because of the similar kinematics, experimental difficulties arise to distinguishing between the colour octet mechanism and diffractive J/ψ production. Even when the scattered lepton is detected and the event kinematics are fully reconstructed, an identification of COM events requires the detection of the target remnants, which at present is not possible at HERMES.

Lepton–nucleon scattering data from the HERA collider experiments have shown no evidence for a rise of the inelastic J/ψ cross section at high z. In Figure 2.18 H1 data are compared to the predictions of the colour singlet and the colour octet model. It was concluded, that possible COM contributions in lepton–nucleon scattering are about an order of magnitude smaller than suggested by the pp-collision data [H1:96, ZEUS:97].

In the inelastic region of low-z and higher transverse momenta, the colour octet state is formed by the emission of a hard second gluon. The ${}^1S_0$, ${}^3S_1$, and ${}^3P_{0,1,2}$ colour octet matrix elements contribute. NRQCD calculations predict a COM contribution to the cross section of similar magnitude as the colour singlet mechanism. However, no conclusive result on the size of the colour octet contributions has been obtained from the data yet [CK:96].

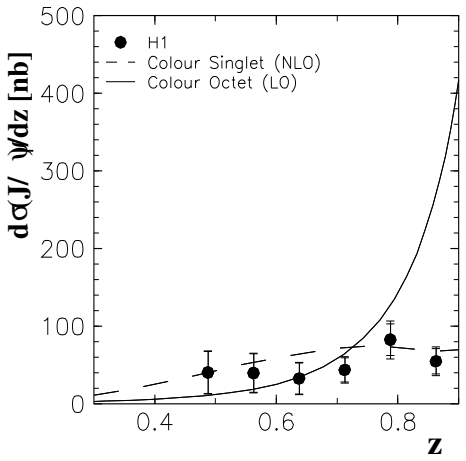

Figure 2.18.: Inelastic J/ψ cross section versus z. Points are data, the prediction of CSM (COM) is indicated by the dashed (solid) line. The Figure is taken from Ref. [H1:96].

2.2.3. Spin Asymmetries in Inelastic Charm Production

Open Charm Production

Double–spin asymmetries in heavy quark production via photon–gluon fusion can be related to the size of the gluon contribution to the nucleon spin since the high mass of the quarks ensures the hard scale of the process and allows for reliable pQCD calculations. The unpolarised (polarised) cross section for production of a $c\bar{c}$ pair in photon–gluon fusion can be factorised into a convolution of the cross section for the hard photon–gluon scattering subprocess $\gamma g \to c\bar{c}$ and the gluon structure functions $g(x_g)$ ($\Delta g(x_g)$) [Wat:81], it holds true for the general case of heavy quark (c, b, t) production [GR:88]. In the limit of $Q^2 = 0$ in quasi–real photoproduction the unpolarised cross section σ and the cross section difference for parallel and anti–parallel beam and target spin configuration $\Delta\sigma$ are given by

$$\sigma^{\gamma N\to c\bar{c}}(\hat{s}) = \int_{4m_q^2}^{2M\nu} d\hat{s}\ \hat{\sigma}^{\gamma g\to c\bar{c}}(\hat{s}) g(x_g,\hat{s}),\ \ \Delta\sigma^{\gamma N\to c\bar{c}}(\hat{s}) = \int_{4m_q^2}^{2M\nu} d\hat{s}\ \Delta\hat{\sigma}^{\gamma g\to c\bar{c}}(\hat{s}) \Delta g(x_g,\hat{s}). \quad (2.49)$$

Here $\hat{s} = (q+g)^2$ is the centre–of–mass energy in the photon–gluon system with q and g the 4-momenta of photon and gluon, and $x_g = s_{\gamma^\star g}/s_{\gamma^\star N}$ denotes the fractional gluon momentum with respect to the nucleon momentum. The hard scattering cross sections $(\Delta)\hat{\sigma}$ are fully determined by the event kinematics and the centre–of–mass velocity $\beta^2 = 1 - 4m_c^2/\hat{s}$ of the quarks

$$\hat{\sigma}(\hat{s}) = e_c^2 \frac{2\pi\alpha_e\alpha_s}{\hat{s}} \left[\ln\frac{1+\beta}{1-\beta} - 3\beta\right],\ \ \Delta\hat{\sigma}(\hat{s}) = e_c^2 \frac{2\pi\alpha_e\alpha_s}{\hat{s}} \left[\frac{1}{2}(3-\beta^4)\ln\frac{1+\beta}{1-\beta} - \beta(2-\beta^2)\right]. \quad (2.50)$$

The photon–nucleon asymmetry[4] $A^{\gamma N \to c\bar{c}}$ for longitudinally polarised beam and target is given by

$$A^{\gamma N \to c\bar{c}} = \frac{\sigma^{\gamma N \to c\bar{c}}_{\rightleftarrows} - \sigma^{\gamma N \to c\bar{c}}_{\rightrightarrows}}{\sigma^{\gamma N \to c\bar{c}}_{\rightleftarrows} + \sigma^{\gamma N \to c\bar{c}}_{\rightrightarrows}} = \frac{\Delta\sigma^{\gamma N \to c\bar{c}}}{\sigma^{\gamma N \to c\bar{c}}}. \tag{2.51}$$

In open charm production the two charm quarks fragment independently of each other. The fragmentation process is assumed to be independent of the helicity state of the quark and does not influence a possible spin dependence in the prior photon–gluon interaction. Therefore, spin asymmetries in open charm production can be used as a direct measurement of the gluon contribution to the nucleon spin Δg. This measurement was originally proposed for the COMPASS experiment [COMPASS:96].

The application of the formalism developed for open $c\bar{c}$ production to J/ψ photoproduction has been discussed in Ref. [GR:88]. With respect to the CSM, this ansatz has the advantage, that it is not restricted to the inelastic region and $p_T > 0.1$. At low Q^2 the hard scale is determined by the J/ψ mass and the fractional gluon momentum x_g is given by the approximation

$$x_g \approx \frac{m^2_{c\bar{c}}}{s_{\gamma^\star N}} \approx \frac{m^2_{J/\psi}}{s_{\gamma^\star N}}. \tag{2.52}$$

The convolution integrals in Equation 2.49 can be avoided [GR:88] and the longitudinal photon asymmetry is related to the gluon polarisation $\Delta g/g$ as

$$A^{\gamma N \to J/\psi}(x_g) \simeq \frac{\Delta\hat{\sigma}(x_g, m^2_{J/\psi})}{\hat{\sigma}(x_g, m^2_{J/\psi})} \frac{\Delta g(x_g)}{g(x_g)}. \tag{2.53}$$

Possible non–perturbative effects in the formation of the J/ψ meson prevent reliable predictions for the hard scattering asymmetry $\hat{a} = \Delta\hat{\sigma}/\hat{\sigma}$. The authors of [GR:88] conclude that a comparison of spin asymmetries in open charm and J/ψ production may be used as a tool to study these non–perturbative effects.

Colour Singlet Model

In the framework of the colour–singlet model spin asymmetries in J/ψ production in longitudinally polarised lepton–nucleon scattering can be related to the polarised and unpolarised gluon distribution functions as [BJ:81, Gui:88]

$$A^{lN \to J/\psi}(z) = \frac{\int dx_B \int \frac{dx}{x} \Delta g(\frac{x_B}{x}, S_c)(1-(1-y)^2)\Delta\hat{\sigma}(x, z, Q^2)}{\int dx_B \int \frac{dx}{x} g(\frac{x_B}{x}, S_c)\,[(1+(1-y)^2)\hat{\sigma}_T(x, z, Q^2) + 2(1-y)Q^2\hat{\sigma}_L(x, z, Q^2)]}. \tag{2.54}$$

Here the asymmetry is given as a function of the fractional energy z. The terms $(1 \pm (1-y)^2)$ take the effective photon polarisation into account, hence the expression describes the lepton–nucleon asymmetry. In the denominator the unpolarised cross sections for the hard subprocess $\gamma g \to J/\psi$ are explicitely given for transverse and longitudinal photons. In Reference [Gui:88] the kinematic variables x, y, z have been defined with respect to the gluon momentum $x = \frac{Q^2}{2g\cdot q}$, $y = \frac{g\cdot q}{g\cdot k}$, $z = \frac{g\cdot p_{J/\psi}}{g\cdot q}$, the scale of the hard subprocess is given by

[4] The photon–nucleon asymmetry $A^{\gamma N}$ and the lepton–nucleon asymmetry A^{lN} correspond to the definitions of A_1 and $A_{||}$ in deep–inelastic scattering (cf. Appendix A.4).

$S_c = m^2_{J/\psi} + p^2_T$, and x_g is equal to the ratio of Bjorken-x to x: $x_g = x_B/x$. The relation of A^{lN} to the photon asymmetry $A^{\gamma N}$ and the gluon polarisation can be approximated by

$$A^{lN\to J/\psi} \cdot \frac{1}{D} \simeq A^{\gamma N\to J/\psi} \simeq \hat{a}\frac{\Delta g}{g}, \tag{2.55}$$

where D is the photon depolarisation factor. The hard scattering asymmetry $\hat{a} = \Delta\hat{\sigma}/\hat{\sigma}$ of the QCD subprocess acts as an effective dilution of the measurement and reduces its analysing power. At HERMES kinematics $\hat{a}$ is about 0.55 [HERMES:97c].

Colour Octet Mechanism

Spin asymmetries in hadron–hadron collisions and lepton–nucleon scattering have been calculated in the colour octet model for several charmed final states [GM:96, TT:97, NT:98]. Here, a spin asymmetry in J/ψ production can be related to the gluon polarisation $\Delta g/g$ in the simple form

$$A^{\gamma p\to J/\psi} = \frac{\Delta\Theta}{\Theta} \cdot \frac{\Delta g(x)}{g(x)}. \tag{2.56}$$

The ratio $\Delta\Theta/\Theta$ includes, besides the hard scattering asymmetry, combinations of the different colour octet matrix elements. Values for $\Delta\Theta/\Theta$ vary between 1.7 and 6.6, which reflects the uncertainty in the extraction of the matrix elements from the data as well as the theoretical uncertainties within the model. In the case that only s wave states contribute to J/ψ formation, $\Delta\Theta/\Theta$ is unity.

In a recent publication [JNT:99] the sensitivity of double–spin asymmetries in J/ψ photoproduction to different sets of colour octet matrix elements has been investigated in an energy range representative for fixed target experiments like HERMES and Compass, shown in Figure 2.19. The solid line corresponds to the CSM prediction, the dashed (dashed-dotted) curves represent the case when the colour octet matrix element $[8,^1P_0]$ ($[8,^1S_0]$) is set to zero. Two sets of matrix elements are indicates in the figure: one at leading order (LO) and a second taking higher order corrections (HO) into account. Using higher order corrections yields smaller colour octet contributions in comparison to the CSM than leading order. At low $z < 0.7$ the uncertainties due to the COM contributions in respect to the CSM prediction are acceptable and a measurement of the gluon polarisation in J/ψ production seems feasible. The colour octet contributions become large at high z. Here, a measurement of $A^{\gamma N\to J/\psi}$ might be a tool to test the colour octet model.

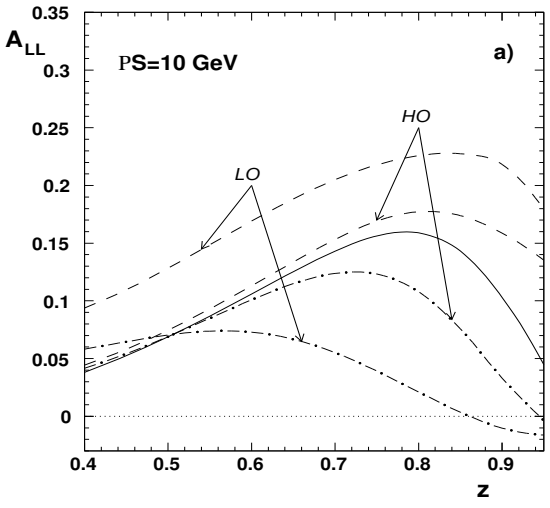

Figure 2.19.: Sensitivity of double–spin asymmetries in J/ψ photoproduction to COM matrix elements; the solid line corresponds to the CSM, the dashed lines represent different sets of COM matrix elements. The Figure is taken from [JNT:99].

3. The HERMES Experiment

The HERMES experiment is located at the Deutsches Elektronen–Synchronton (DESY) in Hamburg, Germany in the east section of the HERA collider, which consists of two storage rings with counter–rotating beams of protons and positrons or electrons with a circumference of 6.335 km. In 1995 to 1997 the machine was operated with a proton beam of 820 GeV and a positron beam of 27.5 GeV. In lepton–nucleon scattering there is no difference between electrons and positron at leading order QED and the term 'positrons' will be generically used for both in the following. Figure 3.1 shows a schematic view of the HERA facility with its four experiments. Positron–proton collisions are analysed by the experiments H1 and ZEUS to study the structure of the proton over a wide kinematic range in unpolarised deep–inelastic scattering. Presently being installed is the HERA–B experiment that will use target wires brought into the halo of the proton beam to measure possible CP-violation in B-meson production.

The HERMES experiment is designed for precision measurements of the spin structure functions of proton and neutron by the analysis of inclusive and semi–inclusive spin asymmetries in polarised deep–inelastic lepton–nucleon scattering. It uses an unique experimental technique: a longitudinally polarised internal gas target is brought into the longitudinally polarised circulating HERA positron beam. The HERMES forward spectrometer is optimised for the detection of semi–inclusive events. Besides its wide acceptance, it has excellent particle identification capabilities, since the interpretation of semi–inclusive measurements in terms of quark flavours is more clear if the hadron types are identified. Given these prerequisites, HERMES is also able to analyse the (spin–dependent) production of decaying particles like vector mesons. Besides the polarised targets, HERMES uses a variety of unpolarised target gases to study hadronisation in nuclei and nuclear effects in lepton–nucleon scattering.

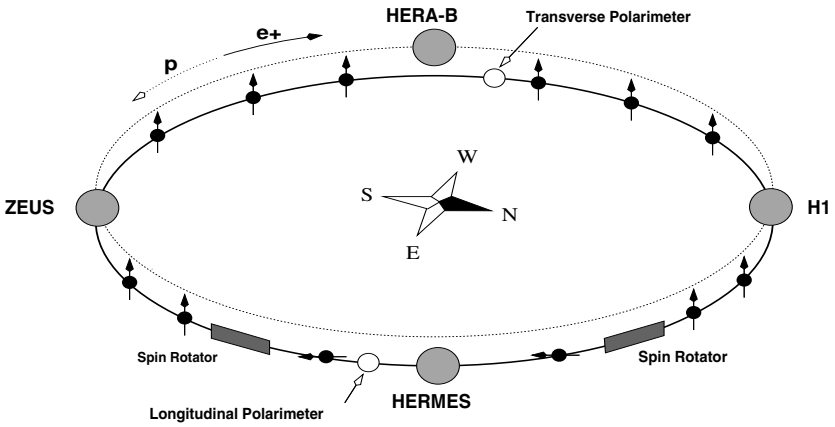

Figure 3.1.: Schematic view of the HERA collider.

3.1. Polarised Beam

The lepton beam is injected unpolarised. A transverse polarisation of the positron (electron) beam parallel (anti–parallel) to the magnetic dipole fields builds up naturally through the Sokolov–Ternov effect [ST:64], an asymmetry of the small spin flip amplitudes of synchrotron radiation in the bending dipoles. The beam polarisation P_B rises exponentially with time

$$P_B(t) = p_\infty \cdot \left(1 - e^{-t/\tau}\right), \tag{3.1}$$

where τ is a time constant determined by the beam energy and the radius of the accelerator and p_∞ is the asymptotic polarisation in the equilibrium of the spin flip processes in the dipoles. In an ideal flat machine of 27.5 GeV (i.e. a two dimensional ring with only vertical magnetic fields) p_∞ has a value of 92% and τ is 37 minutes. In the real machine, the maximum polarisation p_∞ is reduced and τ becomes larger because of depolarising effects like horizontal magnetic fields, spin diffusion, and depolarising resonances that cause precession of the positron spin [Due:95]. The average beam polarisation at HERA is about 55%, while the maximum polarisation reached is about 70%.

To obtain a longitudinal beam polarisation at HERMES, the transverse spin direction is turned $90°$ by a spin rotator in front of the experiment. A second spin rotator behind the experiment restores the transverse polarisation. Spin rotation is obtained by small horizontal and vertical deflections of the beam that cause precession of the positron spin. The longitudinal polarisation is positive or negative depending on the direction of the vertical deflection. Nevertheless, a reversion of the longitudinal beam polarisation requires a mechanical shift of the deflecting magnets and the beam pipe and can be only performed during a shutdown of the machine. In Figure 3.1 the positions of the spin rotators are shown, small arrows indicate the polarisation direction of the positron beam. Also indicated in the figure are the two Compton polarimeters for measuring the beam polarisation.

Both polarimeters use circularly polarised laser light scattered off the beam particles. The Compton cross section for scattering circularly polarised laser light off transversely polarised positrons shows an azimuthal $\cos\phi$ dependence with respect to the positron spin direction. This yields a spatial up–down asymmetry of the backscattered photons in a segmented position sensitive calorimeter [Due:95, Tip:99]. The circular polarisation of the laser is flipped between left and right at a rate of 90 Hz. Its intensity is chosen such that the probability for Compton scattering of a single photon per bunch is about 2%, thus avoiding multiple photon interactions (single photon method). The transverse beam polarisation is determined from the asymmetry of the spatial photon distributions between the left and right circular photon polarisation states.

The longitudinal beam polarisation is directly measured in the HERMES section of the positron ring [Lor:97]. The spin–dependent angular distribution of the Compton process yields a spin–dependent energy distribution of the photons that are backscattered off the longitudinally polarised positrons. The longitudinal polarimeter uses a high intensity laser beam so that several thousand photons are scattered per positron bunch and detected by a calorimeter. The beam polarisation is determined from the asymmetry of the energy deposition in the calorimeter for left–and right–circular polarisation states of the laser light.

Figure 3.2 shows the beam polarisation for one positron fill of the 1997 data taking period, measured with the two separate polarimeters. The polarisation rises exponentially at the beginning and stays stable for the entire length of the fill. In the analysis, the statistical

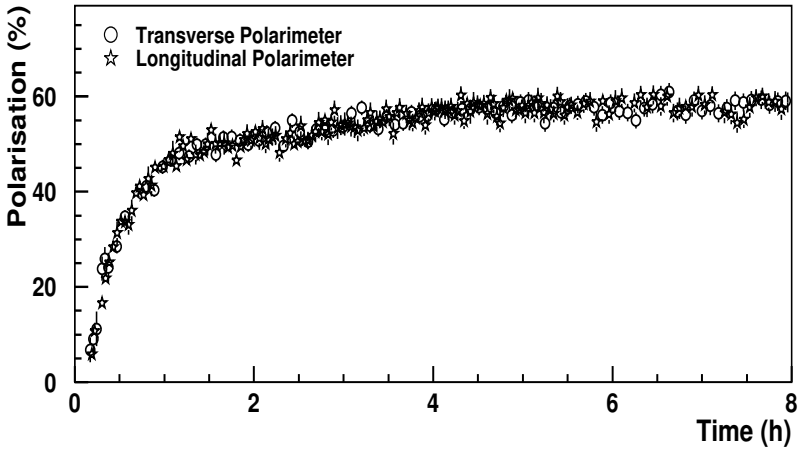

Figure 3.2.: Polarisation of the HERA positron beam for one fill. For display purposes only every fifth polarisation measurement is shown.

uncertainty of the polarisation measurement can be neglected, since the polarisation measurement is smoothed per fill by the fit of an exponential. The systematic uncertainty is about 5.5% for 1995, when only the transverse polarimeter was available, and 3.4% for 1996 and 1997.

3.2. Internal Gas Target

HERMES is using an internal gas target, where the polarised target gas is injected into a windowless storage cell directly in the vacuum of the positron beam pipe. This technique has the advantage that a single atomic species at a high degree of polarisation is injected, free from dilution by additional material like target windows. Polarised gas targets allow a rapid reversal of the polarisation state, reducing the systematic uncertainties of the asymmetry measurement. HERMES used a polarised helium–3 target in 1995, and a polarised hydrogen target in 1996 and 1997. In addition, unpolarised hydrogen (H_2), deuterium (D_2), helium–3 (^3He) and nitrogen (N_2) targets were used in the years 1995 to 1997. Additionally, in 1999 a data sample of krypton (Kr) was taken.

Figure 3.3 shows a schematic view of the target region. The target gas is injected through a side tube into the middle of the storage cell that is a 400 mm long open–ended thin aluminium tube of elliptical cross section, confining the target gas around the beam. After the diffusion of the target gas to the ends of the cell it is pumped away by a differential vacuum pump system that maintains the ultra high vacuum in the beam pipe. A triangular density distribution of the target gas is generated by the equilibrium of the injection at the centre and the diffusion to the ends of the storage cell, reflected by the shape of the z vertex distribution shown in Figure 3.3. A set of collimators in front of the target protects the storage cell and the spectrometer from synchrotron radiation and secondary particle showers. A thin 0.3 mm stainless steel exit window allows the scattered particles to emerge into the spectrometer. The gaps between the storage cell and the up– and down–stream end of the beam pipe are bridged by wake field suppressors to ensure the continuity of the beam enclosure reducing radio frequency (RF) excitations induced by the bunch structure of the beam.

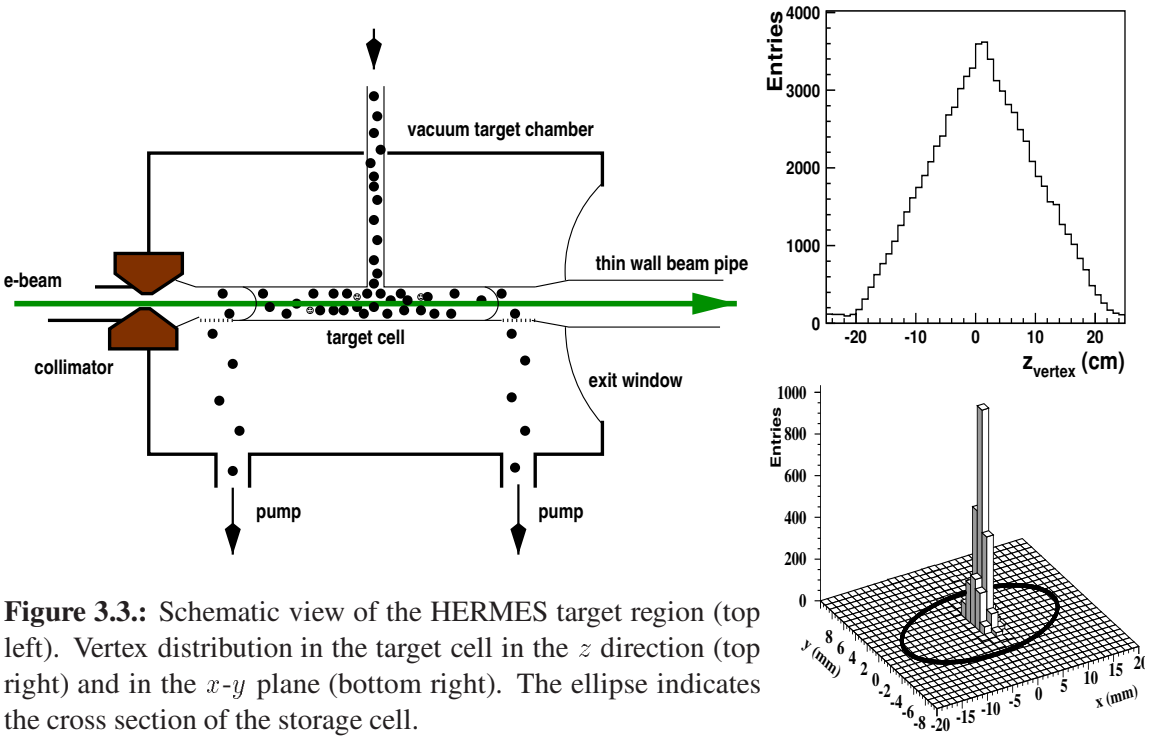

Figure 3.3.: Schematic view of the HERMES target region (top left). Vertex distribution in the target cell in the z direction (top right) and in the x-y plane (bottom right). The ellipse indicates the cross section of the storage cell.

Polarised Hydrogen Target

Molecular hydrogen ^{2}H is dissociated into a beam of ^{1}H hydrogen atoms by a strong 13.56 MHz radio frequency in an atomic beam source (ABS). These atoms are electron polarised by Stern–Gerlach separation in a sextupole magnet system. Gradient high frequency magnetic fields (RF transitions) induce adiabatic transitions between the four hyperfine states of the hydrogen, such that only the states with the required nucleon polarisation are populated [Ste:97]. The target polarisation can be reversed by changing the high frequency, such that the hyperfine states with the opposite nuclear polarisation become populated. During data taking the target polarisation was selected about once per minute, where the sequence of polarisation states is chosen randomly to avoid systematic biasing of the data. A longitudinal quantisation axis for the spins is given by a solenoid magnetic holding field of 335 mT that also prevents depolarisation of the hydrogen by the transient transverse magnetic fields generated by the circulating positron bunches [HERMES:99a].

The target cell is coated with Drifilm and a layer of ice introduced by a small fraction of 20 ppm oxygen added to the target gas. This coating minimises molecular recombination and depolarisation of the hydrogen atoms through their collisions with the cell wall. To slow down thermal diffusion of the target gas to the ends of the cell, it is operated at 100 K, which is the minimum temperature before recombination of the hydrogen atoms at the cell wall takes place. The target density at this temperature is about $8 \cdot 10^{13}$ atoms/cm^2; the storage cell technique increases the target density by two orders of magnitude with respect to a free gas jet crossing the positron beam.

A small fraction of the target gas is collected by a sample tube. This sample is analysed by a Breit–Rabi polarimeter (BRP) that reverses the entire polarisation procedure. To measure the target polarisation, the relative occupancy of the hyperfine states of the hydrogen atoms is determined using a sextupole magnet, RF transitions, and an atomic beam detector [Bra:97]. A target gas analyser (TGA) with a mass spectrometer determines the relative amount of

molecular and atomic hydrogen in the target cell. The target polarisation P_T is calculated using the following expression

$$P_T = \alpha_0 \left(\alpha_r + (1 - \alpha_r)\,\beta\,\right) P_T^{atom}, \tag{3.2}$$

where α_0 is the initial atomic fraction of 0.99 ± 0.01(syst), α_r is the fraction of hydrogen atoms that do not recombine in the target cell, and $(1 - \alpha_r)$ is the fraction of recombined molecules with relative polarisation β. Since the target gas is not analysed directly within the target cell, small Monte Carlo sampling corrections have to be applied to the measurements of the BRP and the TGA: $\alpha_r = c_\alpha \alpha_r^{TGA}$ and $P_T^{atom} = c_p p^{BRP}$ [Bau:98]. The average atomic fraction was 0.88 ± 0.3 in 1996 and 0.93 ± 0.04 in 1997. The polarisation of the molecules β could be constrained between 0.2 and 1 [Kol:98b]. It is the main contribution to the systematic uncertainty of the target polarisation. For the 1996 data, the systematic uncertainty of the target polarisation calculated by Equation 3.2 is large because of the low atomic fraction α_r. To reduce this uncertainty, the target polarisation for the 1996 data was normalised to the 1997 data by comparing the measured inclusive asymmetries. The 1996 target polarisation is then directly determined from the polarisation measurement of the BRP as $p_t = 0.92 \cdot p^{BRP}$ [HS:97]. The average target polarisation for the combined 1996 and 1997 data on the polarised hydrogen target is 0.88 ± 0.05, where the uncertainty is purely systematic and includes the uncertainty of the normalisation procedure for 1996. Since 1998, HERMES is using a polarised deuterium target. Although the hyperfine structure of deuterium is more complex, the principle of polarisation is the same.

Polarised Helium Target

Helium-3 is used as a polarised neutron target, since it can be approximately viewed as a spin–polarised neutron with a dilution of two opposite spin polarised protons. In the polarisation process, a small fraction of ^{3}He atoms is shifted from the ground state $^1S_0$ to the metastable $^3S_1$ state by a weak RF field. Within a quartz cell, circularly polarised infrared laser light excites transitions from the $^3S_1$ state to the $^3P_0$ state. It decays back to the $^3S_1$ state by the emission of unpolarised light such that the net angular momentum of the laser light remains with the metastable atoms. Their nuclear polarisation is transfered into a stable polarised ground state by metastability exchange collisions, where the electron clouds between metastable and ground state atoms are exchanged. The HERMES ^{3}He target had a density of about $1 \cdot 10^{15}$ nucleons/cm^2 and an average polarisation of $46 \pm 0.05\%$ [S$^+$:98]. In this work, the ^{3}He data is only used for the J/ψ cross section analysis, neglecting the target polarisation.

Unpolarised Targets

The unpolarised gas feed system (UGFS) is a simple device, where the target gas is simply blown into the target cell. Gas targets allow a fast exchange of the target material and at least two target gases were switched on an hourly basis to reduce the uncertainty in the relative normalisation. The density of polarised hydrogen targets is restricted by the intensity of the current polarised sources. In contrast, the density of unpolarised targets, typically $10^{15\cdots17}$nucleons/cm^2, is only restricted by the fact that the reduction of the beam life time must not exceed a certain limit, if the unpolarised measurements are performed in parallel to the other HERA experiments. In the case of dedicated HERMES data taking, the target density is only restricted by the maximum throughput of the data acquisition system.

3.3. The HERMES-Spectrometer

The HERMES experiment uses an open magnet spectrometer [HERMES:98a] shown in Figure 3.4, horizontally divided into a symmetric upper and lower half by the positron and the (unused) proton beam lines. A dipole spectrometer magnet provides an integrated field strength of 1.3 Tm. A massive iron plate shields the beams as they travel through the magnet and determines the spectrometer acceptance at low scattering angles. The vertical and horizontal acceptance cover $40 < |\theta_y| < 140$ mrad and $|\theta_x| < 170$ mrad, respectively. Field clamps minimise the influence of fringe fields on the adjacent drift chambers.

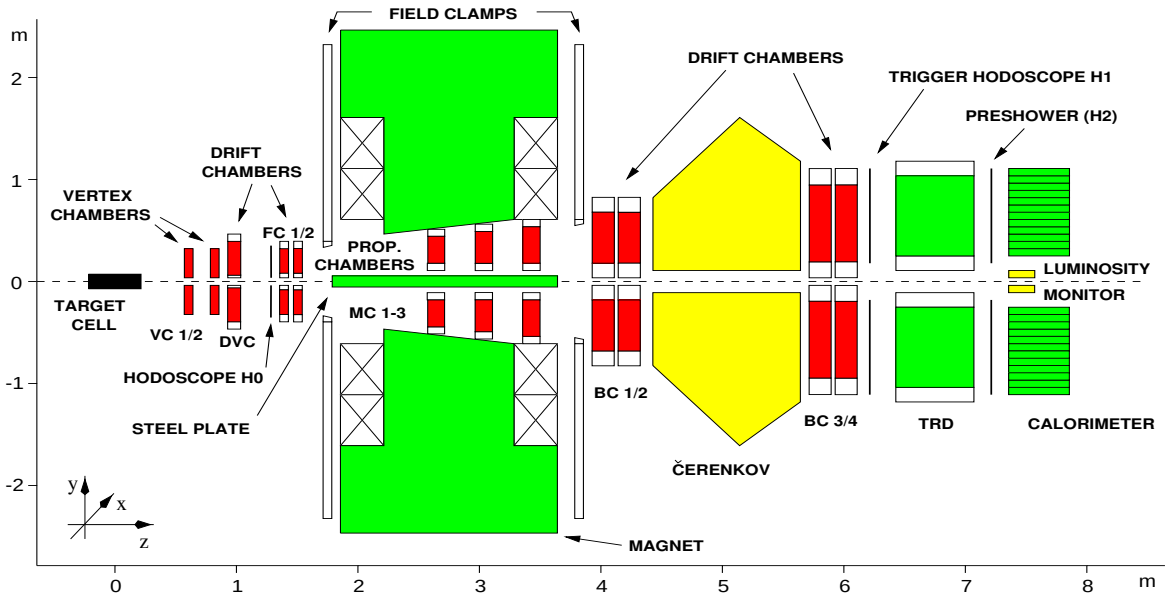

Figure 3.4.: Schematic side view of the Hermes spectrometer

Tracking

The polar (θ) and azimuthal (ϕ) scattering angles and the initial trajectory for the determination of the particles momentum are determined by the front part of the tracking system, consisting of a micro-strip gas chamber vertex detector (VC) and a set of drift chambers, DVC and FC1/2. Four drift chambers (BC1-4) behind the magnet provide tracking after the particle tracks are deflected within the magnet. Three proportional chambers (MC1-3) located within the opening of the magnet are used for the reconstruction of tracks with low momenta that are bend out of the acceptance and do not reach the rear part of the spectrometer. All tracking devices measure space points in three coordinates: vertical(x) and at stereo angles $\pm 30°$ (u, v). The tracking system of each spectrometer half has 24 active planes in front and behind the magnet as well as 9 planes within the magnet.

All drift chambers have the same principle construction, although their geometrical size increases with the distance from the target. They consist of six layers of drift cells, where each layer is constructed of a plane of alternating cathode and anode wires between cathode planes of aluminised mylar. The (nearly) quadratical drift cells have a size of 6×6 (DVC),

7×8 (FC) and 15×16 mm (BC). Two consecutive planes have the same wire inclination, while their drift cells are staggered by half a cell width to resolve left–right ambiguities $(uu'xx'vv')$. All drift chambers are operated with the same $Ar(90\%)/CO_2(5\%)/CF_4(5\%)$ gas mixture with a drift velocity of about 70μm/ns at the average field strength of $E = 800$ V/cm. A total of 11072 channels is read out via amplifier cards directly mounted to the chambers and by FastBus TDC's with a time resolution of 0.5 ns. The spatial resolution per plane is about 220 μm for the DVC's and FC's and about 300 μm for the BC's at an average efficency of more than 99% for positrons and 97% for hadrons.

The drift vertex chambers (DVC) were installed in 1997 to increase the redundancy in the front tracking system. In addition, their active area exceeds the standard acceptance providing additional space points in an enlarged acceptance of $|\theta_y| < 270$ mrad. Together with the information of muon detectors behind the calorimeter and the spectrometer magnet, installed in 1998 and 1999, they will allow reconstruction of muons from J/ψ decays and semi leptonic D-meson decays that pass through the iron yoke of the magnet [HERMES:97c].

The multi–wire proportional chambers MC1-3, operated in the strong field of the magnet, have a cell size of 4×4 mm and use a gas mixture with the same components as the drift chamber gas but optimised for the MWPC operation: $Ar(65\%)/CO_2(30\%)/CF_4(5\%)$. A total of 11008 channels is read out by a digital one–bit read out. The three planes per module (u, x, v) provide a resolution of about 700 μm per space point.

Micro-strip gas chambers (MSGC-VC1/2) are used for a high precision measurement of the primary vertex position. Metal cathodes and anodes strips at a pitch of 193 μm are etched onto a 200 μ glass substrate. The operation principle of MSGC's is similar to conventional drift chambers: charged particles ionise a 3 mm thick gas volume of $DMC(50\%)/Ne(50\%)$ above the substrate; the ionisation clusters drift to the anodes and are amplified by an avalanche process. A total of 24800 channels is read out by analogue pipeline chips (APC) directly bonded to the substrates. The resolution of the VC's is 65 μm with an efficiency of 95%.

The HERMES reconstruction program employs two efficient techniques: a tree–search algorithm for the track finding and a look–up table for the momentum determination [Wan:96]. The reconstruction algorithm is based on the fact that all chambers have the same u, x, v structure. So–called tree–lines in each of the three coordinates are determined by an iterative pattern recognition algorithm, separately for the front and back part of the spectrometer. The hit pattern in the detector planes are compared to a pattern data base and combinations are rejected that can not be caused by straight tracks. In each iteration step the resolution of the pattern comparison is doubled and only 11 iterations are necessary for the track finding. The tree–lines of the u, x, v coordinates are combined to front and back spatial partial tracks, subsequently matched in the magnet centre. The momentum of the tracks is determined from a look–up table, generated only once during the initialisation of the program, saving the computing time to calculate the momentum from the deflection in the magnet. Over the kinematic range of the experiment, the momentum resolution for positrons is 0.7-1.25 % and the uncertainty in the scattering angle is about 0.6 mrad.

Because of difficulties with the readout chips, the VC's became operational only in 1997 at the same time the DVC's were installed. Therefore, the 1995 to 1997 data sample used in this work is split in terms of reconstruction methods. All tracking devices in the front part of the spectrometer (VC,DVC,FC1/2) are used in the so–called standard reconstruction method (STD), available only for the 1997 data on the polarised hydrogen target. All other data is reconstructed with the NOVC–reconstruction method, using only the front drift chambers

FC1/2. Here, an additional space point for the determination of the front track is provided by the back partial track projected into the centre plane of the magnet. It turned out, that the NOVC method causes only a moderate loss in resolution for the kinematic variables. Nevertheless, the vertex resolution is reduced by a factor of two.

Particle Identification

The HERMES spectrometer provides an excellent positron–hadron separation using four sub–systems for particle identification (PID): a lead–glass electromagnetic calorimeter, a preshower detector, a transition radiation detector and in 1995 to 1997 a threshold Cherenkov detector. A hadron rejection factor of at least 10^4 ensures a very clean DIS positron sample with a hadron contamination of below 1% over the entire kinematic range of the experiment. In addition, pions with momenta above the Cherenkov threshold can be identified. Figure 3.5 shows the individual responses of the four particle–identification detectors to positrons and hadrons with momenta above 6 GeV. To select pure positron and hadron samples for each of these plots stringent cuts are placed on the remaining detectors.

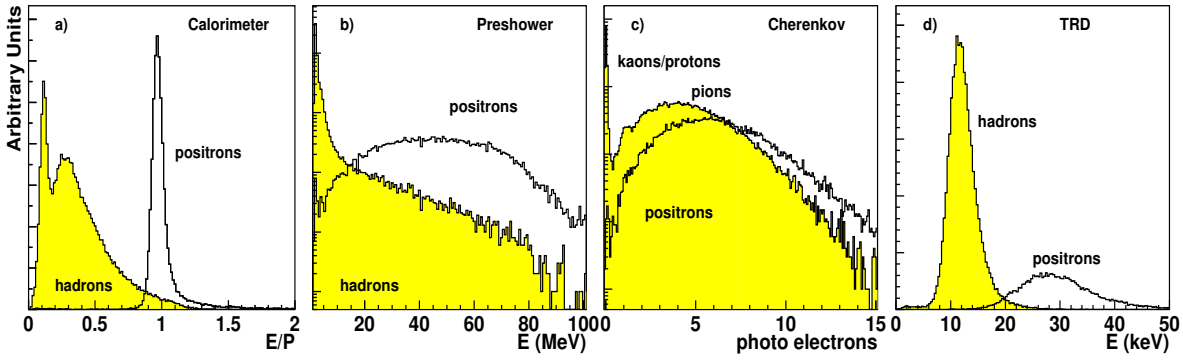

Figure 3.5.: Response of the four particle identification detectors of the HERMES spectrometer to positrons (open histograms) and hadrons (shaded) with momenta of $p > 6$ GeV.

Both identical calorimeter halves consist of 42×10 lead–glass blocks of $9 \times 9 \times 50$ cm^3 ($\sim 18X_0$), read out at the rear by a single photomultiplier. The energy resolution of the calorimeter is $\sigma(E)/E[\%] = 1.5 + 5.1/\sqrt{E[\mathrm{GeV}]}$. Figure 3.5 a) shows the ratio of the energy deposit in the calorimeter to the particles momentum: it is unity for positrons, clearly separated from hadrons that do not deposit all their energy in the calorimeter. The peak around 0.1 is due to minimum ionising particles. As it will be discussed in Section 4.3, a minimum energy loss in the calorimeter will be used for muon identification.

The hodoscopes H1 and H2, in conjunction with the front hodoscope H0 and the calorimeter, provide fast signals for the first level trigger discussed in detail in Section 4.6. Both H1 and H2 are constructed of 42 vertical scintillator slabs per detector half, where $91 \times 9.3 \times 1$ cm^3 scintillators overlap to avoid insensitive areas between them. Each scintillator is read out by a single photomultiplier that is coupled to the outer end by a light guide. A passive radiator of 11 mm (two radiation lengths) of lead sandwiched between two 1.3 mm stainless–steel sheets converts the hodoscope H2 into a preshower detector for the calorimeter. It provides discrimination between positrons and hadrons, since the radiator initiates electromagnetic showers that deposit a typical energy of 20-40 MeV in the scintillators, much more than minimum ionising particles (cf. 3.5 b).

Each module of the threshold Cherenkov counters has a depth of the gas radiator volume of 1.17 m; Cherenkov photons are directed to 24 photomultipliers of 12.7 cm diameter by spherical mirrors of 1.56 m radius. In 1995 pure nitrogen was used as radiator gas yielding a threshold for pions, kaons, and protons of 5.5, 19.8, and 37.6 GeV, respectively. The thresholds were lowered in 1996 and 1997 to 3.8, 13.6, and 25.8 GeV by a mixture of 70% nitrogen and 30% perfluorbutane (C_4F_{10}). In Figure 3.5 c) the response of the Cherenkov detector to particles with momenta above the pion threshold is shown: kaons and protons are clearly separated from pions. On the other hand, pions and positron cause similar signals, thus the contribution of the Cherenkov to the lepton–hadron separation is limited. In 1998, the threshold Cherenkov has been upgraded to a dual radiator (C_4F_{10} gas and aerogel) ring imaging Cherenkov (RICH) [C$^+$:97], that will provide pion, kaon, and proton identification over the full momentum range of the hadronic spectrum.

The HERMES transition radiation detector (TRD) consists of six identical modules per spectrometer half. Each module has a 6.35 cm thick radiator, pseudo–randomly filled with 20 μm thin plastic fibers, and a conventional proportional wire chamber for photon detection. These chambers have 256 wires at a pitch of 1.27 cm, operated with a $Xe(90\%)/CH_4(10\%)$ gas mixture. At HERMES kinematics only positrons produce transition radiation photons, while hadrons lose energy only by the ionisation of the gas mixture in the detector chambers. As shown in Figure 3.5 d) the energy deposit of positrons is about twice as much as that of hadrons. The quantity shown in the figure is the truncated mean of all six modules, where the largest signal is dismissed and the average from the remaining five is taken, providing a pion rejection factor of more than 10^2.

A clean sample of positrons or hadrons can be selected by stringent but inefficient cuts on the individual response of the four particle identification detectors, used typically only for detector studies and for the determination of trigger efficiencies. A much better efficiency is achieved by the use of probability functions $P_j^i(p,x)$ that a particle of type i and momentum p will yield a certain response x in detector j. The probabilities P_j^i are determined by comparing the detector responses for each track to typical response functions (parent distributions) that are derived from data or Monte–Carlo simulations. By combining the probabilities of all four PID detectors the so–called PID4 [Kai:97] scheme is defined

$$\mathrm{PID4} = \log_{10} \frac{P^e_{cal} P^e_{Pre} P^e_{Cer} P^e_{TRD}}{P^h_{cal} P^h_{Pre} P^h_{Cer} P^h_{TRD}}, \tag{3.3}$$

that gives the logarithmic likelihood that a certain particle has been identified by all four detectors as a positron rather than as a hadron. An improved particle identification scheme PID3+PID5 [Men:98] combines the probabilities of the calorimeter, preshower, and Cherenkov (PID3) and treats all six TRD modules per spectrometer half as independent measurements (PID5):

$$\mathrm{PID3{+}PID5} = \log_{10} \frac{P^e_{cal} P^e_{Pre} P^e_{Cer}}{P^h_{cal} P^h_{Pre} P^h_{Cer}} + \log_{10} \frac{\prod_{i=1}^{6} P^e_{TRD_i}}{\prod_{i=1}^{6} P^h_{TRD_i}}. \tag{3.4}$$

The distribution of the PID parameter PID3+PID5 for particles above 6 GeV is shown in Figure 3.6, the positron–hadron separation at HERMES has an efficiency of better than 98% and a contamination of less than 1%. Since PID3+PID5 has not yet been available for the 1995 data PID4 was consistently used in the J/ψ cross section analysis; while PID3+PID5 was used for the analysis of ρ meson production using the 1996 and 1997 data on the polarised hydrogen target only.

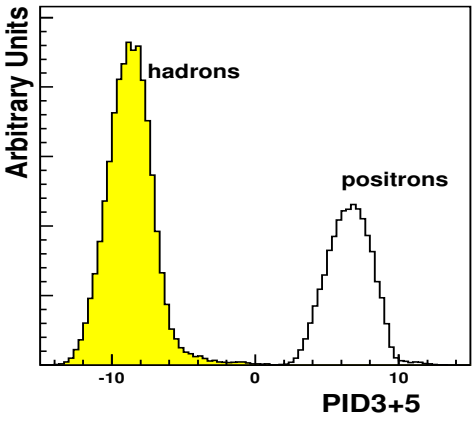

Figure 3.6.: Logarithmic likelihood PID3+PID5 for positrons and hadrons with momenta $p > 6$ GeV.

Luminosity Monitor

The primary task of the luminosity monitor [Ben:98b] at HERMES is to provide a relative luminosity measurement between the opposite target spin states for the asymmetry measurements. The luminosity monitor detects coincident e^+e^- pairs produced by Bhabha (Moller) scattering of the beam positrons (electrons) with the shell electrons of the target gas, where the cross sections for both purely electromagnetic processes are precisely known. Located 7.2 m behind the target centre, the luminosity monitor consists of two calorimeters symmetric to the beam axis with a horizontal acceptance of 4.6 to 8.9 mrad. In comparison, the symmetric scattering angle is 6.1 mrad when both particles have half of the 27.5 GeV beam energy. Each calorimeter is built of 3×4 radiation hard $2.2 \times 2.2 \times 20$ cm^3 $NaBi(WO_4)_2$ crystals, each read out by a photomultiplier. The statistical uncertainty of the luminosity measurement is about 1% within a time window of 100 s.

Data Acquisition

The HERMES data acquisition system is based on FastBus, using two CERN host interfaces as bus masters. All drift chambers are read out by FastBus TDC's (time to digital converters), while vertex and magnet chambers are read out by a PCOS IV system that allows only one information bit per channel. All photo multipliers and the TRD photon detectors are read out by ADC's (analogue to digital converter). In addition, the trigger hodoscopes are read out by TDC's to allow time of flight determination. The electronics is located in a trailer, separated by a shielding wall from the experiment. During a fill of the positron machine that typically lasts 8 to 12 hours the data is written onto staging disks in the online computer system. After the fill, the data is transfered by a FDDI link to a tape robot on the DESY main site and a backup is written to local DLT tapes. In the years 1995 to 1997 about 2, 4.1, 7.5 TByte of data were stored on tape, respectively. The maximum manageable event rate of the DAQ with low dead time was 150 Hz in 1995/96 and about 300 Hz in 1997.

4. Measurement of the J/ψ Cross Section

A clear J/ψ signal in the two di–leptonic decay channels $J/\psi \to e^+e^-$ and $J/\psi \to \mu^+\mu^-$ was extracted from the HERMES data of the years 1995 to 1997. The invariant mass distributions for both decay channels are shown by the histograms in Figure 4.1. The solid line in the figures indicates the fit of a Gaussian plus an exponential function to describe the signal and the combinatorial background. The shaded area represents the invariant mass distribution for background events where both tracks have the same charge normalised to the histogram; the dashed line is a fit by an exponential function that reproduces the combinatorial background underneath the signal. The number of events is 70 ± 8 over a background of 25 ± 5 for $J/\psi \to e^+e^-$ and 30 ± 5 over 4 ± 2 for $J/\psi \to \mu^+\mu^-$. All available data on polarised and unpolarised targets are combined.

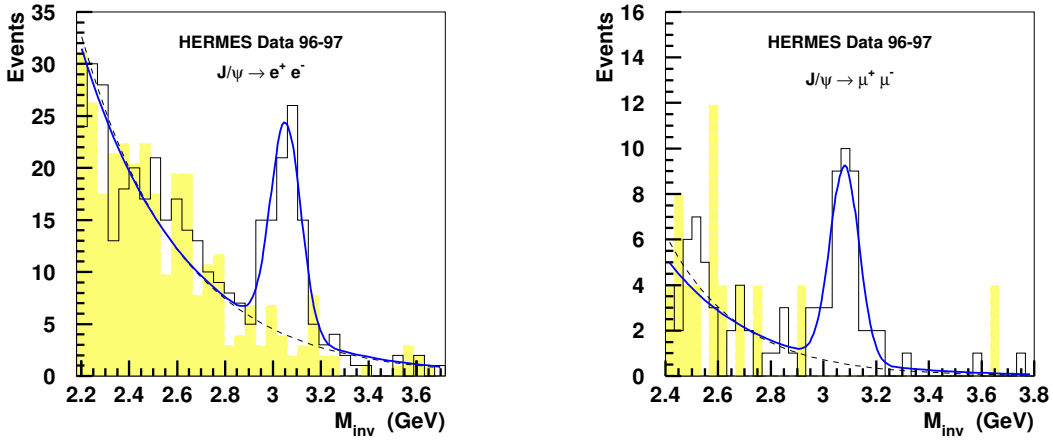

Figure 4.1.: Invariant mass spectrum in the decay channels $J/\psi \to e^+e^-$ (left) and $J/\psi \to \mu^+\mu^-$ (right) fitted by a Gaussian plus an exponential function (solid lines). The shaded areas indicate background from events where both tracks have the same charge; it is normalised to the histogram and fit by an exponential function (dashed lines).

At HERMES, the J/ψ's are dominantly produced in photoproduction at low Q^2 where the scattered positron remains inside the beam pipe. For the detection of J/ψ's decaying into e^+e^- the HERMES spectrometer is ideal in terms of particle identification and trigger. The HERMES PID system accomplishes an excellent positron identification. All e^+e^- particles from a J/ψ decay accepted by the HERMES spectrometer have momentum greater than 5 GeV and will hence generate a standard DIS trigger by themselves, i.e. without a deep–inelastic scattered positron.

The second decay channel, $J/\psi \to \mu^+\mu^-$, became only accessible after a dedicated trigger upgrade in the beginning of 1996. Until 1997 the HERMES spectrometer did not have a muon detector. Therefore, particle identification for muons was achieved by requiring minimum ionising particles in the calorimeter and the preshower detector in coincidence with a signal in the Cherenkov detector.

The total number of detected J/ψ's is small, because the HERMES experiment was not designed for the analysis of charmed final states. The acceptance of the spectrometer for J/ψ detection is about 10% only. In addition, for most of the events the scattered positron remains undetected inside the beam pipe preventing the full reconstruction of the event kinematics. The beam energy of 27.5 GeV allows charm production only near threshold where the cross section is small. But, the threshold behaviour of charm production is an interesting topic by itself and only a limited amount of data on J/ψ production near threshold exists from experiments using real photon beams. The HERMES measurement is the first data obtained from lepton–nucleon scattering in this kinematic region. The understanding of the data obtained in the extraction of the (unpolarised) cross section is a necessary prerequisite for the later analysis of the spin dependence of hidden charm production.

4.1. Data Samples

Since the J/ψ signal at HERMES is small, the data of all polarised and unpolarised targets from the years 1995 to 1997 had to be combined to allow for a statistically significant cross section measurement. In Table 4.1 the available data samples are summarised. To illustrate their relative luminosities the number of DIS events (after data quality requirements discussed below) are given. The cuts applied to select a DIS-candidate are listed in Section 4.5. A total number of 18.5×10^6 DIS events are recorded corresponding to a luminosity of 400 pb^{-1}.

In the year 1995 the polarised helium target $(^3\vec{H}e)$ was used to measure the spin structure function g_1^n of the neutron. The very small data samples of 1995 on unpolarised targets (H_2, D_2) have been excluded from this analysis since they contain basically no J/ψ candi-

Year	Target Type	Total number of DIS events ($\times10^6$)	Analysed Decay Channel $J/\psi \to e^+e^-$	Analysed Decay Channel $J/\psi \to \mu^+\mu^-$
95	$^3\vec{H}e$	4.11	•	
	H_2	0.29		
	D_2	0.39		
96	$\vec{H}_1$	0.97	•	•
	H_2	1.42	•	
	D_2	2.28	•	
	^3He	0.76	•	
97*	$\vec{H}_1$	2.08	•	•
	H_2	1.56	•	•
	D_2	2.42	•	•
	N_2	2.19	•	•

Table 4.1.: Summary of HERMES data samples from 1995-1997. $^{(\star)}$For the 1997 data on the polarised hydrogen target $(\vec{H}_1)$ the STD reconstruction method was used.

dates. In 1996 and 1997 HERMES was running with the polarised hydrogen target ($\vec{H}_1$) to measure g_1^p of the proton. Additionally, a large amount of data was taken on several unpolarised targets. Because of the high density of the unpolarised targets, this data have been collected in the rather short time of about six weeks distributed over the two years. The NOVC reconstruction method (cf. Section 3.3) has been used for all data, except the the 1997 data on the polarised hydrogen target, which where reconstructed using the STD method. The second J/ψ decay channel $J/\psi \to \mu^+\mu^-$ became accessible for the polarised ($\vec{H}_1$) 1996 and all 1997 data due to the trigger upgrade to be discussed in Section 4.6. A main task of the analysis described in the following is to understand possible differences between the J/ψ subsamples to combine them for the cross section measurement.

4.2. Burst Selection and Data Quality

Both the HERMES spectrometer and the target are complex technical devices and reliable data taking requires, beside stable beam conditions, that all components are functioning properly. Therefore, certain selection criteria are applied to ensure a good quality of the data. HERMES data sets are divided in fills, runs and bursts. A fill denotes one filling of the HERA–positron ring and lasts typically between 8 and 12 hours. The length of a run is determined by the file size of about 500 MByte that is stored by the data acquisition system (DAQ) to a tape robot. Depending on the event rate a run lasts between 10 and 30 minutes. The (somewhat arbritrary) time period of 10 seconds is called a burst. All data which are not related to the physics events but to the detector components like voltages, currents, parameter settings and measurements, polarisations, etc. are read out on the burst level by the slow control system.

Data quality information is mainly based on the slow control information automatically recorded during data taking, but it also includes the results of several offline data quality, consistency, and calibration analyses. After their reconstruction the physics events are merged with the slow control and data quality information into so called μDST; all necessary information to perform a physics analysis is stored in one single file per run. Data quality cuts are applied on the burst level, i.e. all events in a burst marked 'bad' are not used.

The burst selection criteria used for the J/ψ analysis are derived from the data quality criteria developed for the inclusive measurement of the spin structure function g_1 [HERMES:97b, Gut:99]. For the J/ψ cross section analysis of all available data from polarised and unpolarised targets some of these data quality criteria had to be adjusted and all cuts related to the polarisation information of beam and target were discarded. Because of the opening angle between the decay particles in the laboratory frame one of them is usually detected in the top and one in the bottom half of the spectrometer. Therefore, bursts were only accepted for the J/ψ analysis if the data quality marks top and bottom half of the spectrometer as 'good'.

Although the general structure of the burst selection is similar for all three years from 1995 through 1997, some details differ due to the different targets and the progress in understanding hardware and data. Table 4.2 summarises the data quality criteria for the cross section analysis, explained in the following.

General Data Quality The runs are pre–selected by the information from the data taking logbook. Since 1996 the shift crew marks each single run as analysable or non–analysable in a log file which is read during the μDST production, i.e. data taken for special detector tests or calibration purposes as well as data with known problems are removed by hand.

During the production of the μDST, when redundant data are available, several quality and consistency checks are performed. Bursts with synchronisation problems between physics events and slow control data, with time jumps and jumps in the numbering of events or bursts, or with missing or corrupted information are not used for analysis. In the beginning of each run several detector and readout initialisations are performed. For example the thresholds of the pre–amplifiers of the drift chambers are raised for a short time to suppress oscillations that would reduce the drift chamber efficiencies. At the end of a run the last burst might be split between two runs. Therefore the first and last burst of each run are discarded.

Criterion		1995	1996	1997(NOVC)	1997(STD)
Logbook	OK	•	•	•	•
DQ μ-DST	OK		•	•	•
First/Last Burst	Reject	•	•	•	•
DAQ Efficiency		$0.5 \leq \epsilon_{DAQ} \leq 1$	$0.5 \leq \epsilon_{DAQ} \leq 1$		
Burst Length	[s]	$9 \leq T_{Burst} \leq 11$	$0 \leq T_{Burst} \leq 11$		
Beam Current	[mA]	$8 < I_e < 32$	$5 < I_e < 50$		
Lumi Rate	[Hz]	$40 < R_L < 210$	$5 < R_L < 1000$		$5 < R_L < 60$
Target Gas		${}^3\vec{H}e$	$\vec{H}_1, H_2, D_2$	H_2, D_2, N_2	$\vec{H}_1$
Target Density	$\frac{10^{15}}{\mathrm{cm}^2}$	$0.85 < \rho < 1.4$			
$R_L/I_e/\rho$	$\frac{\mathrm{cm}^2}{10^{15}\mathrm{mAs}}$	$5 < \frac{R_L}{I_e \rho} < 7.2$			
FC Efficiency		$\epsilon_{FC} > 0.8$			
BC Efficiency		$\epsilon_{BC} > 0.94$			
HV Trips	None		•	•	•
DQ VC	OK				•
GMS-Calo	OK	•	•	•	•
Scaler H1/H2	OK	•			
GMS-Lumi/H2	OK	•	•	•	•
DQ TRD	OK	•	•	•	•
DQ Cherenkov	OK	•	•	•	•
Remaining Bursts		$\sim 35\%$	58.5%	83.1%	76.7%

Table 4.2.: Summary of data quality criteria applied to the 1995 to 1997 data for the cross section analysis. For explanation see text.

Data Acquisition System If a trigger occurs while the previous event is still read out it cannot be accepted by the DAQ and the corresponding event is lost. The efficiency of the data acquisition system ϵ_{DAQ} is given by the ratio of triggers accepted by the DAQ to the total number of generated triggers:

$$\epsilon_{DAQ} = \frac{N_{accepted}}{N_{generated}}. \tag{4.1}$$

This efficiency is sensitive to the event rate which is determined by target density, beam current, and trigger setup. In addition, it is sensitive to background showers that increase the number of 'hits' in the detectors and hence the time needed for the event read out. Background showers have three main sources: fluctuations in the positron beam, showers emerging from the collimators in front of the target, and the proton beam halo. The typical efficiency of the DAQ is above 95% at a maximum throughput of about 500 Hz. A cut on the trigger efficiency and an additional cut on the length of a burst removes data taking periods with bad background conditions or problems with the data acquisition system itself.

Beam Performance Cuts on the beam current and on the count rate of the luminosity monitor are used to select periods of stable beam conditions. The lower limit of the beam current rejects periods with small event rates in which insufficient statistics was collected per burst for consistency checks. Other beam parameters, like slopes and positions with respect to the spectrometer are monitored as well but are not used as data quality criteria. The luminosity monitor is sensitive to fluctuations in the beam orbit; the cut on its count rate ensures a stable beam and removes spikes from the luminosity monitor readout.

Target Performance In contrast to the case of polarised targets, the gas feed system for the unpolarised targets is a rather simple device. To reduce the systematic uncertainty for the measurement of cross section ratios, the type of unpolarised target gas is changed on a time–scale of one hour. An electronic readout of the valve settings in the gas feed system ensures that the used target gas is known. In addition, the target gas is checked by an offline analysis comparing normalised luminosity rates. Periods where the targets were exchanged and a gas mixture is in the target cell are excluded from the analysis. In 1995 an explicit cut was used on the target density and a consistency check was done by monitoring the ratio of luminosity rate versus target density and beam current.

Tracking Detector Performance If the current drawn by a drift chambers exceeds a certain limit the high voltage is switched off ('trip') to prevent the thin drift chamber wires from damage. For example, these trips can be caused by high background or particle showers due to unstable beam. During a high voltage trip and shortly afterwards, when the voltage is switched on again, the affected drift chamber plane has a low efficiency and does not reliably contribute to tracking. In 1995 the efficiency of the tracking detectors was obtained from the reconstructed data. An explicit cut on the efficiency of a each single drift chamber plane was placed to detect high voltage trips. Since 1996 the drift chambers were running much more stable and at high efficiencies close to unity removing the need for an explicit cut on the chamber efficiencies. The high voltage status of the drift chambers is read out by slow control and since 1996 this information is used to remove data in the case of high voltage trips. Operation and read out of the vertex chambers (VC) are separate from the drift chambers and an own offline data quality analysis ensures their stable function and the proper synchronisation of the readout with the DAQ.

Performance of Particle Identification Detectors All detectors read out by photomultipliers, like calorimeter, hodoscopes, luminosity detector, and Cherenkov detector are using a gain–monitoring system (GMS). At a rate of about 3 Hz a well defined laser pulse is fed by a glass fiber into each lead glass block or scintillator slab; the Cherenkov gas volume is lit by LED's. The photomultiplier responses are compared to a reference detector and periods with unstable or missing PM signals are rejected. Offline analyses identify periods with problems in a certain PID detector. Similar to drift chambers, the Cherenkov detector and the TRD are using gas filled volumes and their performance is influenced by the actual gas mixture and by atmospheric pressure. Especially for the TRD, the air pressure influences its response and a careful run–wise calibration of the detector has to be performed.

In **1995** the experiment was commissioned. A large amount of testing has been done, and these periods, as well as periods of instable detector, beam, or target performance have been removed by the information from the logbook. From the remaining data sample (which is about 50% of all data written to tape) 70% can be used for the unpolarised cross section analysis. The dominant loss of data after the pre–selection by the logbook information is due to high voltage trips in the front drift chambers and the insufficient synchronisation between DAQ and slow control necessary at the beginning of each run.

In **1996** several changes were made. A more stable operation of the back chambers was achieved by correcting the high voltage for air pressure changes, and additionally the high voltage of the BC's was raised, yielding a better resolution. The threshold of the Cherenkov detector was lowered by increasing the amount of C_4F_{10} in the radiator gas. In total $\sim 60\%$ of the bursts remain for analysis, where the largest data loss is due to tests of the PID detectors at the beginning of the year.

In **1997** about 83% of the bursts from unpolarised targets and 77% of the bursts from the polarised target can be used for the cross section analysis. The data loss is very small and reflects the stable operation of the experiment in 1997.

4.3. Event Selection

Event Selection Criteria

In order to extract the J/ψ signal, three types of event selection criteria were used. Most important were the PID cuts which turned out to be normally sufficient to identify the signal. Cuts on the vertex position and on kinematic variables were applied to improve the signal–to–background ratio. The extracted signals were found to be stable against variations of cuts. The criteria are chosen similar for all three years, however, small adjustments had to be made to maximise the signal–to–background ratio. Table 4.3 and 4.4 summarise the event selection criteria per data sample for both decay channels that will be explained in the following.

Positron Identification For the positron identification the particle identification scheme PID4 (cf. Section 3.3) was used, since the revised particle identification scheme PID3+PID5 has not been available for all data. The differences between the use of different PID schemes was studied carefully for the 1996 and 1997 data; the influence on the extracted $J/\psi \to e^+e^-$ signal was found to be small.

Data Sample	PID	d (cm)	$\|z_1-z_2\|$ (cm)	$\|zvx\|$ (cm)	ω (rad)	$P_{1,2}$ (GeV)	$E_{J/\psi}$ (GeV)
95	PID4>2	<1	<5	<30	>0.2	>5	$15<E<27.5$
96	PID4>2	<1	<5	<30	>0.2	>5	$15<E<27.5$
97(NOVC)	PID4>2	<1	<5	<30	>0.2	>5	$15<E<27.5$
97(STD)	PID4>2	$<.2$	<2	<20	>0.2	>5	$15<E<27.5$

Table 4.3.: Summary of event selection criteria for the decay channel $J/\psi \to e^+e^-$. For explanation see text.

Data Sample	PID E_{calo}(GeV); E_{pre}(MeV) Cer (photo electrons)	d (cm)	$\|z_1-z_2\|$ (cm)	$\|zvx\|$ (cm)	ω (rad)	$P_{1,2}$ (GeV)	$E_{J/\psi}$ (GeV)
96	$0.3<E_{calo}<2.5$ $1<E_{pre}<5$ $Cer>0.25$	$<.5$	<3	<30	>0.2	>7	$20<E<27.5$
97(NOVC)	$0.6<E_{calo}<1.5$ $1<E_{pre}<5$ $Cer>0.25$	$<.5$	<3	<30	>0.2	>7	$20<E<27.5$
97(STD)	$0.6<E_{calo}<1.5$ $1<E_{pre}<5$ $Cer>0.25$	$<.2$	<2	<20	>0.2	>7	$20<E<27.5$

Table 4.4.: Summary of event selection criteria for the decay channel $J/\psi \to \mu^+\mu^-$. For explanation see text.

Muon Identification Muon identification for the decay $J/\psi \to \mu^+\mu^-$ was accomplished by requiring that the two decay particles of the J/ψ behave like minimum ionising particles in the calorimeter and the preshower detector and produce a signal in the Cherenkov detector. Figure 4.2 shows the calorimeter and preshower responses to one decay particle ('Track1') versus the other ('Track2') for the J/ψ candidate sample of 1997 containing those events where two tracks yield a reconstructed invariant mass of more than 2 GeV. The major background for the di–muon decay channel consists of events with misidentified pions or kaons. Non–resonant background of minimum ionising pion pairs, dominating the data sample at low invariant masses, is strongly suppressed by the requirement of the high J/ψ mass. The probability for two minimum ionising pions to appear in the J/ψ ($M_{inv} > 2$ GeV) candidate sample has been estimated from Monte Carlo simulations to be about 13%. A 50 Hz electronics noise in the calorimeter was corrected by software in 1996 and completely suppressed electronically in 1997. However, the minimum ionising peak in the calorimeter was wider in 1996 and the cut on the calorimeter energy had to be adjusted accordingly.

The Cherenkov cannot discriminate between muons and pions, since its threshold for both particles is the same. Kaons and protons have higher thresholds, thus the requirement of a signal in the Cherenkov detector suppresses their contribution to the background.

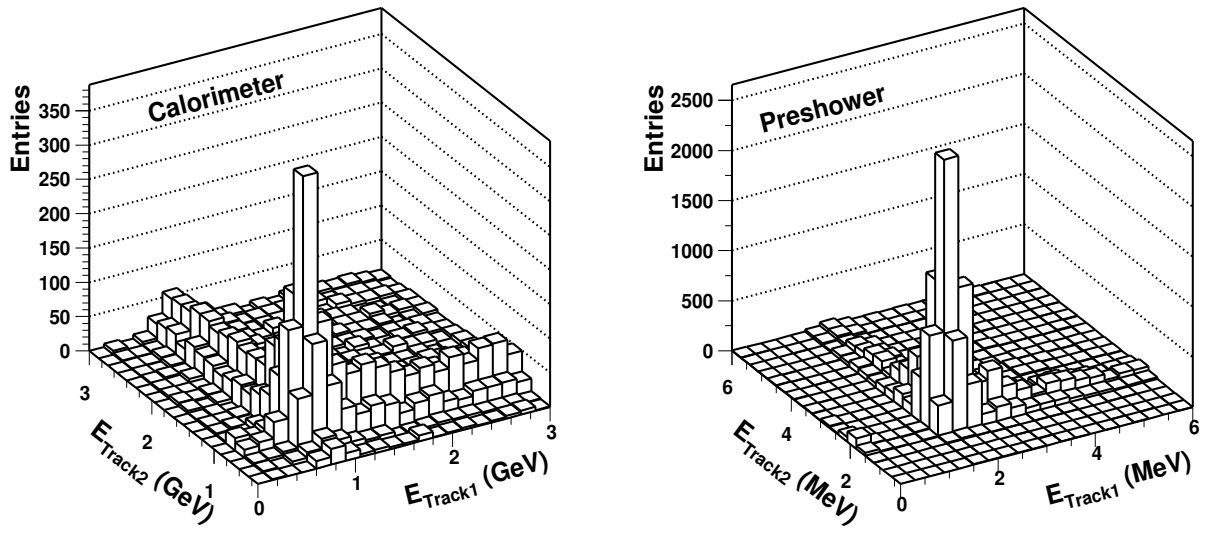

Figure 4.2.: Minimum ionising signals in the calorimeter and the preshower detector for 1997 data.

Figure 4.3 shows the comparison of a Monte Carlo simulation (cf. Section 4.4) and experimental data for the energy deposit by muons from J/ψ decays in the calorimeter and in the preshower detector, and for their signal in the Cherenkov detector. The data sample of identified muons is selected by the signal of the decay $J/\psi \to \mu^+\mu^-$ in 1997; the details of the extraction of the J/ψ signal will be discussed below. As can be seen, there is good agreement between Monte Carlo simulation and data within the statistical uncertainty. A clear Landau distribution can be seen for the energy deposit in the calorimeter and the preshower detector. The signal in the Cherenkov detector is comparable to the signal for pions shown in Figure 3.5.

In comparison to the decay channel $J/\psi \to e^+e^-$ the particle identification for muons is not as strong. To extract the J/ψ signal, the vertex and kinematic cuts are more important and had to be chosen more restrictive.

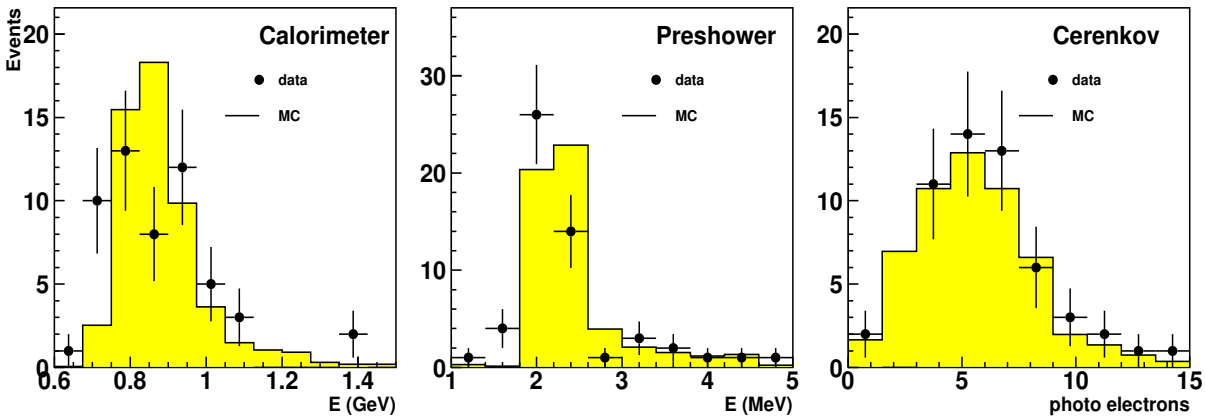

Figure 4.3.: Comparison of Monte Carlo and experimental data for the energy deposit in the calorimeter, preshower detector, and for the signal in the Cherenkov detector used for muon identification. The data sample of muons is selected by the signal of the decay $J/\psi \to \mu^+\mu^-$ in 1997.

Cuts on the Decay Vertex The point of closest approach between the two tracks is used as an approximation for the J/ψ decay vertex. Three different vertex requirements are applied; the cut variables are defined as:

- d, the distance of closest approach between the tracks of the two decay particles.
- $|zvx|$, the z–position of their common vertex.
- $|z_1 - z_2|$, the z–position difference of the vertices defined by each of the two tracks with the beam axis.

Because of its better vertex resolution the vertex cuts for the STD reconstruction method can be slightly stronger than for the NOVC method.

Kinematic Cuts The kinematic cuts are chosen with the help of the kinematic distributions obtained from Monte Carlo simulations (cf. Section 4.4). Cuts are applied on the following kinematic variables:

- p_1, p_2, the momenta of the decay particles.
- ω, the opening angle between the tracks of the decay particles in the laboratory frame.
- $E_{J/\psi}$, the reconstructed J/ψ energy.

The event selection described here is aiming at the most significant J/ψ signals. Note that for the later measurement of the J/ψ cross section a more restrictive cut on the J/ψ energy was applied to both decay channels to avoid the kinematic region with very low spectrometer acceptance.

Extracted Signals

In Figure 4.4 the invariant mass spectra separated by decay channel and year are shown. Burst level data quality criteria have been applied. A Gaussian function is fitted to the mass peak; the combinatorial background is described by an exponential function. A mass window of 2σ around the mean of the Gaussian function indicated by the shaded area is chosen as the signal region, independently for each data sample. It ensures that always the same event sample relative to the Gaussian is used in the analysis, independent of the slightly different apparatus resolutions for each data sample. The number of signal events (S) is taken from the integration of the fitted Gaussian, the number of background events (BG) from the integration of the exponential within the $\pm 2\sigma$ mass window. Both values are shown on the plots of Figure 4.4. As a measure of the significance of the signal above the background serves the ratio

$$\mathrm{signf} = \frac{\mathrm{S}}{\sqrt{\mathrm{S} + \mathrm{BG}}}. \tag{4.2}$$

In order to take the statistical uncertainty of the background determination into account, it is propagated into the analysis by using $\delta(\mathrm{S}) = \sqrt{\mathrm{S} + \mathrm{BG}}$ as the statistical uncertainty of the signal. Although the signals in the separate data samples are small, the fit of a Gaussian over an exponential function to describe signal and background is remarkably stable. This has been tested by repeating the fit for different binning of the mass spectra, e.g. the number of bins was varied between 20 and 100. The spread in the of number of signal and background events obtained from those fits follows a Gaussian distribution. From its width, a systematic uncertainty of the of the signal extraction from the invariant mass distribution of 2% for the channel $J/\psi \to e^+e^-$ and 4% for the channel $J/\psi \to \mu^+\mu^-$ has been obtained.

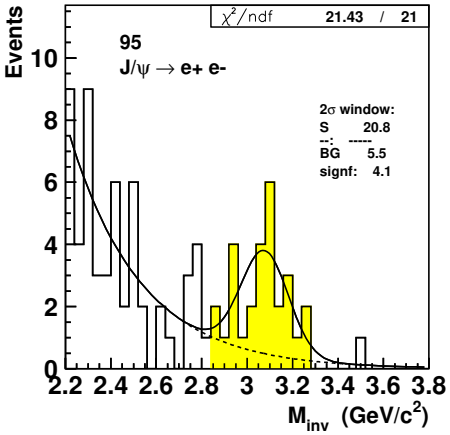

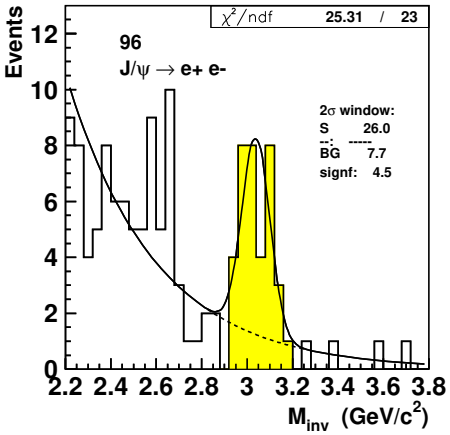

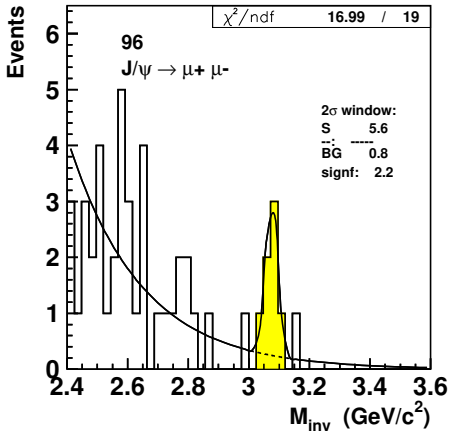

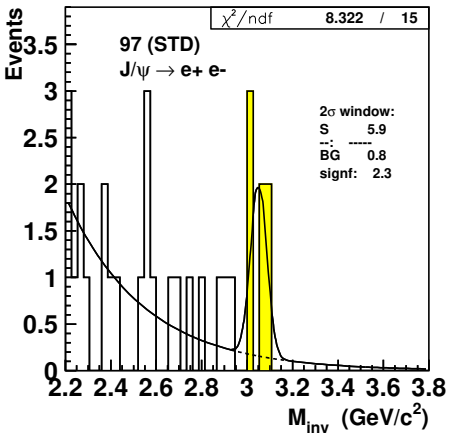

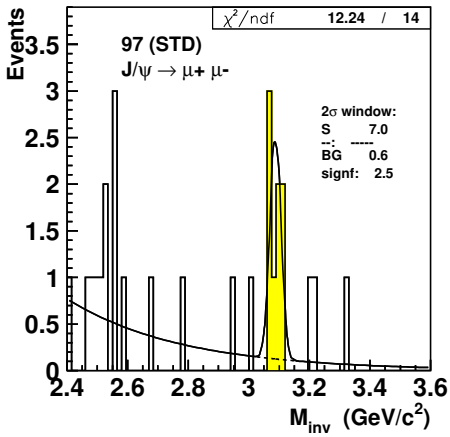

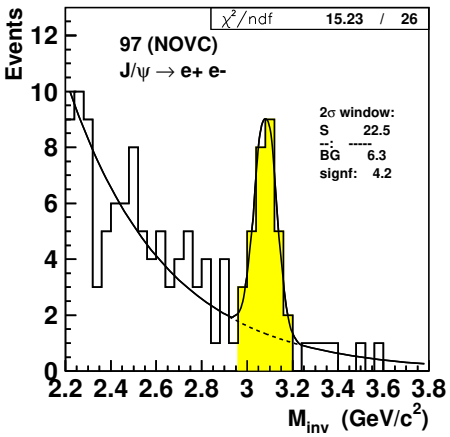

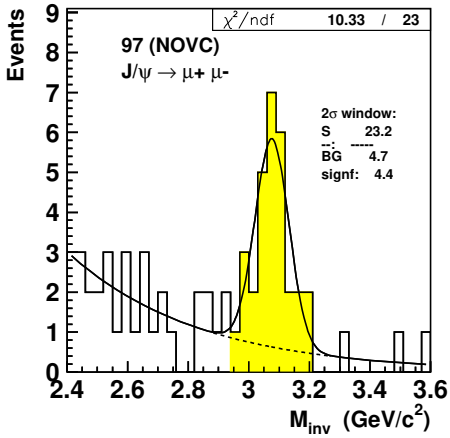

Figure 4.4.: Invariant Mass spectra for the decay channel $J/\psi \to e^+e^-$ (left) and $J/\psi \to \mu^+\mu^-$ (right) for the years 1995 to 1997 (from top to bottom). Burst level data quality criteria have been applied. The trigger for the detection of the decay $J/\psi \to \mu^+\mu^-$ has been available in 1996 only for the data on the polarised hydrogen target and for all data in 1997. For the 1997 data the two reconstruction methods STD and NOVC are distinguished.

4.4. Comparison of Data to Monte Carlo Simulation

Monte Carlo Event Generation

For the Monte Carlo studies the HERMES event generation and Monte Carlo simulation package GMC-HMC (Version 90.a) [DGM$^+$:99] has been used. A sample of 10000 events in each J/ψ decay channel was generated with the AROMA generator [IRS:96] separately for each reconstruction scenario discussed below. After the application of all event selection requirements each Monte Carlo event sample is at least an order of magnitude larger than the corresponding data sample.

For the kinematic distributions and the determination of reconstruction efficiencies the AROMA generator works reliably; the events are generated as a mixture of elastic and inelastic processes at a ratio of 70:30 which agrees with the values estimated at HERMES energies (see the discussion in Section 4.11). The EPJPSI generator [Jun:94] which distinguishes between elastic and inelastic J/ψ production was used to cross check the results obtained with AROMA. It was also used to estimate the systematic uncertainty of the extrapolation from the acceptance of the HERMES forward spectrometer to a full 4π acceptance.

The modeling of the spectrometer is based on the GEANT package [B$^+$:94]. In order to model the various data taking periods, the generated physics events are digitised and reconstructed with different geometry files, detector parameters, and reconstruction methods. Four reconstruction scenarios have been used: 95, 96, 97(NOVC) and 97(STD). No significant difference has been found in various kinematic distributions after the reconstruction.

Kinematic Distributions

Kinematic distributions have been compared between reconstructed experimental data and reconstructed Monte Carlo simulations. Both decay channels are treated separately, but the small data samples from different years and reconstruction methods had to be combined.

The Monte Carlo events for each of the four scenarios described above are weighted by the relative luminosities of the corresponding data samples (cf. Table 4.1) and combined. The final Monte Carlo distributions are normalised to the total number of data J/ψ candidates.

To subtract the contribution of combinatorial background to the kinematic distributions of the data, events from sidebands left and right of the peak in the invariant mass distribution are used. The events from the sidebands are weighted such that their integral is equal to the number of background events under the mass peak within the $2\,\sigma$ J/ψ signal region. For each kinematic distribution the weighted events from the mass sidebands are subtracted from the events of the signal region. The statistical uncertainty due to the background subtraction is small and can be neglected since the number of events in the mass sidebands is much larger than in the signal region, The background events where both tracks have the same charge, shown by the shaded areas in Figure 4.1 cannot be used for background correction since their statistics are too small.

Figures 4.5 and 4.6 show the comparison for the different kinematic distributions: momentum p of the decay particles (top left), opening angle ω of the decay particles (top right), energy $E_{J/\psi}$ of the J/ψ (bottom left), and squared transverse momentum p_T^2 of the J/ψ (bottom right) for the decay $J/\psi \to e^+e^-$ and $J/\psi \to \mu^+\mu^-$, respectively. Within statistical errors there is good agreement between data and Monte Carlo.

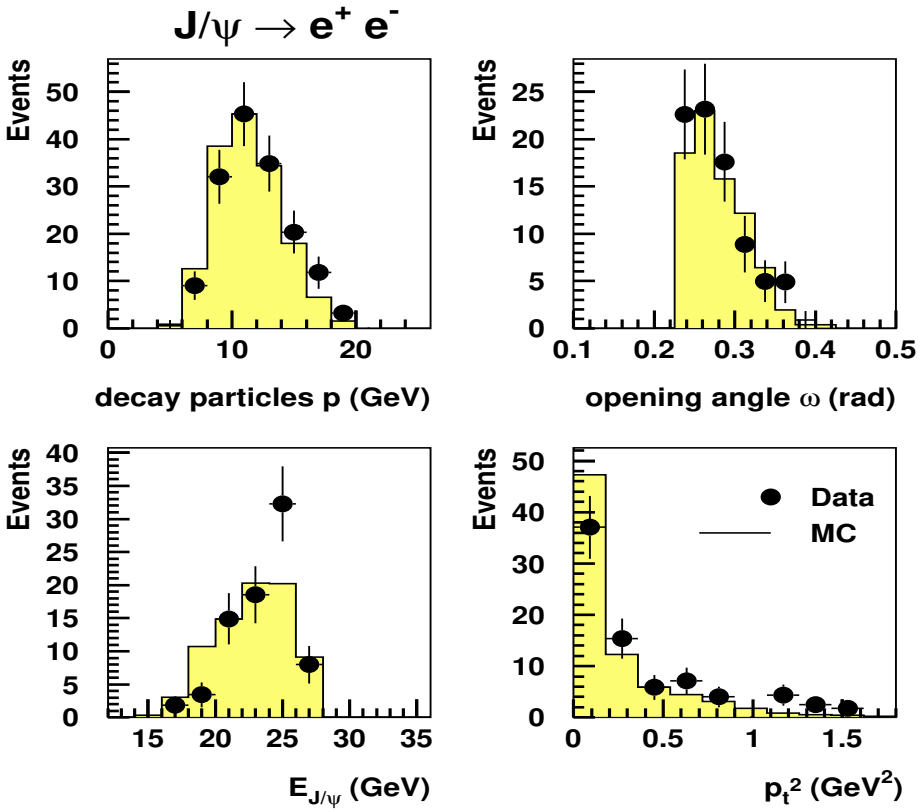

Figure 4.5.: Data vs. Monte Carlo comparison of kinematic variables for the decay channel $J/\psi \to e^+e^-$.

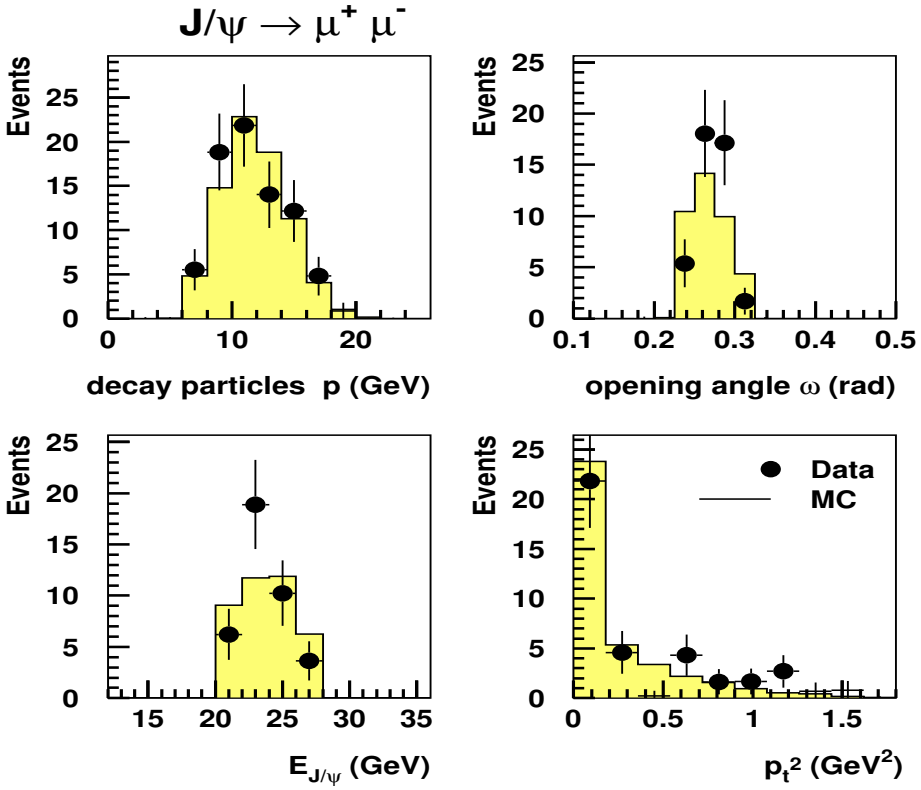

Figure 4.6.: Data vs. Monte Carlo comparison of kinematic variables for the decay channel $J/\psi \to \mu^+\mu^-$.

Reconstructed J/ψ Mass

Figure 4.7 displays the values of the reconstructed J/ψ mass and their statistical uncertainties obtained by fitting a Gaussian to the J/ψ signal, separated by year, decay channel, and reconstruction method as it was shown in Figure 4.4. The vertical line indicates the nominal J/ψ mass of 3.097 GeV [C$^+$:98]. As it can be seen, the reconstructed J/ψ mass is systematically shifted to lower values for all data samples. The average shift is 35 ± 9 MeV for the decay channel $J/\psi \to e^+e^-$ and 21 ± 6 MeV for the decay channel $J/\psi \to \mu^+\mu^-$.

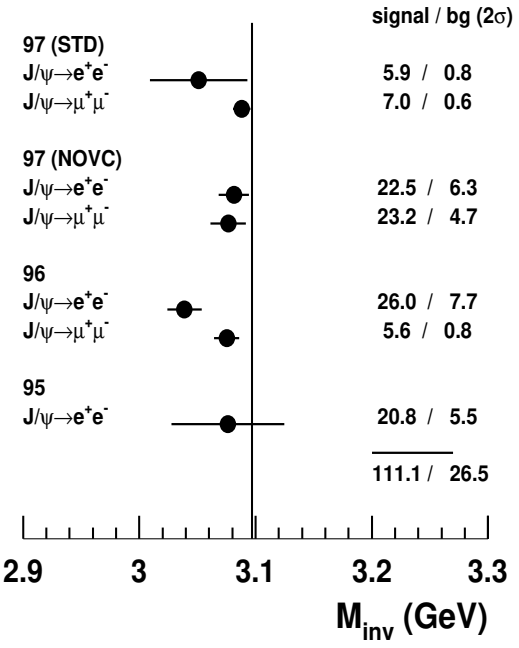

Figure 4.7.: Fitted J/ψ mass separated by decay channel, year, and reconstruction method.

The Monte Carlo simulations predict a mass shift of 26 ± 3 MeV for the decay $J/\psi \to e^+e^-$ caused by the energy loss of electrons and positrons in the detector. Only a small shift of 6 ± 2 MeV is predicted for the decay $J/\psi \to \mu^+\mu^-$. Both values are obtained from the fit of a Gaussian to the Monte Carlo distributions in Figure 4.8, where the invariant mass spectra of data and Monte Carlo are compared for both decay channels. Monte Carlo simulation and experimental data agree within the statistical uncertainties. As in the previous section, the data from different years and reconstruction methods were combined and the Monte Carlo samples for the different reconstruction scenarios are weighted by the luminosity and added. The data are corrected for combinatorial background by subtracting the exponential function that was fitted to the invariant mass distribution.

The values for the J/ψ mass obtained from data agree with the Monte Carlo predictions within $0.9\,\sigma$ and $1.8\,\sigma$ for the decay $J/\psi \to e^+e^-$ and $J/\psi \to \mu^+\mu^-$, respectively. The small deviation of about 10 MeV in the reconstructed J/ψ mass corresponds to the uncertainty in the alignment between the top and the bottom half of the spectrometer [BGS:99].

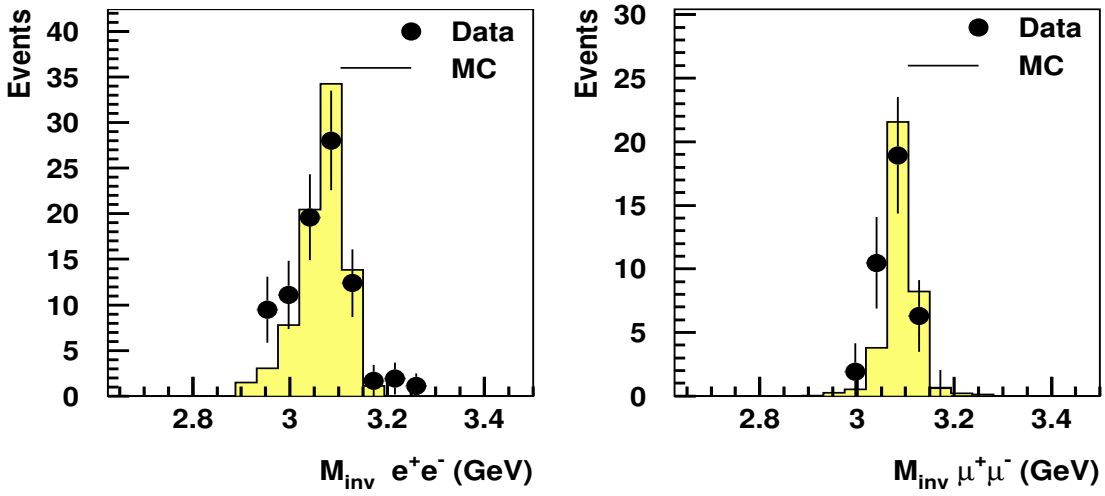

Figure 4.8.: Invariant mass spectrum for the decay $J/\psi \to e^+e^-$ (left) and $J/\psi \to \mu^+\mu^-$ (right).

4.5. Luminosity Determination

Luminosity Determination with the Luminosity Detector

The HERMES luminosity detector measures the rate of Bhabha–scattering of the beam particles with the shell electrons of the target nuclei. The luminosity is determined from the product of the measured rate f_{Bhabha} of detected coincident e^+e^- pairs, the length of the burst T_{Burst}, and the luminosity normalisation constant C_{Lumi}, summed over all bursts of the data sample:

$$L_{Lumi} = \sum_{bursts} C_{Lumi} \cdot f_{Bhabha} \cdot T_{Burst} \cdot \left\{ \begin{array}{ll} 1. & (H, H_2) \\ 1.5 & (^3He) \\ 2. & (D_2, N_2) \end{array} \right\}. \tag{4.3}$$

A target factor 1, 1.5, and 2 takes the ratio in the number of nucleons to shell electrons in different target nuclei into account. In contrast to an asymmetry measurement, where only relative luminosities are important, a cross section measurement needs an absolute normalisation. The luminosity normalisation constant C_{Lumi} relates the measured coincident rate to the known cross section of Bhabha scattering; at a given beam energy it depends on the acceptance and efficiency of the luminosity detector. For the 1996 data taking the luminosity normalisation constant was determined to be

$$C_{Lumi} = 0.448\ \mu b^{-1} \tag{4.4}$$

with a systematic uncertainty of 6.5% [Ben:98b, Ben:98a]. The statistical uncertainty of the luminosity measurement is about 1% within a time window of 100 s and will be neglected.

Consistency Check of the Luminosity Determination

As a consistency check for the validity of the normalisation constant C_{Lumi} for all data samples, the luminosity determined with the luminosity monitor was compared to the luminosity determined from the number of DIS positrons, i.e. the known DIS cross section. DIS positrons are selected by the following requirements:

- The lepton with the highest momentum is selected.
- A lepton is defined by PID4 > 1.
- The DIS candidate has to pass the following kinematic and acceptance cuts:

$$\begin{aligned} &Q^2 > 1\ \mathrm{GeV}^2, \quad W^2 > 4\ \mathrm{GeV}^2, \quad 0 < y < 0.85, \\ &|\theta_x| < 0.17\ \mathrm{rad}, \quad 0.04 < |\theta_y| < 0.14\ \mathrm{rad}, \end{aligned}$$

  where θ_x and θ_y are the angles of the scattered positron in the laboratory frame.

The number of DIS positrons N_{e^+} is corrected for background from charge symmetric processes by the number of electrons N_{e^-} which fulfil the DIS cuts. For a given target $(targ)$ the luminosity L_{DIS} is determined by the relation

$$L_{DIS}(targ) = C_{DIS}\ \frac{1}{\epsilon_{DAQ}}\ (N_{e^+} - N_{e^-})\ \frac{\sigma_{DIS}(^3He)}{\sigma_{DIS}(targ)}, \tag{4.5}$$

where ϵ_{DAQ} is the DAQ efficiency. The luminosity normalisation constant C_{DIS} was determined by a data–Monte Carlo comparison of the DIS cross section for the 1996 data taken with the ^3He target:

$$C_{DIS} = 21.8 \text{ pb}^{-1}10^{-6}\text{DIS},$$

with a systematic uncertainty of 4% [Bro:98a]. The ratio $\sigma_{DIS}(^3He)/\sigma_{DIS}(targ)$ in Equation 4.5 takes into account that the DIS cross sections for different targets are not the same. For this correction, total deep–inelastic cross sections are used, obtained from world data on the unpolarised structure function F_2 for different targets, integrated over the covered kinematic range of the HERMES experiment and corrected for radiative effects:

$$\begin{aligned} \sigma_{DIS}(H) &= 60.9 \text{ nb}, & \sigma_{DIS}(D) &= 53.8 \text{ nb}, \\ \sigma_{DIS}(^3He) &= 56.2 \text{ nb}, & \sigma_{DIS}(N) &= 54.5 \text{ nb}. \end{aligned}$$

The systematic uncertainty of these values is 3% determined by the normalisation uncertainties of the data on F_2 [Bru:98]. For Equation 4.5 the assumption is made that the probability to reconstruct the track of a scattered positron within the acceptance is the same for the different targets, years, and reconstruction methods.

The ratio, between the luminosity determined from the DIS positrons and the one measured with the luminosity detector L_{DIS}/L_{Lumi} should be unity. It was calculated run–wise for all data samples separated by year, reconstruction method, and target. As an example the ratio L_{DIS}/L_{Lumi} is plotted in Figure 4.9 for the data taken with the unpolarised hydrogen target in 1997. The distribution is purely Gaussian, showing that there are no effects other than statistical fluctuations around the mean of the distribution. In Table 4.5 the ratio L_{DIS}/L_{Lumi} is listed for all data samples, the statistical uncertainties of below $1 \cdot 10^{-3}$ are neglected. The spread between different targets within one year is 2% for 1996 and 4% for the 1997(NOVC) data sample.

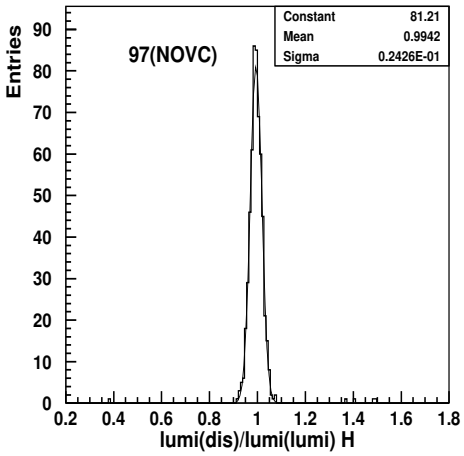

Figure 4.9.: Ratio L_{DIS}/L_{Lumi} for the 1997 data on the unpolarised hydrogen target.

Both methods of luminosity determination give consistent results; except for the two data samples 1995 and 1997(STD) all ratios are about unity:

- The strong deviation in 1995 is related to the exchange of the photomultipliers of the luminosity detector after the 1995 data taking. Therefore, the luminosity constant determined for 1996 and afterwards is not valid for 1995. Under the assumption of a constant total efficiency to detect a DIS–positron, the 1995 value for the constant L_{Lumi} can be corrected with the help of the luminosity ratio L_{DIS}/L_{Lumi} by a correction factor 1.25.

- The ratio $L_{DIS}/L_{Lumi} = 0.94$ in 1997 for polarised hydrogen is significantly lower than for unpolarised hydrogen. This is attributed to a somewhat lower reconstruction efficiency for the standard reconstruction method, caused by inefficiencies in the vertex chambers (VC).

- There seems to be a trend to slightly smaller values of L_{DIS}/L_{Lumi} in the 1997 data and an average correction of 0.97 is used for the 1997 luminosity constant L_{Lumi}.

Data Sample	Target	L_{DIS}/L_{Lumi}
95	${}^3\vec{H}e$	1.25
96	$\vec{H}_1$ & H_2	1.00
	D_2	1.02
	${}^3He$	1.02
97(STD)	$\vec{H}_1$	0.94
97(NOVC)	H_2	0.99
	D_2	0.97
	N	0.95

Table 4.5.: Mean and width of the ratio L_{DIS}/L_{Lumi}, separated by year, reconstruction method, and target.

Depending on the target type and running conditions the count rate of the luminosity detector is 4 to 8 times higher than the count rate of DIS positrons. Therefore, the luminosity obtained from the luminosity detector was finally used for the determination of the cross section to take advantage of its smaller statistical uncertainty.

4.6. Trigger

Two different triggers have been used for the detection of J/ψ events that will be discussed in this section. The main physics trigger (numbered 21) is not only sensitive to DIS positrons, but also to the decay products of the decay channel $J/\psi \rightarrow e^+e^-$. For the decay $J/\psi \rightarrow \mu^+\mu^-$ a trigger was designed (numbered 28) that is sensitive to the decay topology and does not require the scattered positron. Table 4.6 compiles the logic of the triggers used. As an example, trigger 17 requires coincident signals in the scintillator hodoscopes H0, H1 and the preshower detector (H2) (cf. Figure 3.4), in either the top or the bottom half of the spectrometer. Triggers 18-20 are sub–triggers needed for the determination of efficiencies. The set up of trigger 28, not yet existing in 1995, differs slightly for 1996 and 1997 due to changes in the hardware implementation.

Determination of Efficiencies

The efficiency of a trigger for the detection of a certain event type (e.g. a deep–inelastic scattering event) has to be calculated from the individual efficiencies of the separate trigger sub–components to detect the final state particles of the event (e.g. the DIS positron). The individual detector efficiencies of the hodoscopes H0 and H1 and the preshower H2 to detect a certain particle type are determined with the sub–triggers 18 to 20, the efficiency of the

Trigger	Logic
17	$(H0 \cdot H1 \cdot H2)_T \ + \ (H0 \cdot H1 \cdot H2)_B$
18	$(H1 \cdot H2 \cdot Ca)_T \ + \ (H1 \cdot H2 \cdot Ca)_B$
19	$(H0 \cdot H1 \cdot Ca)_T \ + \ (H0 \cdot H1 \cdot Ca)_B$
20	$(H0 \cdot H2 \cdot Ca)_T \ + \ (H0 \cdot H2 \cdot Ca)_B$
21	$(H0 \cdot H1 \cdot H2 \cdot Ca)_T \ + \ (H0 \cdot H1 \cdot H2 \cdot Ca)_B$
28 (1996)	$[(H0 \cdot H1 \cdot H2)_T \cdot (H0 \cdot H1 \cdot H2)_B] \cdot$ $(2 \leq H0 \leq 8 \cdot 2 \leq H1 \cdot 2 \leq H2 \cdot 2 \leq BC1)$
28 (1997)	$(H0 \cdot H1 \cdot H2 \cdot BC)_T \cdot (H0 \cdot H1 \cdot H2 \cdot BC)_B$ $(H0 \leq 8)$

Table 4.6.: Logic of the triggers used in the analysis.

calorimeter is determined using trigger 21 and 28:

$$\epsilon(H0) = \frac{T18 \cdot T21}{T18}, \quad \epsilon(H1) = \frac{T20 \cdot T21}{T20}, \quad \epsilon(H2) = \frac{T19 \cdot T21}{T19}, \quad \epsilon(Ca) = \frac{T21 \cdot T28}{T28}. \quad (4.6)$$

For example: The hodoscope H0 is the only difference in the configuration of trigger 18 and 21; the efficiency of H0 is the number of events seen by trigger 18 **and** 21 divided by the number of events at least seen by trigger 18.

These efficiencies have to be calculated from a sample of events containing only a single particle of the type in question. To obtain an unbiased data sample for the determination of the efficiency of the preshower detector H2, this detector should not be used for particle identification in the event selection when calculating $\epsilon(H2)$. Thus, instead of the particle identification scheme PID4, cuts on the remaining PID detectors have to be used to select positrons or hadrons. The same holds true for the determination of the calorimeter efficiency $\epsilon(Ca)$.

Trigger 21 – Detection of $J/\psi \to e^+e^-$

Topology Trigger 21 requires coincident signals in the scintillator hodoscopes H0, H1, H2 and an energy deposit of the scattered positron in the electromagnetic calorimeter (Ca), in either the top or the bottom half of the spectrometer. The scintillator in front of the magnet (H0), not present in 1995, suppresses hadronic background caused by the proton beam line, since it allows to discriminate forward and backward going particles by the time of about 18 ns a relativistic particle needs to travel from H0 to the back elements of the trigger. To include the calorimeter in the trigger, the signals of all calorimeter blocks of every pair of neighbouring columns are summed up. A minimum energy deposit in the calorimeter is required to suppress triggers generated by low energy hadronic background. For data taking with polarised targets the calorimeter threshold was set to 3.5 GeV in 1995 and lowered to 1.4 GeV in 1996 and 1997 to extend the accessible kinematic range to events with high fractional photon energy y at low x. In the case of unpolarised targets with higher target

densities the calorimeter threshold had to be set to 3.5 GeV to restrict the trigger rates, avoiding an inefficiency of the DAQ of more than 10%.

Efficiency To determine the efficiency of trigger 21 for the decay $J/\psi \to e^+e^-$ a sample of DIS positrons was chosen to model the decay products. The efficiencies of the sub–components of the DIS trigger 21 for positrons $\epsilon_e(H0)$, $\epsilon_e(H1)$, $\epsilon_e(H2)$, and $\epsilon_e(Ca)$ are sharply peaked at one (distributions not shown). The efficiency of trigger 21 for the detection of a DIS positron is calculated as:

$$\epsilon_e(T21) = \epsilon_e(H0) \cdot \epsilon_e(H1) \cdot \epsilon_e(H2) \cdot \epsilon_e(Ca). \tag{4.7}$$

In Figure 4.10 the efficiency of trigger 21 is plotted versus the positron momentum. The turn on of the efficiency above the calorimeter threshold of 3.5 GeV is clearly visible. Above threshold the trigger 21 efficiency is more than 98%; it is close to unity for positron momenta of more than 7 GeV. As it can be seen from the top-left plot of Figure 4.5 the momenta of the two decay leptons in the channel $J/\psi \to e^+e^-$ are always larger than 5 GeV and well above the trigger threshold. The efficiency of trigger 21 to detect at least one particle of these positron–electron pairs, where both particles can generate a trigger, is unity. Therefore, no correction for the trigger efficiency needs to be applied for the decay channel $J/\psi \to e^+e^-$.

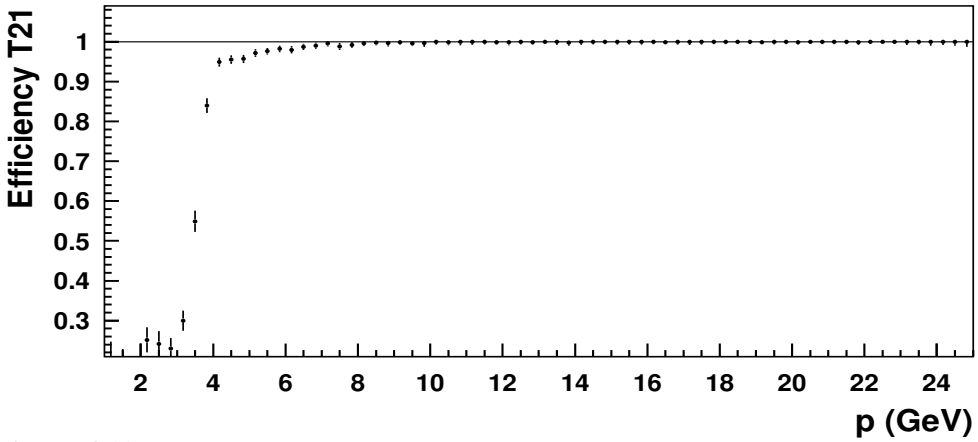

Figure 4.10.: Efficiency of trigger 21 versus positron momentum for a calorimeter threshold of 3.5 GeV.

Trigger 28 – $J/\psi \to \mu^+\mu^-$

Topology The detection of the decay channel $J/\psi \to \mu^+\mu^-$ is more complicated with the given spectrometer not containing a muon detector in the years 1995 through 1997. As known from Monte Carlo simulations, for most of the events the positron, when scattered at low Q^2, remains inside the beam pipe and cannot generate a trigger. The muons themselves cannot produce a DIS trigger since they are minimum ionising particles, i.e. their energy deposit in the calorimeter does not exceed the calorimeter threshold of trigger 21.

A new trigger was tested in 1996 and fully implemented in 1997 to be sensitive to quasi–real photoproduction at low Q^2 [M$^+$:96]. This trigger, numbered 28, does not include the calorimeter. To reduce the trigger rate, background is suppressed by multiplicity cuts in the back chambers BC1-top/bottom and cuts on the pulse heights in front hodoscopes H0, which have the effect of a cut on the particle multiplicity in the front region of the spectrometer.

Additionally, the requirement of at least one track in the top and at least one track in the bottom half of the spectrometer is made. Monte Carlo simulations show, that the top/bottom requirement is fulfilled by over 95% of the di–lepton J/ψ decays within the HERMES acceptance. In 1996 only two planes, BC1-x in both top and bottom half of the spectrometer, were included in trigger 28, in 1997 two planes per spectrometer half were used yielding a higher trigger efficiency.

Efficiency

Clearly identified muons to determine the efficiency of trigger 28 for the decay $J/\psi \to \mu^+\mu^-$ are not available for the 1995–1997 data sample and the muon statistics selected by the decay itself are too small. However, the muon as a minimum ionising particle behaves similar to a hadron in the hodoscopes and the particle identification detectors. For the determination of the hadron efficiencies $\epsilon_h(H0)$, $\epsilon_h(H1)$, and $\epsilon_h(H2)$ using Equations 4.6 only those events were selected which contained only a single hadron track. A momentum cut of $p > 5$ GeV is applied, corresponding to the minimum momentum of a J/ψ decay muon (cf. Figure 4.5).

To determine the efficiency of trigger 28 an additional quantity is needed: the combined efficiency $\epsilon_{hh}(BC \cdot H0_{mult})$ of the drift chamber component, the pulse height cut in the front hodoscope H0, and the top-bottom requirement:

$$\epsilon_{hh}(BC \cdot H0_{mult}) = \frac{T21 \cdot T28}{T21}. \tag{4.8}$$

A further separation of this efficiency is not possible since not all necessary sub-triggers were available. For the determination of $\epsilon_{hh}(BC \cdot H0_{mult})$ those events were used that had at least one hadron in the top and one in the bottom half of the spectrometer but no electrons or positrons. Again a momentum cut of $p > 5$ GeV is applied.

In Figure 4.11 the efficiencies of the different components of trigger 28 to detect a hadron (H0, H1, H2), or to detect a top–and–bottom hadron track topology ($\mathrm{BC} \cdot \mathrm{H0}_{mult}$) are shown. Each entry corresponds to one run. The average hadron efficiency of H0 is 98 $\%$. The hadron efficiency of H1 is 97%, but drops by about 5% for periods with high calorimeter threshold. The reason for this efficiency drop is still under investigation, it was checked that the efficiency for positrons of H1 is stable and close to unity for these periods. The hadron efficiency of the preshower detector H2 is 99% and slightly higher than for H0 and H1.

The efficiency $\epsilon_{hh}(BC \cdot H0_{mult})$ for the detection of the two hadron–track topology is shown in Figure 4.11 separately for 1996 and 1997. It is dominated by the configuration of

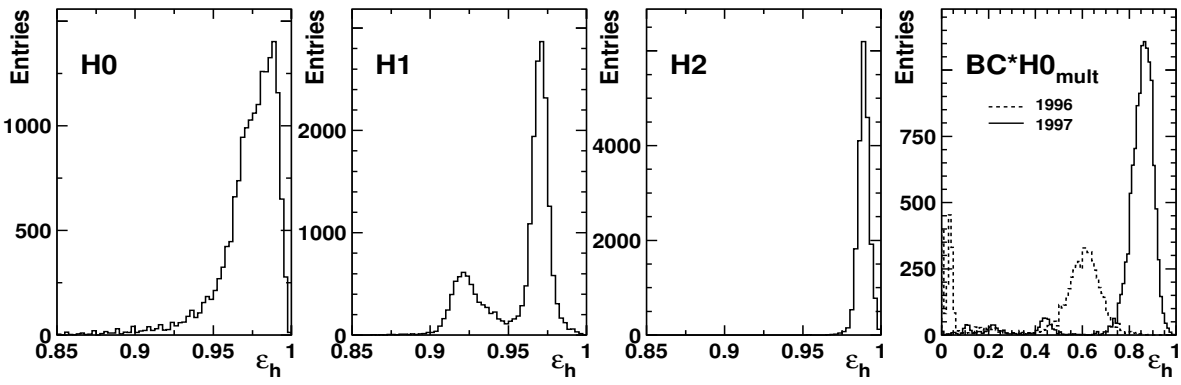

Figure 4.11.: Efficiencies of the sub-components of trigger 28 for the detection of hadrons (H0, H1, H2) and a top–and–bottom hadron track topology ($\mathrm{BC} \cdot \mathrm{H0}_{mult}$).

the drift chamber planes in trigger 28. Additional entries of efficiencies below 0.5 are due to periods when the trigger was prescaled [1] because of high rates during data taking with unpolarised targets.

In **1996**, when only one BC1-plane per spectrometer half was included in the trigger, $\epsilon_{hh}(BC \cdot H0_{mult})$ was about 61%. The maximum drift time in the drift cells of the back chambers is 250 ns [B$^+$:98]. Due to the time constraints of the first level trigger, the window for the arrival of the multiplicity signal from the drift chamber planes was only 120 ns wide. This resulted in a restricted geometrical acceptance, since long drift times (and therefore long drift distances) were cut out.

In **1997** a second BC-plane was additionally included in the trigger and the efficiency $\epsilon_{hh}(BC \cdot H0_{mult})$ increased to 86%. The two drift chamber planes are staggered by half a drift cell, therefore the insensitive areas around the potential wires of one plane are covered by the other plane. In addition the readout electronics were changed yielding an increase of the time window for the drift chamber multiplicity. The hadron efficiency of those BC planes which are included in the trigger is 95% and thus $2-3\%$ lower with respect to all other drift chamber planes. This seems to be an effect of the additional electronics introduced to the drift chamber readout.

The total efficiency of trigger 28 for events with two top-bottom hadron tracks is given by

$$\epsilon_{hh}(T28) = \epsilon_{hh}(BC \cdot H0_{mult}) \cdot \epsilon_h(H0)^2 \cdot \epsilon_h(H1)^2 \cdot \epsilon_h(H2)^2, \tag{4.9}$$

where the square of the hodoscope and the preshower detector efficiencies appear because two hadron tracks have to be detected. In the analysis the efficiency $\epsilon_{hh}(T28)$ is calculated on a run–by–run basis, where the efficiencies of H0 and H1 are taken from the mean of the histograms in Figure 4.11 since they do not vary with time. Figure 4.12 shows the efficiency of trigger 28 separately for 1996 (left) and 1997 (right) having mean values of 52% and 73%, respectively. Runs with lower values of the trigger 28 efficiency originate from periods where it was prescaled. It was checked that the efficiency of trigger 28 is uniform over the whole spectrometer acceptance.

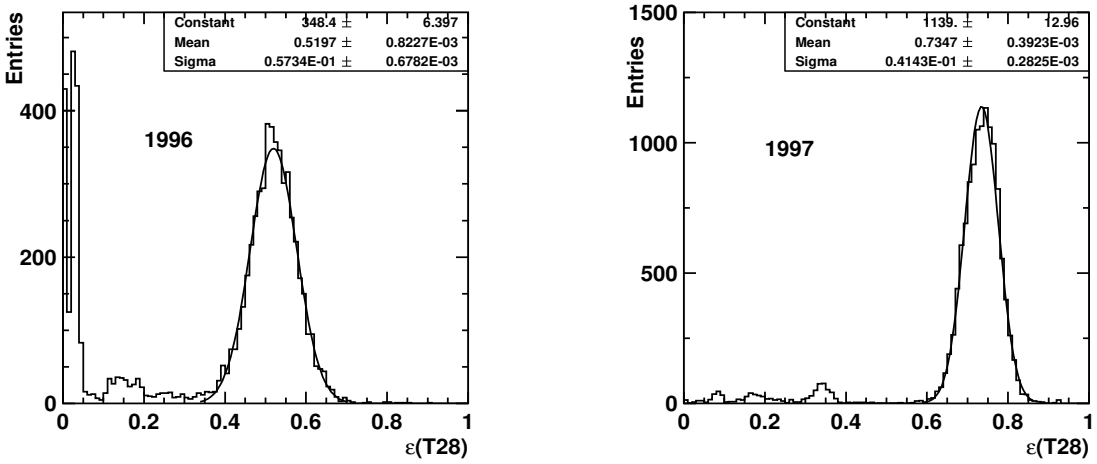

Figure 4.12.: Efficiency of trigger 28 for 1996 (left) and 1997 (right) data.

[1] If a trigger is prescaled by the pre-scale factor n, only every n-th occurrence of this trigger leads to a read–out of the DAQ restricting the event rate written to tape.

In the analysis the requirement $\epsilon(T28) > 0.4$ is applied to avoid large efficiency corrections. It rejects about 20% of the $J/\psi \to \mu^+\mu^-$ events. Almost all data taken with a prescaled trigger 28 are excluded from the analysis by this requirement. Pre-scaling of trigger 28 was necessary during most of the 1996 data taking with unpolarised targets. Consequently, only the data collected on the polarised hydrogen target with (lower target density) are available for the analysis of the di–muon J/ψ decay leading to the small signal in 1996.

Systematic Uncertainties of Trigger Efficiencies

The individual signals of the trigger sub–components are fed into a programmable logic unit (PLU) that forms the triggers based on the logic given in Table 4.6. The signal of a certain detector (H0, H1, $\cdots$) is the same for all triggers it appears in. Therefore, the ratios of Equations 4.6 do not have a systematic bias for a given event sample. A systematic error of the obtained efficiencies can only be caused by a contamination of the event sample with particles of a different type. The efficiency of trigger 21 for DIS positrons is close to unity above 7 GeV. Therefore, a noticeable contribution from hadrons which would reduce $\epsilon_e(T21)$ can be excluded and no systematic uncertainty is assigned to the trigger 21 efficiency.

Hadrons, which are at HERMES mainly pions, were used to determine the efficiency of trigger 28 for muon–pairs. It is presently not possible to cross check this efficiency with muons because the statistics of the muon sample identified by the di–muon J/ψ decay is too small. It is assumed that the hadron efficiencies for the trigger components H0, H1, and H2 are known with a negligible uncertainty, since the contamination of the hadron sample by positrons is below 1%. In trigger 28, especially the pulse height cut in H0 might be sensitive to the few percent difference in energy loss between muons and pions . To estimate the uncertainty of $\epsilon_{hh}(BC \cdot H0_{mult})$ a two–track event sample was used, which contained at least one lepton. A difference of about 3% was found for $\epsilon_{lh}(BC \cdot H0_{mult})$ which is assigned as systematic uncertainty to the efficiency of trigger 28.

4.7. Yields

Yields are determined by the number of J/ψ candidates per 10^6 DIS events, where the number of DIS events is corrected for the different DIS cross sections per target (cf. Section 4.5), so converting for each target into a corresponding yield for a hydrogen target. Due to the limited statistics there are only a few systematic checks which can be performed on the J/ψ data. One possibility is the determination of yields, separated by decay channel, target, year, and eventually reconstruction method. There are 14 different data samples to be compared in this way marked by • in Table 4.1.

For each target, year, and decay channel the invariant mass distributions are fitted separately (not shown), thus dividing some of the invariant mass distributions of Figure 4.4 into smaller subsamples. DIS positrons are counted for each data sample separately after data quality criteria were applied. The uncertainty of the yields is dominated by the statistical error of the fitted signals.

Yields of $J/\psi \to e^+e^-$ and $J/\psi \to \mu^+\mu^-$

Figure 4.13 shows the yields for the decay channel $J/\psi \to e^+e^-$. There is a tendency to somewhat lower values for the 1997 data, although the yields for all data samples are

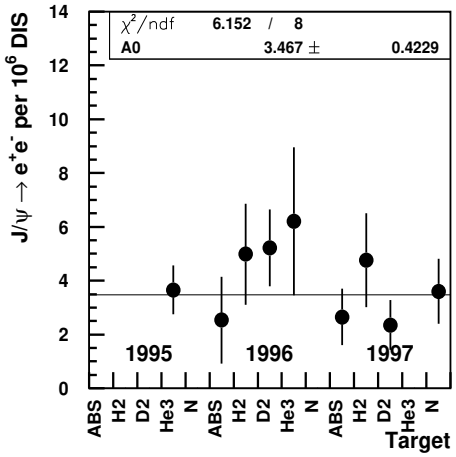

Figure 4.13.: J/ψ yields in the decay channel $J/\psi \to e^+e^-$ per target and year

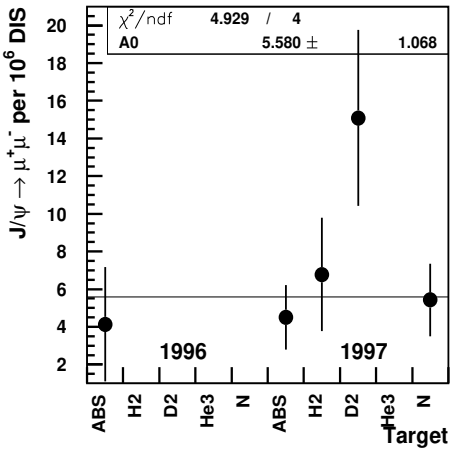

Figure 4.14.: J/ψ yields in the decay channel $J/\psi \to \mu^+\mu^-$ per target and year.

consistent with a common mean. The yield for the production of $J/\psi \to e^+e^-$ at HERMES averaged over all targets and running periods is 3.5 ± 0.4 per 10^6 DIS events.

To take the different efficiencies of trigger 28 for 1996 and 1997 into account the number of $J/\psi \to \mu^+\mu^-$ events has to be corrected by the measured efficiency of trigger 28 to arrive at a trigger efficiency of $\epsilon_{hh}(T28) = 1$. As mentioned before, the periods when trigger 28 was prescaled are excluded from the analysis by the requirement $\epsilon_{hh}(T28) > 0.4$ to avoid large efficiency corrections to the small event samples. Figure 4.14 shows the yields obtained per year and target in the di–muon decay of the J/ψ. A fit to a constant has a χ^2 close to one, showing the consistency of all yields within the statistical uncertainty. Here, the value for the 1997 deuterium target sticks out by 2σ. An average yield of 5.6 ± 1.0 $J/\psi \to \mu^+\mu^-$ per 10^6 DIS is obtained. The yield is higher than for the decay $J/\psi \to e^+e^-$ due to the higher efficiency of the event selection for the di-muon decay, as will be discussed in Chapter 4.8.

A–Dependence

The A-dependence of the yields for both decay channels is plotted in Figure 4.15. Data from different years as well as the polarised H_1 and the unpolarised H_2 data are combined. Within statistical uncertainties no significant dependence of the yields on the atomic number of the target can be concluded and the data from all targets will be combined for the measurement of the J/ψ cross section.

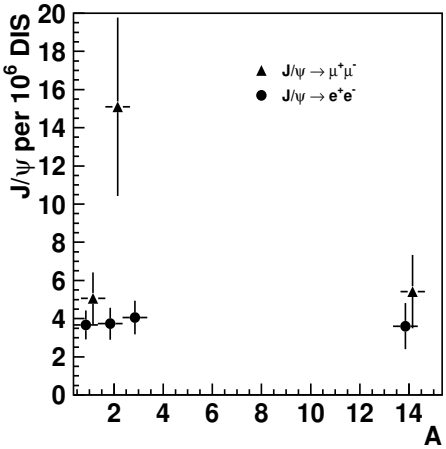

Figure 4.15.: J/ψ yields versus the atomic number of the target integrated over all years.

4.8. Acceptance and Efficiencies

The yield can be converted in a measurement of the J/ψ cross section by applying corrections for detector acceptance and accounting for the efficiency of reconstruction and event selection. Using Monte Carlo simulations the correction for acceptance and reconstruction efficiency will be calculated separately for each year, decay channel, and reconstruction method.

Spectrometer Acceptance for Single Tracks

The geometrical acceptance for electrons and positrons is determined in x (horizontally) by the aperture of the front field clamp of the spectrometer magnet and in y (vertically) by the septum plate and the back field clamp (cf. Figure 4.16). Muons are able to pass through the iron field clamps. Their acceptance is given by the size of the active areas of the tracking detectors that extend beyond the aperture of the spectrometer magnet.

The geometrical acceptance is defined here in terms of the horizontal and vertical slopes θ_x and θ_y of the track in the front part of the spectrometer. Its dependence on the longitudinal position of the track vertex is taken into account since the Monte Carlo events used for the acceptance correction are generated with the triangular vertex distribution determined by the the storage cell geometry. The lateral vertex distribution is sharply peaked at $x = y = 0$ and therefore not simulated (cf. Figure 3.3).

Figure 4.16 shows a Monte Carlo comparison of the acceptance for single positrons and muons. For completeness, pions are also included in the figure. The larger acceptance for muons can be clearly seen. At low y, where the septum plate determines the aperture of the spectrometer, the acceptance is the same for all particles. Due to the approximate left/right and top/bottom symmetry of the spectrometer only one quarter of the geometry has to be taken into account for this simulation.

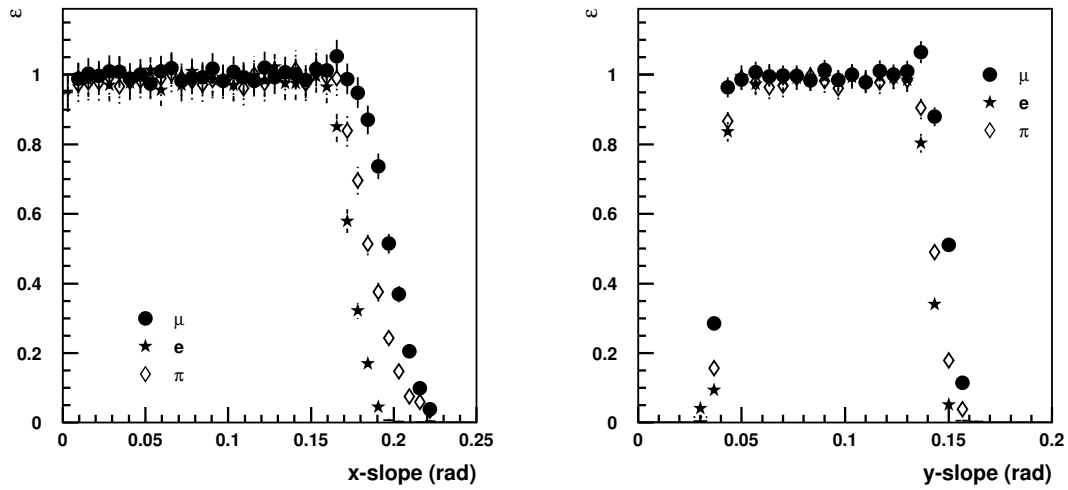

Figure 4.16.: Monte Carlo comparison of acceptance in θ_x (left) and θ_y (right) between electrons, muons, and pions.

Reconstruction Efficiency

Within the acceptance, the reconstruction efficiency for single tracks is constant. The reconstruction efficiency is determined by the efficiency of each single drift chamber plane to detect a particle track, the number of planes m in front and behind the magnet, and by the maximum number n of missing hits per track allowed by the reconstruction program. It follows a binominal distribution with n missing hits out of m planes [Wan:96]. Already for single plane efficiencies above 95% the reconstruction efficiency is close to unity.

The reconstruction efficiency of the NOVC method for the 1996 and 1997 data on unpolarised targets which is the dominating data sample for the cross section analysis was determined to be close to one for positrons and above 99% for hadrons. The reconstruction efficiency for the STD reconstruction method is about 99% and 98% for positrons and hadrons, respectively. For the 1995 data the reconstruction efficiency is 2% lower than for the NOVC method in 1996 and 1997. The uncertainty of these efficiencies is estimated to be about 2% [Böt:99]. Since two tracks have to be detected in J/ψ production it is counted twice and a 3% systematic uncertainty is assigned to the cross section measurement.

Apart from tails caused by multiple scattering, the momentum resolution of the HERMES spectrometer for DIS positrons is $0.7-1.25\%$ over the kinematic range; the uncertainty in the positron scattering angle is below 0.6 mrad everywhere [HERMES:98a]. The spectrometer resolution for the momentum and scattering angle of muons is assumed to be equal or better than for positrons since muons undergo less multiple scattering than positrons. This is also reflected in a better vertex resolution for the di–muon decay, where stronger vertex cuts were used in the event selection (cf. Table 4.4). As it was discussed in Section 4.4 the nominal J/ψ mass is reconstructed with an accuracy of about 10 MeV and uncertainties in the reconstruction of kinematic variables can hence be neglected in this analysis.

Acceptance for J/ψ Decays

The HERMES experiment uses a forward spectrometer with a reduced acceptance in the forward direction due to the septum plate. In comparison to inclusive DIS events, the spectrometer acceptance decreases for decaying particles by about an order of magnitude per additional track to be detected.

The acceptance for J/ψ detection is a function of the J/ψ energy $E_{J/\psi}$ because the opening angle of a decay in the laboratory frame decreases with increasing energy of the parent particle. In Figure 4.18 b) the generated (solid line) and the reconstructed (shaded histogram) J/ψ energy spectra are shown from a Monte Carlo simulation. As can be seen, a J/ψ can be reconstructed only for J/ψ energies above 15 GeV. Table 4.7 lists the numbers of Monte Carlo J/ψ events in both decay channels (in percent) remaining after certain steps of the generation and reconstruction. The geometrical acceptance of the spectrometer is 6.0% for the decay channel $J/\psi \rightarrow e^+e^-$ and 8.1% for the decay channel $J/\psi \rightarrow \mu^+\mu^-$ corresponding to the 'Generated in Acceptance' column of Table 4.7.

Despite the identical spatial distribution of the decay particles, the geometrical acceptance is different for both J/ψ decay channels due to the different acceptance for positrons and muons. Figure 4.17 shows a side view of the the front and the magnet region of the spectrometer including a di–muon J/ψ decay. The track in the top half passes through the back field clamp and the frames of the magnet chambers; back and front part of the track could be matched, although there are no hits in the magnet chambers. For both decay channels the geometrical acceptance of the spectrometer is the dominating correction for a cross section measurement.

$J/\psi \to e^+e^-$					
Data	Generated		Reconstructed		2σ Mass
Sample	Total	in Acceptance	no Cuts	all Cuts	Window
95			5.6%	4.7%	3.0%
96	100%	6.0%	5.8%	5.0%	3.3%
97(NOVC)			5.8%	5.0%	3.2%
97(STD)			5.6%	4.8%	2.8%
$J/\psi \to \mu^+\mu^-$					
Data	Generated		Reconstructed		2σ Mass
Sample	Total	in Acceptance	no Cuts	all Cuts	Window
96			8.0%	4.6%	4.2%
97(NOVC)	100%	8.1%	8.0%	4.4%	4.0%
97(STD)			8.0%	4.6%	4.0%

Table 4.7.: Number of Monte Carlo events in percent after several stages of generation and reconstruction separated by decay channel and data sample.

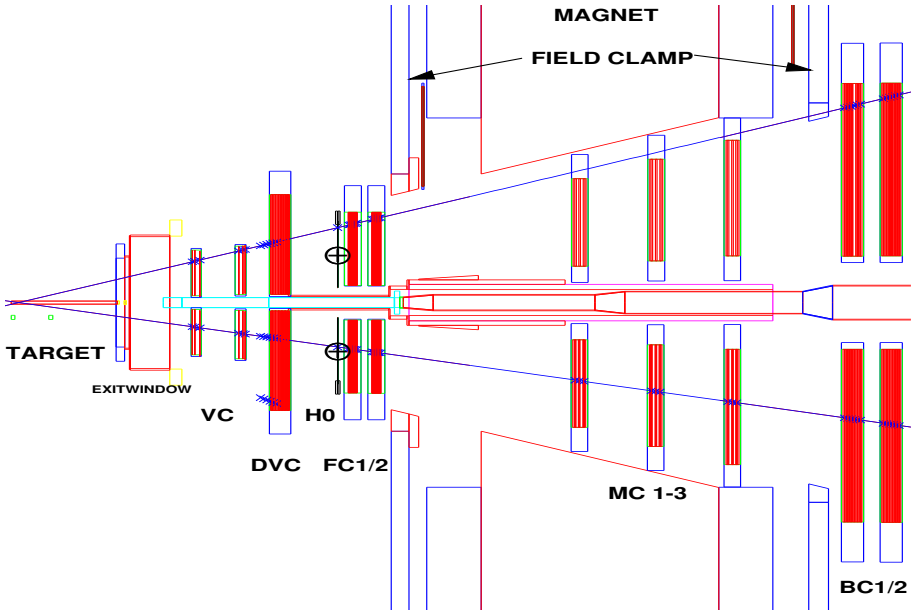

Figure 4.17.: Detail of a $J/\psi \to \mu^+\mu^-$ event. The muon track in the top half of the spectrometer passes through the magnet chamber frames and the back field clamp.

Efficiency of Event Selection

The 'Reconstructed, all Cuts' column of Table 4.7 contains the fraction of events after all event selection requirements have been applied. For the di–muon decay, the larger geometrical acceptance is about compensated by the more restrictive kinematic cuts necessary because of the less efficient muon PID. Thus in comparison to the decay $J/\psi \rightarrow e^+e^-$ a larger fraction of the reconstructed di–muon events was rejected by the event selection.

The events finally used for the analysis are selected within the 2σ window with respect to the mean value of the fit to the invariant mass spectrum. Electrons undergo considerable energy loss while passing through the spectrometer. Hence the invariant mass distribution of the decay $J/\psi \rightarrow e^+e^-$ is smeared out towards smaller values (cf. Figure 4.18 a). This reduces the fraction of events within the 2σ mass window for this decay by about one–third compared to the decay $J/\psi \rightarrow \mu^+\mu^-$.

The values given in the last column of table 4.7 have a statistical accuracy of $\pm 0.2\%$, determined by the statistics of the available Monte Carlo simulations. Within this uncertainty no significant differences were found between the the various reconstruction scenarios for both decay channels. With respect to the statistical uncertainty of the data samples the statistical uncertainty of the Monte Carlo Simulation is neglected.

Steps of Acceptance and Efficiency Correction

The detector acceptance is parameterised as a function of the J/ψ energy and each event is corrected individually. The corrections for reconstruction and event selection efficiencies are applied during the acceptance correction. The total efficiency $\epsilon_{J/\psi}$ is determined as:

$$\epsilon_{J/\psi}(E_{J/\psi}) = \epsilon_{acc}(E_{J/\psi}) \times \epsilon_{rec} \times \epsilon_{sel} \tag{4.10}$$

Here $\epsilon_{acc}(E_{J/\psi})$ denotes the geometrical acceptance, ϵ_{rec} the reconstruction efficiency, and ϵ_{sel} the efficiency of the event selection, which in case of the decay $J/\psi \rightarrow e^+e^-$ includes the influence of smearing due to the energy loss of electrons and positrons. Figure 4.18 summarises the subsequent steps to obtain the final number of J/ψ once corrections for acceptance, efficiencies, and background are applied. The individual plots shown in Figure 4.18 subsequently illustrate the different corrections:

a) The invariant mass spectrum is reconstructed for Monte Carlo events and all event selection cuts are applied. The distribution is fitted and events within the 2σ mass window (indicated by the shaded area) are regarded as Monte Carlo J/ψ candidates. Here the spectrum for the decay $J/\psi \rightarrow e^+e^-$ from the 1997(NOVC) Monte Carlo simulation is shown. The smearing to lower mass values due to the energy loss of the electrons/positrons can be clearly seen. Its effect is included in the efficiency correction, since the candidate sample is taken from the 2σ mass window.

b) The generated (solid line) and the reconstructed (shaded histogram) J/ψ energy distributions are shown. Events with J/ψ energy $E_{J/\psi} < 15$ GeV are completely outside the spectrometer acceptance.

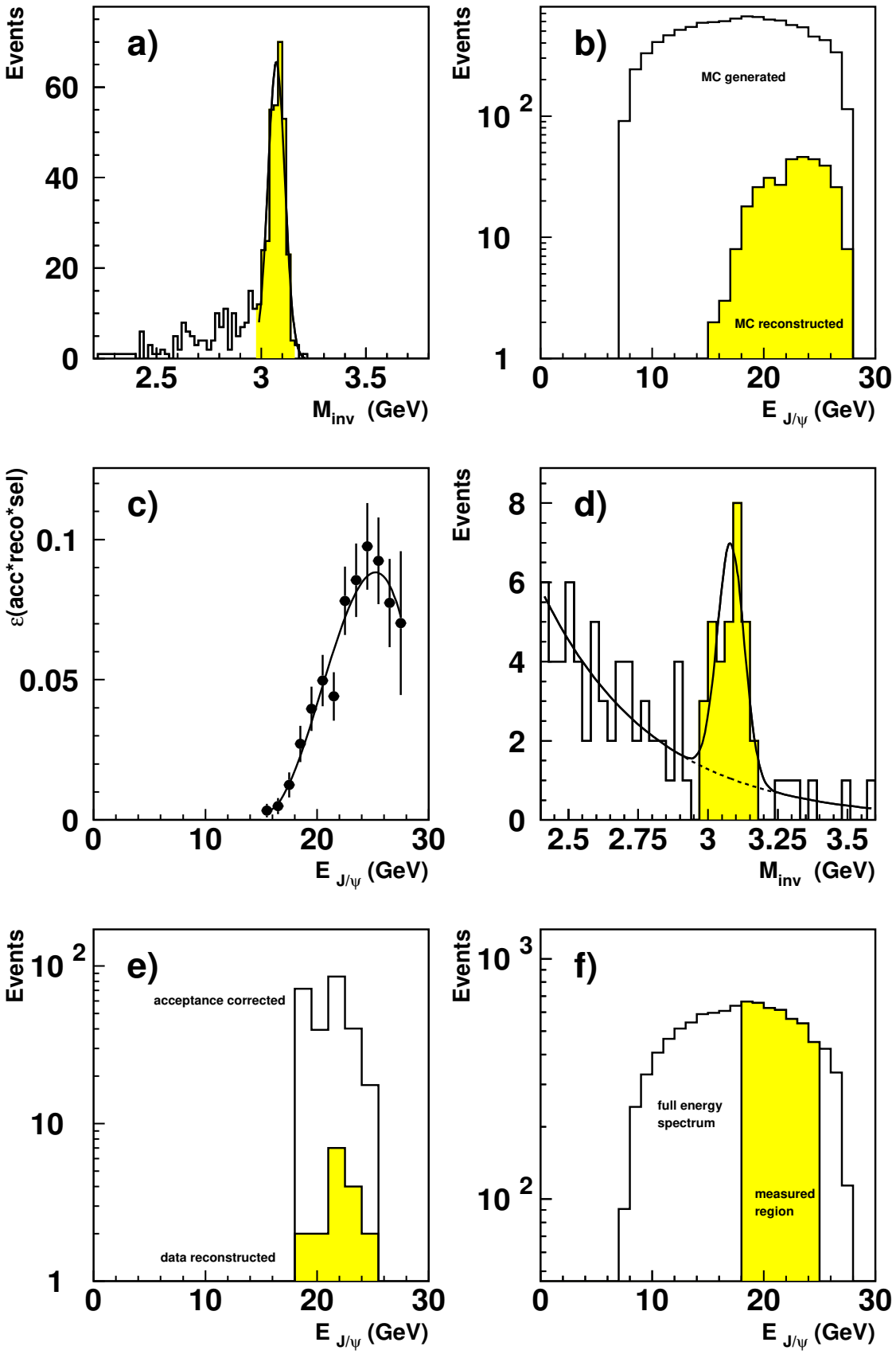

Figure 4.18.: Steps to obtain the total number of J/ψ corrected for acceptance, efficiency, and background. As an example, the unpolarised $J/\psi \to e^+e^-$ data of 1997 is chosen. For explanation see text.

c) The acceptance is parameterised as a polynomial function that is fitted to the ratio of the distributions from b). The efficiencies of reconstruction and event selection are implicitly contained in this parameterisation. To to avoid large acceptance corrections the 'measured' region in $E_{J/\psi}$ was restricted. For the cross section measurement in the decay channel $J/\psi \to e^+e^-$ only events with $18 < E_{J/\psi} < 25$ GeV were used. For the decay channel $J/\psi \to \mu^+\mu^-$ the measured region is $20 < E_{J/\psi} < 25$ GeV where the lower limit is given by the event selection (cf. Table 4.4).

d) From the fit to the invariant mass spectrum of the experimental data, the number of signal and background events within the 2σ mass window is obtained.

e) The energy spectrum for the J/ψ candidates from data within the 2σ mass window is plotted (shaded histogram). The same data is shown (solid line) after acceptance and efficiency corrections. Each data event is weighted with the correction function obtained in c) and corrected for the background (BG) by the fraction of signal events (S) to the total number of candidates

$$w(E_{J/\psi}) = \frac{1}{\epsilon_{J/\psi}(E_{J/\psi})} \times \frac{\mathrm{S}}{\mathrm{S}+\mathrm{BG}}. \tag{4.11}$$

This background correction assumes that the efficiency function is the same for background and signal events. The number $N^{J/\psi}_{18<E<25}$ of J/ψ's within the measured energy range, corrected for acceptance, efficiencies, and background is obtained from the integral of the weighted distribution:

$$N^{J/\psi}_{18<E<25} = \sum_{i_{data}} w_i(E_{J/\psi}). \tag{4.12}$$

f) In the last step the measured region has to be extrapolated to the full energy spectrum. The energy distribution for the generated Monte Carlo events is plotted with the solid line; the shaded histogram indicates the events within the measured energy range. The ratio of the total number of generated events to the number of events within the measured region is determined and multiplied with $N^{J/\psi}_{18<E<25}$ to obtain $N^{J/\psi}_{total}$ the total number of J/ψ's in the full energy range:

$$N^{J/\psi}_{total} = \frac{N^{MC}_{generated}}{N^{MC}_{generated\ 18<E<25}} \cdot N^{J/\psi}_{18<E<25}. \tag{4.13}$$

Systematic Uncertainties of the Acceptance Correction

To study the systematic uncertainty of the acceptance and efficiency correction it has been applied to various Monte Carlo J/ψ event samples. The number $N^{J/\psi}_{E_{min}<E<E_{max}}$ of Monte Carlo J/ψ's events obtained by the acceptance and efficiency correction was compared to the known number of generated events. Systematic studies included variation of the measured region in $E_{J/\psi}$, the event selection requirements, and the invariant mass window. Different treatments of the acceptance function were tested like a linear parameterisation or an energy independent correction factor. An uncertainty of 5% has been obtained for the acceptance and efficency correction procedure.

It turned out that the acceptance and efficiency corrections do not depend on the details of the J/ψ event generation. The acceptance functions obtained from Monte Carlo samples generated with AROMA are consistent with the ones obtained from EPJPSI. However, the extrapolation from the measured region to the total energy spectrum in Figure 4.18-f) depends directly on the energy distribution of the assumed production mechanisms. To estimate the systematic uncertainty of the extrapolation to the full energy spectrum the EPJPSI generator was used, which generates diffractive and inelastic processes separately.

Figure 4.19 compares the normalised J/ψ energy distributions given by AROMA (solid line) with the purely elastic (dashed line) and the purely inelastic (dotted line) EPJPSI Monte Carlo simulations. As can be expected, the AROMA distribution lays between the two extreme cases and tends to be more close to the purely elastic sample. In the inelastic process energy is transfered to the target, and therefore the corresponding J/ψ energy distribution shows a strong decrease at the upper limit.

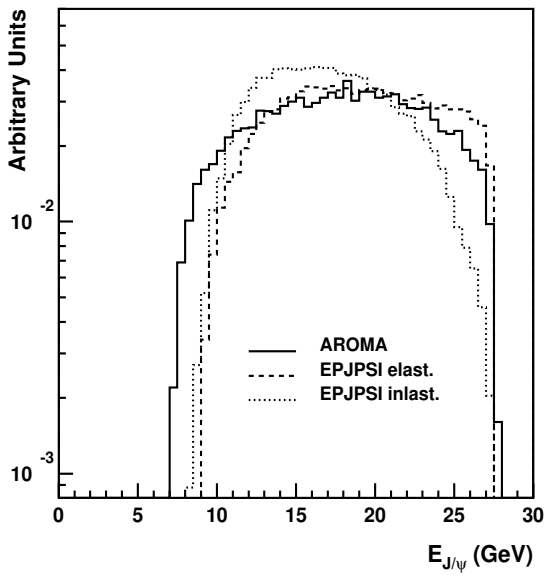

Figure 4.19.: Comparison of the generated J/ψ energy distribution between different Monte Carlo generators.

The ratio of the integral from the total distribution to that of the measured region of $18 < E_{J/\psi} < 25$ GeV for the decay $J/\psi \to e^+e^-$ is 2.28, 2.43, and 2.59 for the EPJPSI elastic, AROMA, and EPJPSI inelastic Monte Carlo simulations, respectively. This corresponds to a 6% uncertainty between AROMA and both EPJPSI elastic and inelastic for the extrapolation of the energy spectrum. Because of the smaller measured energy region $20 < E_{J/\psi} < 25$ GeV the extrapolation uncertainty is larger in the case of the di–muon decay. The ratio of the integrals is 3.3, 3.6, and 4.2 for the EPJPSI elastic, AROMA, and EPJPSI inelastic Monte Carlo simulations, respectively. This corresponds to a difference of 9% between EPJPSI elastic and AROMA and a 17% between the latter and EPJPSI inelastic. Both differences are averaged, weighted by the presently estimated ratio of $70 : 30$ of elastic and inelastic processes (cf. Section 4.11), yielding a 11% extrapolation uncertainty for the di–muon J/ψ decay.

4.9. Electroproduction Cross Section

The total cross section for J/ψ leptoproduction can be calculated from $N_{total}^{J/\psi}$, the total number of J/ψ's per decay channel corrected for acceptance, efficiencies, and background by

$$\sigma_{eN\to J/\psi X} = \frac{1}{Br \cdot L \cdot \epsilon_{DAQ} \cdot \epsilon_{Trig}} N_{total}^{J/\psi\mapsto e^+e^-,\mu^+\mu^-}. \tag{4.14}$$

Here L is the luminosity , Br the known branching ratio of $6.0 \pm 0.2\%$ [C$^+$:98], ϵ_{DAQ} and ϵ_{Trig} are the DAQ and trigger efficiencies. In Figure 4.20 the cross sections obtained separately for each decay channel, year, and reconstruction method are shown for comparison. A fit to a constant yields an average value of

$$\sigma_{eN\to J/\psi X}(E = 27.5 \text{ GeV}) = 0.080 \pm 0.008_{\text{stat}} \text{ nb}, \tag{4.15}$$

indicated by the shaded band in Figure 4.20. This result is the first measurement of the J/ψ leptoproduction cross section in the HERMES kinematic region. There are no other data below lepton beam energies of 200 GeV; the kinematically closest data are from the BFP experiment on J/ψ leptoproduction using a 209 GeV muon beam on an iron target [BFP:79] and from the EMC/NMC collaboration using a muon beam of 200 to 280 GeV on iron, ammonia, helium, and deuterium targets [EMC:80] [EMC:83] [EMC:92a] [NMC:92, Mar:91]. Data on J/ψ production in the HERMES kinematic region are only available from experiments using real photon beams. In order to compare the HERMES result to the world data on J/ψ photoproduction, the HERMES leptoproduction cross section has to be converted to a cross section for photoproduction by using the photon flux. this will be described in Section 4.10.

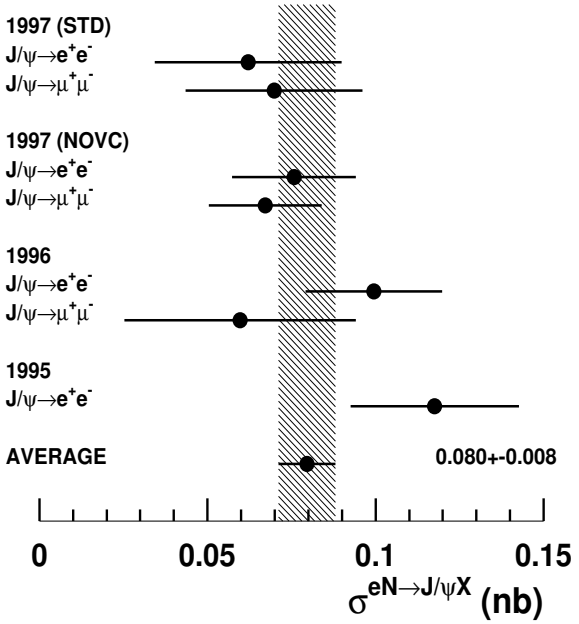

Figure 4.20.: Total J/ψ leptoproduction cross section, separated by decay channel, year, and reconstruction method.

Discussion of Result and Systematic Uncertainties

Because of the small statistics of the J/ψ signal at HERMES, the systematic studies to determine the uncertainty of the cross section measurement are limited. If the event selection cuts are varied in a reasonable range it is not possible to separate systematic effects from statistical fluctuations. It was extensively checked that all separate signals in Figure 4.4 are stable against variation of the event selection within the given statistical uncertainties. None of the event selection criteria is critical in the sense that the signal vanishes if a criteria is changed slightly. In order to study the stability of the cross section measurement the analysis has been performed for seven independent data samples. The separation by decay channel, years, and eventually reconstruction methods corresponds to quite different aspects of the data:

- Different methods of event selection are used for the two decay channels $J/\psi \to e^+e^-$ and $J/\psi \to \mu^+\mu^-$, with separate triggers, different particle identification methods, and different spectrometer acceptance.

  The HERMES spectrometer was optimised for the detection of DIS positrons. Consequently, the trigger efficiency is close to unity, the positron identification has an efficiency above 98% at a contamination of less than 1%, and the corresponding uncertainties are small and well under control.

  The situation for muon detection is completely different. Muon identification has been achieved by the requirement of minimum ionising signals in the calorimeter and the preshower detector and a signal in the Cherenkov detector. Trigger efficiencies had to be determined using a hadronic data sample, where clearly identified muons are not available for a cross check.

- The data were collected in three years of HERMES running from 1995 to 1997 including the commissioning of the experiment in 1995. During this time several changes and improvements of the spectrometer hardware and software took place and more stable running conditions and detector performance were achieved. For the 1997 data two different reconstruction methods were used.

- For each year, the used targets and the relative amount of data taken per target vary. This does not only include the simple exchange of target gases. The 1995 ^3He target was a completely different hardware setup compared to the later used ABS target. Unpolarised targets have an order of magnitude higher density than polarised ones, yielding higher event rates and higher particle fluxes in all spectrometer components.

In Figure 4.20 the cross section is plotted separately for both decay channels and different years. The large statistical uncertainty of the 1996 $J/\psi \to \mu^+\mu^-$ measurement is due to the small J/ψ signal. The fit of a constant to all data points has a reduced χ^2 of 0.8. Within statistics all separate measurements are compatible with the mean value indicated by the shaded band.

If the data are averaged separately for both decay channels the results of the different years are consistent within the decay channel with reduced χ^2's close to unity. For the decay channel $J/\psi \to e^+e^-$ the 1995 and 1996 cross section values are higher than the two 1997 values, here the difference between the average of 1995 and 1996 and the average for 1997 is $1.6\,\sigma$. Within every decay channel there seems to be no significant systematic uncertainty between the different data samples. A possible systematic effect must be much smaller than

	$J/\psi \to e^+e^-$	$J/\psi \to \mu^+\mu^-$	cf. Section
Experimental Uncertainties			
Stability of Fit	2%	4%	4.3
Luminosity determination	6%		4.5
Trigger	-	3%	4.6
Reconstruction Efficiency	3%		4.8
Acceptance correction	5%		4.8
Branching ratio	3%		4.9
Total Experimental	9%	10%	
Weighted Average	9%		
Uncertainty of Extrapolation			
to Full Energy Range	6%	11%	4.8
Weighted Average	8%		

Table 4.8.: Contributions to the total systematic uncertainty of the cross section measurement.

the statistical uncertainty. The difference between the cross section values obtained separately for both decay channels is $1.3\,\sigma$

Experimental systematic uncertainties that are determined independently of the actual J/ψ signal have been discussed in the course of the analysis. They are listed in Table 4.8; uncertainties that are different for both decay channels are given separately. Adding in quadrature yields a total experimental systematic uncertainty of 9% for the decay $J/\psi \to e^+e^-$ and 10% for $J/\psi \to \mu^+\mu^-$. A 9% systematic experimental uncertainty for the cross section measurement combined from both channels is obtained from the weighted average.

The dominating contribution to the systematic uncertainty is caused by the extrapolation from the measured J/ψ energy range to the full energy spectrum. It is given separately since it is determined by the present uncertainty in the ratio of elastic to inelastic processes at HERMES energies, rather than by the experimental conditions. The uncertainty of the extrapolation of the di–muon decay will be reduced by the muon detector added to the spectrometer in 1998[HERMES:97c]. A clean muon PID will allow to relax the event selection requirement on the J/ψ energy, hence to extend the measured energy range.

Presently installed is a forward spectrometer located in the quadrupole magnet downstream of the experiment (FQS) that will detect positrons scattered at low angles, i.e. at low Q^2 [HERMES:97c]. With the FQS, the full J/ψ event kinematics becomes available for about 30% of the J/ψ statistics. This allows to determine the ratio of elastic to inelastic processes at HERMES energies, reducing the uncertainty of the extrapolation which is presently estimated from the two extreme cases of purely elastic and inelastic processes.

The dominating experimental uncertainty is due to the luminosity measurement [Ben:98b]. An improvement of the acceptance correction procedure can be achieved by a more accurate description of the spectrometer acceptance, which requires Monte Carlo event samples with at least an order of magnitude higher statistics than the presently used ones. In addition, the correction for the combinatorial background can be improved using Monte Carlo simulations of the background processes.

The HERMES data of the years 1998 to 2000, mainly taken with a polarised deuterium target, will about double the available J/ψ statistics. For the present cross section measurement the statistical error of 10% is balanced with the experimental systematic uncertainty and the uncertainty of the extrapolation from the measured region to the full energy range. Therefore, a further reduction of the statistical error has to be accompanied by a reduction of the systematic uncertainties.

4.10. Photon Flux for J/ψ Production at HERMES

The general concept of the Weizsäcker–Williams Approach (WWA) and the determination of photon fluxes are discussed in detail in Appendix A.3. In this section the photon flux for J/ψ production at HERMES will be derived.

Photon Flux and Vector Meson Dominance Model

The double–differential cross section of diffractive vector meson production in lepton–nucleon scattering can be expressed as

$$\frac{d^2\sigma^{eN\to eVN}}{dQ^2\,d\nu} = \Gamma(Q^2,\nu)\left(1+\frac{Q^2}{m_V^2}\right)^{-2}\sigma^{\gamma N\to VN}(\nu). \tag{4.16}$$

Here, the photon–nucleon cross section for vector meson production by virtual photons $\sigma^{\gamma^\star N\to VN}(Q^2,\nu)$ has been extrapolated to $Q^2=0$ by means of the VMD photon propagator term. Using the ratio $R=\xi_V^2\cdot Q^2/m_V^2$ of the absorption cross sections for longitudinal and transverse photons in the VMD model from Equation 2.17, the photon flux $\Gamma(Q^2,\nu)$ derived from Equation A.35 contains both longitudinal and transverse components

$$\Gamma(Q^2,\nu) = \frac{\alpha K}{2\pi Q^2\nu^2}\left\{y^2+2(1-y)\left[\frac{1}{\gamma^2+1}\left(1+\xi_V^2\frac{Q^2}{m_V^2}\right)-\frac{Q^2_{min}}{Q^2}\right]\right\}. \tag{4.17}$$

The term $Q^2/(4E^2)\approx 0$ from Equation A.35 has been neglected, while the factor $K=(1-x)\nu$ and the term $1/(\gamma^2+1)$ have been kept in order to estimate their contributions in the energy range of the HERMES experiment.

In the present analysis of J/ψ production the photon flux derived from the vector meson dominance model is used to account for the dominance of diffractive processes. With respect to the photon flux the VMD model, the hard diffractive two–gluon exchange model, and the CSM are compatible, since the ratio R and the effective Q^2 behaviour of the cross sections are similar. Therefore, the photon flux of Equation 4.17 is also valid for the non-separable contribution from inelastic J/ψ production. A small uncertainty remains in expression for the ratio R, but (as will be shown later) the contribution of the term proportional to ξ^2 in Equation 4.17 is small and can be neglected.

Figure 4.21 shows the distribution of the photon flux from Equation 4.17 for J/ψ production in the Q^2-ν plane. At fixed Q^2 it depends only moderately on ν, but for a given ν it is a steep function of Q^2 near the limit $Q^2 \to Q^2_{min}$.

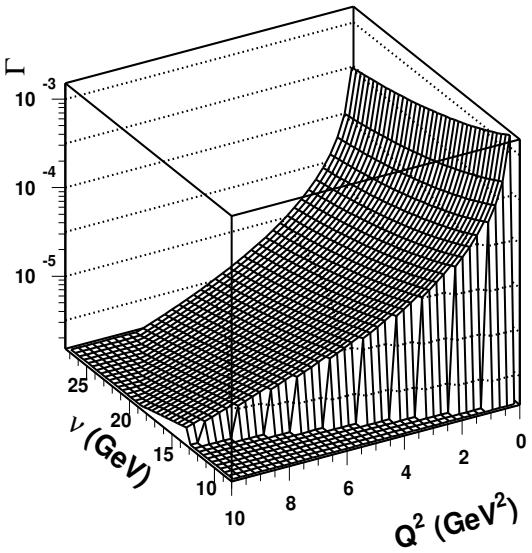

Figure 4.21.: Photon flux for J/ψ production in the Q^2, ν plane.

Kinematic Limits

At HERMES the dominant contribution to the J/ψ signal comes from photoproduction at low Q^2 where the scattered positron remains inside the beam pipe. The cross section is not measured in several (Q^2, ν) bins, but instead within the whole kinematic range of the experiment as one large 'bin'. The kinematic limits of this 'bin' are determined as follows: The minimum photon energy ν_{min} at $Q^2 = 0$ can be derived from the requirement that at the J/ψ production threshold the photon–nucleon centre–of–mass energy has to be larger than the squared sum of nucleon and J/ψ mass:

$$\nu_{min} = \frac{m^2_{J/\psi} + 2m_{J/\psi}m_p}{2m_p} = 8.2 \text{ GeV}. \tag{4.18}$$

The maximum photon energy ν_{max} is determined by the beam energy:

$$\nu_{max} = E - m_e = 27.5 \text{ GeV}, \tag{4.19}$$

where the electron mass cannot be neglected because otherwise the term $2(1-y)\frac{Q^2_{min}}{Q^2}$ diverges in the later integration of Γ. The minimum Q^2 can be derived from the exact definition of the four–momentum of the photon $q^2 = (k-k')^2$; it depends on the fractional photon energy y:

$$Q^2 = -(k-k')^2 = 4EE'sin^2\frac{\Theta}{2} + \frac{m_e^2 y^2}{1-y} \quad \Rightarrow \quad Q^2_{min} = \frac{m_e^2 y^2}{1-y^2}. \tag{4.20}$$

The maximum Q^2 is chosen, according to the observation that under the given experimental conditions at HERMES there are no J/ψ events at $Q^2 > 1$ GeV:

$$Q^2_{max} = 1 \text{ GeV}^2. \tag{4.21}$$

Parameterisation of the Energy Dependence near Threshold

The integration of Equation 4.16 over Q^2 and ν relates the total electroproduction cross section $\sigma^{eN\to eJ/\psi N}$ to the photoproduction cross section $\sigma^{\gamma N\to J/\psi N}$

$$\sigma^{eN\to J/\psi N}_{tot} = \int_{\nu_{min}}^{\nu_{max}} \int_{Q^2_{min}}^{Q^2_{max}} \Gamma(Q^2,\nu) \left(1 + \frac{Q^2}{m^2_{J/\psi}}\right)^{-2} \sigma^{\gamma N\to J/\psi N}(\nu)\ dQ^2 d\nu. \tag{4.22}$$

The integration has to be carried out over the entire kinematic range of the measurement that is close to the threshold for J/ψ production at HERMES centre-of–mass energies. The determination of the photoproduction cross section from Equation 4.22 at a certain photon energy ν_{fix} requires a parameterisation of the threshold behaviour of $\sigma^{\gamma N\to J/\psi N}$. Existing world data near threshold as shown in Figure 4.22 motivated the assumption that the photoproduction cross section is zero at ν_{min} and rises near threshold linearly with the photon energy ν:

$$\sigma^{\gamma N\to J/\psi N}(\nu) = p_1 + p_2\ \nu.$$

Here p_1 and p_2 are the parameters of the linear function. The constant term p_1 cancels expressing the photoproduction cross section as follows:

$$\sigma^{\gamma N\to J/\psi N}(\nu) = \sigma^{\gamma N\to J/\psi N}(\nu_{fix}) + p_2(\nu - \nu_{fix}). \tag{4.23}$$

The insertion of Equation 4.23 into Equation 4.22 yields an expression for the photoproduction cross section at a certain photon energy ν_{fix}:

$$\begin{aligned}\sigma^{\gamma N\to J/\psi N}(\nu_{fix}) &= \frac{\sigma^{eN\to eJ/\psi N}_{tot}}{\int\int \Gamma \left(1+\frac{Q^2}{m^2_{J/\psi}}\right)^{-2} dQ^2 d\nu} + p_2 \left[\frac{\int\int \nu\,\Gamma \left(1+\frac{Q^2}{m^2_{J/\psi}}\right)^{-2} dQ^2 d\nu}{\int\int \Gamma \left(1+\frac{Q^2}{m^2_{J/\psi}}\right)^{-2} dQ^2 d\nu} - \nu_{fix}\right] \\ &= \frac{\sigma^{eN\to eJ/\psi N}}{\Phi} + p_2\left[\langle\nu\rangle - \nu_{fix}\right],\end{aligned} \tag{4.24}$$

where the arguments of Γ and the integration ranges were omitted. The integrated photon flux Φ is given by

$$\Phi = \int_{\nu_{min}}^{\nu_{max}} \int_{Q^2_{min}}^{Q^2_{max}} \Gamma(Q^2,\nu) \left(1 + \frac{Q^2}{m^2_{J/\psi}}\right)^{-2} dQ^2 d\nu. \tag{4.25}$$

The average value $\langle\nu\rangle$ describes the centre–of–gravity of the flux factor distribution within the kinematic range of the measurement. The additive term proportional to p_2 vanishes if the energy ν_{fix} is chosen to be equal to $\langle\nu\rangle$:

$$\sigma^{\gamma N\to J/\psi N}(\nu_{fix}) = \frac{\sigma^{eN\to eJ/\psi N}}{\Phi}. \tag{4.26}$$

In this case one does not need to determine the parameter p_2 from a fit to existing world data, i.e. the determination of the J/ψ photoproduction cross section from lepton–nucleon scattering at HERMES has as the only model assumption the linearity of the photoproduction cross section near threshold.

Numerical Results

In Table 4.9 the numerical results for the integrated photon flux Φ from Equation 4.25 are given. Using a value of one for the parameter ξ^2, an integrated photon flux Φ of 0.025 GeV^{-3} is obtained. The centre–of–gravity of the photon flux distribution (cf. Equation 4.24) was found as $\langle\nu\rangle = 15$ GeV.

Integrated Flux Φ from Equation 4.25		
$(Q^2_{max} = 1\mathrm{GeV}^2, \xi^2 = 1)$	Φ	0.0250 GeV^{-3}
At Centre–of–Gravity	$\langle\nu\rangle$	15 GeV
Limit of K	$(1-x)\nu \to \nu$	- 0.3%
Neglect γ^2	$\frac{1}{\gamma^2+1} \to 1$	<0.1%
Longitudinal Contribution	$\xi^2 = 0.5$	0.2%
Longitudinal Contribution	$\xi^2 = 0$	0.4%
Neglect Mass Term $\propto m_e^2$	$-2(1-y)\frac{Q^2_{min}}{Q^2}$	-4.7%
Neglect Q^2 Dependence	$\left(1+\frac{Q^2}{m^2_{J/\psi}}\right)^{-2}$	-1.3 %

Table 4.9.: Value of the integrated photon flux Φ and relative contributions of different terms in Equations 4.17 and 4.25

In addition, the relative contributions to the integral Φ of certain terms in Equations 4.17 and 4.25 are listed in Table 4.9. They were obtained by leaving the term in question out of the integration, one at a time. Most important are the mass term proportional to m_e^2 and the VMD–propagator term of the $Q^2 \to 0$ extrapolation. The contributions of all other terms including the longitudinal component proportional to ξ^2 are small and will be neglected. The photon flux reduces then to

$$\Gamma_T(Q^2,\nu) = \frac{\alpha}{2\pi Q^2 \nu}\left\{y^2 + 2(1-y)\left(1-\frac{Q^2_{min}}{Q^2}\right)\right\}, \tag{4.27}$$

i.e. containing only the transverse component. The photon flux Γ is steep function of Q^2 near the limit $Q^2 \to Q^2_{min}$. Therefore, the main contribution to the integral Φ of the photon flux comes from the low Q^2 region. The influence the upper integration limit in Q^2 on the integral Φ was found to be negligible by varying Q^2_{max}.

All integrals were calculated using a simple numerical integration with 10^2 steps in ν and 10^8 in Q^2 so that the relative uncertainty of the integration is below 0.2% and can be neglected.

4.11. J/ψ Photoproduction Cross Section

The total J/ψ photoproduction cross section at a photon energy of 15 GeV was determined from the electroproduction cross section by Equation 4.26 to be:

$$\sigma^{\gamma N\to J/\psi X}(E_\gamma{=}15\,\mathrm{GeV}) = 3.20 \pm 0.32_{\mathrm{stat}} \pm 0.29_{\mathrm{syst/exp}} \pm 0.26_{\mathrm{syst/extrap}}\,\mathrm{nb},$$

using the integrated photon flux $\Phi = 0.025$ from Table 4.9. Both the experimental systematic uncertainty (syst,exp) and the uncertainty due to the extrapolation of the measured energy range (syst,extrap) were directly taken from Table 4.8. Adding in quadrature yields a total systematic uncertainty of the cross section measurement of ± 0.38 or 12% which is comparable to the statistical uncertainty of 10%.

In Figure 4.22 the HERMES measurement of the total J/ψ photoproduction cross section is compared to world data. The inner error bars represent statistical errors, and the outer error bars the statistical and systematic uncertainties added in quadrature. Only a limited amount of data exists near the J/ψ threshold [HLW:85]: the measurements at Cornell [G$^+$:75] and SLAC [C$^+$:75] both used a bremsstrahlung beam of real photons. The data point of the BFP experiment [BFP:79] represents the kinematically closest data from lepton scattering experiments. In Figure 2.8 the same data are shown in comparison to the world data at higher energies obtained from the HERA collider experiments.

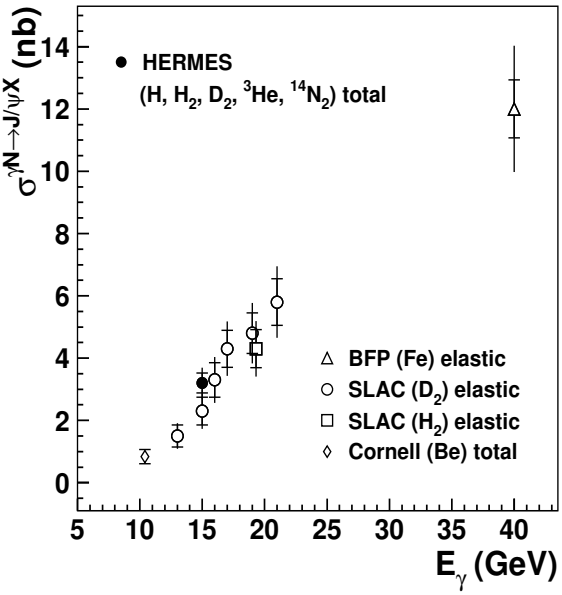

Figure 4.22.: Comparison of the total J/ψ photoproduction cross section measured at HERMES with world data.

The HERMES measurement can be directly compared to the measurement at SLAC since both experiments have similar photon energies. However, there are several differences between the two experiments. HERMES measures the total J/ψ production cross section, including both contributions from elastic and inelastic processes. For different J/ψ energies the SLAC spectrometer was set up to detect J/ψ decays at $90°$ in the J/ψ rest frame. By choosing the bremsstrahlung endpoint energy E_0 to be 0.5 GeV above a given J/ψ energy, preset by the spectrometer geometry, a possible contribution from inelastic production is excluded. Thus the SLAC data shown is for exclusive i.e. elastic J/ψ production only. The SLAC data is taken on a deuterium target and only one data point from hydrogen is available, while the HERMES data set is combined from different targets. Within the uncertainties of the measurements no dependence of the cross section on the target material was found in both experiments (cf. Section 4.7).

At SLAC, in order to assess the total photoproduction cross section, the endpoint energy E_0 was chosen 1 to 5 GeV larger than the J/ψ energy given by the spectrometer setting. Then the total photoproduction cross section at $E_\gamma = 15$ GeV was *estimated* to be 3.05 ± 0.67 nb in comparison to the measured elastic cross section of 2.3 ± 0.45 nb at the same photon

energy, where this values have been corrected to the present branching ratio. The systematic uncertainty of the SLAC measurement is 15%. This result has been interpreted as to *'indicate a possible* $20 - 30\%$ *inelastic contribution'* [C$^+$:75] to the total J/ψ photoproduction cross section.

The HERMES measurement of the total J/ψ photoproduction cross section with half the statistical error and a comparable systematic uncertainty agrees well with the SLAC data. Using the SLAC value for the elastic cross section a contribution of elastic processes to the total cross section of $72 \pm 16\%$ is obtained. This corresponds to a contribution of inelastic processes at HERMES energies of about 30% thereby confirming the above SLAC estimate.

At HERMES, the spectrometer geometry prevents the detection of the scattered positron for the majority of the J/ψ events. In the present data sample the scattered positron was recorded for less than 10 events. With this statistics it is not possible to accomplish a straight–forward separation between exclusive and inelastic processes by the event kinematics. An alternative method to determine the contribution of inelastic processes to the J/ψ data sample was investigated: In an exclusive interaction no other particle than the J/ψ is produced and additional hadron tracks can be used as a tag for inelastic events. However, the acceptance for these additional hadron tracks is small and only a few events of this type could be found, yielding a large statistical uncertainty for the obtained inelastic contribution.

Finally it should be noted that in the case of the nuclear targets J/ψ production can proceed via coherent diffractive scattering (scattering at the target nuclei) or incoherent diffractive scattering (scattering on the target nucleons). These production processes, as well as diffractive processes with dissociation of the target nucleon cannot be separated. No nuclear effects (A-dependence) were observed within the present statistics.

5. Spin Dependence in Exclusive Vector Meson Production

Presently, HERMES is using a longitudinally polarised lepton beam and a longitudinally polarised target. The theoretical understanding of double–spin asymmetries in diffractive processes in polarised lepton–nucleon scattering, i.e. their dependence on the beam polarisation *and* the target polarisation is limited. This is in contrast to the deep–inelastic scattering process where (semi–) inclusive double–spin asymmetries give access to the spin structure functions of the nucleon, and hence reveal information on the composition of the nucleon spin (cf. Appendix A.4).

Two rather different approaches to spin effects in exclusive vector meson production will be discussed in the following sections: the formalism of spin density matrix elements and predictions of two QCD models for double–spin asymmetries in exclusive J/ψ and ρ production.

5.1. Helicity Analysis

The formalism of spin density matrix elements describes the helicity transfer from the virtual photon to the vector meson and the parity of the diffractive exchange process in exclusive vector meson production. Spin density matrix elements cannot yield information on the spin structure of the nucleon since the internal structure of the target is not resolved.

To give the basis for an understanding of the possible relation of spin density matrix elements to the double–spin asymmetries in ρ production the formalism is introduced in Section 5.1.1 for scattering a longitudinally polarised beam off an unpolarised target. The ratio R for the cross sections of longitudinal and transverse photons can be related to spin density matrix elements. Results of the HERMES measurement [Bel:98, Kol:98a, HERMES:99c] of R in exclusive ρ production on an unpolarised target will be summarised since they are used for the later analysis of double spin–asymmetries.

Presently available data on spin density matrix elements are only from experiments using unpolarised targets. Thus, only the helicity transfer from the virtual photon to the final state vector meson has been considered; the spin state of the target and the helicity transfer at the nucleon vertex has not been taken into account. Spin density matrix elements in the case of a polarised target have been discussed in Reference [Fra:74] and are summarised in Section 5.1.2.

5.1.1. Spin Density Matrix Elements and Determination of R

The cross section of diffractive vector meson production in lepton–nucleon scattering, shown schematically in Figure 5.1, can be factorised into a leptonic and a hadronic part similar to Equation A.1 of Section A.1. The emission of the virtual photon $\gamma^\star$ is described by the leptonic tensor representing the photon spin states by a photon spin density matrix $\rho(\gamma)$.

In contrast to deep–inelastic scattering, the hadronic tensor representing the production of the vector meson $\gamma^\star N \rightarrow VN$ is not constructed of structure functions. Instead, vector meson production is described by a vector meson spin density matrix $\rho(V) \propto T\rho(\gamma)T^+$, related to the photon spin density matrix via helicity flip amplitudes T. Without considering the normalisation, the differential cross section can be expressed by [SW:73, WS:78]

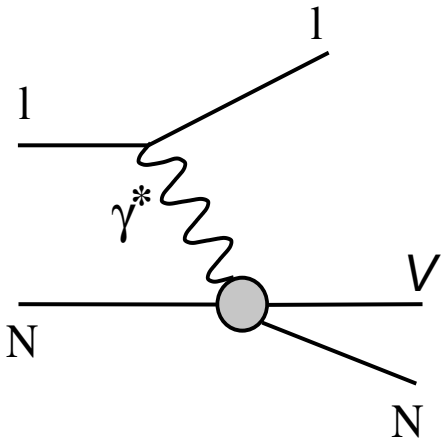

Figure 5.1.: Schematic graph of the elastic vector meson production for the discussion of the helicity analysis.

$$\frac{d\sigma^{\gamma^* N\rightarrow VN}}{dt\, d\Phi} \;\propto\; \frac{1}{4}\sum_{spins}|\mathcal{M}|^2 \;\propto\; \mathrm{Tr}(\rho(V)), \tag{5.1}$$

where the azimuthal production angle Φ (cf. Figure 5.2) reflects the polarisation state of the photon. The vector meson spin density matrix has the general form

$$\rho_{\lambda_V\lambda'_V}(V) \;=\; \sum_{\alpha=0}^{8}\Pi_\alpha\rho^\alpha_{\lambda_V\lambda'_V}, \tag{5.2}$$

with the matrix elements

$$\rho^\alpha_{\lambda_V\lambda'_V} \;=\; \frac{1}{2N_\alpha}\sum_{\lambda_{N'}\lambda_N\lambda_\gamma\lambda'_\gamma} T_{\lambda_V\lambda_{N'}\lambda_\gamma\lambda_N}\Sigma^\alpha_{\lambda_\gamma\lambda'_\gamma}T^\star_{\lambda'_V\lambda_{N'}\lambda'_\gamma\lambda_N}, \tag{5.3}$$

where Π_α and N_α are known normalisation functions. The index $\alpha = 0\ldots8$ denotes the different polarisation states of the virtual photon: transverse photons with scalar (0), linear (1,2), and (in the case of a polarised lepton beam) circular (3) polarisation, longitudinal photons (4), and interference terms between longitudinal and transverse photons in the case of unpolarised (5,6) and polarised (7,8) leptons. The amplitude for a photon of helicity λ_γ to produce a vector meson of helicity λ_V is given by $T_{\lambda_V\lambda_{N'}\lambda_\gamma\lambda_N}$, where $\lambda_i = 0, \pm1$. In Reference [SW:73] an unpolarised target is considered, i.e. the helicities of the initial and the scattered target nucleon, λ_N and $\lambda_{N'}$ are summed over. The Hermitian 3×3 matrices Σ^α represent the photon density matrix $\rho(\gamma)$ and determine which helicity flip amplitudes contribute to a certain matrix element. A full list of the matrix elements can be found in Appendix A of Ref. [SW:73].

The vector meson is observed by its two–body decay. In the vector meson rest frame, the angular distribution $\mathcal{W}(cos\theta, \phi, \Phi)$ of the decay products is then related to the spin density matrix by the Wigner rotation functions D

$$\mathcal{W}(cos\theta, \phi, \Phi) = \frac{3}{4\pi} \sum_{\lambda\lambda'=0,\pm1} D^1_{\lambda 0}(\phi, \theta, -\phi)^\star \rho(V)_{\lambda\lambda'} D^1_{\lambda' 0}(\phi, \theta, -\phi). \tag{5.4}$$

Three angles are necessary for a complete description. Figure 5.2 shows the angle definitions in the $\gamma^\star N$ centre-of-mass frame – the so–called s-channel helicity frame. The azimuthal production angle Φ is the angle between the lepton scattering plane and the vector meson production plane; the Φ dependence of $\mathcal{W}$ in Equation 5.4 enters through $\rho(V)_{\lambda\lambda'}$ only. The vector meson decay is described in the vector meson rest frame by two angles: i) the azimuthal angle ϕ between its production and decay plane and ii) the polar angle θ of the positively charged decay particle with the z–axis of the vector meson rest frame which is defined opposite to the direction of the scattered nucleon.

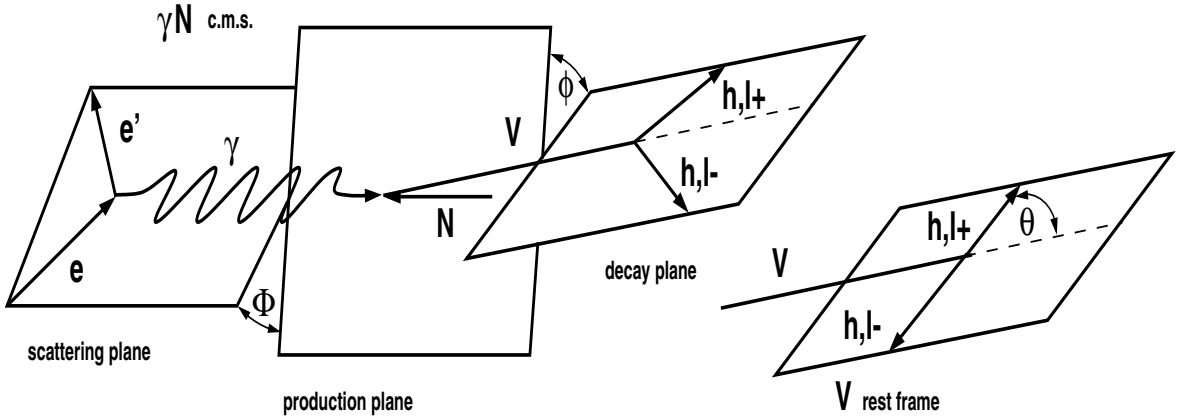

Figure 5.2.: Angle definitions in the s-channel helicity frame for elastic vector meson production.

In the case of a *longitudinally* polarised beam and an *unpolarised* target the 3–dimensional angular distribution $\mathcal{W}$ is a function of 26 independent matrix elements. If the beam energy is fixed, the values of W^2 and Q^2 determine the ratio ϵ of photon fluxes for a given data sample and the contributions from transverse and longitudinal photons cannot be separated. A Rosenbluth separation (measurements at different scattering angles, i.e. at different ratios ϵ for the same values of W and Q^2) is experimentally difficult since the lepton–nucleon cross section decreases rapidly with increasing scattering angle. In this case $(\rho^0_{\lambda\lambda'})$ and $(\rho^4_{\lambda\lambda'})$ have to be combined and the following matrix elements can be measured:

$$r^{04}_{\lambda\lambda'} = \frac{\rho^0_{\lambda\lambda'} + \epsilon R \rho^4_{\lambda\lambda'}}{1 + \epsilon R}, \quad r^{1,2,3}_{\lambda\lambda'} = \frac{\rho^{1,2,3}_{\lambda\lambda'}}{1 + \epsilon R}, \quad \text{and} \quad r^{5,6,7,8}_{\lambda\lambda'} = \sqrt{R}\frac{\rho^{5,6,7,8}_{\lambda\lambda'}}{1 + \epsilon R}. \tag{5.5}$$

The decay angular distribution $\mathcal{W}$ for the decay products is then expressed by 23 independent

matrix elements $r^{\alpha}_{\lambda\lambda'}$ as [SW:73]

$$
\begin{aligned}
W(\cos\theta,\phi,\Phi) = \qquad & (5.6)\\
& \frac{3}{4\pi}\left\{\frac{1}{2}(1-r^{04}_{00})+\frac{1}{2}(3\,r^{04}_{00}-1)\cos^2\theta\right.\\
& -\sqrt{2}\,\mathrm{Re}\,r^{04}_{10}\sin 2\theta\cos\phi - r^{04}_{1-1}\sin^2\theta\cos 2\phi\\
& -\epsilon\cos 2\Phi\left(r^{1}_{11}\sin^2\theta + r^{1}_{00}\cos^2\theta - \sqrt{2}\,\mathrm{Re}\,r^{1}_{10}\sin 2\theta\cos\phi - r^{1}_{1-1}\sin^2\theta\cos 2\phi\right)\\
& -\epsilon\sin 2\Phi\left(\sqrt{2}\,\mathrm{Im}\,r^{2}_{10}\sin 2\theta\sin\phi + \mathrm{Im}\,r^{2}_{1-1}\sin^2\theta\sin 2\phi\right)\\
& +\sqrt{2\epsilon(1+\epsilon)}\cos\Phi\\
& \qquad\times\left(r^{5}_{11}\sin^2\theta + r^{5}_{00}\cos^2\theta - \sqrt{2}\,\mathrm{Re}\,r^{5}_{10}\sin 2\theta\cos\phi - r^{5}_{1-1}\sin^2\theta\cos 2\phi\right)\\
& +\sqrt{2\epsilon(1+\epsilon)}\sin\Phi\left(\sqrt{2}\,\mathrm{Im}\,r^{6}_{10}\sin 2\theta\sin\phi + \mathrm{Im}\,r^{6}_{1-1}\sin^2\theta\sin 2\phi\right)\\
& +P_B\left[\sqrt{1-\epsilon^2}\left(\sqrt{2}\,\mathrm{Im}\,r^{3}_{10}\sin 2\theta\sin\phi + \mathrm{Im}\,r^{3}_{1-1}\sin^2\theta\sin 2\phi\right)\right.\\
& \qquad+\sqrt{2\epsilon(1-\epsilon)}\cos\Phi\left(\sqrt{2}\,\mathrm{Im}\,r^{7}_{10}\sin 2\theta\sin\phi + \mathrm{Im}\,r^{7}_{1-1}\sin^2\theta\sin 2\phi\right)\\
& \qquad+\sqrt{2\epsilon(1-\epsilon)}\sin\Phi\\
& \qquad\qquad\left.\left.\times\left(r^{8}_{11}\sin^2\theta + r^{8}_{00}\cos^2\theta\ -\sqrt{2}\,\mathrm{Re}\,r^{8}_{10}\sin 2\theta\cos\phi - r^{8}_{1-1}\sin^2\theta\cos 2\phi\right)\right]\right\}.
\end{aligned}
$$

The term $P_B\,[...]$ comprises those contributions which are proportional to the beam polarisation. A mass correction $\delta = \frac{2m_e^2}{Q^2}(1-\epsilon)$ was neglected.

Helicity Conservation in the s–Channel and Parity of the Exchange

If the helicities in the $\gamma^\star N$ centre–of–mass system, i.e. in the s–channel, are conserved the helicity of the photon is fully transfered to the vector meson. In this case, there can be no extra spin dependence at the vector meson production vertex and the azimuthal angle Φ of the production plane becomes equally distributed. The azimuthal dependence of $\mathcal{W}$ reduces to $\psi = \phi - \Phi$, thus only two variables remain independent. When assuming s–channel helicity conservation (SCHC), all spin flip amplitudes $T_{\lambda_V\lambda_{N'}\lambda_\gamma\lambda_N}$ with $\lambda_V \neq \lambda_\gamma, \lambda_{N'} \neq \lambda_N$ vanish, leaving only five nonzero matrix elements: r^{04}_{00}, r^{1}_{1-1}, $\mathrm{Im}r^{2}_{1-1}$, $\mathrm{Re}r^{5}_{10}$, and $\mathrm{Im}r^{6}_{10}$. Only three of them are independent since $r^{1}_{1-1} = -\mathrm{Im}r^{2}_{1-1}$, and $\mathrm{Re}r^{5}_{10} = -\mathrm{Im}r^{6}_{10}$ [SW:73].

A small, but significant deviation from SCHC has been found in recent measurements [H1:99] at a Q^2 range of about 3 to 10 GeV^2. The matrix element r^{5}_{00}, approximately proportional to the helicity flip amplitude $T_{\lambda_\gamma=0\lambda_\rho=1\lambda_N\lambda_{N'}}$ for a transverse photon to produce a longitudinal vector meson, is significantly different from zero. This violation of SCHC at higher Q^2 can be reproduced by perturbative QCD calculations, based on the exchange of two gluons [IK:98]. In this calculation, the target nucleon is formally treated as a spinless particle and the helicity flip amplitudes were related to the wave function of the vector meson and to the anomalous dimension γ (cf. Equation 5.18) of the gluon density [MRT:97].

The parity of the exchange object is given by $P = \varepsilon(-1)^L$, with $\varepsilon = \pm 1$ the intrinsic parity determined by its wave function. Natural and unnatural parity exchange are defined by $P = (-1)^L$ and $P = -(-1)^L$, i.e. positive and negative intrinsic parity of the exchange object, respectively. Assuming that the t-channel exchange in the reaction $\gamma^\star N \to VN$ has

natural parity $J^P = (L+S)^{(-1)^L} = 0^+, 1^-, \ldots$, yields the relation $2r^1_{1-1} = (1 - r^{04}_{00})$, which can be used to test the intrinsic parity of the exchange object and reveal information about its nature. Pomeron exchange has natural parity, while unnatural parity exchange is mediated by di-quark objects. At small $|t|$ unnatural parity exchange can be identified with the model of elementary one–pion exchange [Fra:74].

Measurement of R^ρ at HERMES

Angular distributions in exclusive ρ production have been analysed at HERMES [Bel:98, Kol:98a, HERMES:99c] using the 1995 data on the ^{3}He target.[1] The longitudinally polarised positron beam had an average polarisation of 0.48 ± 0.03. Due to statistics, the HERMES analysis was restricted to the four one–dimensional angular distributions $\mathcal{W}(cos\theta)$, $\mathcal{W}(\phi)$, $\mathcal{W}(\Phi)$, and $\mathcal{W}(\psi)$. Each of them is obtained from Equation 5.6 by integrating over the 'other' angles. Seven matrix elements can be extracted

$$r^{04}_{1-1} = \mathrm{Im}(r^3_{1-1}) = \mathrm{Tr}(r^1) = \mathrm{Tr}(r^5) = \mathrm{Tr}(r^8) = 0 \quad \text{and} \quad 2\,r^1_{1-1} = 1 - r^{04}_{00}; \tag{5.7}$$

within the statistical uncertainty they have been found to be in agreement with SCHC and natural parity exchange. Assuming the validity of SCHC and using the known ratio of fluxes $\epsilon = \Gamma_L/\Gamma_T$, the matrix element r^{04}_{00} can be related to the cross section ratio $R = \sigma_L/\sigma_T$ in exclusive ρ production by

$$R = \frac{\sigma_L}{\sigma_T} = \frac{1}{\epsilon}\frac{r^{04}_{00}}{1 - r^{04}_{00}}. \tag{5.8}$$

This allows to determine R at a given value of Q^2 and W^2 from a measurement of the matrix element r^{04}_{00} at this point. The matrix element r^{04}_{00} can be obtained from the one–dimensional angular distribution $\mathcal{W}(cos\theta)$

$$\mathcal{W}(\cos\theta) = \frac{3}{4}\left[1 - r^{04}_{00} + (3\,r^{04}_{00} - 1)\cos^2\theta\right]. \tag{5.9}$$

At HERMES, this measurement was performed in one bin in W but four bins in Q^2. Figure 5.3 shows the extracted values of R in comparison to world data. A parameterisation of R of the form

$$R(Q^2) = c_0(W)\,\left[\frac{Q^2}{m^2_\rho}\right]^{c_1} \tag{5.10}$$

was fitted to the world data. An invariant mass in the photon–nucleon system of about 10 GeV marks the transition region between Regge and Pomeron exchange. Therefore, the fit was performed separately for the data at $W < 10$ GeV and $W > 10$ GeV indicated by the dotted and dashed line in Figure 5.3. The parameter c_0 was obtained as $c_0 = 0.47 \pm 0.03$ for $W > 10$ GeV and $c_0 = 0.35 \pm 0.03$ for $W < 10$ GeV; the common exponent has a value of $c_1 = 0.62 \pm 0.04$. As can be seen from Figure 5.3, the contribution of longitudinal photons dominates vector meson production at high Q^2. For the kinematic range of ρ production at HERMES the contributions from transverse and longitudinal photons are equally important.

[1] Although the 1995 ^{3}He target was polarised, its polarisation was not taken into account and averaged.

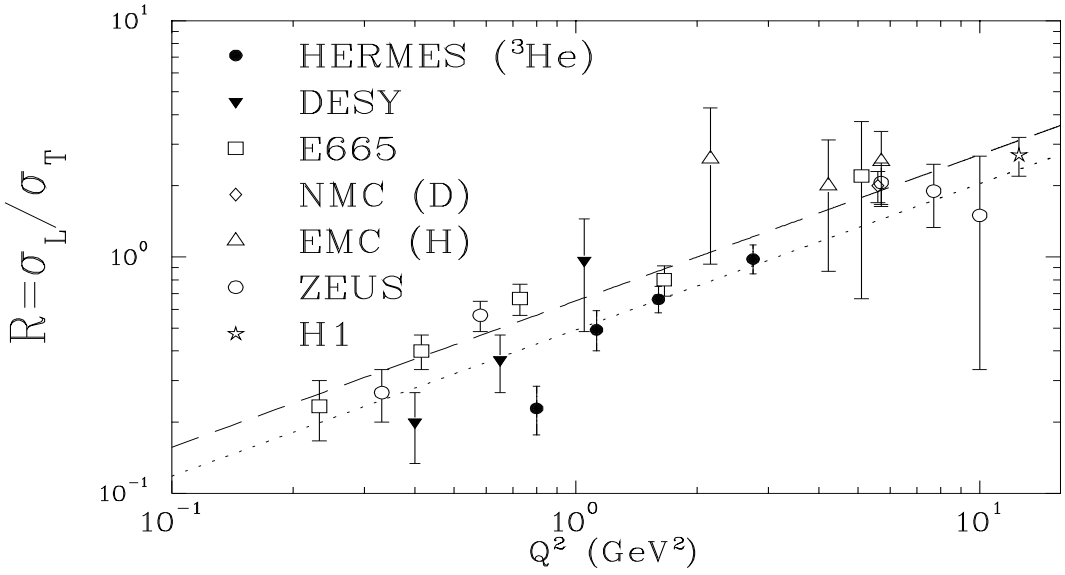

Figure 5.3.: HERMES measurement of R in exclusive ρ production in comparison to world data. The lines represent the parameterisation of Equation 5.10 for $W > 10$ GeV (dashed) and $W < 10$ GeV (dotted).

5.1.2. Spin Density Matrix Elements for a Polarised Target

Spin density matrix elements in the most general case of scattering a (longitudinally polarised) lepton beam off a polarised nucleon target have been discussed for ρ production in Reference [Fra:74]. The main focus of this discussion lies in the investigation of natural and unnatural parity exchange that can distinguish between different models of the exchange process. Until now, no experimental data of spin density matrix elements using polarised targets exist.

The polarisation state of the target nucleon is represented by a nucleon spin density matrix $\rho(N)$. Similar to Equation 5.3, the vector meson density matrix is given by the photon density matrix $\rho(\gamma)$ and the helicity flip amplitudes T as

$$\rho^{\alpha\beta}_{\lambda_V\lambda'_V}(V) \propto \sum_{\lambda_{N'}\lambda_N\lambda'_N\lambda_\gamma\lambda'_\gamma} e^{i\Phi(\lambda_\gamma-\lambda'_\gamma)} T_{\lambda_V\lambda_{N'}\lambda_\gamma\lambda_N}\rho(N)^{\beta}_{\lambda_N\lambda'_N}\rho(\gamma)^{\alpha}_{\lambda_\gamma\lambda'_\gamma}T^{\star}_{\lambda'_V\lambda_{N'}\lambda'_\gamma\lambda'_N}. \quad (5.11)$$

Here the notation of Reference [SW:73] has been used for consistency. In analogy to α, which indicates the different polarisation states of the photon, the index β denotes the polarisation states of the target: unpolarised target $(\beta = 0)$, transversely polarised target with polarisation components parallel $(\beta = 1)$ or perpendicular $(\beta = 2)$ to the vector meson production plane, and longitudinally polarised target $(\beta = 3)$. Summation over the nine different photon and the four different nucleon polarisations yields the vector meson spin density matrix

$$\rho_{\lambda_V\lambda'_V}(V) = \sum_{\alpha=0}^{8}\sum_{\beta=0}^{3}\Pi_\alpha\xi_\beta\rho^{\alpha\beta}_{\lambda_V\lambda'_V}, \quad (5.12)$$

where Π and ξ are known normalisation functions.

The author of Ref. [Fra:74] concludes that having a *longitudinal* target polarisation as an additional degree of freedom does not yield any additional information on the dynamics of ρ production in comparison to an unpolarised target. No observable spin–effects are expected in exclusive ρ production when using a longitudinally polarised target. A *transversely* polarised target is suitable for the investigation of unnatural parity exchange and helicity non–conserving spin flip amplitudes; an additional polarisation of the lepton beam can yield information on natural parity exchange.

5.2. Double–Spin Asymmetries in QCD Models

Two QCD model predictions for double–spin asymmetries in exclusive J/ψ and ρ production will be discussed. In the case of the J/ψ, the diffractive process is described by exchange of two gluons. The only available model for double–spin asymmetries in ρ production is based on the parton–hadron duality hypothesis.

5.2.1. Double–Spin Asymmetries in Exclusive J/ψ Production

In the two–gluon exchange model of exclusive vector meson production [Rys:93, RRML:97] the differential cross section depends on the square of the gluon distribution. Therefore, it appears possible to relate double–spin asymmetries in vector meson production in polarised lepton–nucleon scattering to the (square) of the spin dependent gluon distribution $\Delta g(x)$. Similar to the unpolarised case, this has been first discussed for J/ψ production [Rys:97a] where the high charm quark mass ensures the hard scale of the process even at low Q^2 and low t.

However, in recent calculations [VM:98b, VM:98a] it was shown that exclusive J/ψ production is not a good probe for the polarised gluon distribution. Double–spin asymmetries are expected to be zero, since at leading twist-2 vector meson production depends only on the unpolarised off–forward quark or gluon distributions [VM:98b]. As will be described below, only very small asymmetries are predicted because of Fermi–motion and binding energy effects in the relativistic wave function of the $c\bar{c}$ system [VM:98a].

The matrix elements of the process $\gamma(q,\lambda) + p(p,S) \rightarrow J/\psi(V,\lambda') + p'(p',S')$ are parameterised by polarised and unpolarised off–forward gluon distributions. Here, λ, λ', S, S' denote the helicities of photon, vector meson, initial and scattered target nucleon. For the off–forward parton distributions a simple model was used which is closely related to the usual forward gluon distributions g and Δg. It obeys the forward limits

$$G(x,\xi=0,\mu^2) = xg(x,\mu^2), \quad \text{and} \quad \Delta G(x,\xi=0,\mu^2) = x\Delta g(x,\mu^2). \tag{5.13}$$

with x and ξ from Equations 2.35. Because of collinearity, momentum conservation reduces to helicity conservation. Therefore, only the helicity conserving matrix elements $\mathcal{A}_{\lambda\lambda SS}$ with

$\lambda = \lambda'$ and $S = S' = \pm 1/2$ had to be considered [VM:98a]

$$\mathcal{A}_{\lambda\lambda\pm\pm} \propto \int_1^{-1} dx \left\{ \frac{1}{(x-\xi+i\epsilon)} - \frac{1}{(x+\xi-i\epsilon)} G(x,\xi,\mu^2)[1+\mathcal{O}(\eta)] \right. \\ \left. \pm\lambda\,\xi\,\frac{\eta}{2}\,\frac{1}{(x-\xi+i\epsilon)^2} - \frac{1}{(x+\xi-i\epsilon)^2}\Delta G(x,\xi,\mu^2) \right\}, \tag{5.14}$$

where μ^2, the hard scale of the process, is only given by the J/ψ mass since the calculations are carried out in the photoproduction limit $Q^2 = 0$. Fermi–motion and binding energy effects are taken into account by a small correction factor η. Its value has been estimated from data to be about $\eta \approx 0.07$. The final expression for the longitudinal spin asymmetry involves the integrals $I_G, I_{\Delta G}$ of the off-forward gluon-distributions

$$A^{\gamma^\star N \to J/\psi N} = \eta \frac{Re(I_G^\star I_{\Delta G})}{|I_G|^2}. \tag{5.15}$$

Although this asymmetry depends also on the integral of the polarised off–forward gluon distribution, its analysing power is small since it is significantly reduced by the correction η. Figure 5.4 shows the predicted asymmetry to be of the order of 10^{-2}, depending on the photon energy. In comparison to experiments at high energies, where the exclusive reaction proceeds at small x, fixed target experiments at lower energies are better suited to test the OFPD's in a wider kinematic range. Unfortunately, the predicted effect is well below the projected statistical accuracy of an asymmetry measurement in J/ψ production at HERMES.

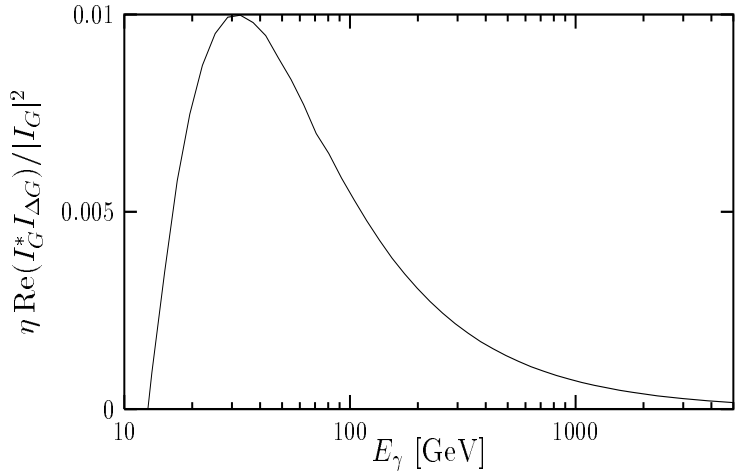

Figure 5.4.: Predicted asymmetry $A_1^{J/\psi}$ from Reference [VM:98a]. The average photon energy of the HERMES Experiment is at about 20 GeV.

5.2.2. Double–Spin Asymmetry in Exclusive ρ Production

In the discussion of QCD models for the production of light vector mesons at HERMES energies difficulties arise for two main reasons: i) the hard scale is not defined by the quark mass and ii) the contribution of transverse photons, where QCD factorisation is still unproven, is equally important as the contribution of longitudinal photons.

This difficulties can be avoided by an ansatz [MRT:97] using the parton–hadron duality hypothesis to calculate the production of light vector mesons, not only by longitudinal but also by transverse photons. In addition, it is the only presently available QCD calculation for double–spin asymmetries in ρ production [Rys:97b]. The model was first applied to calculate the the Q^2 dependence of the ratio R at HERA collider energies. This ratio is not well reproduced by the pQCD models discussed in Section 2.1.5 since the predicted behaviour of σ_T is too steep compared to the data. Predictions for ρ cross sections and the ratio $R = \sigma_L/\sigma_T$ in the kinematic range of the HERA collider experiments are given in Reference [MRT:97]

According to the parton–hadron duality hypothesis the reaction $\gamma \rightarrow \rho \rightarrow \pi\pi$ is replaced by the reaction $\gamma \rightarrow q\bar{q} \rightarrow \pi\pi$ constrained to an invariant mass interval $M_{q\bar{q}}$ around the ρ meson mass. The cross section is expressed as[Rys:97b]:

$$\sigma(\gamma^\star N \rightarrow \rho N) \simeq \sum_{q=u,d} \int_{M_a^2}^{M_b^2} \frac{d\sigma^{\gamma^\star N \rightarrow (q\bar{q})N}}{dM^2} dM^2, \tag{5.16}$$

where M is the invariant mass of the $q\bar{q}$ system and (M_a,M_b) is a mass interval of typically 1 GeV around the ρ mass. The two 'open' quarks do not form a bound vector meson state, but instead, they independently undergo a fragmentation process into final state pions. Therefore, the divergencies can be avoided that arise in pQCD calculations from the integration of the vector meson wave function in the case of transverse photons.

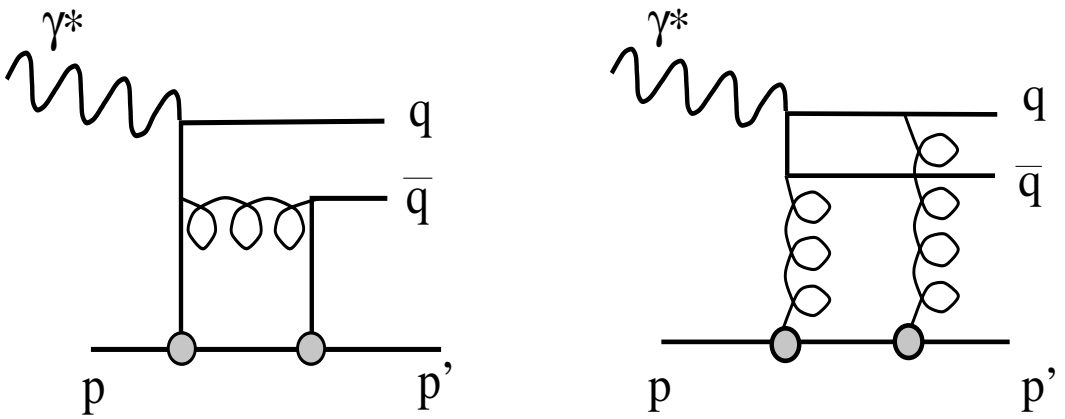

Figure 5.5.: Schematic diagrams for quark (left) and gluon (right) exchange contributing to diffractive vector meson production in the parton–hadron duality hypothesis.

The case of ρ production in polarised lepton–nucleon scattering is discussed in this model in Reference [Rys:97b]. Gluon and quark exchange shown in the schematic graphs in Figure 5.5 contribute to the spin dependent part of the interaction. Longitudinally polarised gluons do not transfer spin information between target and photon, thus at least one exchanged gluon has to be transversely polarised. A possible relation of double–spin asymmetries in exclusive ρ production to the unpolarised and polarised quark and gluon distributions is

suggested assuming u–quark dominance [Rys:97b] [2]

$$A_{\gamma^\star\to\rho} \simeq \frac{\frac{\gamma(g)}{\gamma(\Delta\bar{u})}\Delta\bar{u}(x,\bar{Q}^2) + \frac{\gamma(g)}{\gamma(\Delta u)}\Delta q(x,\bar{Q}^2)}{6g(x,\bar{Q}^2)} - \frac{\gamma(g)}{\gamma(\Delta g)}\frac{\Delta g(x,\bar{Q}^2)}{2g(x,\bar{Q}^2)}, \tag{5.17}$$

with the notation $\bar{Q}^2 = z(1-z)Q^2$. The anomalous dimension γ describes the Q^2 evolution of the parton and gluon distributions. It is defined by

$$f(x,Q^2) = f(x,Q_0^2)\cdot\left(\frac{Q^2}{Q_0^2}\right)^{\gamma}. \tag{5.18}$$

In the kinematic range of ρ production at HERMES at moderate $Q^2 \leq 3.5$ GeV^2 the anomalous dimensions of q, Δq, g, and Δg are approximately the same and their ratios can be replaced by unity. As a consequence, the predicted asymmetry does not depend on Q^2 in this kinematic region. The '$-$' sign in Relation 5.19 is due to the Altarelli-Parisi splitting functions ΔP_{qg}, describing the emission of a quark from a gluon, being negative at small x; this holds for the average value of $\langle x\rangle = 0.07$ for exclusive ρ production at HERMES. At small x, where the diffractive process occurs, the contribution from the polarised u-quark is small and can be neglected, yielding the approximation [Rys:99]

$$A_{\gamma^\star\to\rho} \approx -\frac{\Delta g(x,\bar{Q}^2)}{2\,g(x,\bar{Q}^2)} \tag{5.19}$$

for the relation between the double–spin asymmetry to the polarised quark and gluon distributions.

The size of the left term in Equation 5.17 which contains the contribution of the u quark has been estimated to be below 0.05 for ρ production at HERMES using the GRSV [GRSV:96] parton distributions. Therefore, the small x approximation can be applied to the HERMES ρ data. Note, that the validity of the Relation 5.19 depends on the validity of the underlying parton–hadron duality hypothesis.

[2] Note the reversed sign in the asymmetry definition of Equation 21 in Ref. [Rys:97b].

6. Analysis of Double–Spin Asymmetries

Double–spin asymmetries in exclusive J/ψ and ρ vector meson production in longitudinally polarised lepton–nucleon scattering were investigated using the HERMES data taken with the polarised hydrogen target of 1996 and 1997. No measurements of these cross–section asymmetries exist up to now. The focus of the analysis will be on the ρ meson, since only the statistics of the polarised ρ data sample is large enough to allow for detailed systematic studies.

The definition of the virtual–photon absorption asymmetry A_1 for a longitudinally polarised photon and and a longitudinally polarised nucleon target is independent of the physics process the virtual photon undergoes

$$A_1 \;=\; \frac{\sigma_{1/2} - \sigma_{3/2}}{\sigma_{1/2} + \sigma_{3/2}}. \tag{6.1}$$

Here $\sigma_{3/2}$ and $\sigma_{1/2}$ denote the photon absorption cross sections with $3/2$ and $1/2$ the projection of the total spin in the photon–nucleon system along the photon momentum. The formalism that was developed for spin–asymmetry measurements in deep–inelastic scattering is explained in detail in Appendix A.4. For the analysis of spin asymmetries in vector meson production this formalism will adopted. Still, the interpretation of the measured asymmetry A_1 depends on the physical process. In DIS A_1 is related to the polarised structure functions g_1 and g_2. In exclusive vector meson production there is no theoretical framework for such an asymmetry.

6.1. Experimental Aspects

6.1.1. Experimental Extraction of Spin Asymmetries

Under experimental conditions beam and target polarisation (P_B and P_T) are usually not unity, leading to a reduction of the experimental accessible lepton–nucleon cross section asymmetry $A_{||}$ (cf. Appendix A.4)

$$A_{||}^{measured} = A_{||} \cdot P_B \cdot P_T \cdot f \quad \text{with} \quad A_{||} = \frac{\sigma^{\rightleftarrows} - \sigma^{\rightrightarrows}}{\sigma^{\rightleftarrows} + \sigma^{\rightrightarrows}}. \tag{6.2}$$

Here $\sigma^{\rightrightarrows}$ and $\sigma^{\rightleftarrows}$ are the lepton–nucleon cross sections for a parallel or anti–parallel direction of the target spin with respect to the longitudinal beam polarisation. The factor f takes a possible dilution of the polarised target due to other types of unpolarisable material into account. For the HERMES polarised hydrogen gas target containing only polarised protons

f is equal to unity. From the definition of the experimental accessible asymmetry $A_{||}$ of Equation 6.2, the number of events $N^{\rightrightarrows(\rightleftarrows)}$ per beam and target spin configuration can be derived

$$N^{\rightrightarrows(\rightleftarrows)} = \sigma\mathcal{A} \int_{\rightrightarrows(\rightleftarrows)} \epsilon_{DAQ}(t) \cdot L(t) \cdot \left[1 - (+)\, A_{||}\, P_B(t)\, P_T(t)\, f\right] dt. \tag{6.3}$$

Here $\sigma = \frac{1}{2}(\sigma^{1/2} + \sigma^{3/2})$ is the unpolarised cross section and L is the luminosity. The assumption is made that the acceptance function $\mathcal{A}$ is spin independent. With respect to the time–scale of a burst the target and beam polarisation are constant and the integration in time can be replaced by a summation over the bursts

$$N^{\rightrightarrows(\rightleftarrows)} = \sum_{\rightrightarrows(\rightleftarrows)} n_i, \qquad L^{\rightrightarrows(\rightleftarrows)} = \sum_{\rightrightarrows(\rightleftarrows)} L_i, \qquad L_P^{\rightrightarrows(\rightleftarrows)} = \sum_{\rightrightarrows(\rightleftarrows)} |L_i \cdot P_B \cdot P_T \cdot f|. \tag{6.4}$$

The luminosity L is calculated via the coincidence rate R_{lumi} of the luminosity monitor corrected with the DAQ efficiency ϵ_{DAQ}

$$L = R_{Lumi} \cdot T_{Burst} \cdot \epsilon_{daq}. \tag{6.5}$$

No absolute normalisation of the luminosity is needed, since for an asymmetry measurement only the relative luminosities of the two spin configurations are taken into account. With the summations above, the asymmetry $A_{||}$ can be rewritten

$$A_{||} = \frac{N^{\rightleftarrows} L^{\rightrightarrows} - N^{\rightrightarrows} L^{\rightleftarrows}}{N^{\rightleftarrows} L_P^{\rightrightarrows} + N^{\rightrightarrows} L_P^{\rightleftarrows}}. \tag{6.6}$$

Using Gaussian error propagation the statistical uncertainty of the asymmetry is obtained as

$$\delta(A_{||}) = \frac{L^{\rightrightarrows} L_P^{\rightleftarrows} + L^{\rightleftarrows} L_P^{\rightrightarrows}}{(N^{\rightleftarrows} L_P^{\rightrightarrows} + N^{\rightrightarrows} L_P^{\rightleftarrows})^2} \cdot \sqrt{(N^{\rightrightarrows})^2\, \delta^2(N^{\rightleftarrows}) + (N^{\rightleftarrows})^2\, \delta^2(N^{\rightrightarrows})}. \tag{6.7}$$

The statistical uncertainties of the luminosity and the polarisation measurements are small and can be neglected.

Figure of Merit

Equations 6.6 and 6.7 for the asymmetry and its statistical uncertainty can be simplified using the following assumptions: i) small asymmetries are measured with a large number of events ($N^{\rightrightarrows} \sim N^{\rightleftarrows} \sim N/2$), ii) the spin state of the target is flipped on a short time–scale thus the luminosities per spin state are balanced ($L^{\rightrightarrows} \sim L^{\rightleftarrows}$), and iii) the polarisations P_B and P_T of beam and target are constant ($L_p = |P_B\, P_T\, f|L$):

$$A_{||} \approx \frac{1}{P_B\, P_T\, f} \cdot \frac{N^- - N^+}{N^- + N^+}, \quad \text{and} \quad \delta(A_{||}) = \frac{1}{\sqrt{N} P_B P_T f}. \tag{6.8}$$

From this expression for $\delta(A_{||})$ the *Figure of Merit* for a spin asymmetry measurement is defined as: $N P_B^2 P_T^2 f^2$. Higher statistics increase the Figure of Merit only linearly, whereas the polarisations and the dilution factor contribute quadratically. The Approximations 6.8 are

only used here for the discussion of the Figure of Merit, for the analysis the full Expressions 6.6 and 6.7 were used.

The 1995 polarised ^3He target had an average polarisation of $\langle P_T \rangle = 46\%$ and a dilution factor $f = 1/3$ in comparison to the 1996/1997 polarised hydrogen target with $f = 1$ and $\langle P_T \rangle = 0.9$. Approximately the same statistics were collected for both targets with similar beam polarisation $\langle P_B \rangle$. Consequently, the Figure of Merit for the ^3He data is about 35 times smaller, i.e. the statistical uncertainty $\delta(A_{||})$ about six times larger than for the hydrogen data. In addition, possible nuclear effects in vector meson production have to be taken into account for the ^3He target. Therefore, in contrast to the cross section measurement, the 1995 ^3He data has not been used for the asymmetry analysis.

6.1.2. Data Quality for Beam and Target Polarisation

An essential ingredient of a spin asymmetry measurement is the polarisation of beam and target. For the cross section analysis in Section 4.2, beam and target polarisation did not enter and the corresponding data quality criteria were omitted. Polarisation information is contained burst–wise in the μDST. Table 6.1 lists the requirements necessary for an asymmetry analysis in addition to those listed in Table 4.2.

Criterion		1996	1997
Beam Polarisation		$0.3 < P_B < 0.8$	
Lumi Rate	[Hz]	$5. < R_{Lumi} < 60.$	
Target Type		$\vec{H}_1$ (ABS)	
Spin State	Defined	•	•
Data Quality Target	OK	•	•
Target Polarisation		$0.5 < P_T < 1.05$	
Remaining Bursts w.r.t. Unpolarised Data Quality		76.3%	80.7%

Table 6.1.: Summary of data quality criteria related to beam and target polarisation for the 1996 and 1997 data on the polarised hydrogen target.

Beam Polarisation The beam polarisation values are fitted on a fill–by–fill basis to reduce their sensitivity to fluctuations in the polarisation measurement. The lower limit excludes data with too low weight to the final asymmetry. At HERA the positron beam polarisation cannot be changed on a short time–scale; it requires a mechanical movement of the spin–rotator magnets during a shutdown of the accelerator. Figure 6.1 shows the distribution of the beam polarisation values. It is positive for all 1996 data and negative for most of the 1997 data sample. (During the 1997 data taking the beam polarisation was reversed to positive values for a short period.)

Luminosity After the polarisation of atomic hydrogen in the ABS, the shell electrons of the hydrogen atoms have a small $1-2\%$ residual spin polarisation [Wei:98] caused by inefficiencies in the transitions between the hyperfine states of the hydrogen and by interactions between the polarised hydrogen atoms. This electron polarisation causes a small asymmetry in the Bhabha cross section between both target polarisation states. To correct the luminosity measurement for the polarised data sample for this asymmetry, the luminosity measurement for parallel and anti–parallel beam and target spin states are averaged by a fill–wise fit procedure. These smoothed luminosity rates are used here.

Target Polarisation To reduce the systematic uncertainty of the asymmetry measurement, the longitudinal target polarisation is randomly chosen on a short time–scale of about once per minute. Figure 6.2 shows the distribution of the target polarisation values for both years of data taking. The arrows give the spin orientation of the target with respect to the beam polarisation. A spin flip itself needs only about a second; during this time the target polarisation state is undefined. The corresponding burst is split into three parts: before, during, and after the spin flip and the time of the spin operation is removed from the analysis.

Several offline analyses, using redundant data from different sources, check regularly the reliability of each component of the rather complex target and ensure its stable operation. The target data quality criteria include the values of the target polarisation and the correction parameters α_0 and α_R needed for the calculation of the final polarisation value. The lower limit on the target polarisation excludes data with too low weight to the asymmetry measurement. Since the average target polarisation is about 90%, statistical fluctuations in the polarisation measurement to values above one are possible. Therefore, the upper limit is set at a somewhat higher value.

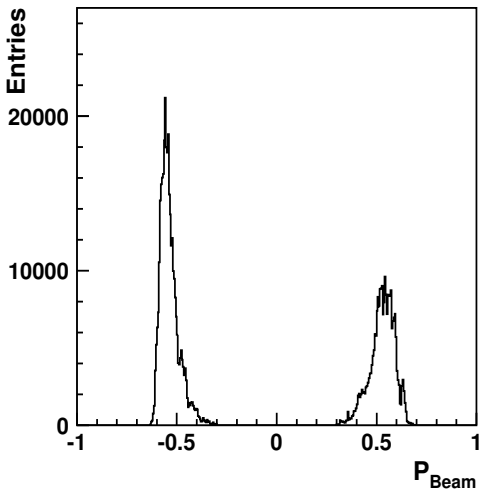

Figure 6.1.: Distribution of the beam polarisation; positive values correspond to all 1996 data and a small fraction of the 1997 data, negative polarisation values are from 1997 data only.

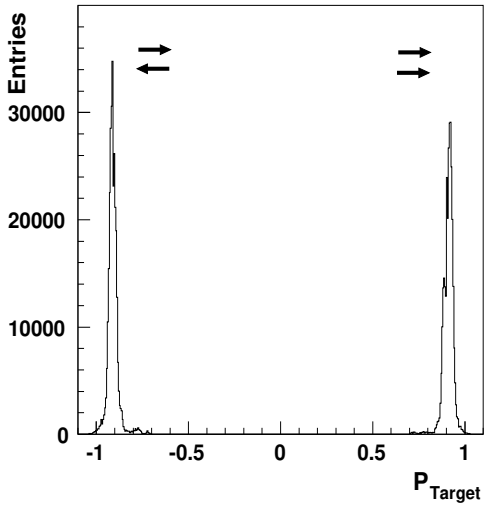

Figure 6.2.: Distribution of the polarisation values for the polarised hydrogen target with respect to the beam polarisation; '$\rightrightarrows$' and '$\rightleftarrows$' denote parallel and anti–parallel beam and target spins.

6.2. Spin Asymmetries in J/ψ Production

From the 1996 and 1997 data on the polarised hydrogen target, the spin asymmetry $A_{\parallel}^{J/\psi}$ in J/ψ photoproduction is extracted. The J/ψ event selection has been previously described in Section 4.3. From the J/ψ candidates shown in Figure 4.4 those events were selected that have been taken on the polarised hydrogen target and fulfil the additional data quality requirements for the beam and target polarisation as explained in Section 6.1.2. A signal of about 20 J/ψ events combined from both years and decay channels was found in the polarised data. Figure 6.3 shows the invariant mass distributions for the selected events *separately* per spin state of beam and target. In the figure the invariant mass distributions are shown separately for the decay channel $J/\psi \to e^+e^-$ (top), $J/\psi \to \mu^+\mu^-$ (middle), and for both channels combined (bottom). A Gaussian function is fitted to the mass peak and the combinatorial background is described by an exponential function. The number of events $N^{\overrightarrow{\Rightarrow}(\overrightarrow{\Leftarrow})}$ per spin state is determined from the integral of the Gaussian within a $2\,\sigma$ mass window. Despite the small statistics, the fits are rather stable.

The sample of J/ψ candidates within the $2\,\sigma$ signal region contains an about 15% inseparable contribution from combinatorial background originating mainly from misidentified semi-inclusive events or misidentified hadrons from other decaying particles. This background is taken into account by the fit of an exponential. Since this fit is performed separately per spin state, the number of J/ψ events $N^{\overrightarrow{\Rightarrow}(\overrightarrow{\Leftarrow})}$ is automatically corrected for a possible background asymmetry.

Using Equations 6.6 and 6.7 the asymmetry $A_{\parallel}^{J/\psi}$ and its statistical uncertainty were calculated. Figure 6.4 shows the obtained asymmetry $A_{\parallel}^{J\psi}$ separately for both decay channels and for both decay channels combined. The asymmetry for the decay channel $J/\psi \to e^+e^-$ is positive, and it is negative for the decay channel $J/\psi \to \mu^+\mu^-$. For both decay channels combined a negative asymmetry of $A_{\parallel}^{J/\psi} = -0.8 \pm 0.5$ is obtained. The experimental accessible asymmetry $A_{\parallel}^{J/\psi}$ can be related to the the virtual photon asymmetry $A_1^{J/\psi}$ by the approximation (cf. Equation 6.15)

$$A_1^{J/\psi} \sim \frac{A_{\parallel}^{J/\psi}}{D}, \tag{6.9}$$

with D the photon depolarisation factor from Equation A.43. From Monte Carlo simulations an average $\langle D \rangle = 0.96$ has been determined for J/ψ production at HERMES. Consequently, the virtual photon absorption asymmetry $A_1^{J/\psi}$ is about equal to the experimental asymmetry $A_{\parallel}^{J/\psi}$.

For an asymmetry measurement the available statistics of J/ψ events is extremely small and the determination of $A_1^{J/\psi}$ is statistically limited. Since both the large negative and the large positive values are consistent with a zero average it can be concluded that within the available statistics no further systematic studies are possible. Both J/ψ decay channels originate from the same production mechanisms, thus there is no physical argument for having different asymmetries. In the cross section analysis no systematic difference between the two decay channels was observed, although the triggers used for detection and their event selection requirements are rather different.

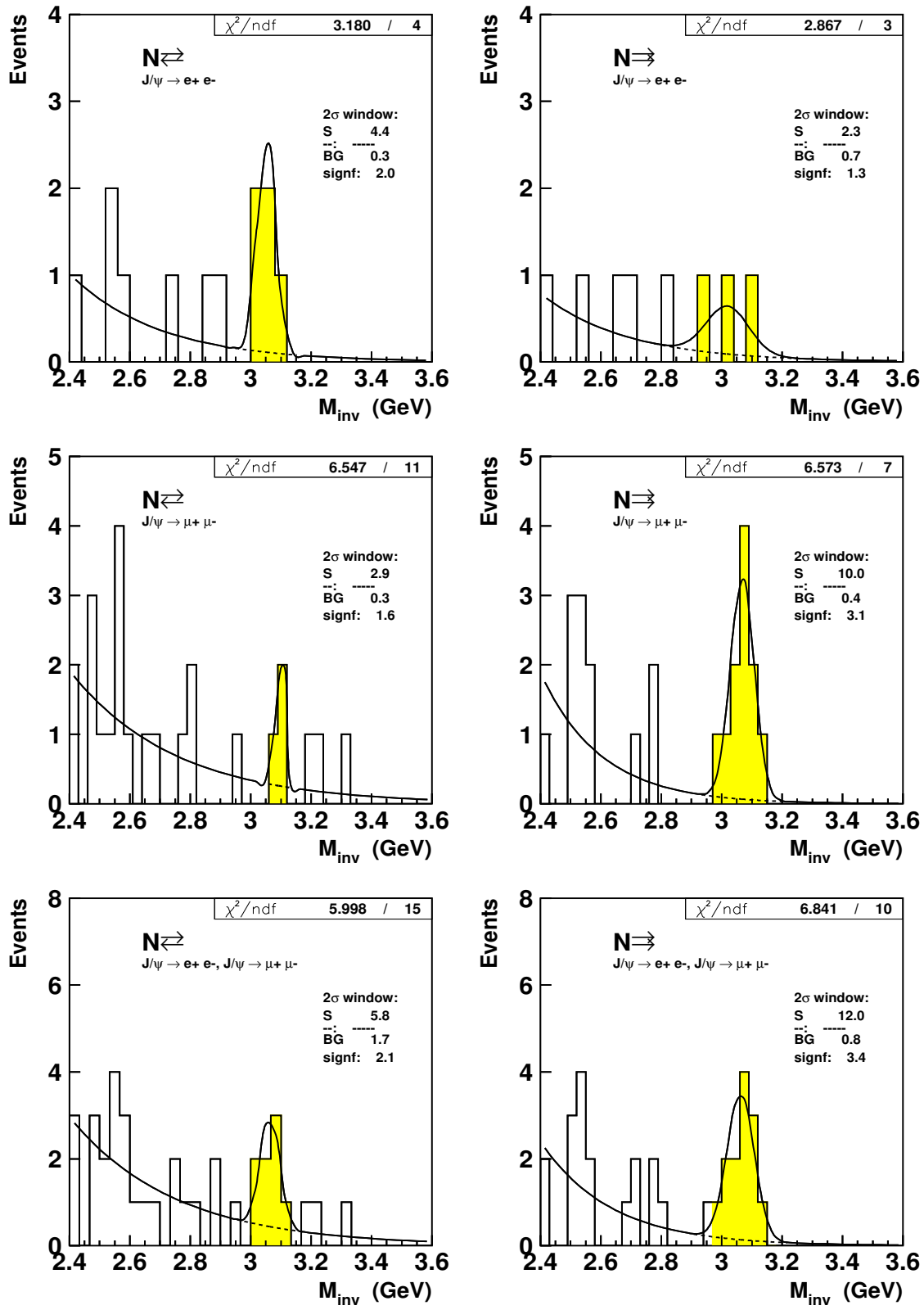

Figure 6.3.: Spin separated mass fit for the decay channel $J/\psi \rightarrow e^+e^-$ (top) , $J/\psi \rightarrow \mu^+\mu^-$ (middle) and for both decay channels combined (bottom).

The different asymmetries for both decay channels cannot be explained by different background contributions, since the number of events is corrected for background by the spin separated mass fit. Additionally, the fraction of background events is too small to cause such a large difference. Therefore it was concluded that the $2\,\sigma$ deviation between the two J/ψ decay channels is a statistical fluctuation. The final asymmetry value of $A_1^{J/\psi} = -0.8 \pm 0.5$ deviates $1.6\,\sigma$ from zero. Since for the J/ψ the scattered positron is not detected this asymmetry includes the inseparable contribution of inelastic processes.

In summary, the present data sample does not allow yet a statistically significant measurement of $A_1^{J/\psi}$ nor even its restriction between the limits $-1 < A_1^{J/\psi} < 1$. With the given statistical significance only an asymmetry of $A_1^{J/\psi} = 1$ is excluded with more than 3σ.

This analysis has proven that the HERMES experiment is in principle able to measure double–spin asymmetries in J/ψ production. In the years 1998 to 2000 HERMES collects data using mainly a polarised deuterium target. This data will increase the statistics available for an asymmetry measurement by one order of magnitude with respect to the present data sample. Therefore it will allow a significant measurement of $A_1^{J/\psi}$.

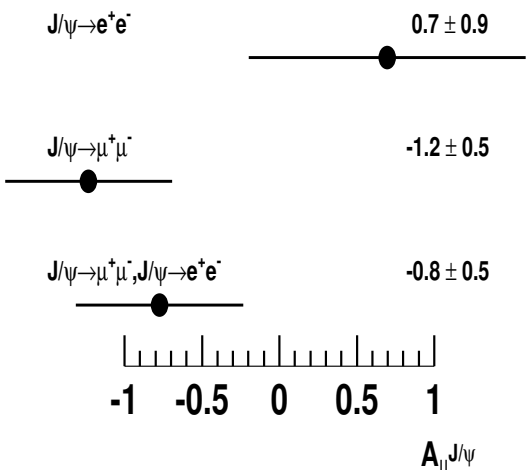

Figure 6.4.: Asymmetry $A_{||}^{J/\psi}$ from spin separated mass fit separately for both decay channels and both decay channels combined. Note that for J/ψ production at HERMES $A_{||}^{J/\psi} \approx A_1^{J/\psi}$ since $D \approx= 1$

6.3. Event Selection for Exclusive ρ Mesons

In the following section the event selection used for the analysis of double–spin asymmetries in exclusive ρ vector meson production will be discussed. The ρ meson is observed by its two–body decay $\rho \to \pi^+\pi^-$ with a 100% branching ratio. In contrast to the analysis of J/ψ production at HERMES, the scattered positron is always detected in addition to the ρ meson decay products and the event kinematics can be fully determined. Table 6.2 summarises the event selection criteria used.

Event Topology In an exclusive process only the decay products of the vector meson have to be identified besides the scattered positron. Therefore only events with exactly three tracks, namely two opposite charged hadrons and a positron are selected. The elastically scattered target proton cannot be detected.

Particle Identification The particle identification scheme PID3+PID5 is used to distinguish between hadrons and positrons. As in the case of the J/ψ, the PID requirements are sufficient to separate a clear signal.

	$\rho \to \pi^+\pi^-$
Topology	Require exactly three tracks: h^+, h^-, e^+
PID	Hadron: PID3+PID5 < 0
	Lepton: PID3+PID5 > 0
Kinematic Cuts	$0.62 < M_{inv}(\pi^+, \pi^-) < 0.92$ GeV^2
	$-.6 < \Delta E < .6$ GeV
	$-t' < 0.4$ GeV^2
	$9 < \nu < 20$ GeV
Vertex and Acceptance Cuts	$\lvert z_{h^\pm} - z_{e^+}\rvert < 20$ cm
	$d\,(h^\pm, \mathrm{beam}) < 2$ cm
	$\lvert zvx_{e^+}\rvert < 18$ cm
	$d\,(e^+, \mathrm{beam}) < 0.75$ cm
	$\lvert\theta_y^{e^+}\rvert > 0.04$ mrad

Table 6.2.: Summary of event selection criteria for exclusive ρ vector mesons.

Event Kinematics The invariant mass spectrum for the decay $\rho \to \pi^+\pi^-$ is shown in Figure 6.5. To select ρ candidates a cut on the reconstructed invariant mass of the hadron pair is used, indicated by the shaded area. The cut on the invariant mass excludes the background of miss-reconstructed ϕ events which appear as the small peak on the left side of the spectrum.

In an exclusive process no energy is transfered to the target, i.e. there is no missing energy ($\Delta E = 0$). A clear peak at zero can be seen in the ΔE distribution shown in Figure 6.5; the shaded area marks the events used for analysis. Events with non–zero ΔE values represent background from non–exclusive processes that will be discussed in Section 6.5.

The cross section for diffractive vector meson production falls exponentially with $-t'$. Since non-diffractive background has a less steep $-t'$ dependence it can be suppressed by a corresponding requirement. Restricting the photon energy $\nu < 20$ GeV forces the energy of the scattered positron to be well above the calorimeter threshold of the trigger and ensures a trigger efficiency close to unity, the $\nu > 9$ GeV cut ensures a good separation of exclusive events by the ΔE cut.

Vertex and Acceptance Cuts Cuts on the vertex of the scattered positron with decay particles are applied to ensure that all particles originate from a common vertex in the target region. These cuts have been explained in Chapter 4.3. One additional cut on the distance of the decay vertex to the beam axis is used. To ensure that the positron, scattered at small angles, is safely within the spectrometer acceptance, a minimum angle θ_y for the positron track is required. As mentioned before, two different methods have been used for the reconstruction of the 1996 and 1997 data on the polarised hydrogen target. Within the scope of the vector meson asymmetry analysis their small differences in efficiency and resolution will be neglected.

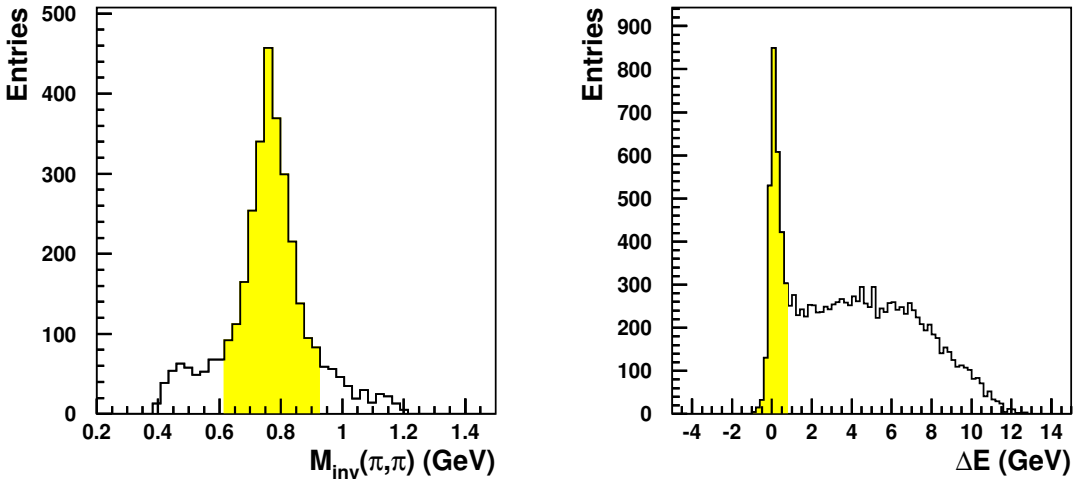

Figure 6.5.: Invariant mass distribution (left) and missing energy ΔE (right) for the decay channel $\rho \to \pi^+\pi^-$ from the combined 1996 and 1997 data on the polarised hydrogen target. The shaded areas mark events that were used for analysis

About 2800 ρ events were selected from the combined 1996 and 1997 data. All of these events are in an unambiguously defined spin state of beam and target, since the data quality criteria for the polarisation analysis of Section 6.1.2 have been applied.

Raw Asymmetry $A_{||}^{\rho}$ in Exclusive ρ Production

The experimental asymmetry $A_{||}^{\rho}$ in exclusive ρ production and its statistical uncertainty were calculated from the number of selected ρ events per spin state using the Equations 6.6 and 6.7. In Figure 6.6 the values of the asymmetry $A_{||}^{\rho}$ are plotted separately for the 1996 and 1997 data as well as combined for both years. On the right side of the plot the numerical values of the asymmetries are given, the integers indicate the number of events per spin state. No correction for the contribution of non–exclusive background was performed for this plot.

For the ρ–meson a significant positive asymmetry is observed which is about 3σ above zero. The data of both years show a consistent result. In contrast to the J/ψ meson, the available statistics of ρ events is large enough to allow for detailed systematic studies that will be discussed in the following sections.

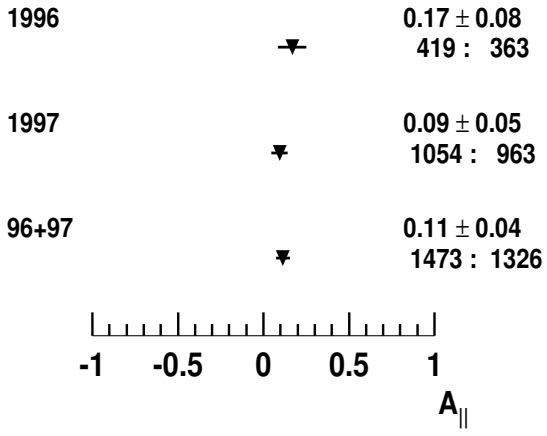

Figure 6.6.: Double spin asymmetry $A_{||}^{\rho}$ separated by year and combined for both years. No background subtraction is performed.

6.4. Comparison of ρ Data to Monte Carlo Simulation

A Monte Carlo generator [BKO:98] for the simulation of diffractive exclusive ρ production has been written in the course of the HERMES analyses of angular distributions and cross sections in exclusive ρ production [HERMES:99c, HERMES:99d]. The main features of the simulation are briefly summarised. Rho events are generated corresponding to the double–differential leptoproduction cross section similar to Equation 4.16 depending on the variables Q^2 and E', where the value of the real–photoproduction cross section $(Q^2 = 0)$ is taken from previous measurements [C$^+$:81]. The photoproduction cross section was generated falling exponentially with t according to Equation 2.10. The events were generated with an invariant mass distribution according to a skewed relativistic Breit-Wigner shape with parameters taken from [RS:66]. The simulation of the detected decay channel $\rho \to \pi^+\pi^-$ follows the angular distributions given by the assumption of SCHC. A more detailed description of the generator can be found in [HERMES:99c].

In the present analysis a simulation of the HERMES spectrometer was performed after the generation of the physics process using the HERMES Monte Carlo simulation package GMC-HMC [DGM$^+$:99]. The two reconstruction methods NOVC and STD were used at a ratio corresponding to the statistics of the 1996 and 1997 data on the polarised hydrogen target. Only the scattering on hydrogen is considered in this analysis. Therefore, only incoherent diffractive scattering on a nucleon is taken into account. Coherent scattering on heavier nuclei which is important for the t distribution was omitted. Figure 6.7 shows

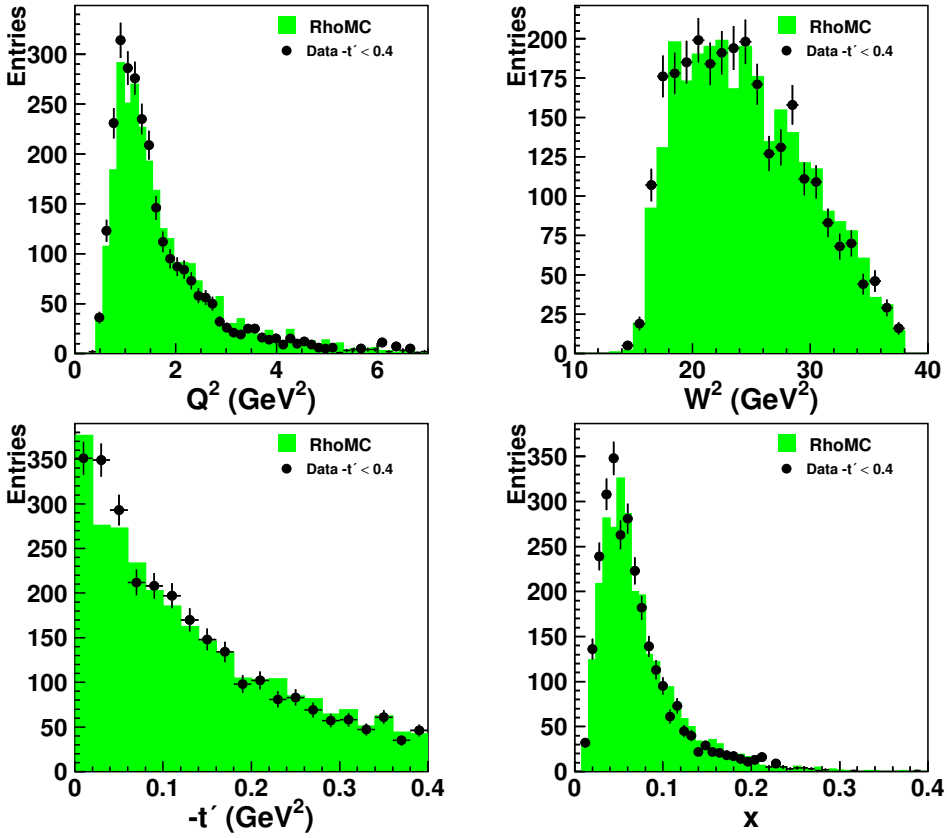

Figure 6.7.: Distribution of the kinematic variables Q^2 (top left), W^2 (top right), $-t'$ (bottom left), and x (bottom right) for the selected ρ data sample (points) in comparison to a ρ Monte Carlo (shaded histograms).

the comparison of the selected ρ data sample (points) to the Monte Carlo simulation (histograms) for several kinematic variables. Here, the Monte Carlo simulation was normalised to the number of events in the data sample. The kinematic distributions of the data are well reproduced by the Monte Carlo.

For exclusive ρ production at HERMES, the average values for these kinematic variables within the event selection requirements are obtained from data as:

$$\begin{aligned} \langle W^2 \rangle &= 24\ \mathrm{GeV}^2, \quad \langle Q^2 \rangle &= 1.7\ \mathrm{GeV}^2, \\ \langle -t' \rangle &= 0.1\ \mathrm{GeV}^2, \quad \langle x \rangle &= 0.07. \end{aligned} \tag{6.10}$$

The Q^2 range of the data extends to values as large as 6 GeV^2, values of Q^2 below 0.5 GeV^2 are cut off by the spectrometer acceptance for the required scattered positron. The t' distribution in figure 6.7 is similar to the distribution of the variable t (not shown) since for the exclusive process $t' \sim t$ (cf. Section 2.1.1).

6.5. Treatment of Background in ρ Data Sample

In non–exclusive processes, which appear as a background to exclusive vector meson production, energy is transfered to the target. As can be seen in the ΔE distribution of Figure 6.5 this background appears at non–zero values of ΔE. In the region of the elastic peak ($\Delta E \sim 0$) this non-exclusive background is not separable on an event–by–event basis. Its main contribution is combinatorial background from deep–inelastic scattering. Its subtraction from the ρ data sample will be discussed in detail below.

The ϕ meson decay $\phi \rightarrow K^+K^-$ appears as a small peak in the $M_{\pi^+\pi^-}$ invariant mass distribution of Figure 6.5 below 0.6 GeV and is excluded by the ρ event selection. The background of diffractive ρ production with dissociation of the target nucleon can be effectively suppressed by the ΔE cut. A contribution of this background of less than $6 \pm 2\%$ to the ρ data sample within the $|\Delta E| < 0.6$ GeV selection cut has been estimated [HERMES:99c] based on previous measurements [E665:97]. Except for the dissociation of the proton target, this process is similar to the exclusive process in question. The contributions of non–resonant elastic pion–pair production and the ω meson decay $\omega(783) \rightarrow \pi^+\pi^-$ (branching ratio 2.2%) cannot be separated in principle; for the present analysis both contributions remain within the ρ sample.

Radiative corrections to the diagram shown in Figure 2.1 have been estimated to yield a 20% correction to the measured ρ production cross section [Aku:97]. The size of the radiative effects is constant over the entire Q^2 range of the experiment. The radiative effects cause a smearing of the ΔE distribution that reduces the statistics within the ΔE event selection requirement. The spin dependence of the radiative processes is expected to be negligible [Aku:99]. Therefore, radiative effects do not affect the measured asymmetry itself.

In the present analysis, the exclusive ρ event sample was corrected for combinatorial background from deep–inelastic scattering with a Monte Carlo simulation. In the later systematic studies, the spin asymmetries in ρ production will be extracted using two additional data based methods of background subtraction to evaluate the influence of the background to the asymmetries. All three methods of background subtraction, denoted by I,II and III, will be explained in the following sections. In addition the raw asymmetries will be extracted using no background subtraction at all (denoted by IV)).

Method I: Background Subtraction with DIS Monte Carlo Simulation

For the subtraction of background from deep–inelastic scattering simulated Monte Carlo DIS events from the standard HERMES [Vol:99] Monte Carlo productions were used. The DIS event generation is based on the LEPTO [IGS:81] generator; subsequently a full simulation of the HERMES spectrometer [DGM$^+$:99] and the reconstruction of the Monte Carlo events were performed.

These Monte Carlo events are subject to the exclusive ρ event selection criteria yielding a ΔE distribution shown by the histogram in Figure 6.8 in comparison to the data (points). The ΔE distribution of DIS Monte Carlo simulation is normalised to the data with only the events in the region of the non–exclusive background at large missing energy $\Delta E > 3$ GeV. The shaded area marks the events within the $|\Delta E| < 0.6$ GeV event selection requirement used for analysis. As can be seen, deep–inelastic scattering is the dominant contribution to the non–exclusive background. The contamination to the ρ data sample within the signal region $|\Delta E| < 0.6$ GeV does not exceed 10%.

Figure 6.9 shows the data sample (points) after the normalised DIS Monte Carlo events are subtracted in comparison to the ΔE distribution of the ρ Monte Carlo (histogram). The Monte Carlo distribution is normalised to the data within the shaded $|\Delta E| < 0.6$ signal region. Figure 6.8 and 6.9 contain all available ρ events. As can bee seen from Figure 6.9,

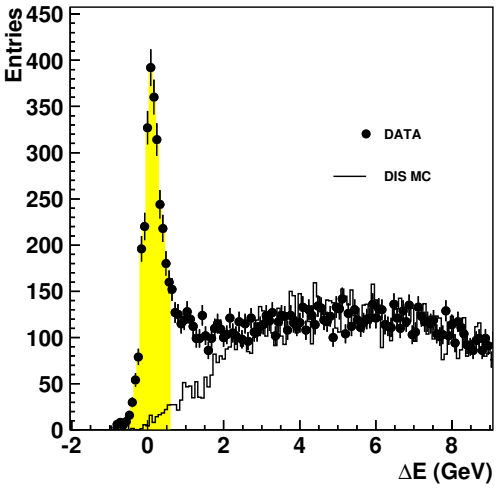

Figure 6.8.: Distribution of ΔE for data (points) and the events from the DIS Monte Carlo simulation (histogram). The shaded area marks the region that is used for analysis

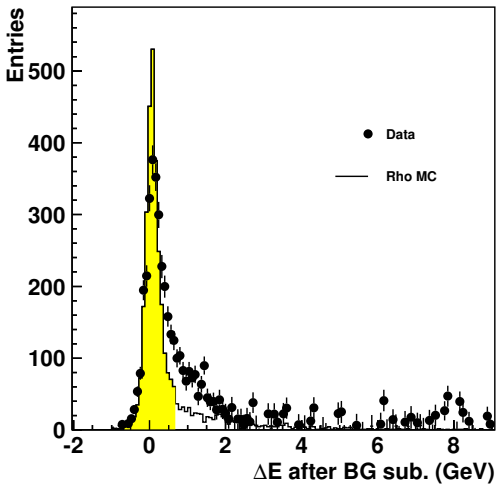

Figure 6.9.: Distribution of ΔE for the data after DIS background subtraction (points) in comparison to the ρ Monte Carlo (histogram). For explanation see text.

the position of the elastic peak in the data after the subtraction of the DIS background is well described by the ρ Monte Carlo simulation. The data shows a small tail in the ΔE distribution that is not fully reproduced by the Monte Carlo simulation. This deviation is attributed to the fact that the ρ Monte Carlo simulates only exclusive ρ production. Other processes that cause a smearing of the ΔE distribution to non–zero values, such as proton dissociation or radiative effects, are not yet included in this generator. Nevertheless, within the selected signal region $|\Delta E| < 0.6$ GeV indicated by the shaded area, the agreement between data and Monte Carlo is satisfactory.

Method II: Background Subtraction with Data at high $-t'$

The cross sections of non–diffractive processes have a less steep $-t'$ dependence than the cross section of the diffractive process. Consequently, the data at higher values of $-t'$ is dominated by non–diffractive background, i.e. background from deep–inelastic scattering events. Figure 6.10 shows the $-t'$ dependence of events within the $|\Delta E| < 0.6$ GeV signal region (full circles) compared to the one of background events at large $\Delta E > 3$ GeV (open circles), both distributions are normalised to one.

The points in Figure 6.11 show the ΔE distribution for the data events within the ρ selection requirements which include a cut $-t' < 0.4$ GeV^2 (cf. Table 6.2). The histogram in Figure 6.11 shows the ΔE distribution for events at high $-t' > 0.7$ GeV^2. It is normalised to the data at $-t' < 0.4$ GeV^2 using only the events in the region of non–exclusive background at $\Delta E > 3$ GeV. The ΔE distribution of the events at high $-t' > 0.7$ GeV^2 has a similar shape than the ΔE distribution of the DIS Monte Carlo event sample in Figure 6.8. The normalised events at $-t' > 0.7$ GeV^2 are subtracted from the data at $-t' < 0.4$ GeV^2, hence correcting for the dominant background contribution from DIS.

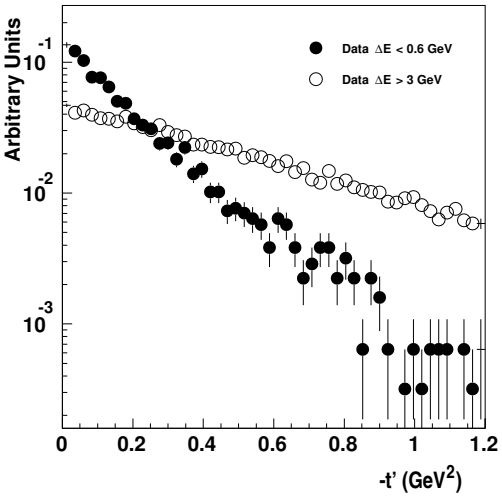

Figure 6.10.: Distribution of $-t'$ for the exclusive ρ data sample at $|\Delta E| < 0.6$ GeV (full circles) in comparison to non–exclusive background at high $\Delta E > 3$ GeV (open circles).

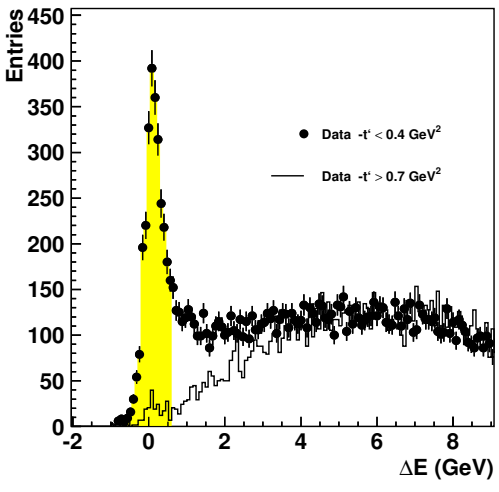

Figure 6.11.: Data at low $-t' < 0.4$ GeV^2 (points) and data at high $-t' > 0.7$ GeV^2 (histogram); both distributions are normalised to each other with events at $\Delta E > 3$ GeV.

In Figure 6.12 the ΔE distribution of the data at $-t' < 0.4$ GeV^2 after the background subtraction (points) is compared to the ΔE distribution of the ρ Monte Carlo, where the latter is normalised to the data within the shaded $|\Delta E| < 0.6$ GeV signal region. The background corrected data show a tail towards higher values of ΔE similar to the DIS Monte Carlo based method I. But here the deviation between data and the ρ Monte Carlo simulation becomes more apparent.

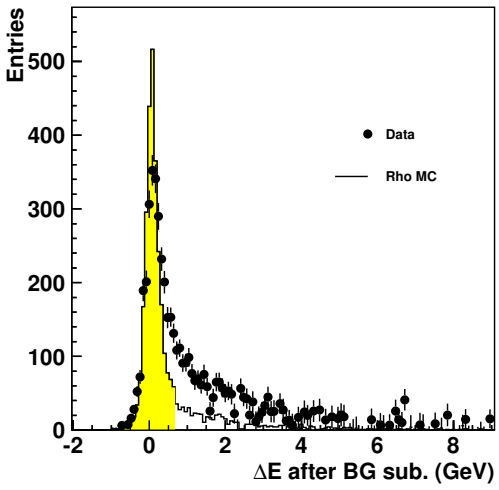

Figure 6.12.: Rho data sample after background subtraction (points) compared to ρ Monte Carlo (histogram). Both distributions are normalised within $|\Delta E| < 0.6$ GeV.

It can be seen in Figure 6.11 that within the $|\Delta E| < 0.6$ GeV signal region a small fraction of exclusive ρ events remains in the background model and is subtracted from the signal. This small elastic peak vanishes with higher values of the $-t'$ cut for the selection of background events, but at the same time the statistical uncertainty of the background correction increases. It has been checked that this imperfection of the background method has no significant influence on the extracted asymmetry. As an example, for the bottom left plot in Figure 6.15, which will be discussed in Section 6.6.1, the $-t'$ cut to select background events was raised $-t' > 1$ GeV^2.

Method III: Background Subtraction by a Fit to the ΔE-Distribution

The third background subtraction method is based on an empirical fit to the missing energy spectrum of the data. This fit is shown by the solid line in Figure 6.13 for the full 1996 and 1997 data set. The peak of exclusive ρ events is described by a Gaussian that is integrated over the range of $0 < |\Delta E| < 0.6$ GeV to determine the number of events. This range, indicated by the shaded area in Figure 6.13, corresponds approximately to a 2σ width of the Gaussian. Similar to the 2σ window of the invariant mass fit which was used for the J/ψ analysis in Section 4, the 2σ range in the ΔE fit gives the highest significance of the signal over the background. The exclusive peak in the ΔE distribution is somewhat better described by a Landau function, but it turned out that the fit of Gaussian is more stable, therefore the latter was used for the analysis. It was checked that both descriptions of the exclusive peak yield similar results. The non–exclusive background is described by a parameterisation of the form

$$f(\Delta E) = \Delta E \cdot \exp\{-\sqrt{\Delta E}\} \tag{6.11}$$

that is indicated by the dotted line in Figure 6.13. This empirical background shape was found by detailed systematic studies that included other exponential functions and higher order polynomials. Besides the reduced χ^2's which are in general about 1.5, the stability of the fit was an important selection criterion for the background parameterisation.

In Figure 6.14 the data after the background subtraction by the ΔE fit method (points) are compared to the ρ Monte Carlo simulation (histogram). As can be seen, data and Monte

Carlo are well matched. Thus, this empirical background correction also removes the background contribution that is not described by the DIS Monte Carlo simulation.

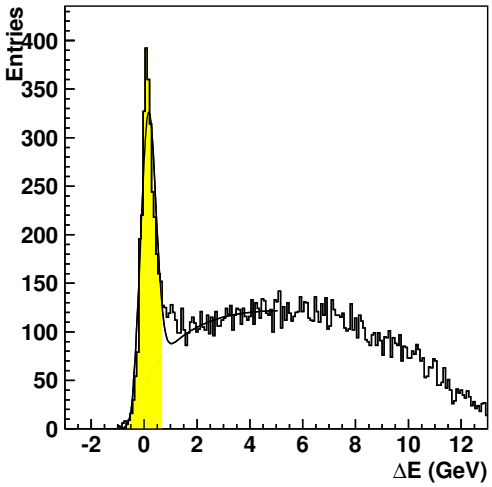

Figure 6.13.: Fit to the ΔE spectrum, the elastic peak is described by a Gaussian (solid line), the background by an exponential (dotted line).

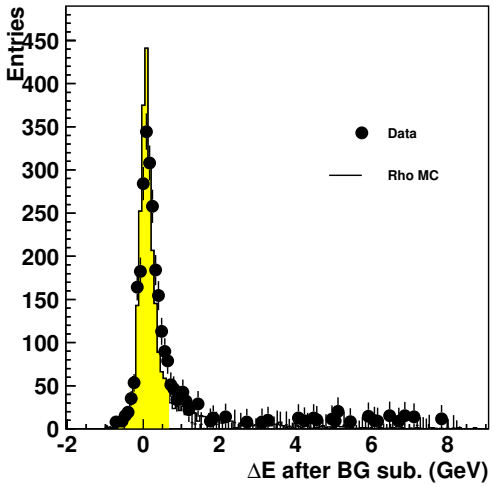

Figure 6.14.: Exclusive ρ sample after background subtraction via a fit to the ΔE spectrum compared to the ρ Monte Carlo.

In the asymmetry analysis the data shown in Figure 6.13 is separated by spin state and divided into several kinematic bins, i.e. into small sub–samples. The shape of background distribution as well as the signal–over–background ratio varies from bin to bin. In addition, the shape of the ΔE distribution in Figure 6.13 is rather complicated and the fit of a Gaussian plus an exponential function is not well constrained at $\Delta E \sim -1$. Therefore, the stability of each fit had to be checked by hand. This background correction method is less stable against variations, e.g. the chosen fit range in ΔE, in comparison to the previously discussed methods I and II.

6.6. Experimental Asymmetry $A_{||}^{\rho}$ in Exclusive ρ Production

6.6.1. Systematic Studies on $A_{||}^{\rho}$

The stability of the experimental asymmetry $A_{||}^{\rho}$ in exclusive ρ production has been extensively tested. For the systematic studies all three methods of background subtraction were used: I) background subtraction using the DIS Monte Carlo simulation, II) using data at high $-t'$, and III) the empirical fit to the ΔE distribution. In addition the raw asymmetries (denoted by IV) are extracted using no background correction as already shown in Figure 6.6.

The asymmetries and their statistical error are calculated using Equations 6.6 and 6.7. As it was done with the invariant mass fit for the J/ψ, each method of background correction is applied separately per spin state in each bin. Therefore, the number of events per spin state $N^{\overrightarrow{\rightarrow}(\overrightarrow{\leftarrow})}$ is corrected for a possible asymmetry of the background. For each background correction method the statistical error of the method is propagated into the statistical error of the asymmetry.

Figure 6.15 shows the asymmetry $A_{||}^{\rho}$ versus the variation of event selection cuts. In the top left plot of Figure 6.15 an example for the variation of a geometrical acceptance cut is shown: the cut on the position of the ρ decay vertex is varied around the value of $|zvx_{\rho}| < 20$ cm that is used for the analysis and corresponds to the length of the target cell. In addition, other acceptance cuts and the particle identification criteria have been checked, and no significant dependence of $A_{||}^{\rho}$ was found.

The grey band at the bottom of the plot denotes the experimental systematic uncertainty of 6% of the measured asymmetry due to the measurements of the beam and target polarisations. It will be discussed below.

The other three plots of Figure 6.15 show the dependence of $A_{||}^{\rho}$ on the variation of kinematic event selection cuts. These kinematic cuts are of special interest since they control the relative amount of background in the data sample to some extent. In the top right plot the variation of the used $|\Delta E|$ range is shown. A less stringent cut on $|\Delta E|$ leaves more non–exclusive events on the right side of the exclusive peak in the data sample (cf. Figure 6.5). The same is true for a less stringent cut on $-t'$, the variation of the $-t'$ cut is shown in

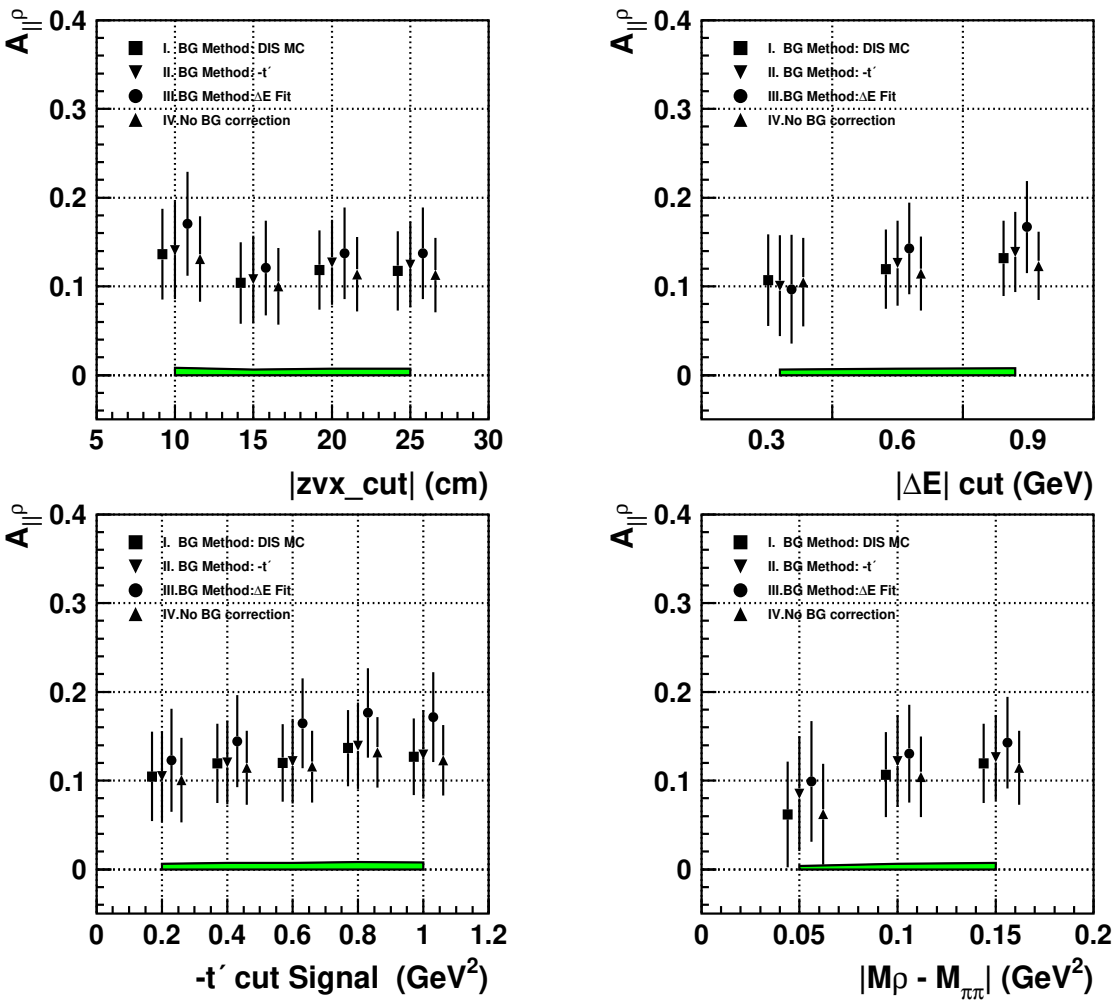

Figure 6.15.: Stability of asymmetry $A_{||}^{\rho}$ versus variation of geometrical cut on the ρ vertex position (top left), and versus variation of kinematic cuts: on the missing energy range $|\Delta E|$ (top right), on the four–momentum transfer $-t'$ (bottom left), and on the invariant mass range $|M_{\rho} - M_{\pi\pi}|$ (bottom right). For discussion see text.

the bottom left plot. For this plot, the $-t'$ cut to select the background events in the subtraction method II has been raised to $-t' > 1$ GeV^2 and no significan effect on the asymmetries of method II can be seen. The variation of the range in the reconstructed invariant mass $|M\rho - M_{\pi\pi}|$ around the nominal ρ mass is shown in the bottom right plot. From the invariant ρ mass distribution in Figure 6.5 it can be seen that the tight cut of $|M_\rho - M_{\pi\pi}| < 0.05$ GeV^2 removes a significant part of the statistics. Consequently, the spread between the asymmetry values obtained with the four different methods of background treatment becomes larger. The invariant mass range was not extended to larger values to avoid the background from misidentified Φ's. In summary, the variations of $A_{||}^{\rho}$ are small and no significant dependence on the specific choice of the event selection criteria could be observed within the statistical uncertainties. The asymmetry is a stable effect.

Figure 6.16 shows the asymmetry $A_{||}^{\rho}$ in separate bins of the missing energy ΔE. For this plot no background corrections have been performed. Around the peak of exclusive ρ events at $(\Delta E = 0)$ GeV the asymmetry is positive. It drops to zero for non-exclusive background at higher missing energy $\Delta E > 1$ GeV. The high value at $\Delta E \sim 2.5$ GeV is interpreted as a statistical fluctuation.

In Figure 6.17 the asymmetry $A_{||}^{\rho}$ is plotted separately for the 1996 and 1997 data sample and combined for both data taking periods. Both years yield consistent results within the statistical uncertainty. The most right bin in this Figure gives the asymmetry for the total data sample.

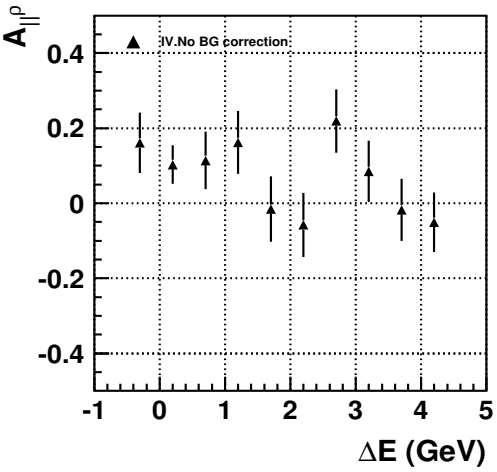

Figure 6.16.: Binning in ΔE; $A_{||}^{\rho}$ is positive around the elastic peak at $\Delta E = 0$ GeV and drops to zero for non-exclusive background at $\Delta E > 1$ GeV.

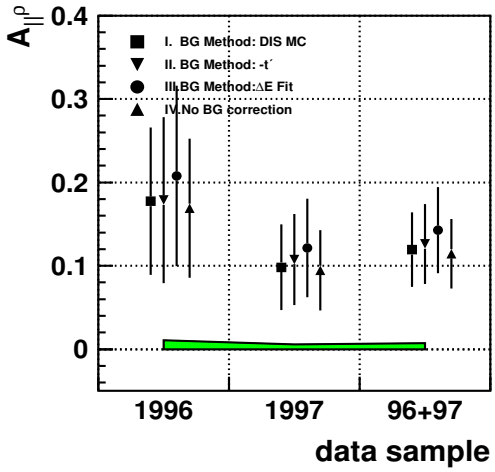

Figure 6.17.: Asymmetry $A_{||}^{\rho}$ separated for the 1996 and 1997 data taking period and for both years combined.

The raw asymmetry values obtained without subtraction of background in Figures 6.15 and 6.17 (denoted by IV) are slightly lower than the asymmetries obtained with any of the three different background subtraction methods. This suggests that background with no or only a small double–spin asymmetry is removed. The asymmetry values obtained with method II using the fit to the ΔE spectrum appear slightly higher than the asymmetries obtained with the other methods. This can be attributed to the fact that this method also removes background which is not described by the DIS Monte Carlo used in method I. On the other hand it is not possible to separate such an effect from the higher uncertainty of method III caused by the fit procedure.

		$A_{\parallel}^{\rho}$	Significance
I	BG Method using DIS Monte Carlo	0.119 ± 0.045	2.6 σ
II	BG Method using Data at High $-t'$	0.126 ± 0.048	2.6 σ
III	BG Method using ΔE Fit	0.143 ± 0.052	2.8 σ
VI	No Background Subtraction	0.114 ± 0.042	2.7 σ

Table 6.3.: Asymmetry $A_{\parallel}^{\rho}$ and its statistical significance for the 1996+1997 data set for all three methods of background correction. In addition the raw asymmetry using no background correction is given.

In Table 6.3 the values of the asymmetry $A_{\parallel}^{\rho}$ for the combined 1996+1997 data are listed for all three methods of background subtraction and for no background subtraction. In addition, the significance $A_{\parallel}^{\rho}/\delta(A_{\parallel}^{\rho})$ of the non–zero asymmetry is given in units of statistical uncertainty.

Between the three very different background subtraction methods no significant systematic difference can be seen within the statistical uncertainty. From the good agreement between the three methods of background subtraction with the raw asymmetry it is concluded that a possible contribution of the background to the asymmetry $A_{\parallel}^{\rho}$ is small compared to the statistical uncertainty.

Therefore, only the contributions from the polarisation measurements of beam and target are assigned as experimental systematic uncertainties to the asymmetry measurement, indicated by the grey bands in Figure 6.15 to 6.17. This uncertainty is obtained by adding the separate systematic uncertainties of the beam and target polarisation measurements (cf. Sections 3) in quadrature. It is 6% of the measured asymmetry for the combined 1996+1997 data.

For the further analysis the background correction method I, based on the LEPTO Monte Carlo simulation, has been chosen since it appears to be the cleanest method. Moreover, in comparison to the other two background subtraction methods it has the largest potential for improvement in future analyses when better Monte Carlo descriptions of the data become available.

6.6.2. Dependence of $A_{\parallel}^{\rho}$ on Kinematic Variables

Compared to the measurement of the inclusive asymmetry in deep–inelastic scattering, which uses up to 10^5 DIS events per spin state and bin for the analysis of the spin structure function g_1, the available statistics of about 2800 ρ events is rather limited. Still, the statistics is sufficient to investigate the dependence of the asymmetry $A_{\parallel}^{\rho}$ on kinematic variables. In Figure 6.7 of Section 6.4 the distributions of the kinematic variables Q^2, W^2, $-t'$, and x were shown for the selected ρ data sample. Three bins containing about equal statistics have been defined for each variable. In Table 6.4 the boundaries, the mean, the number of ρ events before background correction, the asymmetry value and its statistical uncertainty are listed for each bin. Separation of the data into four or five bins has been tried, but the statistical uncertainties per bin become too large for reasonable conclusions.

In Figure 6.18, the dependence of the asymmetry $A_{\parallel}^{\rho}$ on the kinematic variables Q^2, W^2, $-t'$, and x is shown. The shaded band at the bottom of the plots indicates the experimental systematic uncertainty from the beam and target polarisation measurements. Most interesting are the dependencies of the spin asymmetry $A_{\parallel}^{\rho}$ on the variables Q^2 and W^2 since the HERMES data are lying in the transition region from soft to hard models of diffractive vector meson production, as discussed in Section 2.1.7. One may interpret a 'trend' to higher asymmetries with increasing Q^2 and $-t$ as well as a 'trend' to lower asymmetries with increasing W^2 and x. Still, within the statistical uncertainty of the measurements no significant dependence on any of the kinematic variables can be seen. The asymmetry is positive and stable.

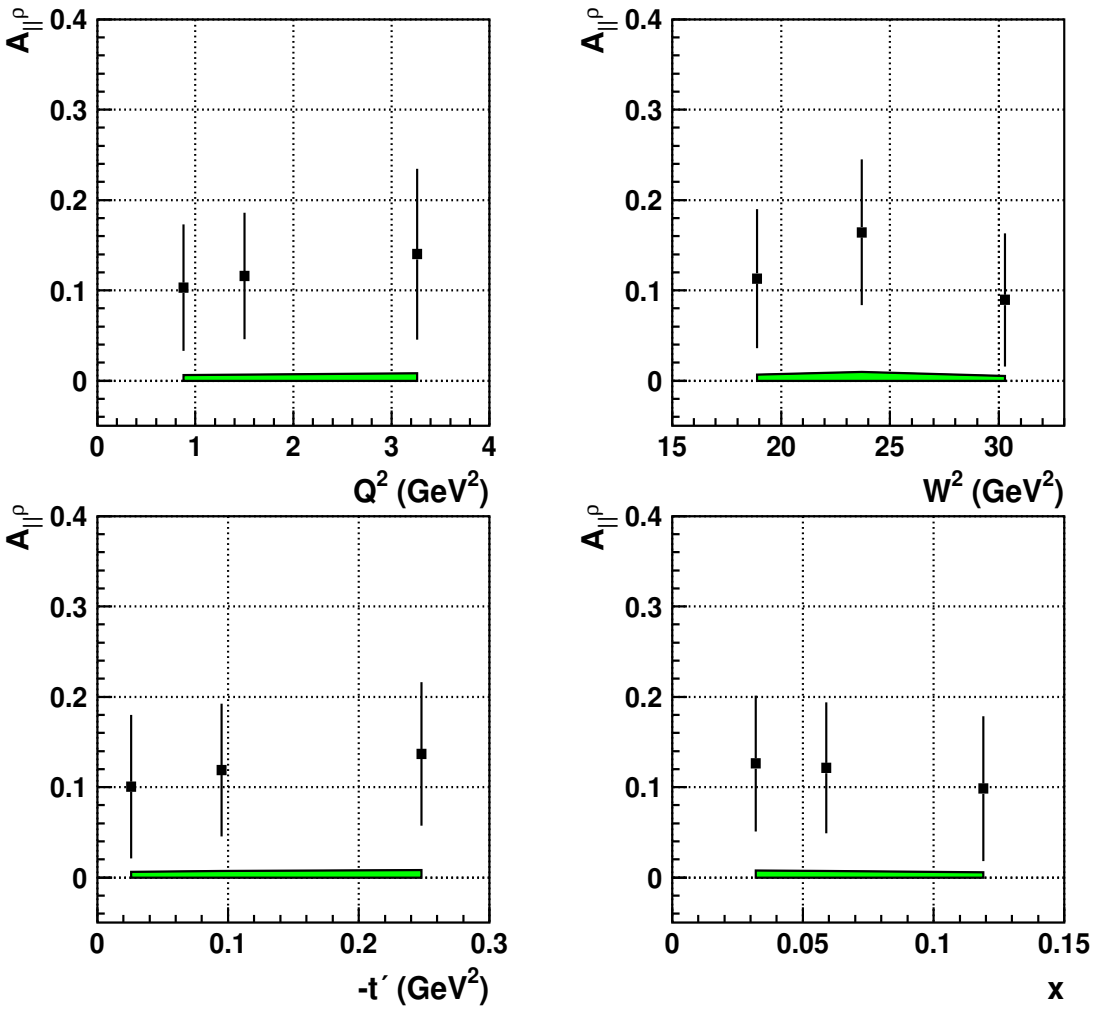

Figure 6.18.: Dependence of the spin asymmetry $A_{\parallel}^{\rho}$ on the kinematic variables Q^2 (top left), W^2 (top right), $-t'$ (bottom left), and x (bottom right). The band indicates the experimental systematic uncertainty.

6.7. Photon Absorption Asymmetry A_1^ρ in Exclusive ρ Production

6.7.1. Determination of A_1^ρ

Within the formalism of asymmetry analysis in deep–inelastic scattering (see Appendix A.4) the longitudinal photon absorption asymmetry A_1 is related to the experimental asymmetry $A_{||}$ and the transverse asymmetry A_2 by

$$A_1 = \frac{A_{||}}{D} - \eta A_2. \tag{6.12}$$

The kinematic factor η is given in Equation A.44 and the photon depolarisation factor D will be discussed below. In the following, the general definition of Equation 6.12 will be adopted for the determination of the photon–nucleon asymmetry A_1 in exclusive vector meson production.

Photon Depolarisation Factor D and Ratio R

The photon depolarisation factor D is given by

$$D = \frac{1-(1-y)\,\epsilon}{1+\epsilon R}, \tag{6.13}$$

with ϵ the ratio of fluxes for longitudinal and transverse photons from Equation A.36. For the calculation of D the ratio $R = \sigma_L/\sigma_T$ of the absorption cross sections for longitudinal and transverse photons is required. In deep–inelastic scattering, the ratio R^{DIS} can be expressed in terms of unpolarised structure functions (cf. Equation A.33). A parameterisation of R^{DIS} was obtained from a fit to world data on deep–inelastic scattering over a wide kinematic range [W$^+$:90, E143:99]; it yields a flat distribution and varies between 0.2 and 0.4.

In exclusive vector meson production, the ratio R can be related to the spin density matrix element r^{04}_{00}, measured via angular distributions. This measurement was performed for exclusive ρ production at HERMES and was reviewed in Section 5.1.1. Figure 5.3 shows the HERMES results on R^ρ in comparison to world data. The ratio R^ρ increases with Q^2 and becomes larger than unity above $Q^2 \geq 3$ GeV^2.

Figure 5.3 additionally shows the parameterisation of R^ρ from Equation 5.10. This parameterisation, with the parameters obtained for the energy range $W < 10$ GeV, is used here for the calculation of D in ρ production. The statistical and systematic uncertainties of the parameterisation are neglected in this analysis. The photon depolarisation factor D is calculated per event. For the determination of A_1^ρ in a certain bin the average D value from all events within this bin is used.

For comparison, in Figure 6.19 the distributions of D for the exclusive ρ data sample are shown when calculated with the parameterisation R^ρ of Equation 5.10 (solid line) and when calculated with R^{DIS} of Reference [W$^+$:90] (dashed line). The average value of D of 0.40 using R^ρ is about 20% smaller than 0.47 when using R^{DIS}.

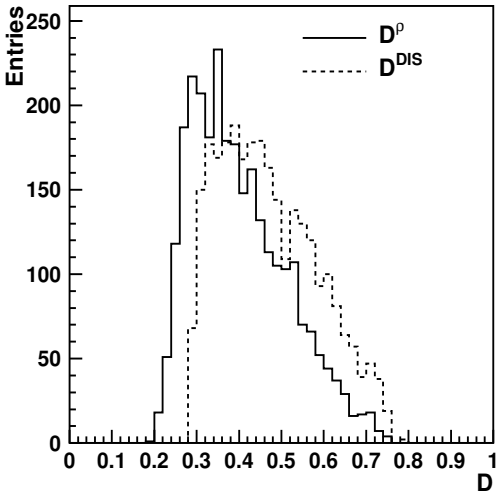

Figure 6.19.: Comparison of the photon depolarisation factor D from Equation A.43 calculated with R^{DIS} from Reference [W$^+$:90] and calculated with the parameterisation of Equation 5.10 for R^ρ.

Systematic Uncertainty from the Unknown Transverse Asymmetry A_2^ρ

In deep–inelastic scattering, the transverse asymmetry A_2 was measured to be positive but close to zero [SMC:97, E143:98]. In Equation 6.12 it is further suppressed by the small kinematic factor η. Therefore the contribution from A_2 is often neglected in the analysis of the spin structure function g_1. In contrast, for vector meson production the asymmetry A_2^ρ is completely unknown. It is only restricted by the positivity limit (cf. Appendix A.4)

$$A_2^\rho \leq \sqrt{R} \tag{6.14}$$

It was discussed above that the ratio R becomes larger than unity with increasing Q^2. In this case, the asymmetry A_2^ρ is restricted by its maximum possible value $|A_2^\rho| \leq 1$.

Since A_2^ρ is unknown, the photon absorption asymmetry A_1^ρ is obtained from the experimental aymmetry $A_{||}$ by the approximation

$$A_1^\rho \sim \frac{A_{||}^\rho}{D}. \tag{6.15}$$

In order to take a possible non–zero transverse asymmetry A_2^ρ in exclusive ρ production into account, its contribution $\eta \cdot A_2^\rho$ in Equation 6.12 is assigned as an systematic uncertainty to the photon absorption asymmetry A_1^ρ:

$$\delta_{syst,A_2^\rho}(A_1^\rho) = \eta \cdot A_2^\rho \quad \text{with} \quad A_2^\rho(Q^2) = \pm \min\left(\sqrt{R^\rho(Q^2)}, 1\right). \tag{6.16}$$

For a conservative estimate of this systematic uncertainty the maximum possible value of A_2^ρ is assumed. In the analysis η is calculated per event using Equation A.44. For the determination of $\delta_{syst,A_2^\rho}(A_1^\rho)$ its average from the events within a certain bin is used. The average value of the kinematic variable η is about 0.06 for the 1996+1997 exclusive ρ data sample.

6.7.2. Dependence of A_1^ρ on Kinematic Variables

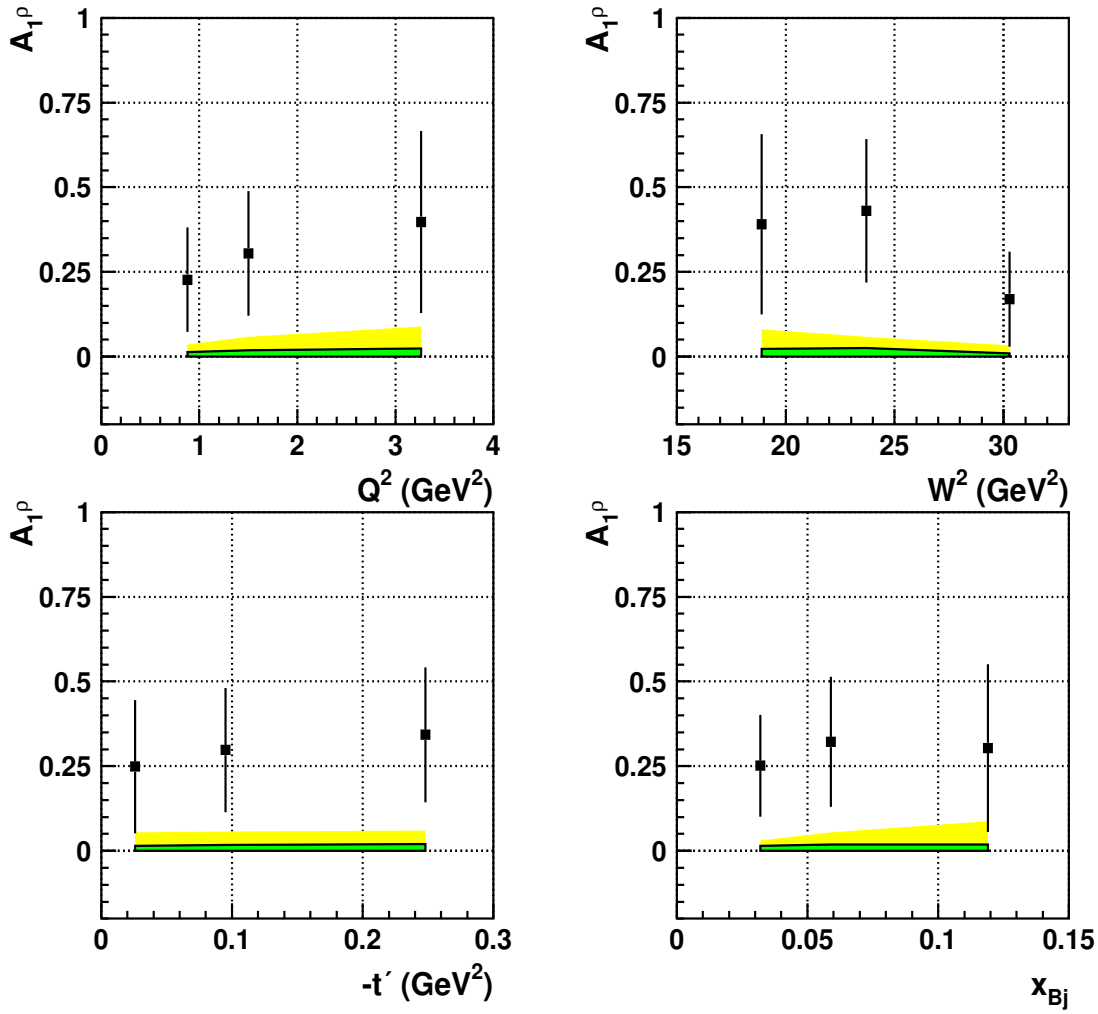

Figure 6.20.: Photon absorption asymmetry A_1^ρ in exclusive ρ production versus Q^2 (top left), W^2 (top right), $-t'$ (bottom left), and x (bottom right). Error bars and the dark band denote the statistical and experimental systematic uncertainties, respectively. The light shaded band gives the total systematic uncertainty when the contribution of the unknown asymmetry A_2^ρ is added in quadrature.

The stability studies discussed in Section 6.6.1 for the experimental asymmetry $A_{||}^\rho$ were also performed for the photon–absorption asymmetry A_1^ρ and no systematic effects were found. The variation of the used event selection requirements did not yield a significant shift of the average photon depolarisation factor D, which is calculated from the data. Hence, no difference was found between A_1^ρ and $A_{||}^\rho$ and no plots for the stability studies of A_1^ρ need to be shown, since they do not yield new information with respect to Figure 6.15.

Figure 6.20 shows the dependence of the photon absorption asymmetry A_1^ρ in exclusive ρ production on the kinematic variables Q^2 (top left), W^2 (top right), $-t'$ (bottom left), and x (bottom right). The error bars denote the statistical uncertainty and the dark band gives the experimental systematic uncertainty of 6% due to beam and target polarisation measurements. For the light shaded bands the systematic uncertainty caused by the unknown asymmetry A_2^ρ is added in quadrature.

Since the contribution of A_2^ρ is moved to the systematic uncertainty, the only remaining difference between the experimental asymmetry $A_{||}^\rho$ and the photon–nucleon asymmetry A_1^ρ is the photon depolarisation factor D. Although the average depolarisation factor D varies from kinematic bin to bin, no general change in A_1^ρ with respect to the experimental asymmetry $A_{||}^\rho$ of Figure 6.18 is seen. No significant trend can be observed in any of the kinematic variables. After all, even if the systematic uncertainty due to the unknown A_2^ρ is included, the photon asymmetries remain significantly non–zero. Table 6.4 lists the asymmetry values and their uncertainties for each bin.

A clear positive longitudinal double–spin asymmetry A_1^ρ in exclusive ρ production at $\langle W^2 \rangle = 24$ GeV^2, $\langle Q^2 \rangle = 1.7$ GeV^2, $\langle -t' \rangle = 0.1$ GeV^2, and $\langle x \rangle = 0.07$ is observed by the HERMES experiment. For the combined 1996+1997 data this asymmetry has a value of

$$A_1^\rho = 0.30 \pm 0.11_{\mathrm{stat}} \pm 0.02_{\mathrm{syst/exp}} \pm 0.05_{\mathrm{syst/A_2^\rho}},$$

The deviation from zero has a statistical significance of about 3σ. The experimental systematic uncertainty is caused by the uncertainty of the polarisation measurements of beam and target. An 'theoretical' systematic uncertainty is assigned for the unknown transverse asymmetry A_2^ρ.

The observed large asymmetry cannot be an effect of a possible contribution from deep–inelastic scattering processes. At the average $x = 0.07$ of the selected ρ data sample the (semi–) inclusive photon asymmetries for a proton target are typically 0.15 [HERMES:99b]. Therefore, even if the background is not subtracted, the about 10 % contribution of DIS events to the selected ρ event sample cannot cause the observed large ρ asymmetry of about 0.3.

The dominant contribution to the systematic uncertainty of A_1^ρ comes from the presently unknown transverse asymmetry A_2^ρ. This contribution can be reduced when data on A_2^ρ become available. It should be mentioned, a transversely polarised target is an option for future HERMES data taking, hence a measurement of A_2^ρ would be feasible at HERMES in the near future.

As already discussed for the case of J/ψ production, the data on the polarised deuterium target taken in the years 1998 to 2000 will increase the available statistics for any asymmetry analysis by an order of magnitude. This will allow a measurement of A_1^ρ with a statistical error comparable to the present systematic uncertainty.

Bin	Boundary	(GeV^2)	$\langle Q^2 \rangle$ (GeV^2)	N^ρ	$A_{\|\|}^\rho$	A_1^ρ
1	Q^2	< 1.15	0.88	1057	0.10 ± 0.07	0.23 ± 0.15
2	$1.15 \leq Q^2$	< 2.05	1.50	1069	0.12 ± 0.07	0.30 ± 0.18
3	$2.05 \leq Q^2$		3.26	673	0.14 ± 0.09	0.40 ± 0.27
Bin	Boundary	(GeV^2)	$\langle W^2 \rangle$ (GeV^2)	N^ρ	$A_{\|\|}^\rho$	A_1^ρ
1	W^2	< 21.5	18.9	960	0.11 ± 0.08	0.39 ± 0.27
2	$21.5 \leq W^2$	< 26.0	23.7	847	0.16 ± 0.08	0.43 ± 0.21
3	$26.0 \leq W^2$		30.3	992	0.09 ± 0.07	0.17 ± 0.14
Bin	Boundary	(GeV^2)	$\langle -t' \rangle$ (GeV^2)	N^ρ	$A_{\|\|}^\rho$	A_1^ρ
1	$-t'$	< 0.05	0.024	838	0.10 ± 0.08	0.25 ± 0.20
2	$0.05 \leq -t'$	< 0.15	0.095	1020	0.12 ± 0.07	0.30 ± 0.18
3	$0.15 \leq -t'$	< 0.4	0.248	941	0.14 ± 0.08	0.34 ± 0.20
Bin	Boundary		$\langle x \rangle$	N^ρ	$A_{\|\|}^\rho$	A_1^ρ
1	x	< 0.045	0.032	920	0.13 ± 0.08	0.25 ± 0.15
2	$0.045 \leq x$	< 0.075	0.059	981	0.12 ± 0.07	0.32 ± 0.19
3	$0.075 \leq x$		0.119	898	0.10 ± 0.08	0.30 ± 0.25

Table 6.4.: Results on asymmetry $A_{\|\|}^\rho$ and A_1^ρ in exclusive ρ production per kinematic bin. Only statistical uncertainties are given.

6.8. Possible Interpretations of A_1^ρ

In inclusive deep–inelastic lepton–nucleon scattering the double–spin asymmetry A_1 is interpreted in terms of the polarised and unpolarised nucleon structure functions: $A_1 \sim g_1/F_1$ (cf. Section A.4). Such a clear interpretation does not exist for the observed double–spin asymmetry in exclusive ρ production.

The optical model of the diffractive interaction and models of vector meson production based on Regge theory neglect the (internal) spin structure of the target nucleon. Therefore, the (naive) expectation is a zero double–spin asymmetry. In a recent publication, asymmetries of less than 10^{-4} were predicted in the kinematic region of the HERA collider experiments for Reggeon exchange [Man:99b]. An extrapolation of this predictions to HERMES energies is not available yet [Man:99a].

No observable spin effects are expected in exclusive ρ meson production for a longitudinally polarised target in the formalism of spin density matrix elements. Conservation of helicity and thus zero spin–flip amplitudes imply a zero double–spin asymmetry. Only a small violation of s-channel helicity conservation was found so far. Here the question arises if the observed violation of SCHC may be reflected in non–zero double–spin asymmetries? And vice versa, do non–zero asymmetries found at small t imply a violation of SCHC?
In the present discussion of off–forward parton distributions, exclusive meson production is considered to be an important tool for understanding the internal structure of the nucleon. However, as has been discussed in Section 2.1.6, at (leading) twist-2 vector meson production is connected to spin–*independent* OFPD's only. In this context, the observation of a rather large spin asymmetry in ρ production is an unexpected effect. It may indicate a relation of vector meson production to the spin–dependent OFPD's already at twist-2, or a large contribution from higher twist.

The validity of OFPD models is presently restricted to longitudinal photons for which QCD factorisation is valid. At HERMES however, the contributions of longitudinal and transverse photons are about equally important. Assuming that the OFPD models discussed above are valid and the asymmetry at twist-2 is zero, the observed asymmetry may also be an effect of the contribution of transverse photons currently not described by QCD calculations based on factorisation. It appears worth noting that large asymmetries are predicted for the diffractive pair–production of charged mesons (cf. Section 2.1.6). The extension of this calculation to the case where a bound vector meson state is formed may yield an explanation for the observed asymmetry.

The two–gluon exchange models for diffractive J/ψ vector meson production appeared to allow access to the gluon polarisation $\Delta G/G$. However, in contrast to earlier hopes, only a small sensitivity to the gluon spin is predicted in this model yielding only a small spin asymmetry for the exclusive production of J/ψ mesons. The statistics of J/ψ events currently available at HERMES does not allow to draw conclusions from the observed spin asymmetry in J/ψ production. For the interpretation of the double–spin asymmetry A_1^ρ in ρ production, presently the open question remains if A_1^ρ can be related to the gluon polarisation $\Delta G/G$ via models involving gluon exchange already at the relatively low mass of the ρ meson.

A special model for spin asymmetries in ρ production, using hadron–parton duality, was discussed in Section 5.2.2. Here, a relation of the spin asymmetry to the gluon polarisation of

the form $A_1^\rho \approx -\Delta G/2G$ is predicted. Using this approximation the positive asymmetry in ρ production would yield a negative gluon contribution to the nucleon spin! This result depends on the validity of the used assumption of parton–hadron duality which is the basis of this calculation.

In summary, the observed asymmetry in ρ production is an unexpected effect for which currently no theoretical explanation is available. In models of vector meson production based on Regge theory the HERMES kinematic range lies in the transition region between Reggeon and Pomeron exchange; in terms of QCD models it lies between quark and gluon exchange. Preliminary results of the SMC collaboration [Tri:99] show a zero asymmetry in exclusive ρ production, however at four times higher W^2. Thus SMC, at a much higher centre–of–mass energy, is dominated by Pomeron or gluon exchange and the different asymmetry results might reflect the transition between different production mechanisms. Therefore, the W^2 or Q^2 dependence of spin asymmetries in vector meson production may help in the future to distinguish between different models of diffractive ρ vector meson production.

7. Summary and Outlook

In the context of this thesis the J/ψ cross section and the double–spin asymmetries in J/ψ and ρ vector meson production in lepton–nucleon scattering at the HERMES experiment were analysed.

Small but clean signals were extracted in both di–leptonic J/ψ decay channels $J/\psi \to e^+e^-$ and $J/\psi \to \mu^+\mu^-$. The di–muon J/ψ decay became only accessible after a dedicated trigger upgrade. Until 1997 the HERMES spectrometer did not have a muon detector, therefore muon identification was achieved by requiring minimum ionising particles in the calorimeter and the preshower detector in coincidence with a signal in the Cherenkov detector. Based on all available data of the years 1995 through 1997 taken with polarised and unpolarised targets the total cross section for J/ψ production at HERMES was determined to be

$$\sigma^{\gamma N \to J/\psi X}(E_\gamma{=}15\,\mathrm{GeV}) = 3.20 \pm 0.32_{\mathrm{stat}} \pm 0.29_{\mathrm{syst/exp}} \pm 0.26_{\mathrm{syst/extrap}}\,\mathrm{nb}.$$

The dominating contribution to the systematic uncertainty is caused by the extrapolation from the measured J/ψ energy range to the full energy spectrum. The results of the cross section analysis for both J/ψ decay channels are in good agreement although they rely on different detection and event selection criteria. For most of the J/ψ events the positron is scattered at small angles and remains undetected. Therefore, a reconstruction of the full event kinematics is not possible and the contributions from elastic and inelastic processes to J/ψ production can not be separated. By comparing the HERMES result to previous data on elastic J/ψ production a contribution of the elastic processes to the total cross section of $72 \pm 16\%$ was determined.

Double–spin asymmetries in J/ψ and exclusive ρ meson production were analysed using the 1996 and 1997 HERMES data taken with a longitudinally polarised hydrogen target. No previous data on spin asymmetries in vector meson production exist. About 2800 ρ and 20 J/ψ events could be selected in the data sample used. For the analysis of double–spin asymmetries in exclusive vector meson production the formalism of asymmetry measurements in inclusive polarised deep–inelastic scattering was adopted.

The asymmetry measurement for the J/ψ meson is limited by statistics. An asymmetry value of $A_1^{J/\psi} = -0.8 \pm 0.5$ is obtained that deviates $1.6\,\sigma$ from zero. The large statistical uncertainty prevents to draw conclusions on the underlying production mechanisms. Only small spin asymmetries are expected in models of diffractive J/ψ production involving the exchange of two gluons; unfortunately the size of the predicted effect is below the statistical accuracy of even future data on J/ψ production at HERMES.

A detailed asymmetry analysis was performed for the ρ meson. Systematic studies included the comparison of the data to Monte Carlo simulations, different methods of background subtraction, and studies on the stability of the extracted spin asymmetry. A significant

positive asymmetry A_1^ρ in exclusive ρ production was found to be

$$A_1^\rho = 0.30 \pm 0.11_{\mathrm{stat}} \pm 0.02_{\mathrm{syst/exp}} \pm 0.05_{syst/A_2^\rho}.$$

The experimental systematic uncertainty is due to the beam and target polarisation measurement. An additional uncertainty arises from the presently unknown transverse asymmetry A_2^ρ. The spin asymmetry A_1^ρ was analysed in 3 bins in each of the kinematic variables Q^2, W^2, $-t'$ and x separately, but no significant dependence was observed in any of these variables.

The theoretical understanding of double–spin asymmetries in exclusive vector meson production, i.e. the dependence of the diffractive process on the polarisation state of the target, is limited. This is in contrast to deep–inelastic scattering, where double–spin asymmetries are analysed to measure the polarised parton distributions of the nucleon.

The phenomenology of vector meson production was discussed in this thesis and several models were introduced. No observable spin effects are expected for a longitudinally polarised target in the models based on Regge theory and in the formalism of spin–density matrix elements. The description of exclusive vector meson leptoproduction in QCD based models, involving the exchange of quarks and gluons, relates the properties of the diffractive process to the internal (spin) structure of the nucleon. The analysis of spin effects not only in vector meson production but also in other exclusive processes, like deep–virtual Compton scattering or the production of pseudo–scalar mesons, may be able to distinguish between different models of recently discussed off–forward parton distributions.

The HERMES kinematic range lies in the transition region between Reggeon and Pomeron exchange or, expressed in terms of QCD models, between quark and gluon exchange. Therefore, the measurement of the dependence of A_1^ρ on kinematic variables may turn out to be a useful tool to distinguish between different models of vector meson production.

The data taken at HERMES in the years 1998 through 2000 on the longitudinally polarised deuterium target will increase the available statistics for an asymmetry analysis by an order of magnitude. This will allow for a significant measurement of the spin asymmetry in J/ψ production and more precise measurements of the asymmetry in ρ production.

In summary, a significant non–zero double–spin asymmetry in exclusive ρ production is an unexpected and exciting result, presently without theoretical explanation.

A. Appendices

A.1. Deep–Inelastic Lepton–Nucleon Scattering and Structure Functions

Deep–Inelastic Lepton–Nucleon Scattering

Lepton–nucleon scattering proceeds in lowest order QED by the exchange of a single virtual photon shown in Figure A.1. Since the wavelength of the photon is inversely proportional to its four–momentum $\lambda \sim 1/\sqrt{Q^2}$, the photon virtuality Q^2 determines the length scale that can be resolved by the interaction[1]. Deep–inelastic scattering (DIS) is usually defined by the kinematic constraints of i) large momentum transfer ($Q^2 \geq 1$ GeV^2) and ii) large photon–nucleon centre–of–mass energy (above the resonance region $W^2 \geq 4$ GeV^2). The double differential cross section of deep–inelastic lepton–nucleon scattering can be expressed as [HM:84, Rob:90]

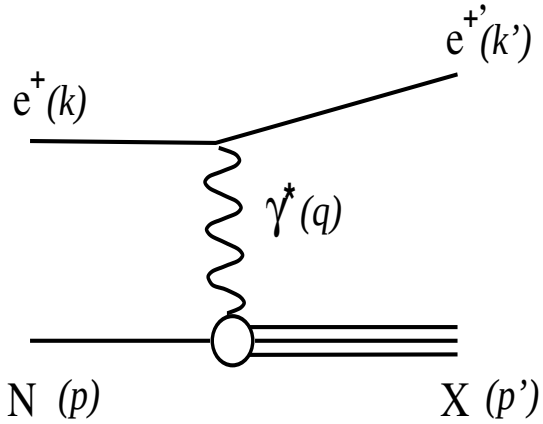

Figure A.1.: Lepton–nucleon scattering in lowest order QED; exchange of a single virtual photon.

$$\frac{d^2\sigma^{eN}}{d\Omega\, dE'} = \frac{\alpha^2}{Q^4}\frac{E'}{E} L_{\mu\nu} W^{\mu\nu}, \tag{A.1}$$

where $\alpha = \frac{e^2}{4\pi} \approx \frac{1}{137}$ is the electromagnetic fine structure constant. The leptonic Tensor $L^{\mu\nu}$ describes the purely electromagnetic emission of the virtual photon and is exactly calculable in QED. It consists of a symmetric and an anti–symmetric part, where the latter describes the dependence on the initial spin state s_β of the lepton

$$L^{\mu\nu}_{(S)} = 2\left[k'^{\mu}k^{\nu} + k'^{\nu}k^{\mu} + (m_e^2 - k'\cdot k)g^{\mu\nu}\right], \tag{A.2}$$

$$L^{\mu\nu}_{(A)} = -i2\epsilon^{\mu\nu\alpha\beta}q_\alpha s_\beta. \tag{A.3}$$

Here $g^{\mu\nu}$ is the metric tensor and $\epsilon^{\mu\nu\alpha\beta}$ is the total anti–symmetric tensor. Since there is not yet an exact theory of strong interactions, the hadronic tensor $W^{\mu\nu}$ cannot be calculated from first principles. Therefore, the (spin) structure of the nucleon is parameterised in terms of structure functions, that have to be determined experimentally. Current conservation at the hadronic vertex and symmetry arguments leave only two independent structure functions $W_1(Q^2,\nu)$ and $W_2(Q^2,\nu)$ of two independent kinematic variables in the symmetric part of

[1] Compare Section 2.1.1 for the definitions of kinematic variables.

the tensor. In the anti–symmetric part, the spin structure of the nucleon is parameterised by the two structure functions $G_1(Q^2,\nu)$ and $G_2(Q^2,\nu)$

$$W^{\mu\nu}_{(S)} = W_1\left(-g^{\mu\nu}+\frac{q^\mu q^\nu}{q^2}\right)+\frac{W_2}{M^2}\left(p^\mu-\frac{p\cdot q}{q^2}q^\mu\right)\left(p^\nu-\frac{p\cdot q}{q^2}q^\nu\right), \quad \text{(A.4)}$$

$$W^{\mu\nu}_{(A)} = \frac{i}{M^2}\epsilon^{\mu\nu\rho\sigma}q_\rho\left[S_\sigma G_1+G_2(\frac{\nu}{M}-\frac{1}{M^2}(S\cdot q)p_\sigma)\right]. \quad \text{(A.5)}$$

Here S_σ is the polarisation vector of the nucleon.

Scaling and Inelastic Structure Functions

In the quark–parton model (QPM) the nucleon consists of non–interacting point–like constituents, interpreted in QCD as spin-1/2 quark objects. In the Bjorken limit, which is defined by $Q^2\to\infty$ and $\nu\to\infty$ at a fixed ratio x

$$x=\frac{Q^2}{2p\cdot q}\overset{lab}{=}\frac{Q^2}{2M\nu}, \quad \text{with} \quad 0<x\leq 1, \quad \text{(A.6)}$$

the deep–inelastic lepton–nucleon interaction can be viewed as elastic scattering of the virtual photon off quasi free quarks. In the infinite–momentum frame, where the nucleon has infinitely large momentum and all particle masses and transverse momenta can be neglected and the dimensionless scaling variable x can be interpreted as the momentum fraction of the nucleon carried by the quark that is struck by the photon. The upper limit on x is reached in elastic scattering when the nucleon stays intact ($W^2=M^2$) yielding $Q^2=2M\nu$ in Equation 2.3. A second dimensionless variable, the relative energy transfer by the photon with respect to the beam energy is commonly defined

$$y=\frac{p\cdot q}{p\cdot k}\overset{lab}{=}\frac{\nu}{E}, \quad \text{with} \quad 0<y<1. \quad \text{(A.7)}$$

Its limit follows from the fact that the photon energy cannot exceed the beam energy minus the lepton mass.

Scattering on point like objects does not depend on the wavelength of the photon. Thus, in the Bjorken limit the structure functions $W_{1,2}$ and $G_{1,2}$ become invariant to the Q^2 scale and are a function of the dimensionless variable x only. Experimentally, a weak dependence of the structure functions on Q^2 (in fact $\ln Q^2$) is observed. This scaling violation is caused by the interaction between the quarks mediated by gluons that is not included in the quark–parton model. The Q^2 dependence of the inelastic structure functions can be described in perturbative QCD in terms of of QCD–evolution equations [GL:72, Dok:77, AP:77]. The dimensionless structure functions $F_{1,2}$, and $g_{1,2}$ of the scaling variable x are defined as

$$\begin{aligned} F_1(x,Q^2) &= MW_1(\nu,Q^2), \quad F_2(x,Q^2) = \nu W_2(\nu,Q^2), \\ g_1(x,Q^2) &= \tfrac{\nu}{M}G_1(\nu,Q^2), \quad g_2(x,Q^2) = \tfrac{\nu^2}{M^2}G_2(\nu,Q^2). \end{aligned} \quad \text{(A.8)}$$

In the Bjorken limit they are interpreted in the quark-parton model in terms of quark distributions q_f, were $q_f\cdot dx$ is the probability to find a quark of flavour f in a certain interval $[x,x+dx]$. Note that the quark distributions q_f contain both the valence and the sea contribution

$$q_f(x,Q^2)=q_f(x,Q^2)+\bar{q}_f(x,Q^2). \quad \text{(A.9)}$$

The structure function F_1 is proportional to the sum of the quark density distributions weighted by the squared quark charge

$$F_1(x, Q^2) = \frac{1}{2} \sum_f e_f^2 \, q_f(x, Q^2), \tag{A.10}$$

while F_2 is correspondingly given as sum of momentum distributions $x \cdot q_f$

$$F_2(x, Q^2) = \sum_f e_f^2 \, x \, q_f(x, Q^2), \tag{A.11}$$

that results in the Callan-Gross-Relation [CG:69]

$$2x F_1(x, Q^2) = F_2(x, Q^2). \tag{A.12}$$

The polarised quark distributions Δq_f are given by the difference of the probabilities $q_f^{\rightrightarrows}$ and $q^{\rightleftarrows}$ to find a quark of flavour f and fractional momentum x with helicity parallel or anti–parallel to the proton momentum

$$\Delta q_f(x, Q^2) = q_f^{\rightrightarrows}(x, Q^2) - q_f^{\rightleftarrows}(x, Q^2). \tag{A.13}$$

In analogy to the unpolarised structure function F_1, the polarised structure function g_1 is proportional to the sum of the polarised quark distributions, weighted by the squared quark charge

$$g_1(x, Q^2) = \frac{1}{2} \sum_f e_f^2 \, \Delta q_f(x, Q^2). \tag{A.14}$$

The spin structure function g_2 does not have such an immediate interpretation. When masses and transverse momenta of quarks are neglected in the QPM, g_2 is zero.

Unpolarised Cross Section

For the calculation of the unpolarised lepton–nucleon cross section, the spin states of incoming lepton and target nucleon are summed over, i.e. the asymmetric parts of $L_{\mu\nu}$ and $W_{\mu\nu}$ vanish, and expression A.1 reduces to

$$\frac{d^2\sigma^{eN}}{d\Omega dE'} = \frac{\alpha^2}{Q^4} \frac{E'}{E} L_{\mu\nu}^{(S)} W_{(S)}^{\mu\nu}. \tag{A.15}$$

Using the leptonic and hadronic tensor of the Equations A.2 and A.4 and the following relations $\frac{q^2}{2} = -(k \cdot k' - m_e^2) = q \cdot k = -q \cdot k', \;\; k' \cdot p = k \cdot p \, (1 - y)$, and $L_{\mu\nu} \frac{q^\mu q^\nu}{q^2} = 0$, it can be shown that

$$\begin{aligned} L_{\mu\nu}^{(S)} \left(-g^{\mu\nu} + \frac{q^\mu q^\nu}{q^2} \right) &= 2 \left[-2k' \cdot k + 4(k \cdot k' - m_e^2) \right] \\ &= 2Q^2 \left(1 - \frac{2m_e^2}{Q^2} \right), \end{aligned}$$

and

$$\begin{aligned} L^{(S)}_{\mu\nu}\left(p^\mu - \frac{p\cdot q}{q^2}q^\mu\right)\left(p^\nu - \frac{p\cdot q}{q^2}q^\nu\right) &= L^{(S)}_{\mu\nu}p^\mu p^\nu \\ &= 2\left[2\,k'\cdot p\;k\cdot p - (k'\cdot k - m_e^2)p^2\right] \\ &= 4(k\cdot p)^2(1-y) + q^2M^2 \\ &= 4E^2M^2\left(1 - y - \frac{Q^2}{4E^2}\right). \end{aligned}$$

Then, the unpolarised cross section becomes

$$\frac{d^2\sigma^{eN}}{d\Omega dE'} = \frac{\alpha^2 E'}{Q^4 E}\left[2Q^2\left(1-\frac{2m_e^2}{Q^2}\right)W_1(\nu,Q^2) + 4E^2\left(1-y-\frac{Q^2}{4E^2}\right)W_2(\nu,Q^2)\right]. \tag{A.16}$$

It is important to mention that for the later discussion of the photon flux the term proportional to the mass of the beam particle $\frac{2m_e^2}{Q^2}$ has been explicitely kept.

In the Bjorken limit the nucleon structure functions $W_{1,2}$ are replaced by the inelastic structure functions $F_{1,2}$ using the Equations A.8

$$\frac{d^2\sigma^{eN}}{dQ^2dx} = \frac{4\pi\alpha^2}{Q^4}\left[y^2\left(1-\frac{2m_e^2}{Q^2}\right)F_1(x,Q^2) + \left(1-y-\frac{Q^2}{4E^2}\right)\frac{F_2(x,Q^2)}{x}\right], \tag{A.17}$$

where the Jacobians $\frac{d^2\sigma}{d\Omega\,dE'} = \frac{EE'}{\pi}\frac{d^2\sigma}{dQ^2\,d\nu}$, and $\frac{d^2\sigma}{dQ^2\,d\nu} = \frac{2M\nu^2}{Q^2}\frac{d^2\sigma}{dQ^2\,dx}$ are used to convert the dependence of the differential cross section on different kinematic variables.

A.2. Definition of Photon Polarisations

In spin physics the term polarisation refers to the spin vector of the particles; an ensemble of objects is said to be polarised if the average over all objects shows a prefered spin direction. The polarisation state of a relativistic particle can be expressed in terms of helicity, defined as the projection of the spin vector $\vec{s}$ onto the particles momentum $\lambda = \vec{s}\cdot\vec{p}/|\vec{s}||\vec{p}|$. If spin and momentum are aligned parallel or anti–parallel the particle is longitudinally *spin* polarised with helicity states $\lambda = \pm 1$. A transverse *spin* polarisation corresponds to the helicity state $\lambda = 0$ were the spin vector is perpendicular to the momentum.

In the case of photons (and vector mesons) the definition of spin polarisation must not be confused with the photon polarisation of classical electrodynamics. In classical electrodynamics a free massless (real) photon is described by a plane wave

$$A = \vec{e}\,A_0\,e^{i(\vec{k}\cdot\vec{r}-\omega t)},$$

with $\vec{k}$ the propagation vector and $\vec{e}$ an unit (polarisation) vector giving the direction of the $\vec{E}$ field. Gauge invariance requires that the propagation vector $\vec{k}$ is perpendicular to the $\vec{E}$ and $\vec{B}$ field ($\vec{e}\cdot\vec{k} = 0$), therefore massless free photons are called *transverse*. If one takes $\vec{k}$ into the z direction, $\vec{A}$ has only two linearly independent components since e_z and A_z are zero

$$A_x = e_x\,A_0\,e^{i(k_z-\omega t+\delta)}, \quad \text{and} \quad A_y = e_y\,A_0\,e^{i(k_z-\omega t)}, \tag{A.18}$$

with δ the relative phase, $e_x^2 + e_y^2 = 1$, and e_x and e_y the two independent linear polarisation directions. If the relative phase δ is zero, the plane wave is said to be linearly polarised with its electric field vector having an angle $\theta = \arctan(e_y/e_x)$ to the polarisation direction e_x. In the general case that the phase δ is nonzero, the plane wave is elliptically polarised. If e_x and e_y have the same magnitude and the phase difference δ is $\pm\pi/2$, the plane wave is circularly polarised; the vector of the electric field has a constant size and rotates around the propagation direction.

The polarisation vectors of classical electrodynamics can be associated with the spin state of the free photon in the quantum mechanical particle interpretation. A right–handed rotation of the electric field vector corresponds to a positive helicity $\lambda = +1$ with the spin parallel to the photon momentum. Correspondingly, a left–handed rotation yields a negative helicity $\lambda = -1$ with the spin anti–parallel to the photon momentum. Again, gauge invariance restricts massless $(Q^2 = 0)$ real photons to these two helicity states. For a more detailed discussion see [Jac:75, Per:87].

Quasi–real transverse photons at $Q^2 \cong 0$ emitted by an unpolarised lepton beam will always have helicity states $\lambda \pm 1$, but since the beam itself is unpolarised the photon helicities will average to zero. In the case of a longitudinally polarised lepton beam one photon helicity state will dominate because of angular momentum conservation at the lepton–photon vertex and the photons will also be longitudinally spin polarised.

For a virtual photon with nonzero invariant mass $(Q^2 > 0)$ an additional component of the propagation vector $\vec{k}$ longitudinal to the $\vec{E}$ (and $\vec{B}$) field is possible. Then these *longitudinal* (or scalar) photons have a *transverse* spin polarisation with the spin vector perpendicular to the photon momentum, thus helicity $\lambda = 0$.

Commonly, the definitions of photon polarisations of classical electrodynamics are also used in the discussion of vector meson production and s–channel helicity conservation. Here, a longitudinally polarised photon is said to produce a longitudinally polarised vector meson (having helicity 0) and a transverse photon produces a transversely polarised vector meson (having helicity ± 1).
In Summary: At low Q^2, a *longitudinally spin* polarised lepton beam will produce a flux of *transverse* photons with *longitudinal spin* polarisation. With higher Q^2 a component of *longitudinal* photons with *transverse spin* polarisation appears. In vector meson production a *longitudinally* polarised photon will produce *longitudinally* polarised vector meson both with a transverse spin polarisation, i.e. helicity zero.

A.3. Photon–Nucleon Scattering and Determination of Photon Fluxes

The process of lepton–nucleon scattering can be described by a flux of virtual photons, emitted by the lepton beam and subsequently absorbed by the nucleon. Extrapolation of photon absorption cross sections measured by virtual photon exchange in leptoproduction to $Q^2 = 0$ allows comparison with experiments using real photon beams. In this section the derivation of the photon flux within the theoretical framework of deep–inelastic scattering is summarised. The somewhat special case of J/ψ production at HERMES is discussed in Section 4.10. The concept of the Equivalent Photon Approximation is described in detail in [BGMS:75], this section follows the discussions given in [HM:84, Rob:90, Bur:94].

Weizsäcker–Williams Approach

To calculate the cross section of an interaction, usually the amplitudes for the different subsequent processes are added, and the square modulus of the sum is taken. In the Weizsäcker–Williams Approach (WWA), also called the Equivalent Photon Approximation (EPA), the lepton–nucleon interaction is factorised into two independent processes, indicated in Figure A.2. The probabilities for the photon emission and its subsequent absorption by the nucleon are determined separately and multiplied afterwards. This technique is not restricted to photons, it can also be used to describe gluon exchange QCD calculations [HM:84].

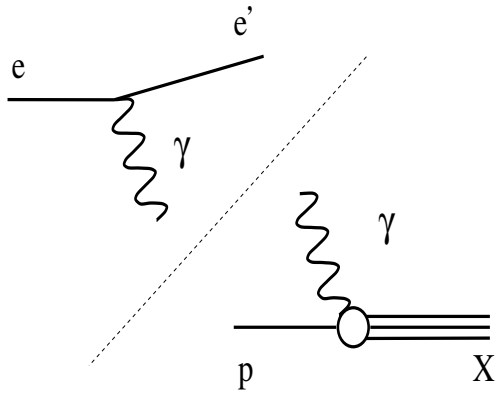

Figure A.2.: Schematic graph for the Weizsäcker–Williams Approach in lepton–nucleon scattering. The interaction is approximated by two independent processes, the photon emission and subsequent absorption.

The lepton–nucleon interaction is reduced to the photon absorption by the nucleon, while the lepton beam is represented by a photon spectrum dn; the lepton–nucleon cross section is then given as the product of the photon spectrum, also called the equivalent photon number, and the absorption cross section at the hadronic vertex [BGMS:75]

$$\frac{d^2\sigma^{eN}}{dQ^2 d\nu} = dn(Q^2,\nu)\ \sigma_{\gamma N}(Q^2,\nu). \tag{A.19}$$

Fermi first mentioned the similarity between the field of a fast moving charged particle and electromagnetic radiation [Fer:24]. The photon spectrum dn emitted from a spin 1/2 particle was calculated in a semi–classical approach by Weizsäcker and Williams [vW:34, Wil:34]. Two simplifications were used: i) real photons are emitted on mass shell and ii) it turned out that photons emitted from an electron are dominantly transverse, therefore contributions from longitudinal (or scalar) photons were neglected.

Real photons ($Q^2 = 0$) are strictly transverse, while virtual photons ($Q^2 > 0$) may have additional longitudinal components. Relation A.19 can be generalised to the (double) differential cross section of the lepton–nucleon interaction $d\sigma^{eN}$ as the sum of fluxes for transverse and longitudinal virtual photons Γ_T and Γ_L, each multiplied with their corresponding absorption cross section σ_T and σ_L, respectively [Han:63]

$$\frac{d^2\sigma^{eN}}{dQ^2 d\nu} = \Gamma_T(Q^2,\nu)\,\sigma_T(Q^2,\nu) + \Gamma_L(Q^2,\nu)\,\sigma_L(Q^2,\nu). \tag{A.20}$$

Equation (A.20) is commonly rewritten as

$$\frac{d^2\sigma^{eN}}{dQ^2\,d\nu} = \Gamma_T(Q^2,\nu)\sigma_T(Q^2,\nu)(1+\epsilon R) \tag{A.21}$$

with the definition of R as the ratio of absorption cross sections and ϵ as the ratio of fluxes

$$R = \frac{\sigma_L}{\sigma_T} \quad \text{and} \quad \epsilon = \frac{\Gamma_L}{\Gamma_T}. \tag{A.22}$$

The definition of a flux describing the number of virtual photons available to the interaction is somewhat arbitrary and a matter of convention. In that sense σ_T and σ_L have not the precise meaning of cross sections, only the product of a flux and an absorption cross section is unambiguously defined. Several conventions to *choose* a flux definition have the common limit of a flux of real photons at $Q^2 = 0$ were the longitudinal absorption cross section vanishes

$$\lim_{Q^2\to 0} \sigma_T(Q^2,\nu) = \sigma_{eN}(\nu), \quad \lim_{Q^2\to 0} \sigma_L(Q^2,\nu) = 0. \tag{A.23}$$

Commonly used is the convention by Hand [Han:63] with a kinematic variable K chosen such that the photon–nucleon centre–of–mass energy becomes independent of Q^2 for a specific value of K, and corresponds to the energy a real photon needs to create the same final state [2]

$$W^2 = m_p^2 + 2m_p\nu - Q^2 \;\text{ becomes }\; W^2 = m_p^2 + 2m_pK, \tag{A.24}$$

with

$$K = \nu - \frac{Q^2}{2m_p} = \frac{Q^2(1-x)}{2m_px} = \nu(1-x). \tag{A.25}$$

For the limit $Q^2 \to 0$, K becomes equal to the energy of the real photon beam: $K \to \nu$.

Photon–Nucleon Scattering

The cross section for the absorption of a *real* photon by a nucleon target, depicted in the lower graph of Figure A.2, can be derived from Feynman rules [HM:84]

$$\sigma_\lambda(\gamma N \to X) = \frac{4\pi^2\alpha}{K}\epsilon_\lambda^{\mu\star}\epsilon_\lambda^\nu W_{\mu\nu}, \tag{A.26}$$

were ϵ_λ^ν denote the polarisation vectors of the real photon with the two helicities $\lambda = \pm 1$. In order to interpret the hadronic tensor $W_{\mu\nu}$ in A.26 as total photon–nucleon cross section in the same way as for lepton–nucleon scattering in Section A.1, it is important to consider the absorption of a *virtual* photon. In this case, the energy $K = \nu$ of a real photon becomes that of a virtual one $K = \nu(1-x)$ and three helicity states $\lambda = \pm 1, 0$ are possible, expressed by the polarisation vectors as [BGMS:75]

$$\epsilon_{\lambda=\pm1} = \mp\frac{1}{\sqrt{2}}(0;1,\pm i,0) \quad \text{and} \quad \epsilon_{\lambda=0} = \pm\frac{1}{\sqrt{Q^2}}(\sqrt{\nu^2+Q^2};0,0,\nu). \tag{A.27}$$

For a longitudinally polarised transverse photon and and a longitudinally polarised nucleon target, the absorption cross sections for parallel or anti–parallel spin orientation $\sigma_{3/2}$ and $\sigma_{1/2}$ can be expressed in terms of the DIS structure functions introduced in Section A.1 [Rob:90]

$$\sigma_{3/2} = \frac{4\pi^2\alpha}{KM}\left[F_1(Q^2,x) - g_1(Q^2,x) + \gamma^2 g_2(Q^2,x)\right], \tag{A.28}$$

$$\sigma_{1/2} = \frac{4\pi^2\alpha}{KM}\left[F_1(Q^2,x) + g_1(Q^2,x) - \gamma^2 g_2(Q^2,x)\right]. \tag{A.29}$$

[2] Another convention was later introduced by Gilman [Gil:68], treating the virtual photon as any other massive particle $K = \sqrt{\nu^2+Q^2}$, which will not be used here.

Here $3/2$ and $1/2$ denote the projection of the total spin in the photon–nucleon system along the photon momentum. The total cross section for transverse photons is given by the average of $\sigma_{3/2}$ and $\sigma_{1/2}$, if the target and/or beam are unpolarised

$$\sigma_T = \frac{1}{2}(\sigma_{3/2} + \sigma_{1/2}) = \frac{4\pi^2\alpha}{KM}\left[F_1(Q^2, x)\right]. \tag{A.30}$$

The absorption cross section for longitudinal photons σ_L depends only on the unpolarised structure functions F_1 and F_2, while the interference between transverse and longitudinal photons σ_{LT} is given by the polarised structure functions g_1 and g_2

$$\sigma_L = \frac{4\pi^2\alpha}{KM}\left[\frac{1+\gamma^2}{2x}F_2(Q^2, x) - F_1(Q^2, x)\right], \tag{A.31}$$

$$\sigma_{LT} = \frac{4\pi^2\alpha}{KM}\gamma\left[g_1(Q^2, x) + g_2(Q^2, x)\right], \tag{A.32}$$

with $\gamma^2 = \frac{Q^2}{\nu^2}$. Using the above definitions, the ratio R in deep–inelastic scattering can be expressed as

$$R = \frac{\sigma_L}{\sigma_T} = \frac{1+\gamma^2}{2x}\cdot\frac{F_2}{F_1} - 1. \tag{A.33}$$

It can be extracted from unpolarised inclusive cross section measurements, which span a wide kinematic range in Q^2 and x, as realised by SLAC [W$^+$:90] and NMC [NMC:97]. Rearranging Equation A.33 yields an expression, that differs from the Callan-Gross relation A.12

$$2xF_1(x, Q^2) = \frac{1+\gamma^2}{1+R(x, Q^2)}F_2(x, Q^2). \tag{A.34}$$

This deviation can be explained by the fact in the quark–parton model the partons do not carry transverse momenta and hence cannot not absorb longitudinal photons. The deviation vanishes in the kinematic limit $Q^2 \to 0$ where real photons are purely transverse and $\sigma_L = 0$.

Determination of Fluxes

Fluxes of transverse and longitudinal photons are obtained from the unpolarised cross section as follows. The structure functions F_1 and F_2 can be expressed in terms of the absorption cross sections σ_T and σ_L using the Equations A.30 and A.31. Insertion into Equation A.17 for the unpolarised lepton–nucleon cross section and rearrangement w.r.t. σ_L and σ_T yields

$$\frac{d^2\sigma^{eN}}{dQ^2\,d\nu} = \frac{\alpha K}{2\pi Q^2\nu^2}\left\{\begin{array}{l}\left[y^2\left(1-\frac{2m_e^2}{Q^2}\right)+2\frac{1}{1+\gamma^2}\left(1-y-\frac{Q^2}{4E^2}\right)\right]\sigma_T \\ \\ +2\frac{1}{1+\gamma^2}\left(1-y-\frac{Q^2}{4E^2}\right)\sigma_L\end{array}\right\}. \tag{A.35}$$

Here, the dependence on the differential cross section from the energy ν has been chosen for convenience in the discussion of J/ψ production near threshold. The fluxes of transverse and longitudinal photons can be identified by comparing with Equation A.20.

Bjorken Limit of Deep–Inelastic Scattering

In the Bjorken limit the term proportional to the squared mass of the beam particle m_e^2 can be neglected. The flux of transverse photons and the ratio of fluxes ϵ are then expressed as

$$\Gamma_T = \frac{\alpha K}{2\pi Q^2 \nu^2}\left[y^2 + \frac{2}{1+\gamma^2}\left(1 - y - \frac{Q^2}{4E^2}\right)\right] \quad \text{and} \quad \epsilon = \frac{1 - y - \frac{Q^2}{4E^2}}{1 - y + \frac{y^2}{2} + \frac{Q^2}{4E^2}} \tag{A.36}$$

Limit of Quasi–Real Photon Exchange

Quasi–real photon exchange is the limit of low Q^2 and low Bjorken–x. At HERMES energies the term $Q^2/(4E^2)$ is below 10^{-3} and can be neglected. The flux factor K of Equation A.25 becomes $K \to \nu$ and the pre–factor reduces to $\alpha/(2\pi Q^2 \nu)$. All terms $1/(1+\gamma^2)$ become unity since $\gamma^2 = Q^2/\nu^2$ vanishes. With the minimum four–momentum transfer by the photon $Q^2_{min} = y^2 m_e^2/(1-y)$ required for the interaction to take place (cf. Equation 4.20), Equation A.35 becomes the often quoted form

$$\frac{d^2\sigma^{eN}}{dQ^2 d\nu} = \frac{\alpha}{2Q^2\pi\nu}\left\{\left[1 + (1-y)^2 - 2(1-y)\frac{Q^2_{min}}{Q^2}\right]\sigma_T + 2(1-y)\sigma_L\right\}. \tag{A.37}$$

Nevertheless, for a given experimental setup and a certain physics process the validity of all these simplifications has to be justified. The case of J/ψ production at HERMES is discussed in Section 4.10.

A.4. Polarised Deep–Inelastic Scattering

The spin dependent nucleon structure functions can be determined by the measurement of double–spin asymmetries in deep–inelastic lepton–nucleon scattering when both beam and target are polarised.

Polarised Cross Section

For a longitudinally polarised beam, the following relation can be derived for the cross section *difference* between opposite orientations of the target polarisation with respect to the beam [Jaf:95]

$$\begin{aligned}\frac{d^3(\sigma(\alpha) - \sigma(\pi-\alpha))}{dx\,dy\,d\phi} = \frac{e^4}{4\pi^2 Q^2}\Bigg\{&\cos\alpha\left[\left(1 - \frac{y}{2} - \frac{y^2}{4}\gamma^2\right)g_1(x,Q^2) - \frac{y}{2}\gamma^2 g_2(x,Q^2)\right] \\ &- \sin\alpha\cos\phi\sqrt{\gamma^2\left(1 - y - \frac{y^2}{4}\gamma^2\right)}\left(\frac{y}{2}g_1(x,Q^2) + g_2(x,Q^2)\right)\Bigg\}\end{aligned} \tag{A.38}$$

Here, the symmetric parts of the leptonic and the hadronic tensors cancel and the cross section difference depends only on the spin structure functions g_1 and g_2; the spin of the final states is not considered and summed up in the calculation.

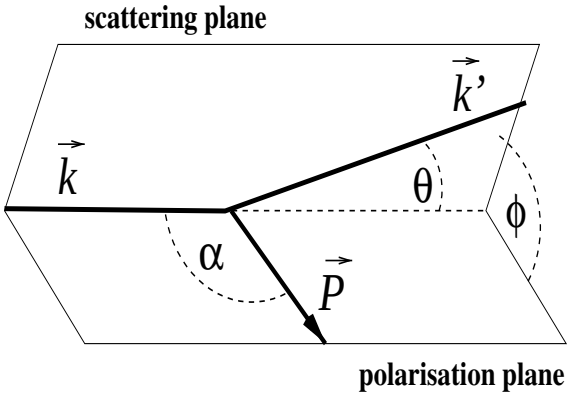

Figure A.3.: Definition of scattering plane and polarisation plane in lepton–nucleon scattering off a fixed target.

Figure A.3 depicts the definitions of the angles θ, ϕ and α . The angle θ is the scattering angle in the laboratory frame. The azimuthal angle between the scattering plane and the polarisation plane spanned by the beam axis and the polarisation vector of the target is denoted by ϕ.

The polar angle of the target polarisation vector with respect to the beam direction is denoted by α. If the target is longitudinally polarised, the target polarisation is aligned with the beam direction and α is 0 or π. In this case, the second term in Equation A.38 vanishes and the cross section difference is dominated by the spin structure function g_1, since g_2 is suppressed by a kinematic factor. For a transversely polarised target α is $\pi/2$. Consequently, the first term of Equation A.38 vanishes and a combination of both spin structure functions determines the cross section difference.

Asymmetries in Lepton–Nucleon Scattering

In comparison to the total (unpolarised) lepton–nucleon cross section, the spin dependent difference of the absolute cross sections is small and difficult to measure. Therefore, the spin structure functions g_1 and g_2 are determined by a measurement of double–spin asymmetries, having the advantage that all spin independent contributions vanish and no absolute normalisation of the measurement is necessary. In spin dependent lepton–nucleon scattering the experimentally accessible double–spin asymmetries are defined as

$$A_{\parallel} = \frac{\sigma^{\overrightarrow{\Leftarrow}} - \sigma^{\overrightarrow{\Rightarrow}}}{\sigma^{\overrightarrow{\Leftarrow}} + \sigma^{\overrightarrow{\Rightarrow}}} \quad \text{and} \quad A_{\perp} = \frac{\sigma^{\uparrow\leftarrow} - \sigma^{\uparrow\rightarrow}}{\sigma^{\uparrow\leftarrow} + \sigma^{\uparrow\rightarrow}}. \tag{A.39}$$

For a longitudinally polarised target, the lepton–nucleon cross section asymmetry $A_{\parallel}$ is defined by the difference of the cross sections with the target spin direction parallel ($\overrightarrow{\Rightarrow}$) or anti–parallel ($\overrightarrow{\Leftarrow}$) to the longitudinal beam polarisation, normalised to their sum. In the case of a transversely polarised target, the azimuthal asymmetry $A_{\perp}$ with respect to the angle ϕ between the polarisation and the scattering plane is measured. At HERA, the longitudinal beam polarisation cannot be reversed on a short time–scale, and to perform an asymmetry measurement the polarisation direction of the target nucleons must be flipped.

Virtual–Photon Absorption Asymmetries

As discussed in Sections A.1 and A.3, lepton–nucleon scattering can be factorised into the emission of virtual photons by the lepton beam, exactly calculable in QED, and into the subsequent absorption of these photons by the nucleon. Two asymmetries of absorption cross sections for virtual photons are defined for the investigation of the spin dependence of the photon–nucleon vertex: the asymmetry A_1 in case of a longitudinally polarised target and the asymmetry A_2 for transversely polarised targets

$$A_1 = \frac{\sigma_{1/2} - \sigma_{3/2}}{\sigma_{1/2} + \sigma_{3/2}} = \frac{g_1 - \gamma^2 g_2}{F_1}, \qquad A_2 = \frac{\sigma_{LT}}{\sigma_T} = \frac{\gamma(g_1 + g_2)}{F_1}. \tag{A.40}$$

Here, the definitions of the photon absorption cross sections and their relation to the nucleon structure functions are given by Equations A.28 and A.32. For the transverse asymmetry A_2 a positivity limit can be derived from the interference term $\sigma_{LT} \leq \sqrt{\sigma_T \sigma_L}$

$$A_2 \leq \sqrt{\frac{\sigma_T \sigma_L}{\sigma_T^2}} = \sqrt{R}. \tag{A.41}$$

The virtual–photon absorption asymmetries are related to the experimental asymmetries by

$$A_{\parallel} = D \cdot (A_1 + \eta A_2), \qquad A_{\perp} = D \cdot (\xi A_2 - \frac{\eta}{\xi} A_1), \tag{A.42}$$

where D is the effective polarisation of the photon, commonly (and incorrectly) called the photon 'depolarisation' factor

$$D = \frac{1 - (1 - y)\,\epsilon}{1 + \epsilon R}, \tag{A.43}$$

and where η and ξ are additional kinematic factors

$$\eta = \frac{2M\epsilon\sqrt{Q^2}}{s[1 - (1 - y)\epsilon]}, \qquad \xi = \sqrt{\frac{2\epsilon}{1 + \epsilon}}, \tag{A.44}$$

with ϵ, the ratio of fluxes for transverse and longitudinal photons of Equation A.36.

Up to now, HERMES was using only longitudinally polarised targets. The experimental asymmetry $A_{\parallel}$ can be related to the ratio of the spin structure function g_1 to the unpolarised structure function F_1 using Equations A.40 and A.42

$$\frac{g_1}{F_1} = \frac{1}{1 + \gamma^2} \left(\frac{A_{\parallel}}{D} - (\eta - \gamma) A_2 \right). \tag{A.45}$$

The structure function g_1 can be extracted from this ratio, when using Equation A.34 for the relation between F_1 and F_2, and parameterisations of F_2, A_2 and R from previous measurements; the HERMES results on g_1 for neutron and proton can be found in [HERMES:97a, HERMES:98b].

A. Appendices

Bibliography

[ABFR:98] G. Altarelli, R. D. Ball, S. Forte and G. Ridolfi, Acta Phys.Polon. **B29**, 1145 (1998).

[Aku:97] I. Akushevich, *Radiative Correction to Cross Section of Exclusive ρ^0 Electroproduction*, HERMES Internal Note 97-059, 1997.

[Aku:99] I. Akushevich, Private Communication, 1999.

[AP:77] G. Altarelli and G. Parisi, Nucl. Phys. **B126**, 298 (1977).

[B$^+$:94] R. Brun et al., *GEANT detector description and simulation tool (long writeup W5013)* , CERN-CN Application Software Group, Geneva, 1994.

[B$^+$:98] H. Böttcher et al., Nucl. Instr. Meth. **A416**, 45 (1998).

[Bau:98] C. Baumgarten, The HERMES internal polarized hydrogen and deuterium targets, in *The 13^{th} International Symposium on High Energy Spin Physics*, Protvino, Russia, 1998.

[BBL:95] G. T. Bodwin, E. Braaten and G. P. Lepage, Phys. Rev. **D51**, 1125 (1995).

[Bel:98] E. Belz, *Measurement of Decay Angle Distributions in Diffractive Electroproduction of ρ^0 Mesons and an Extraction of $R(Q^2)$*, HERMES Internal Note 98-028, 1998.

[Ben:98a] T. Benisch, Private Communication, 1998.

[Ben:98b] T. Benisch, *Polarisierte Bhabha-Streuung und Luminositätsmessung im HERMES-Experiment*, Dissertation, Universität Erlangen-Nürnberg, 1998.

[BFG$^+$:94] S. J. Brodsky, L. Frankfurt, J. F. Gunion, A. H. Mueller and M. Strikman, Phys. Rev. **D50**, 3134 (1994).

[BFP:79] A. R. Clark et al. (BFP Collaboration), Phys. Rev. Lett. **43**, 187 (1979).

[BGMS:75] V. M. Budnev, I. F. Ginzburg, G. V. Meledin and V. G. Serbo, Phys. Rep. **C15**, 181 (1975).

[BGS:99] H. Böttcher, Y. Gärber and U. Stößlein, Hermes Internal Report in preparation, 1999.

[BJ:81] E. L. Berger and D. Jones, Phys. Rev. **D23**, 1521 (1981).

[BKO:98] E. Belz, M. Kolstein and T. G. ONeill, *Monte Carlo Code for exclusive diffractive ρ production*, 1998.

[BL:82] J. Bartels and M. Loewe, Z. Phys. **C12**, 263 (1982).

[Bor:99] A. Borissov, *Diffractive physics at HERMES*, in *Proceedings of 7th International Workshop on DIS and QCD (DIS 99)*, Zeuthen, Germany, 1999.

[Böt:99] H. Böttcher, Private Communication, 1999.

[BR:82] R. Baier and R. Rueckl, Nucl. Phys. **B201**, 1 (1982).

[Bra:97] B. Braun, *The Hermes Polarimeter*, in *Proceedings of the 7^{th} Workshop on Polarised Gas Targets and Polarised Beams*, Urbana-Champaign, USA, 1997.

[Bro:97] S. Brons, *Results on Charm Production at HERMES*, in *Proc. of Workshop on 'Deep Inelastic Scattering of Polarised Targets'*, 1997.

[Bro:98a] S. Brons, Private Communication, 1998.

[Bro:98b] S. Brons, *Analysis of $D^{*+} - D^0\pi^+$ & $D^{*-} - D^0\pi^-$ in the 1996 and 1997 HERMES Data* , HERMES Internal Note 98-057, 1998.

[Bru:98] A. Bruell, Private Communication, 1998.

[BSYP:78] T. Bauer, R. Spital, D. Yennie and F. Pipkin, Rev. Mod. Phys. **50**, 261 (1978).

[Bur:94] B. D. Burow, *A Measurement of the Total Photon-Proton Cross Section in the Center of Mass Energy Range 167 to 194 GeV*, PhD thesis, University. of Toronto, 1994.

[BvHK:98] A. Bravar, D. von Harrach and A. Kotzinian, Phys. Lett. **B421**, 349 (1998).

[C$^+$:75] U. Camerini et al., Phys. Rev. Lett. **35**, 483 (1975).

[C$^+$:78] D. G. Crabb et al., Phys. Rev. Lett. **41**, 1257 (1978).

[C$^+$:81] D. Cassel et al., Phys. Rev. **D24**, 2787 (1981).

[C$^+$:90] D. G. Crabb et al., Phys. Rev. Lett. **65**, 3241 (1990).

[C$^+$:97] E. Cisbani et al., *Proposal for a Dual Radiator RICH for HERMES*, DESY-HERMES 97-003, 1997.

[C$^+$:98] C. Caso et al., Eur. Phys. J. **C3**, 1 (1998).

[CDF:92] F. Abe et al. (CDF Collaboration), Phys. Rev. Lett. **69**, 3704 (1992).

[CDF:93] F. Abe et al. (CDF Collaboration), Phys. Rev. Lett. **71**, 2537 (1993).

[CF:61] G. F. Chew and S. C. Frautschi, Phys. Rev. Lett. **7**, 394 (1961).

[CF:62] G. F. Chew and S. C. Frautschi, Phys. Rev. Lett. **8**, 41 (1962).

[CFS:97] J. C. Collins, L. Frankfurt and M. Strikman, Phys. Rev. **D56**, 2982 (1997).

[CG:69] C. G. Callan and D. J. Gross, Phys. Rev. Lett. **22**, 156 (1969).

[CK:96] M. Caccaiari and M. Krämer, Phys. Rev. Lett. **76**, 4128 (1996).

[COMPASS:96] G. Baum et al. (COMPASS Collaboration), *COMPASS: A proposal for a common muon and proton apparatus for structure and spectroscopy*, CERN preprint, CERN SPSLC/96-14, 1996.

[Cri:97] J. A. Crittenden, *Exclusive Production of Neutral Vector Mesons at the Elextron–Proton Collider HERA*, Springer Tracts in Modern Physics 140, 1997.

[DFJK:99] M. Diehl, T. Feldmann, R. Jacob and P. Kroll, Eur. Phys. J. **C8**, 409 (1999).

[dFSS:98] D. de Florian, O. A. Sampayo and R. Sassot, Phys. Rev. **D57**, 5803 (1998).

[DGM$^+$:99] M. Dueren, P. Geiger, N. Makins, E. Volk et al., *The HERMES Monte Carlo program*, http://www-hermes.desy.de/hmc/, 1995-1999.

[DGP:98] M. Diehl, T. Gousset and B. Pire, *Exclusive electroproduction and off–diagonal parton distributions*, hep-ph/9811220, DESY-980168, 1998.

[dJ:91] M. de Jong, *Muonproduction of J/ψ -mesons and the gluon distribution in nucleons*, PhD thesis, Vrije Universiteit te Amsterdam, 1991.

[DL:84] A. Donnachie and P. V. Landshoff, Nucl. Phys. **B231**, 189 (1984).

[DL:92] A. Donnachie and P. V. Landshoff, Phys. Lett. **B296**, 227 (1992).

[DL:95] A. Donnachie and P. V. Landshoff, Phys. Lett. **B348**, 213 (1995).

[Dok:77] Y. Dokshitzer, Sov. J. Phys. JETP **46**, 461 (1977).

[Due:95] M. Dueren, *The HERMES-Experiment: From the design to the first results*, Habilitationsschrift, Universität Erlangen-Nürnberg, DESY-HERMES 95-02, 1995.

[E143:98] K. Abe et al. (E143 Collaboration), Phys. Rev. **D58**, 112003 (1998).

[E143:99] K. Abe et al. (E143 Collaboration), Phys. Lett. **B452**, 194 (1999).

[E154:97] K. Abe et al. (E154 Collaboration), Phys. Lett. **B405**, 180 (1997).

[E665:96] M. R. Adams et al. (E665 Collaboration), Z. Phys. **C71**, 391 (1996).

[E665:97] M. R. Adams et al. (E665 Collaboration), Z. Phys. **C74**, 237 (1997).

[EMC:80] J. J. Aubert et al. (EMC Collaboration), Phys. Lett. **B89**, 267 (1980).

[EMC:83] J. J. Aubert et al. (EMC Collaboration), Nucl. Phys. **B213**, 31 (1983).

[EMC:88] J. Ashman et al. (EMC Collaboration), Phys. Lett. **B 206**, 364 (1988).

[EMC:92a] J. Ashman et al. (EMC Collaboration), Z. Phys. **C56**, 21 (1992).

[EMC:92b] J.Ashman et al. (EMC Collaboration), Z. Phys. **C56**, 21 (1992).

[F$^+$:78] G. Fidecaro et al., Phys. Lett. **76B**, 369 (1978).

[Fer:24] E. Fermi, Z. Phys. **29**, 315 (1924).

[FH:95] H. Frauenfelder and E. M. Henley, *Teilchen und Kerne*, Oldenbourg, 1995.

[FKS:96] L. Frankfurt, W. Koepf and M. Strikman, Phys. Rev. **D54**, 3194 (1996).

[FKS:98] L. Frankfurt, W. Koepf and M. Strikman, Phys. Rev. **D57**, 512 (1998).

[FPPS:99] L. L. Frankfurt, P. V. Pobylitsa, M. V. Polyakov and M. Strikman, Phys. Rev. **D60**, 014010 (1999).

[FPS:81] M. Fontannaz, B. Pire and D. Schiff, Z. Phys. **C11**, 211 (1981).

[Fra:74] H. Fraas, Ann. Phys. **87**, 417 (1974).

[Fre:67] P. G. O. Freund, Nuovo Cimento **A48**, 541 (1967).

[FRS:75] H. Fraas, B. J. Read and D. Schildknecht, Nucl. Phys. **B88**, 301 (1975).

[G$^+$:75] B. Gittelman et al., Phys. Rev. Lett. **35**, 1617 (1975).

[Gil:68] F. J. Gilman, Phys. Rev. **167**, 1365 (1968).

[GL:72] V. Gribov and L. Lipatov, Sov. J. Nucl. Phys. **15**, 438 (1972).

[GLR:83] L. V. Gribov, E. M. Levin and M. G. Ryskin, Phys. Rep. **100**, 1 (1983).

[GM:96] S. Gupta and P. Mathews, TIFR/TH/96-53 (1996).

[GR:88] M. Glück and E. Reya, Z. Phys. **C39**, 569 (1988).

[GRBH:85] B. Geyer, D. Robaschik, M. Bordag and J. Horejsi, Z. Phys. **C26**, 591 (1985).

[GRSV:96] M. Glück, E. Reya, M. Stratmann and W. Vogelsang, Phys. Rev. **D53**, 4775 (1996).

[Gui:88] J. P. Guillet, Z. Phys. **C39**, 75 (1988).

[Gut:99] A. Gute, *Messung der polarisierten Strukturfunktion g_1^p des Protons im HERMES–Experiment*, Dissertation, Universität Erlangen–Nürnberg, 1999.

[GV:99] M. Guidal and M. Vanderhaeghen, *Deeply Virtual Electroproduction of Photons and Mesons*, hep-ph/9901298, 1999.

[H1:95] S. Aid et al. (H1 Collaboration), Nucl. Phys. **B449**, 3 (1995).

[H1:96] A. Aid et al. (H1 Collaboration), Nucl. Phys. **B472**, 3 (1996).

[H1:99] C. Adloff et al. (H1 Collaboration), DESY-99-010, to appear in Eur.Phys.J. C (1999).

[Han:63] L. N. Hand, Phys. Rev. **129**, 1834 (1963).

[HERMES:97a] K. Ackerstaff et al. (HERMES Collaboration), Phys. Lett. **B404**, 383 (1997).

[HERMES:97b] N. Akopov et al. (HERMES Collaboration), *Determination of the 1995 Data Quality and the Extraction of the Spin Structure Function of the Neutron*, HERMES Internal Report 97-007, 1997.

[HERMES:97c] M. Amarian et al. (HERMES Collaboration), *The HERMES Charm Upgrade, Proposal to the PRC*, DESY-PRC 97-03, 1997.

[HERMES:98a] K. Ackerstaff et al. (HERMES Collaboration), Nucl. Instr. Meth. **A417**, 230 (1998).

[HERMES:98b] A. Airapetian et al. (HERMES Collaboration), Phys. Rev. Lett. **B442**, 484 (1998).

[HERMES:99a] K. Ackerstaff et al. (HERMES Collaboration), Phys. Rev. Lett. **82**, 1164 (1999).

[HERMES:99b] K. Ackerstaff et al. (HERMES Collaboration), Phys. Lett. **B464**, 123 (1999).

[HERMES:99c] K. Ackerstaff et al. (HERMES Collaboration), Eur. Phys. J. (to be submitted) (1999).

[HERMES:99d] K. Ackerstaff et al. (HERMES Collaboration), Phys. Rev. Lett. **82**, 3025 (1999).

[HERMES:99e] A. Airapetian et al. (HERMES Collaboration), Phys. Rev. Lett. (in press), hep–ex/990720 (1999).

[HKK:96] L. P. A. Haakmann, A. Kaidalov and J. H. Koch, Phys. Lett. **B365**, 411 (1996).

[HLW:85] S. D. Holmes, W. Lee and J. E. Wiss, Ann. Rev. Nucl. Part. Sci. **35**, 397 (1985).

[HM:84] F. Halzen and A. D. Martin, *Quarks and Leptons*, John Wiley & Sons, 1984.

[HS:97] D. Hasch and U. Stößlein, Private Communication, 1997.

[IGS:81] G. Ingelman, G. Gustafson and T. Sjoestrand, Z. Phys. **C9**, 233 (1981).

[IK:98] D. Y. Ivanov and R. Kirschner, Phys. Rev. **D58**, 114026 (1998).

[IRS:96] G. Ingelmann, J. Rathsman and G. A. Schuler, *AROMA 2.2 - A Monte Carlo Generator for Heavy Flavour Events in ep Collisions*, DESY 96-058, 1996.

[Jac:75] J. D. Jackson, *Classical Electrodynamics*, Wiley & Sons, 1975.

[Jaf:95] R. L. Jaffe, *Spin, twist and hadron structure in deep inelastic processes*, in *Proceedings of the Ettore Majorana International School of Nucleon Structure: 1st Course: The Spin Structure of the Nucleon*, Erice, Italy, 1995.

[Ji:97a] X. Ji, Phys. Rev. **D55**, 7114 (1997).

[Ji:97b] X. Ji, Phys. Rev. Lett. **78**, 610 (1997).

[JKGW:93] H. Jung, D. Krücker, C. Greub and D. Weyler, Z. Phys. **C60**, 721 (1993).

[JNT:99] G. Japaridze, W.-D. Nowak and A. Tkabladze, *Color Octed Contribution to J/ψ Photoproduction Asymmetries*, hep-ph/9908336, 1999.

[Jun:94] H. Jung, *EPJPSI 3.3 – Monte Carlo Generator for J/ψ–Mesons*, DESY, 1994.

[Kai:97] R. B. Kaiser, *Measurement of the Spin Structure of the Nucleon using Polarised Deep inelastic Scattering*, PhD thesis, Simon Fraser University, 1997.

[Kol:98a] M. Kolstein, *Exclusive ρ^0–Meson Electroproduction at HERMES*, PhD thesis, Vrije Universiteit Amsterdam, 1998.

[Kol:98b] H. Kolster, *The HERMES gaseous internal polarized proton target and its use in the HERA positron storage ring*, Dissertation, Ludwig-Maximilians-Universität München, 1998.

[Krä:96] M. Krämer, Nucl. Phys. **B459**, 3 (1996).

[Kri:90] A. D. Krisch, Z. Phys. **C46**, 133 (1990).

[Kro:99] P. Kroll, *Probing the Nucleon At large Momentum Transfer*, hep-ph/9907301, 1999.

[KZSZ:95] M. Krämer, J. Zunft, J. Steegborn and P. Zerwas, Phys. Lett. **B348**, 657 (1995).

[LDMS$^+$:99] B. Lehmann-Dronke, M. Maul, S. Schaefer, E. Stein and A. Schäfer, Phys. Lett. **B457**, 207 (1999).

[Lor:97] W. Lorenzon, *Beam polarimetry at HERA*, in *Proceedings of the 7^{th} Workshop on Polarised Gas Targets and Polarised Beams*, Urbana-Champaign, USA, 1997.

[LSS:98] E. Leader, A. V. Sidorov and D. B. Stamenov, Phys. Rev. **D58**, 114028 (1998).

[M$^+$:96] F. Meißner et al., *Photoproduction Trigger for HERMES*, HERMES Internal Note 96-026, 1996.

[Man:99a] S. I. Manayenkov, Private Communication, 1999.

[Man:99b] S. I. Manayenkov, *Regge Description of Spin-Spin Asymmetry in Photon Diffractive Dissociation*, DESY 99-016, hep-ph/9903405, 1999.

[Man:99c] L. Mankiewicz, Private Communication, 1999.

[Mar:91] C. Mariotti, Nucl. Phys. **A532**, 437 (1991).

[Mar:99] J. Martin, *Measurement of the Spin Asymmetry $A_{||}$ in the Photoproduction of High-pT Hadron Pairs*, PhD thesis, Massachusetts Institute of Technology, 1999.

[Mei:98] F. Meißner, *Charm Production at HERMES*, in *The 13^{th} International Symposium on High Energy Spin Physics*, Protvino, Russia, 1998.

[Men:98] F. Menden, *Measurement of the Valence Quark Spin Distributions of the Nucleon Using Deep Inelastic Scattering at HERMES*, Masters Thesis, Simon Fraser University, 1998.

[Mer:99] P. Merkel, Private Communication, 1999.

[MM:97] H. Merabet and J.-F. Mathiot, Z. Phys. **C75**, 495 (1997).

[MMMG:94] H. Merabet, J.-F. Mathiot and R. Mendez-Galain, Z. Phys. **C62**, 639 (1994).

[MNS:87] A. D. Martin, C.-K. Ng and W. J. Stirling, Phys. Lett. **B191**, 200 (1987).

[MP:99] L. Mankiewicz and G. Piller, *Comments on Exclusive Electroproduction of transversely Polarized Vector Mesons*, hep-ph/9905287, 1999.

[MPR:99] L. Mankiewicz, G. Piller and A. Radyushkin, Eur. Phys. J. **C10**, 307 (1999).

[MPW:98] L. Mankiewicz, G. Piller and T. Weigl, Eur. Phys. J. **C5**, 119 (1998).

[MPW:99] L. Mankiewicz, G. Piller and T. Weigl, Phys. Rev. **D59**, 017501 (1999).

[MRT:97] A. D. Martin, M. G. Ryskin and T. Teubner, Phys. Rev. **D55**, 4329 (1997).

[NMC:91] D. Allasia et al. (NMC Collaboration), Phys. Lett. **B258**, 493 (1991).

[NMC:92] J. Ashman et al. (NMC Collaboration), Z. Phys. **C56**, 21 (1992).

[NMC:97] M. Arneodo et al. (NMC Collaboration), Nucl. Phys. **B483**, 3 (1997).

[NT:98] W.-D. Nowak and A. Tkabladze, Phys. Lett. **B443**, 379 (1998).

[Per:74] M. L. Perl, *High Energy Hadron Physics*, Wiley & Sons, 1974.

[Per:87] D. H. Perkins, *Introduction to High Energy Physics*, Addison-Wesley, 1987.

[Rad:96] A. V. Radyushkin, Phys. Lett. **B380**, 417 (1996).

[Rad:97] A. V. Radyushkin, Phys. Rev. **D56**, 5524 (1997).

[Rob:90] R. G. Roberts, *The Structure of the Proton*, Cambridge University Press, 1990.

[RRML:97] M. G. Ryskin, R. G. Roberts, A. Martin and E. M. Levin, Z. Phys. **C76**, 231 (1997).

[RS:66] M. Ross and L. Stodolsky, Phys. Rev. **149**, 1172 (1966).

[Rys:93] M. G. Ryskin, Z. Phys. **C57**, 89 (1993).

[Rys:97a] M. G. Ryskin, Phys. Lett. **B403**, 335 (1997).

[Rys:97b] M. G. Ryskin, *Diffractive ρ-meson Leptoproduction on Polarized Nucleon*, hep-ph/9706505, 1997.

[Rys:99] M. G. Ryskin, Private Communication, 1999.

[S$^+$:98] D. D. Schepper et al., Nucl. Instr. Meth. **A 419**, 16 (1998).

[Sak:60] J. J. Sakurai, Ann. Phys. **11**, 1 (1960).

[Sak:69] J. J. Sakurai, Phys. Rev. Lett. **22**, 981 (1969).

[Sch:99] A. Schäfer, Private Communication, 1999.

[SMC:97] D. Adams et al. (SMC Collaboration), Phys. Rev. **D56**, 5330 (1997).

[SMC:98a] B. Adeva et al. (SMC Collaboration), Phys. Rev. **D58**, 112002 (1998).

[SMC:98b] B. Adeva et al. (SMC Collaboration), Phys. Lett. **B420**, 180 (1998).

[SS:72] J. J. Sakurai and D. Schildknecht, Phys. Lett. **B40**, 121 (1972).

[SSS:99] D. Schildknecht, G. A. Schuler and B. Surrow, Phys. Lett. **B449**, 328 (1999).

[ST:64] A. Sokolov and I. Ternov, Sov. Phys. Doklady **8**, 1203 (1964).

[Ste:97] J. Stewart, The HERMES Polarized Hydrogen Internal Gas Target, in *Proceedings of the 7^{th} Workshop on Polarised Gas Targets and Polarised Beams*, Urbana-Champaign, USA, 1997.

[SW:73] K. Schilling and G. Wolf, Nucl. Phys. **B61**, 381 (1973).

[Tip:99] B. Tipton, *Measurement of Polarized Parton Distributions With Spin-Dependent Deep-inelastic Scattering*, PhD thesis, Massachusetts Institute of Technology, 1999.

[Tri:99] A. Tripet, *Exclusive Rho Production in Polarized DIS at SMC*, in *Proceedings of 7th International Workshop on DIS and QCD (DIS 99)*, Zeuthen, Germany, 1999.

[TT:97] O. Teryaev and A. Tkabladze, Phys. Rev. **D56**, 7331 (1997).

[VGG:98] M. Vanderhaeghen, P. A. M. Guichon and M. Guidal, Phys. Rev. Lett. **80**, 5064 (1998).

[VM:98a] M. Vänttinen and L. Mankiewicz, *Exclusive J/ψ photoproduction and gluon polarization*, hep-ph/9807287, 1998.

[VM:98b] M. Vänttinen and L. Mankiewicz, *Hard exclusive J/ψ production on polarized targets*, hep-ph/9805338, 1998.

[Vol:99] E. Volk, Private Communication, 1999.

[vW:34] C. F. v. Weizsäcker, Z. Phys. **88**, 612 (1934).

[W^+:90] L. W. Whitlow et al., Phys. Lett. **B250**, 193 (1990).

[Wan:96] W. Wander, *Rekonstruktion hochenergetischer Streuereignisse im HERMES-Experiment*, Dissertation, Universität Erlangen-Nürnberg, 1996.

[Wat:81] A. D. Watson, Z. Phys. **C12**, 123 (1981).

[Wei:98] C. Weiskopf, *Untersuchung der Bhabha-Asymmetrien mit dem HERMES-Luminositätsmonitor*, Diplomarbeit, Universität Erlangen-Nürnberg, 1998.

[Wil:34] E. J. Williams, Phys. Rev. **45**, 729 (1934).

[WS:78] G. Wolf and P. Söding, Many–Body Processes, in *Electromagnetic Interactions of Hadrons, Vol.2*, Plenum Press, New York, 1978.

[ZEUS:97] J. Breitweg et al. (ZEUS Collaboration), *Measurement of Inelastic J/ψ Photoproduction at HERA*, DESY 97-147, 1997.

[ZEUS:99] J. Breitweg et al. (ZEUS Collaboration), Eur. Phys. J. **C6**, 603 (1999).

Acknowledgements

The past four years of work in the inspiring atmosphere of the HERMES collaboration at Hamburg have been a challenging and enjoyable time. I would like to thank all my colleagues for their help and advice during my work; a successful completion of this thesis would not have been possible without it. I apologise to all those whose names are left out in the following.

First of all, I want to thank my supervisor Dr. Wolf–Dieter Nowak of DESY–Zeuthen for giving me the opportunity to work at the HERMES experiment. I appreciate his valuable advice, the fruitful discussions, and last but not least the freedom he gave me to follow my own interests in the physics analyses.

I am indebted to Prof. Thomas Lohse for taking over the official support of this thesis at the Humboldt–University Berlin. For his advice and his valuable support, especially at the final stage of this work, I am very grateful to Prof. Klaus Rith of Erlangen.

Working in the friendly atmosphere of the Zeuthen–HERMES group was always a pleasure. I wish to thank Stephan Brons for his hints and guidance and the help with the Monte Carlo simulations; I enjoyed working together with him on the charm analysis. I benefited from many fruitful discussions especially with Elke Aschenauer, Uta Stößlein, Helmut Böttcher, Wolf-Dieter Nowak, and Adolf Schwind. From all those I learned a lot about physics, data analysis, and detectors.

Thanks to Alexander Borissov for having made the first steps in the J/ψ analysis at HERMES. I wish to express thanks to the members of the vector meson analysis group, especially to Tom O'Neill for the cross check of the results of the ρ asymmetry analysis. I am grateful to the NMSU-trigger group: Pam Chumney, Gary Kyle, Steve Pate, and Gunar Schnell for their help and the discussions concerning trigger design and analysis. I wish to thank Avto Tkabladze for checking my calculations and for his help with my physical understanding. For the asymmetry analysis I benefited a great deal from the results and the cooperation of the inclusive analysis group: Delia Hasch, Uta Stößlein, Yvo Gärber, Manfred Ferstl, and Andreas Gute. The members of the HERMES software group: Klaus Ackerstaff, Erik Volk, Manfred Ferstl, Marc–Andre Funk, and Wolfgang Wander helped improve my programming skills; I learned a lot about software and computers from them.

Uta Stößlein, Pam Chumney and Wolf–Dieter Nowak have been a great help when writing this thesis; I am indebted to them for their suggestions and comments on its content, structure, and language. I wish to thank Elke Aschenauer, Delia Hasch, Ciara Simani, Marc Beckmann, and Helmut Böttcher for proofreading parts of this work.

Staying in Hamburg was not only a physics challenge. The Offsite Meetings have been a good place to relax after work and enjoy non–physics related conversations. I greet the colleagues and offsiters Antje, Chiara, Naomi, Brendan, Ed, Erik, Greg, James, Jeff, Jim, Jeroen, Klaus, Machiel, Marc, Phillip, Thomas, and Wolfgang: knowing that this list will be incomplete. A special thanks goes to Maf who was a great help not only with physics discussions but also to relax in the Bermuda triangle of Ottensen. I want to thank my part–time flat mate Andreas for his enjoyable company. A special greeting goes to Delia: yep we got this done as well. I want to thank Jens, Sylvia, and Pam for helping me not to lose my shape on the computer terminal completely by making me move once in a while. In this sense, keep on running Greg!
I want to thank Pam for all her patience and love.